University of Southampton

Biomineralisation and Geochemistry of Hydrothermal Vent Fauna

by Ellis Maginn

A dissertation submitted for Degree of Doctor of Philosophy

School of Ocean and Earth Science

March 2002

This thesis was submitted for examination in March 2002. It does not necessarily represent the final form of the thesis as deposited in the University after examination.

Graduate School of the Southampton Oceanography Centre

This PhD dissertation by

Ellis Maginn

has been produced under the supervision of the following persons:

Supervisors

Dr Rachel A. Mills

Dr Richard J. Herrington
(Natural History Museum of London)

Chair of Advisory Panel
Dr Steve Roberts

Members of Advisory Panel

Dr Ian C. Harding

Dr Crispin T.S. Little
(University of Leeds)

UNIVERSITY OF SOUTHAMPTON

ABSTRACT

FACULTY SCHOOL OF SCIENCE, SCHOOL OF OCEAN AND EARTH SCIENCE

Doctor of Philosophy

Biomineralisation and Geochemistry of Hydrothermal Vent Fauna

By Ellis Maginn

Hydrothermal vent fauna, particularly vestimentiferan and polychaete worm tubes, are occasionally preserved in the geological record. The early stages of mineralisation are particularly important in defining whether or not preservation will occur, and they are poorly understood. This dissertation describes 3 separate studies of vent fauna undergoing early mineralisation associated with active seafloor vent systems. Tube samples of the polychaete worm Alvinella pompejana collected from 13°N on the East Pacific Rise were studied to identify the processes occurring during early sulphide mineralisation. Iron sulphide mineralisation is present within the walls of the organic dwelling tube, and is induced by microbial fauna preserved within the tube micro-layers. A laminated tube structure was formed, comprising alternating layers of tube material and microbially templated iron sulphide-rich interlayers. The iron monosulphides mackinawite and greigite, have been identified as intermediate phases that occur as precursor minerals during the formation of pyrite. Later marcasite mineralisation is observed to form over some of the pyritised organic layers.

Later stagemineralisationprocesses in a selection of fossil tube structures recovered from an extinct sulphide mound on the Southern East Pacific Rise were studied. The similarity to existing faunal assemblages suggests that these structures were also associated with Alvinella sp. polychaete worms. Two generations of pyrite were identified along with a later stage chalcopyrite phase. Fine scale variability in tube wall geochemistry was demonstrated with electron micro-probe transects across the structures and this is inferred to reflect early mineralisation processes as identified in living

polychaete worms. Sulphur isotope analyses of the different sulphide phases gave $\delta^{34}S$ values higher than any previously measured for chimney structures on a sediment-free ridge setting ($\delta^{34}S$ = 3.8-10.8‰). A two stage model is proposed whereby early pyrite / marcasite laminae originally laid down in association with biogenic tube structures, are replaced by euhedral pyrite, and later stage primary chalcopyrite precipitation.

A study of Ridgea piscesae from the Juan de Fuca Ridge demonstrated that silicification processes proceed so rapidly that the vestimentiferan tubes can become mineralised during the worm's life cycle. The organic component of the worm tube is rapidly replaced by amorphous silica which undergoes dewatering to form opal-A. This mineralisation is then overgrown by barite laths, and microbially templated amorphous silica. With time, prograde mineralisation causes the further precipitation and consequent overprinting of the primary mineral suite with iron- and zinc-sulphides. Other observations from samples studied here include micro-tubes (~50 μm length) associated with adult R. piscesae and a silicified mucus lining to inhabited worm tubes. Associated with the mucus lining is a ligament which runs along the inside of the tube, and is tentatively inferred to be a form of anchor, allowing the worm to rapidly retract into the tube when threatened.

Once mineralisation has replaced the organic tube material there is scope for the tube structure to be preserved along with the host sulphide body. Understanding of the mechanisms of early sulphide and silica/barite mineralisation as inferred from detailed observations and measurements of tube worm samples is an important contribution to the growing field of hydrothermal palaeobiology.

Contents

Acknowledgements

I sincerely wish to thank my supervisors Dr. Rachel Mills and Dr. Richard Herrington, for their continual hard work, support and advice during this study, for some memorable nights out, and for giving me such a wonderful opportunity. I thank Dr. Steve Roberts for his efforts as Chair of my thesis panel (and particularly for arranging for most of our meetings to be in the coffee bar), and Dr. Ian Harding for his efforts as an independent advisor, for taking on the (possibly) thankless task of internal examiner, and mainly for lighting the way during my undergraduate years. I also wish to give special thanks to Dr. Cris Little for putting in as much, if not more, effort as any supervisor ever could, and for being the primary driving force behind this project.

I wish to acknowledge D. Desbruyères, the co-chief scientist of the 1991 HERO cruise for collecting the samples used in Chapter 4 and M. Segonzac for donating the sample to the Natural History Museum of London Collection; P. Herzig, chief scientist of 1995 GEOMETEP-5 for collecting the samples used in Chapter 5 and donating them to the Natural History Museum of London Collection; C. L. van Dover, chief scientist of the 1995 High Rise Expedition for collecting the samples used in Chapter 6, and J. Copley for donating them to me.

I thank R. Jones and J. Ford (A.K.A the basement-boys: Bob & John) for sample preparation; B. Marsh for photographic support; K. Grant for FT-IR tuition (and numerous table tennis defeats at lunch times), J. Spratt for support with EMP analysis; Adrian Boyce (SURRC, Glasgow) for sulphur isotope tuition and support; John Marshall

for florescence microscopy tuition; B. Cressey who gave support for SEM analyses at the Southampton Oceanography Centre; and Chris Jones for SEM and HFSEM support at the Natural History Museum.

I thank Rachel Mills, Richard Herrington, Crispin Little, Adrain Boyce, Jon Copley and Nikki Standing for comments on the various versions that this work has taken in manuscript form and their relative (and always constructional) comments .

Finally, and most importantly, I wish to thank my parents, family and especially my girlfriend, Nikki for supporting me (in almost every way possible) during, what has turned out to be, some difficult years for all of us – Thanks...!.

This project was funded by a NERC CASE studentship GT4/97/273/ES and the Natural History Museum of London.

Chapter 1

Introduction: fluid flow and hydrothermal venting.

1 - Introduction.

Submarine hydrothermal vent sites have been located in a variety of different tectonic settings, such as: mid-ocean ridges; back-arc basins; island arcs; seamounts and hotspot-generated island chains (Karl, 1995). A large number of convergent, and divergent seafloor boundaries have been explored, and over 150 vent sites have been found, showing evidence of significant seafloor hydrothermal activity, in the past or present (Rona & Scott, 1993), and of these 150 sites, 35 have been confirmed to be presently active (Figure 1.1: Butterfield, 1999), each forming mineralised structures of some type. Within the expansive scientific literature, there is a wide spectrum of information available documented from the earliest stages of vent development, where maybe only water column plume studies indicate hydrothermal anomalies, through to hydrothermal systems which have been repeatedly sampled and thoroughly explored. However, despite the immense interest in seafloor hydrothermalism in recent years, countless questions remain about the interplay between their geological, physical, chemical, and biological components.

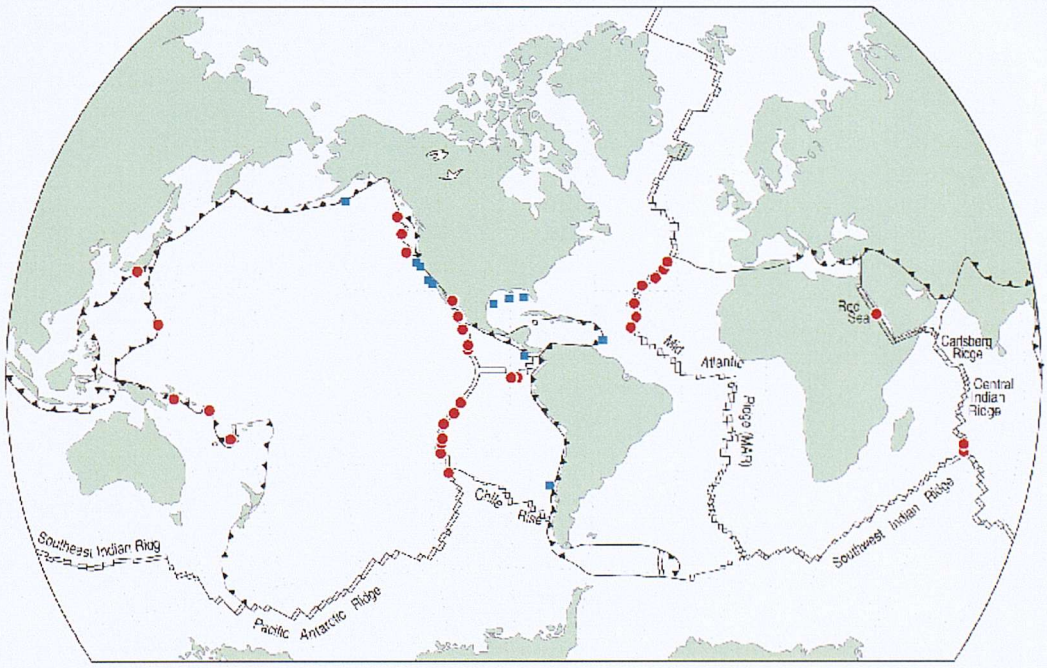

Figure 1.1 – The global ocean showing known sites of hydrothermal vents and cold seeps. Vents are shown in red. Seeps are shown in blue. Adapted from MBARI mapping program data.

1.1 - Submarine hydrothermal systems and vent formation.

Hydrothermal structures are produced by the venting of heated (30 - 400°C), mineral-rich fluids through cracks and fissures (Figure 1.2) (Haymon *et al.*, 1984; Fouquet *et al.*, 1991). These fluids are derived from ambient seawater that is entrained by hydrothermal convection cells within the newly formed lithosphere (Figure 1.3), and are driven by magmatic heat at depth. Submarine hydrothermal systems are an integral component of crustal construction along the global system of mid-ocean ridges. Thermally-induced circulation of seawater through the permeable parts of the crust and upper mantle has been estimated to account for 34% of the predicted global oceanic heat flux, which in turn comprises close to 25% of the total heat flux of the Earth Stein, 1994. Because the new lithosphere is hot and buoyant, cooling fractures are created, providing a pathway for the downwelling of seawater towards a sub-seafloor heat source, *via* a process known as recharge.

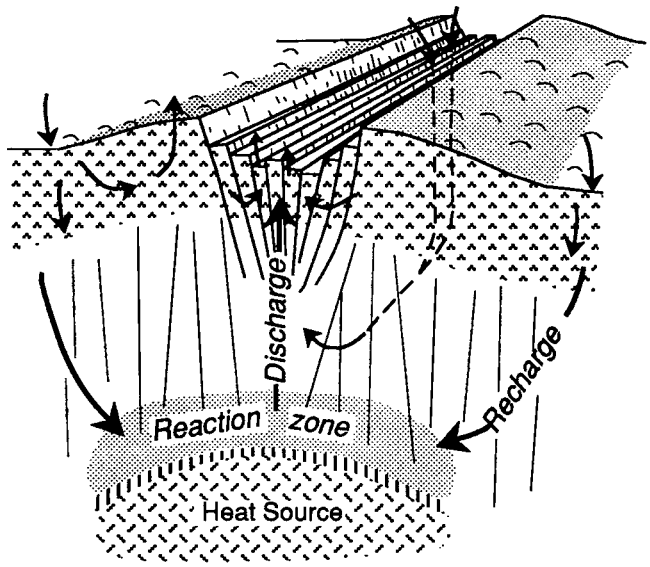

Figure 1.2 - A schematic cross-section of a mid-ocean ridge system. The heat source (magma chamber) driving the sub-surface circulation is clearly visible, along with inferred circulation paths of seawater-derived hydrothermal fluid. The location of the cracking front,is located just above the magma melt. A combination of relatively low temperatures, high temperatures, and abundant fresh rock at the cracking front of the crystallising magma chamber promotes rock alteration and fluid composition interchange. Permeable fractures characterise the upflow zone, and allow fluids to ascend the lithosphere, until venting occurs at the seafloor surface (from Alt, 1995).

1.1.1 - Recharge

During recharge, cold seawater (~2°C) permeates through the lithospheric crust in a broad zone where temperatures are relatively low (generally <350°C) (Alt, 1995). As fluid percolates down through the sub-seafloor, the temperature rises causing the fluid to interact chemically with the surrounding rock. This leads to an exchange of chemical elements between the evolved seawater and the crust. The nature of these basalt-seawater reactions is temperature dependent. At 70°C, the reactions are relatively slow; Mg, Na and K are removed from the fluid, whilst Ca and silica are added (Seyfried & Bischoff, 1979). At 150°C, the reactions are more rapid; Mg and sulphate are removed from the water, whilst Ca, Na, K, Fe, Mn, Zn, Cu, Ba and silica are all added (Seyfried & Bischoff, 1979; Seyfried & Mottl, 1982). Finally, above 150°C, the retrograde solubility of anhydrite ceases and Ca and sulphate ions are removed from the water by the anhydrite precipitation (Berndt *et al.,* 1988). Anhydrite is saturated in seawater at temperatures of

below 150°C (Shock, 1996). The removal of dissolved sulphate by heating during recharge has been measured as 27mmol/kg (at 25°C), and 9mmol/kg (at 350°C), with the precipitation of magnesium-hydroxysulphide stripping the fluid of sulphate ions still further (Bischoff, 1978).

1.1.2 – Reaction

After the recharge zone, which is characterised by descending fluid flow, the convecting fluid enters a region known as the 'reaction zone' above the top of the solidifying magma chamber. This region is generally thought to occur at the maximum penetration depth of the fluid. It is characterised by temperatures in excess of 375°C (Berndt *et al.*, 1989) and horizontal fluid flow over the thin (sub decimeter), cracking front (Alt, 1995). The elevated temperatures in the reaction zone lead to extensive seawater-basalt reactions including the exchange of metals and cations and the further removal of sulphate from the water (Seewald & Seyfried, 1990). The cracking front and the adjacent reaction zone form a unique geochemical environment. Near the critical point, the kinematic viscosity of seawater is ~1/16th of that of cold seawater; its mass flow rate through a given crack for a given pressure gradient is thus 16 times greater(Alt, 1995). During crystallization, the components of the magma which do not readily enter the crystalline lattices, e.g. dissolved gases, are concentrated into the intergranular boundaries. After the rock solidifies at ~980 °C, further cooling of the crystalline matrix leads to differential contraction of the mineral grains, opening the intergranular boundaries to the penetration of seawater at the cracking front, allowing extraction of these mobile components, and reaction of those minerals least stable under these conditions, e.g. olivine. This mechanism accounts for the depletion of Fe, Mn, and other elements in crystalline ocean crust rocks relative to rapidly quenched glassy rocks, the formation of ore-forming hydrothermal solutions by seawater convection through the crust and the usefulness of studies of glassy rocks for estimating the global hydrothermal flux of magmatic components such as the rare gases (Corliss, 1971).

The dominant chemical effects in the reaction zone can be summarized as follows:

(1) The reduction of the fluids by reaction with ferrous iron in the basalt, both by reduction of the sulphate (McDuff and Edmond, 1982) (1a):

$$8FeO + SO_4^{2-} \rightarrow 4Fe_2O_3 + S^{2-} \quad (1a)$$

and presumably by the dissociation of water (1b):

$$2FeO + H_2O \rightarrow H_2 + Fe_2O_3 \quad (1b)$$

where the Fe^{+2} is understood to be in a primary basalt mineral, such as olivine, and the Fe^{+3} is incorporated into the clay minerals saponite or chlorite. Saponite is a typical alteration product of ocean crust basalts found abundantly along the fracture surfaces of dredged rocks (Humphris and Thompson, 1978; Seyfried and Bischoff, 1979; Stakes and O'Neil, 1982).

(2) The removal of Mg from the fluid contributes H^+ (1c):

$$Mg^{2+} + 2H_2O \rightarrow Mg(OH)_2 + 2H^+ \quad (1c)$$

where the $Mg(OH)_2$ (brucite) forms an interlayer in the typical saponite-chlorite clay (Rosenbauer and Bischoff, 1983). In the experimental studies, a magnesium bearing phase was produced, magnesium-hydroxysulphate-oxide (Bischoff and Seyfried, 1978), which has also been found as a minor component of deposits around the vents (Haymon and Kastner,1981). The formation of this phase can account for some of the depletion in sulphate and magnesium, and thus the increase in acidity, but its quantitative importance relative to sulphate reduction and saponite formation in natural systems remains to be clarified.

(3) The reaction of these acid solutions with the basalt to form clays releases silica and a variety of cations (Ca^{+2}, Ba^{+2}, Fe^{+2}, Mn^{+2}, Cu^{+2}, Zn^{+2}) initially present in the basalt silicate lattices (1d):

$$Basalt + H^+ + H_2O \rightarrow SiO_2(into\ soln) + Clays + Cations \quad (1d)$$

Of these cations, the reduced transition metals will stay in solution in the presence of sulphide at high temperature, due to the stability of chloride complexes (Krauskopf, 1967). But they will precipitate on mixing with cold sea water, as seen in the smokers, because these complexes become unstable at low temperature. The calcium will precipitate as anhydrite in the presence of sulphate at high temperature and tend to

dissolve on cooling (e.g. Bischoff and Seyfried, 1978). Some anhydrite is found in deposits around the high temperature vents. McDuff and Edmond (1982) argue, on the basis of the absence of a strontium depletion, that gypsum production is not responsible for the observed depletion of sulphate in the equilibrium fluids in the Galapagos or 21° N EPR samples. Barium is deposited as barite on mixing of the fluids with cold, sulphate bearing sea water; abundant barite is found in vent deposits (Haymon and Kastner, 1981).

Estimates of the typical residence time of fluids in the reaction zone can be made from radioisotope studies and range from less than 3 years (Kadko & Moore, 1988) to 20 years (Grasty *et al.,* 1988). It is expected that the reaction zone spans a temperature range from ~400°C at its top to ~1200°C at its base. The subsequent vertical temperature gradient gives rise to a conductive heat flux which delivers heat from the magma chamber to the water in the convection cell. Thermal calculations show that the reaction zone must be fairly thin (~ 100 m) in order to maintain the typical power output (~100 MW) of a hydrothermal system (Lowell & Germanovich, 1994). These authors argue that such a thin boundary layer might be maintained by downward migration of the hydrothermal system into freshly frozen magma. It is argued, however, that these mechanisms are not necessary in order to restrict the thickness of the thermal boundary layer. Rather, it is shown that a thin boundary layer spanning the temperature range ~400°C to ~1200°C is an inevitable consequence of the nonlinear thermodynamic properties of water. The leaching of elements from the ductile basaltic magma (Shock, 1996) and into the migrating fluid (*via* fluid-rock exchange) results in the production of hydrothermal fluids, which ascend the newly forming seafloor *via* vertical fractures (Seyfried & Mottl, 1995). On longer time scales, these water-rock interactions play a role in regulating the chemistry of seawater, although the magnitude of the associated elemental fluxes are not well constrained.

1.1.3 – Discharge

After the reaction zone, the convecting water enters a 'discharge zone' through which it ascends to the hydrothermal vents on the seafloor. The typical dimensions of a hydrothermally active region of the seafloor (<100 m) are considerably less than the

expected dimensions of the magma chamber (~ 1000 m) and so the upflow zone is inevitably focused. It is probable that high permeability pathways, caused by fractures, faults or textural inhomogeneities in the crust, serve to focus the upflow in the discharge zone. It must be stressed, however, that these inhomogeneities in crustal permeability are not *necessary* in order to impose the required structure on the cell. Some degree of focusing is unavoidable in a convection cell, even in the absence of any high permeability pathways. Two mechanisms cause the fluid to cool as it rises through the discharge zone: conductive heat loss and adiabatic cooling. The former is caused by horizontal temperature gradients in the discharge zone, while the latter is a consequence of depressurisation. As an example, consider a hydrothermal vent field 2.5 km below sea level, where the pressure is ~25 MPa. If the reaction zone lies a further 1 km below the seafloor, then the upwelling fluid depressurises from ~35 MPa to ~25 MPa during its ascent through the discharge zone. Under adiabatic cooling alone, water leaving the reaction zone at ~400°C would cool to ~352°C on ascent to the seafloor (Alt, 1995). The presence of conductive heat loss means that the true degree of cooling in the discharge zone is somewhat greater.

1.1.4 – Venting

Finally, after ascending through the discharge zone, the convecting fluid is expelled at hydrothermal vents on the seafloor. The minerals dissolved in the fluid precipitate on contact with the cold ocean waters to form mineralic chimneys with an internal diameter of ~0.01 m to ~0.1 m (Lowell *et al.,* 1995). The effluent typically exits from these chimneys at a speed of ~1 ms^{-1} (Tivey, 1995). Thus, if these exit speeds are comparable with the speed of ascent in the discharge zone, the fluid could ascend from the reaction zone to the seafloor in a matter of a few minutes (Dickson, 1998). This possibility of a 'rapid' ascent is sometimes correlated with the inference that the fluid does not lose much heat on its ascent through the discharge zone. It might then be argued that a 'rapid' ascent is necessary to ensure that conductive heat losses during ascent are minimal. Qualitatively this is true, but it must be stressed that definition of what constitutes a 'rapid' ascent depends on the rate at which heat is lost conductively by the ascending fluid. Numerical models can show that minimal heat loss can occur during

ascent even when there are no high permeability pathways and the ascent time is as large as several years.

1.1.5 – Constraints, distribution and variability

The most rigid constraint on hydrothermal fluid circulation is provided by the temperature of the fluid expelled at the seafloor. No hydrothermal effluent hotter than 404°C has been observed (Campbell *et al.,* 1988). This is particularly remarkable because it is so much less than the temperature of the heat source (~1200°C: Lister, 1996; Lowell *et al.,* 1995; Wilcock, 1998). Consequently, a successful model for hydrothermal circulation must explain the discrepancy between the inferred temperature of the heat source and the observed temperature of the effluent at the seafloor (~800°C). For some time it has been suspected that the nonlinear thermodynamic properties of water (above ~200°C) might be responsible for this temperature difference. However, the claim has never been rigorously tested or explained (Bischoff & Rosenbauer, 1985; Johnson & Norton, 1991).

Hydrothermal fluids have radically different chemical and thermal properties from seawater. It is mainly the changes in fluid density, coupled with differences in fluid-filled fracture geometry (Cann *et al.*, 1985) that causes rapid flow rates towards the seafloor surface. As the critical point for the fluid is approached, the molar volume of the fluid increases exponentially and the fluid rapidly rises through the lithospheric crust, to be expelled at the seafloor. Flow rates measured by Converse *et al.* (1984) measured direct, flow rates between 0.7 and 3.4 ms^{-1} (at hot springs located at 21°N East Pacific Rise (EPR) and the Juan de Fuca Axial Ridge, respectively). Circulation of seawater through the oceanic crust and upper mantle gives rise to a complex series of physical and chemical reactions that lead to the formation of seafloor mineral deposits and to the existence of unique biological communities. In addition, alteration of the basement rocks and mineral precipitation within fractures dramatically influence the thermal structure and physical properties of the oceanic lithosphere, and change the chemistry of the crustal material that is returned to the mantle by subduction. Off-axis fluid flow may extend out to the crustal sealing age of 650 million years, and may be responsible for more than 70% of the hydrothermal heat flux (Stein, 1994).

1.2 - Rock-water interactions in the oceanic crust.

Venting fluids and sea floormineralisationrepresent the end result of a complex series of physical and chemical reactions that occur between crustal rocks and seawater in the subsurface portion of active hydrothermal systems. The fluids are generally considered to achieve their characteristics at the base of the hydrothermal cell in a reaction zone where temperatures are 375 – 425° C and water/rock ratios are low (e.g. Seewald, 1990; Seyfried Jr., 1991). However, the link between the subsurface alteration assemblages and the fluid chemistry of active hydrothermal vents is not yet well constrained (Gillis, 1993). As the oceanic crust is transported away from the ridge, the water-rock reactions evolve. This is because the characteristics of the hydrothermal circulation respond to cooling, changes in the physical properties of the crust (in particular porosity and permeability), and reorganization of the pathways of fluid flow. Consequently, the mineralogy and chemistry of hydrothermally altered rocks recovered from the sea floor and from ophiolites reflect the integrated effects of all axial and ridge flank hydrothermal processes and provide a record of the extent of chemical exchange between the crust and seawater, the nature of the reactions that have taken place, and the variation in the composition of the circulating fluids. These diagenetic changes are also reflected in the nature of the palaeontology observed in hydrothermally derived settings.

Over the last fifteen years, studies of altered rocks from the sea floor and from ophiolites have been combined with experimental and theoretical studies to investigate the variations in water-rock interactions in different portions of submarine hydrothermal systems (Alt, 1995). Perhaps one of the most significant areas of progress in recent years have been the investigation of alteration processes within lower crustal rocks. These studies have been enhanced by drilling into oceanic crust, which has recovered stratigraphic sections from the lower sheeted dikes and upper gabbros (Alt *et al.*, 1996). In combination with studies of ophiolite sequences and experimental work, these investigations have resulted in the recognition that the reaction zone (where hydrothermal fluids are thought to acquire their final composition) may well lie within the lower part of the sheeted dikes and in the upper gabbros.

Hydrothermal convection in the oceanic crust is inferred to be layered, with large volumes of seawater circulating through the upper volcanics and reacting at temperatures of <150° C, and only a small percentage penetrating into the sheeted dikes and upper gabbros (Alt, 1986; Gillis, 1990; Hart, 1994). The mineralogy and chemistry of the lower 500-600 m of the sheeted dikes include secondary Ca-rich plagioclase (which is locally replaced by anhydrite) and hornblende, increasing Al and Ti contents of amphibole, and lower $\delta^{18}O$ values, suggestive of high temperatures of alteration (400 – 500° C) and consistent with $\delta^{18}O$ values attributed to the reaction zone (Alt, 1994). Hydrothermally altered plutonic rocks from the sea floor collected by dredging, drilling and from submersibles indicate that the reaction zone extends into the upper gabbros, forming a mineral suite at depth, typically consistant with greenschist facies metamorphism (Von Damm, 1988).

This general sequence of events - plastic deformation and metamorphism at high temperatures, followed by brittle deformation and the circulation of fluids, and then cooling with further alteration at lower temperatures - is observed in other sea floor metagabbros(Alt, 1994), although the details vary in response to the magmatic and tectonic interactions within each area. However, the timing of fluid penetration, the pathways of fluid flow, and the depth of penetration of hydrothermal fluids into the gabbros are not yet well constrained, these are questions that are only recently beginning to be addressed by deep crustal drilling (Kelley, 1993).

Permeability is the most critical variable controlling patterns of fluid flow in hydrothermal systems both in space and time. Early observations of the wavelengths of elongate, off-axis heat flow anomalies combined with numerical models of fluid flow through homogeneous porous media and assumptions of high crustal permeability down to depths of >1 km, implied that hydrothermal circulation systems reached depths of several kilometres (Alt, 1995). However, the permeability structure of the oceanic crust is strongly layered and only the top few hundred meters are highly permeable (Becker, 1989; Becker, 1991). Little is known about the lateral heterogeneity of the crustal permeability structure or the spatial and temporal persistence of layers with distinct hydrogeological properties.

Despite the difficulties associated with using sea floor measurements to infer the existence and character of subsurface hydrothermal circulation cells, considerable progress has been made in the last few years by combining detailed geophysical and geochemical data from field surveys and drilling with increasingly sophisticated numerical modelling techniques. At the Juan de Fuca Ridge, results from drilling an axial hydrothermal system have been combined with off-axis geophysical and geochemical studies to further our understanding of how hydrothermal systems change as they are transported away from the ridge crest. Permeability measurements made proximal to an active vent site at the Juan de Fuca Ridge, indicate the presence of several discrete zones of exceptionally high hydraulic conductivity, which, if typical of oceanic basement at spreading centres, must dominate circulation patterns in axial hydrothermal systems (Becker, 1994).

1.3 - Fluid composition at hydrothermal vents.

The composition of vent fluids is strongly influenced by fluid temperature, and it is well known that different venting localities can exhibit a wide range of temperature and chemical compositions (Fouquet *et al.*, 1991; Seyfried & Mottl, 1995; van Dover, 1995). The differences in vent fluid composition arise from the interaction with shallow sub-surface hydrology, namely the entrainment and mixing of seawater and low temperature fluids with rising high temperature fluids (Table 1.1). However, the physico-chemical composition of high temperature vent fluids (categorically, those fluids that have not had any contact with sub-seafloor fluids), is remarkably similar from one vent site to another (Von Damm, 1995). The main chemical changes in hydrothermal fluids occur closest to the magma chamber. Here high temperatures and abundant liquid cause reactions with fresh basalt along the cracking front. This results in the liberation of hydrogen sulphide, polymetallic sulphides, gases and various inorganic oxides in acidic solution. Fluid acidity of egressing fluids range from highly acidic solutions (pH 2) to near neutral and even mildly alkaline solutions (Fouquet *et al.,* 1991). Due to the high temperatures (400°C) and pressures (400 atm) in the sub-seafloor environment, the sulphides and oxides generated can remain in solution, usually until heat loss, and/or mixing, occurs. Heat loss can occur by two main methods: conduction into the country rock, or mixing with the ambient

seawater, and adiabatic heat loss (Seyfried & Mottl, 1995). It has been suggested by Seewald & Seyfried (1990) that conduction into the country rocks whilst ascending in the 'upflow zone', could be a significant method of heat loss in the hydrothermal environment. This is deduced by theoretical and experimental data (Seyfried & Mottl, 1995), which shows that the chemical composition of many black smoker fluids venting at 350°C on the sea floor actually formed at temperatures in excess of 400°C, allowing a wide range of minerals to be precipitated during the hydrothermal fluids' ascent through the upflow zone (Hannington Scott, 1998).

The hydrothermal circulation of fluids within the oceanic crust is not only restricted to regions in the immediate vicinity of spreading centers, but continues off-axis for possibly tens of millions of years. Although relatively little is known about this process, it is now recognized that fluid circulation and the associated alteration reactions and mineral precipitation play a profound role in the evolution of the physical properties of the oceanic crust (Stein & Stein, 1995).

	Seawater	EPR (13°-21°N)	Guaymas	S. Juan de Fuca	MAR (23°-26°N)	Lau Basin
Temp (°C)	2	273-354	315	300-350	321-390	334
pH	7.8	3.1-3.8	5.9	3.2	3.8	2
$SiO_{2\ (mM)}$	0.16	15.6-22	9.3-13.8	22.7-23.3	18.2-22	14
Cl (mM)	541	489-760	580-637	896-1090	559-659	650-800
SO_4 (mM)	28	0	0	0	0	0
B (μM)	419	-	-	-	518-530	770-870
Na (mM)	465	432.596	472-513	700-800	509-584	520-615
Li (μM)	26	591-1448	630-1076	1110-1810	411-1030	580-745
K (mM)	9.8	23.2-29.8	32.5-49	37.3-51.6	17-24	55-80
Rb (μM)	1.3	14.1-33	57-86	28-37	10-11.9	60-75
Mg (mM)	53	0	0	0	0	0
Ca (mM)	10.2	11.6-55	26.6-41.5	77.3-96.4	4.8-26	28-41
Sr (μM)	87	62-182	158-253	230-312	50-99	105-135
Ba (μM)	0.14	-	15-54	5-35	-	20-60
Cs (nM)	2.2	-	-	-	100-180	280-370
Fe (μM)	0.001	600-10170	8-180	10300-18700	1640-2180	1200-2900
Mn (μM)	0.001	361-2932	128-236	2610-4480	443-1000	5800-7100
Cu (μM)	0.007	2.-44	<0.02-1.1	<2	10-17	15-35
Zn (μM)	0.01	2-106	0.1-40	<900	50	1200-3100
Cd (nM)	1	17-180	0-46	-	-	700-1500
Pb (nM)	0.01	14.359	0-652	-	-	3800-7000
As (nM)	27	-	283-1074	-	-	6000-11000

Table 1.1 - End-member fluid values for different hydrothermal vents. Adapted from Forquet *et al.* (1991).

1.4 - Venting processes at the seafloor.

The sub-seafloor processes at hydrothermal systems are expressed at the surface by hydrothermal plumes and deposits. Hydrothermal plumes are responsible for significant heat and mass transfer from the lithosphere into the oceans (Rudnicki & Elderfield, 1992). As hot, buoyant, acidic hydrothermal fluids are discharged into cold, dense, alkaline seawater, the precipitation of polymineralic vent deposits and particle-rich hot plumes are observed. Hydrothermal deposits are diverse, and a variety of mineral phases have been recorded, these include sulphides, sulphates, oxides, hydroxides, silicates, and carbonates of a number of metallic cations (Karl, 1988; Fouquet *et al.*, 1991; Mills *et al.*, 1994; Winn *et al.*, 1995; Juniper & Tebo, 1996; Tivey, 1996; Little *et al.*,

1997). The most significant mineral phases forming at hydrothermal sites are massive sulphides and iron-silicon-manganese rich oxides (Tivey, 1996). The term 'massive sulphide' does not refer to either deposit size or texture, but instead implies a bulk composition of at least 60% sulphide (Sangster & Scott, 1976). Individual hydrothermal vent fields show a variable area ranging from hundreds to millions of square meters (Seyfried & Mottl, 1995). Within a field, sulphide deposits and active vents may typically cover 20 - 50% of the area. The largest sulphide bodies are typically composite masses, formed from the combination of adjacent hydrothermal mounds or the coalescence of adjacent chimneys and diffuse venting edifices (Hannington *et al.*, 1995).

Although black smoker vents are arguably the most spectacular features of seafloor hydrothermal systems, their generated heat flux may represent only 5% of the total heat flux generated from a hydrothermal mound as a whole (Schultz *et al.*, 1992). The majority of venting being achived by diffuse venting and white smokers.

1.4.1 - Diffuse venting and white smokers.

Areas of low temperature (2° - 330°C) hydrothermal venting and mineral deposition are well documented (Rona, 1988; Juniper & Tebo, 1995; Reyes *et al.*, 1995; Pentecost, 1996; Setter, 1996; Tivey, 1996). Diffuse venting is the main source of hydraulic interchange throughout the life cycle of a hydrothermal system (Hannington *et al.*, 1995). The heat and mass flux is often an order of magnitude greater than focused flow, and is generally accepted as the first flow-type identified at newly evolved vent sites. During episodes of vigorous venting, diffuse vents are often located around the periphery of high temperature, black smoker edifices, and are caused by seawater mixing within the hydrothermal mound, or sub-seafloor. These are often manifested as areas of shimmering water. Chemical analysis of hydrothermal fluids show that high and low temperature vents share a common hydrothermal fluid source at depth (von Damm *et al.*, 1987; Seyfried & Mottl, 1995; Tivey, 1996). Diffuse flow also exemplifys the declining stages of a hydrothermal system's life cycle, but despite the low flow-rates and relatively low temperatures (<10 – 50°C) diffuse vents may still sustain a fervent biological populace, and tube worm fields in the order of 100's of square meters are not uncommon. Mineralogical vent constructions, on the other hand, are uncommon, mainly because the

low temperature fluids associated with diffuse vents do not transport significant quantities of dissolved metals and sulphur (Ginster *et al.*, 1994). Where low-temperature chimneys are produced, they are often partially constructed of the remnants of tube worm colonies, encrusted with amorphous precipitates of Fe- and Mn-oxides and hydroxide complexes, silica (SiO_2) and authigenic clays.

Where the temperature increases to between 100 – 300°C, 'white smoker' chimney structures form. White smokers are particulate white precipitates of silica, barite ($BaSO_4$), marcasite and anhydrite ($CaSO_4$) which form on contact with seawater. Seawater mixing in the sub-seafloor, or conductive cooling of hydrothermal fluid during transport, are the two principal reasons for the formations of white smokers (and indeed, diffuse flow vents) rather than black smoker chimneys. (Tivey, 1995). Black smokers and white smokers often occur in the same vent field indicating that complex plumbing pathways exist at depth, causing thermal alterations, and/or local seawater entrainment of the end-member hydrothermal fluid (Tivey, 1995). They could possibly be interpreted as the first stage of black smoker construction. Mixing of fluids within the sub-seafloor would inevitably cause sub-surface mineral precipitation. This in-turn, will cause further modification of the sub-surface fluid-flow pathways.. Barite and silica are insoluble in cold seawater (anhydrite is saturated in seawater at temperatures below 150°C: Shock, 1996), and therefore allow large, cemented chimney structures to form. Analysis of amorphous silica solubility carried out by Fournier (1983) and Chen & Marshall (1982), has shown that a degree of conductive cooling is required to precipitate the silica observed to form within white smoker chimney walls and conduits. Many of the chimney structures seen on the Juan de Fuca Ridge achieve elevations of many tens of meters, principally because of the silica and barite cementing processes in action. Calcite-rich ($CaCO_3$) cementation may also be observed, especially in sedimented ridges systems such as the Guaymas Basin (Koski *et al.*, 1985).

The formation of a chimney wall (as described above) serves to thermally isolate the venting fluids from the seawater by inhibiting mixing, and consequently allows progressively hotter fluids to precipitate Fe-, and Zn-sulphides on the inner wall of the chimney. This leads to the distinctive mineral zonation which characterises most chimney structures (Graham *et al.*, 1988; Tivey, 1996). Many white smokers, however, have more

complex spire-like architecture. This is the result of the basal growth of multiple venting edifices, which grade to a narrower, often single, vent structure at the top (Hannington *et al.*, 1995). White smokers rarely have a single central conduit, but instead fluid flows through a complex network of interconnecting pores and channel ways. Tube worm masses often act as fluid pathways, either inadvertently when in life position, or directly when overgrown and incorporated by mineral precipitates (Hannington & Scott, 1988).White smoker 'snow-ball' structures from the EPR, described by Fustec *et al.* (1987), are thought to be biogenic edifices constructed almost entirely by outwardly orientated *Alvinella* sp. tubes. As progressive, late stage silica is deposited within the smoker structure, pores and conduits rapidly clog up and inhibit fluid flow to such an extent that either new vents are formed locally, or hydrothermal flow is cut off altogether.

1.4.2 - Black smoker chimney formation.

Various growth models for black smoker chimneys have been proposed (Haymon, 1983; Seyfried & Mottl, 1995; Tivey, 1996). These are invariably based on the solubility and precipitation relationships of the sulphide-sulphate-silica minerals that make up the chimney structure. Two major growth stages are recognised in black smoker evolution models: a sulphate-dominated stage and a sulphide replacement stage (Haymon, 1983; Reyes *et al.*, 1995; Tivey, 1996). The first stage is characterised by contact between hot (275° - 400°C) hydrothermal fluids and with cold seawater (Seyfried & Mottl, 1995). This causes precipitation of sulphates (anhydrite and/or barite), with only a minor sulphide component (fine grained pyrrhotite, pyrite, sphalerite; Haymon, 1983). This results in the formation of a porous wall which serves as the framework of the chimney structure (Reyes *et al.*, 1995; Tivey, 1996). Upflow of the hot fluid causes vertical and lateral growth of the sulphates through the top of the edifice and through the porous matrix of the walls. Very rapid growth rates of up to 80 cm/day have been observed (Hekinian *et al.*, 1980). Such structures are highly unstable and usually collapse. Ambient seawater percolating inwards through the walls catalyses the process of mineralisation, and precipitates sulphates together with small amounts of sulphides and silicates inside the pore spaces of the matrix. Precipitation in this manner forms a strong, impermeable chimney structure composed dominantly of anhydrite or barite, with restricted lateral flow. Reducing the porosity of the chimney matrix serves to reduce the thermal gradient

across the wall, and thus allowing the fluid within the chimney to cool at a slower rate (Reyes *et al.*, 1995). This gives rise to the second growth stage, coupled with the fact that less heat will be conducted away from the fluids by country rocks in the upflow zone.

Cu, Fe and Zn sulphides may now begin to precipitate along the inside of the vent conduits, and grow outwards, into the vent wall by remineralisation of the original sulphates (Figure 1.3). At high temperatures barite is particularly susceptible to pseudomorphic replacement by sulphides (Reyes *et al.*, 1995). This often continues until the vent structure has been completely replaced by sulphides. Replacement of the original wall structure causes remobilisation and migration of aqueous barium and sulphate ions, and subsequent reprecipitation as new crystals elsewhere in the hydrothermal system (Tivey, 1996).

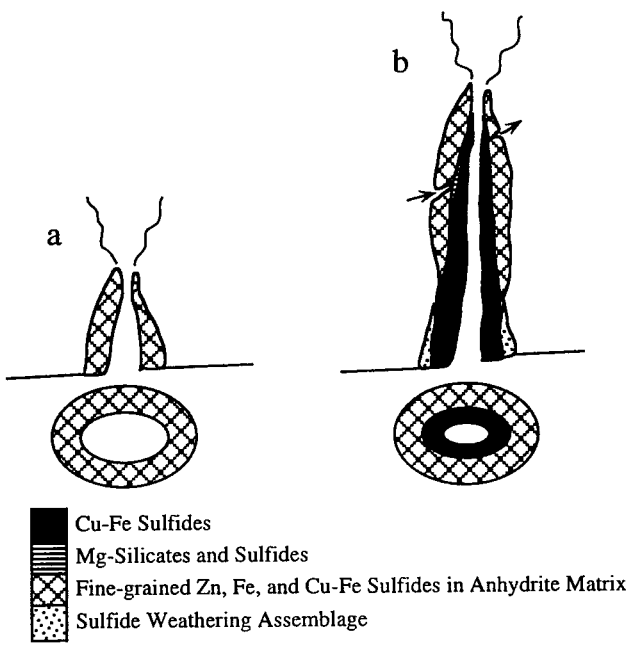

Figure 1.3 – A schematic of two hydrothermal vent chimneys (in vertical and cross section). (A) represents the early (anhydrite dominated) stage of chimney growth. (B) represents a mature chimney (dominated by Fe- and Cu- sulphides). The chimney walls remain porous, and allow the two way lateral passage of fluids (seawater inwards and vent fluid outwards) (adapted from Tivey, 1995).

During the final stages of venting, a third mineral phase can often be observed: silicification and barite deposition. This final stage causes reinforcement of the sulphide

chimney, and if flow rates are low enough may even bring on the termination of venting, and cap the chimney. Dissolution of any remaining anhydrite will then occur unless ambient temperatures are above 150°C, or the anhydrite is overgrown by a less soluble mineral such as silica. Dendritic barite precipitation on the outer wall of the chimney structures has also been recorded, caused by ambient fluid flow around the chimneys (Reyes *et al.*, 1995).

It is also important to realise that there are a variety of different hydrothermal regimes active within any given hydrothermal system, where vent fluid ranges from low temperature, diffuse seeps to vigorous, high-temperature black smokers, each forming a variety of vent structures (Figure 1.4), and distinctly different deposit types and sizes (Shanks 2001).

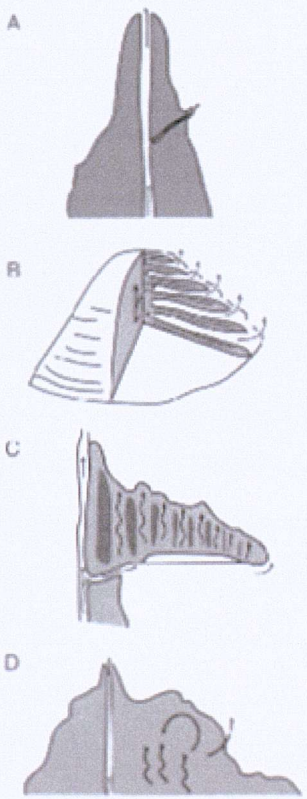

Figure 1.4 – The variable morphology of hydrothermal chimneys (A) depicts a typical EPR columnar chimney,(B) shows a cut away section of a Beehive structure, horizontal layering and conduits are shown, and allow for transport of hot (up to 350°C) vent fluids, (C) a flange structure is shown (arrows illustrate the flow of hot (~350°C) fluid, and (D) a complex (Juan de Fuca or Endeavour type) chimney mound structure. (From Alt, 1995)

1.5 – The geological setting of hydrothermal vents

The geological settings of hydrothermal vent sites are significant on a range of different scales. The sub-marine ridges that host hydrothermal vent sites split the surface of the globe into a mosaic of geologically dynamic plates. Tectonic forces deep within the asthenosphere cause the plates to move. These either move together or apart to form convergent, or divergent margins, respectively. Where plates diverge, new lithospheric crust is erupted, at ridge crests, and generally remains devoid of sediment, until it cools, sinks, and becomes part of the deep ocean floor. Sub-oceanic volcanism accounts for around 75% of global volcanism, yet the rate of production of lava is variable on a macro-scale along the ridge axes. Therefore a variety of spreading rates are found to occur along the various ridge systems, which in turn lead to a variety of hydrothermal vent field styles.

1.5.1 – Divergent margins.

1.5.1.1 – Slow spreading ridges.

Slow spreading ridges are characterised by full spreading rates of between 10 – 50mm y^{-1}. Presently around 50% of all active spreading ridges are classified as slow spreading (van Dover, 2000). The Mid-Atlantic Ridge (MAR) system is the prime example of this type of ridge system. The MAR is characterised by steep sided and faulted rift scarps which form wide and deep rift valleys. Another characteristic of slow spreading ridges is the presence of intermittent, deep magma chambers (Shanks, 2001). Slow spreading ridges have infrequent eruptive events and are therefore dominated by tectonic processes. Hydrothermal venting may either occur on-axis (e.g. Snake Pit hydrothermal field), or off axis *via* transform faults (e.g. Trans-Atlantic Geotraverse - TAG - hydrothermal field). The major features associated with the TAG field, are: high temperature venting of the TAG hydrothermal mound (Rona *et al.*, 1993) which has formed a large (3.9 million tonne) sulphide deposit, and two rellct hydrothermal fields Mir, and Alvin; and an area of low temperature venting high on the median wall (Thompson *et al.*, 1985).

1.5.1.2 – Intermediate spreading ridges.

Intermediate spreading ridges are characterised by full spreading rates of 50 – 90mm y^{-1}. Examples of intermediate spreading ridge hydrothermal systems include the Galapogos Ridge, and the Northern Pacific Ridge systems (21°N EPR, and the Juan de Fuca Ridge system). Hydrothermal sites associated with intermediate spreading rates have the most variable geological settings, forming very large sedimented-hosted deposits, large fault controlled fields, off axis ridge flank systems, and fields associated with eruptive centres within neovolcanic zones (Fornari & Emberly, 1995)

1.5.1.3 –Fast and super-fast spreading ridges.

Fast spreading ridges are characterised by full spreading rates of 90 – 150 mm y^{-1}, and super fast spreading ridges of >150mm y^{-1}. The only examples of active hydrothermal sites hosted on fast and super-fast ridges are 11 – 13°N EPR, and 17-22°S EPR, respectively. Curiously however, magnetic anomalies suggest that over half of the extant oceanic crust was formed at rates of over 90 mm y^{-1} (Lonsdale, 1977). Fast spreading ridges have continuously present, shallow magma chambers, and are subject to many more eruptive events than slower spreading ridges. The top of the magma chamber at 11 – 13°N EPR has been measured using seismic methods, and estimated to be present at the relatively shallow depth of 1.5Km (Fornari & Emberly, 1995), whereas magma bodies at slow spreading ridges may reside at over twice this depth. Typically the faulted rift zones of fast and super-fast spreading centres are shallower in depth than slower spreading ridges, and have shallower and less steeply orientated fault scarps. Hydrothermal vents, and inactive sulphide deposits maybe numerous, and at 13°N EPR, vents are spaced around 200 – 300m apart along the axial valley. The hydrothermal output (based on water column sampling, Lupton & Craig, 1981) of the Southern EPR is at least an order of magnitude higher than that from the Juan de Fuca Ridge (Lupton, 1995).

1.5.14. – Rifted continental settings

Known hydrothermal systems from rifted continental settings are less numerous, and include the Guaymas Basin, in the central Gulf of Cailifornia, and the brine pools of

the Red Sea. At Guaymas Basin chimney structures venting fluids up to 315°C have been observed, forming deposits composed mainly of calcite. This style of deposit is attributed to interactions with overlying sediments (Campbell *et al.*, 1988). The Red Sea vents are manifested as negatively buoyant pools of brine. Also on the African continent, giant salk-lakes are manifest due to the rifting of the continental shield, at locations such as Lake Baikal, and Lake Tanganyika

1.5.2 – Convergent margins

Where tectonic plates collide, convergent margins are formed. Back-arc spreading centres form along the active, convergent, plate margins where thick, old oceanic crust is subducted below continental crust moving in the same direction. The sinking oceanic plate creates friction which drags on the edge of the overlying continental plate, creating extensional faults behind the subduction arc. This causes magma to periodically well up into the extensional zone, on time scales of millions of years rather than continuously at mid-ocean ridge spreading centres. The magma chemistry of back-arc spreading centres is influenced by the incorporation of seawater (incorporated into the old, subducted crust, and the passage of the magma through continental crust). Examples of back-arc basins include: the Okinawa Trough, the Mariana Trough, the Manus Basin, the North Fiji Basin, the Lau Basin , and the Izu-Bonin Arc, most of which are found in the Western Pacific.

1.5.3 – Seamount related

Hydrothermal venting is also known to occur away from ridge associated settings, at active sub-marine volcanoes and seamounts (Karl, 1988). Seamounts are mid-plate volcanic features which allow for the accumulation of basaltic crust, and may lead to the production of volcanic island arcs, such as the Hawaiian island chain. Where there is sufficient hydrothermal heat and porosity present to set up hydrothermal circulation of fluids, hydrothermal venting may occur. Examples of active hydrothermal seamounts include: Loihi, located south off Hawiai, and the Pito Seamount, located close to 22°N EPR. Seamounts may prove important as stepping stones for hydrothermal species dispersion (van Dover 2000).

1.6 - Aims and objectives.

Biological organisms can influence mineralisation during hydrothermal venting by providing a substrate for mineral precipitation. They also influence mineralisation by altering flow pathways, and even provide thermal insulation for new vents (Tunnicliffe & Fontaine, 1987). Sedentary animals living on the surfaces of hydrothermal chimneys may be progressively overgrown by mineral precipitates, and can then pass into the fossil record. However, fine-grained sulphides and metastable mineral phases such as pyrrhotite, marcasite and wurtzite are frequently overgrown or replaced by silica and iron oxides or more crystalline phases such as pyrite, chalcopyrite, and sphalerite. Therefore primary mineral textures and geochemical characteristics are lost, along with evidence of original paragenesis. The widespread recrystallisation and overprinting of primary mineral precipitates due to successive hydrothermalism in a mound or chimney setting is probably one of the main reasons that fossil vent organisms and chimney structures are rarely preserved in ancient hydrothermal deposits (Oudin, 1983; Oudin & Constantinou, 1984).

This study aims to identify the early fossilisation processes active in a variety of hydrothermal vent faunal specimens recovered from sites in the Pacific Ocean. Specifically this study aims to:

- Interpret and relate textural and mineralogical features to geochemical processes.
- Identify a possible geochemical 'finger-print' in mineral precipitates indicative of organic origins.
- Assess the relative importance of microbial interactions on mineralisation processes.
- Investigate the relative importance of replacive mineral precipitates in hydrothermal vent faunas, and assess the impact of later paragenetic precipitates on fossilisation.
- Construct theoretical models for preservation of selected of hydrothermal vent faunas.

Chapter 2 provides a detailed introduction to the biological and palaeontological aspects of hydrothermal vents. Chapter 3 describes the geological settings of the locations from which the studied faunal specimens were collected, and the analytical and observational techniques used. Chapter 4 investigates pyrite and marcasite precipitation within the inter-tube layers of a dwelling tube of the polycheate worm *Alvinella pompejana*, sampled from 12°48'N EPR. For the first time a process of microbially templated sulphide precipitation associated with dwelling tube structure, is described. Chapter 5 investigates the later paragenetic precipitation of pyrite and chalcopyrite mineralising *Alvinella* sp. tubes recovered from a recently extinct sulphide chimney located at 7°S EPR, a site discovered in 1995. This composes the first geochemical study of fossilised vent fauna from this recently discovered, and relatively unexplored vent site, and also yields some of the isotopically heaviest $\delta^{34}S$ values for vent sulphides yet to be recognized. Chapter 6 considers the early silification and sulphate precipitation of *Ridgea piscesae* worm tubes, and the later precipitation of sulphide minerals (collected from the Juan de Fuca Rise), and examines worm tubes which predictably become fossilised during the lifetime of their inhabitants. Finally, conclusive remarks and schematic models are outlined, along with directions for further work, in Chapter 7.

Chapter 2

Introduction: biology and palaeontology of hydrothermal vent sites.

2.1 - The deep ocean environment.

The deep ocean environment is cold, dark and inhospitable to most marine animals. Light does not penetrate below about 1000m, and the temperature of oceanic bottom waters rarely exceeds 3°C (Gregg, 1973). Pressures range from 200 atmospheres at ocean ridges, to in excess of 1000 atmospheres in the deepest trenches. The pressure on the abyssal seafloor is typically between 300 - 400 atmospheres (Riley & Chester, 1971). The deep ocean is commonly thought to be a food limited environment, with primary production being the main nutrient source. The observed reduction in biomass and number of individuals with increasing depth is a function of decreasing light penetration. Many of the organisms in the aphotic zone survive on the rain of euphotic-derived material in the form of 'marine snow' or less commonly as faecal pellets. This is transported from the photic zone by sedimentation or advective transport (Honjo, 1976; Gage and Tyler, 1991). The population characteristics of most deep-sea environments are typically sparse, and slow growing. However, in contrast, hydrothermal vent sites and cold seeps enable localised, isolated animal communities to flourish in the deep oceans (Laubier & Desbruyeres, 1985).

2.2 - The first hydrothermal vent discoveries.

The biological exploration of hydrothermal vents began when luxuberant colonies of gigantic, suspension-feeding molluscs size were discovered. These were photographed at a depth of about 2500m, by an unmanned vehicle towed across the axis of the Galapagos Rift spreading centre in 1976 (Lonsdale, 1977; Weiss *et al.*, 1977). This unique observation was obtained during a geological mapping expedition, which confirmed the hypothesised existence of hydrothermal springs on the sea floor. From these observations Lonsdale (1977) made many key observations. This encouraged substantial research and ultimately led to our present understanding of hydrothermal systems. For instance, Lonsdale hypothesised that interactions between the biota and the venting hydrothermal fluids may be directly responsible for the communities present, and

that chemoautotrophy by micro-organisms could provide a local food source for the organisms present.

The first dedicated biological investigation of the Galapagos site began early in 1977. The manned submersible ALVIN made 24 dives along the Galapagos Rift spreading axis. Direct observations of the extraordinary biological communities, mineral deposits, and hydrothermal springs were made, along with the collection of water samples for microbiological analysis (Corliss *et al.*, 1979; Karl, 1995). This was followed by a second ALVIN cruise in 1979 to test Lonsdale's original (1977) chemoautotrophic primary production hypothesis (Jannasch & Wirsen, 1979; Karl *et al.,* 1980; Jannasch, 1984). These primary investigations led to the discovery of hydrothermal and biological activity at further locations, (Karl, 1988; Rona, 1988; Tunnicliffe & Fountaine, 1987; Jannasch, 1994; Desbruyeres, 1995; van Dover, 1995; Barns *et al.*, 1996: Appendix A)

2.3 - Biological life at hydrothermal vent sites.

The discovery of complex communities of living organisms living within and around the hot spring vents has proved to be biologically significant. The 10-20°C fluid which were first sampled and analysed turned out to have enormous concentrations of thermophillic bacteria, from 10^8 to 10^9 cells per cm^3 (Corliss *et al.,* 1979). The first researchers concluded that vent communities "appear to utilize chemosynthesis by sulphur-oxidizing bacteria to derive their entire energy supply from reactions between the seawater and the rocks at high temperatures, rather than photosynthesis" (Corliss *et al.,* 1979). Subsequent investigations (e.g. Jannasch and Wirsen, 1979; Karl, Wirsen and Jannasch, 1980; Felbeck and Somero, 1982; Tuttle, Wirsen and Jannasch, 1983) have clearly established and characterized the basis of submarine vent communities.

The variety of metabolic schemes utilized by the bacteria have been summarized by Lilley *et al.* (1983) and Jannasch and Mottl (1985). These organisms mediate the oxidation-reduction reactions which are thermodynamically accessible within the mixing zone of the submarine hot springs. The electron donors (H_2, CH_4, H_2S, NH_3) are created in equilibrium with the reduced iron in the magma from the earth's mantle, while the

electron acceptors (O_2, SO_4^{2-}, CO_2, NO^{3-}) are often, ultimately the product of the effect of solar ultraviolet radiation on the atmosphere in the presence of catalytic systems within photosynthetic organisms, and are derived directly from seawater.

2.4 - Microbial processes

The primary producers in hydrothermal systems are chemoautotrophs. Chemosynthesis is carried out by free-living bacteria and prokaryotic symbionts. The sharp geochemical and redox gradients present in hydrothermal systems provide multiple niches for a wide range of microbial functions (Jannasch and Mottl, 1985). The reduced electron donors that are enriched in hydrothermal fluids (H_2, CH_4, H_2S, Fe^{2+}, Mn^{2+}) react with terminal electron acceptors (e.g. O_2, NO_3^-, SO_4^{2-}) and the microbes utilise the available energy, mediating these inorganic reactions (Jannasch, 1995).

The most important electron donor in seafloor hydrothermal systems is H_2S which reacts with O_2 in seawater (Jannasch, 1997). Sulphide oxidation provides approximately 99% of the energy that is available for chemosynthesis (Mandernack and Tebo, 1999). However the metabolic versatility, small size and high tolerance to adverse conditions lead to ubiquitous occurrence of microbes in hydrothermal systems (Karl, 1995). Microbes can tolerate the extreme ranges in pressure, pH and metal content associated with hydrothermal venting. The high temperatures within hydrothermal systems put a limit on the microbial habitat; hyperthermophiles cannot apparently tolerate temperatures above 113°C (Cary *et al.,* 1988). These hyperthermophiles are anaerobic chemolithotrophic bacteria or archaea (Jannasch, 1997).

Classification of organisms based on their RNA has led to a new understanding of the relationships between archaea bacteria and eukarya (Figure. 2.1).

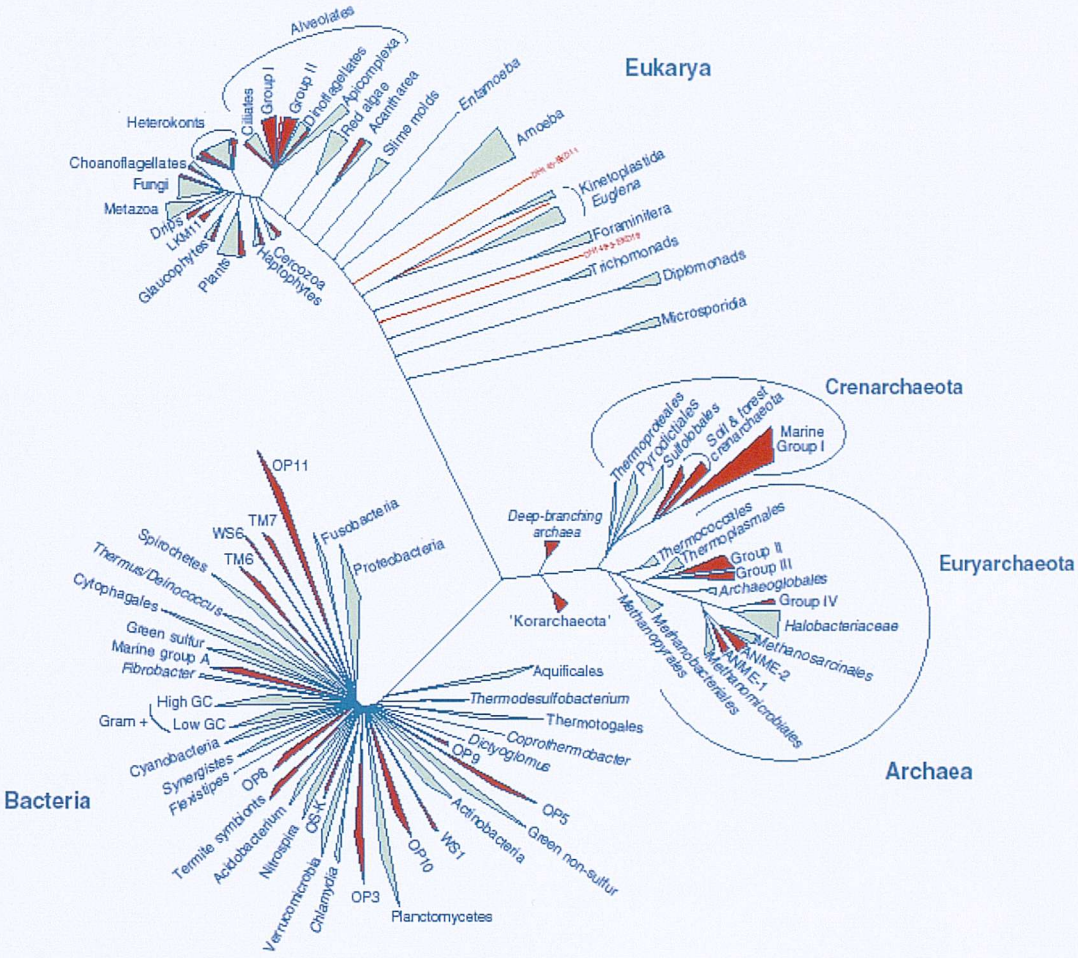

Figure 2.1 – A schematic representation of the tree of life based on distance analysis of small sub-unit RNA sequences (from Moreira & Lopez-Garcia, 2002)

The phylogenetic tree suggests that the hyperthermophiles that are classified as deep branching archaea are some of the oldest surviving lineages Vent microbiological communities include complex assemblages of both bacteria and archaea.

Hydrothermal vent biota have been extensively studied for the past twenty three years (Corliss *et al.,* 1979; Childress *et al.*, 1986; Desbruyeres, 1995; Gaill *et al.,* 1992b; Hessler & Desbruyeres, 1991; Rona *et al.,* 1986; Segonzac, 1992; Tunnicliffe, 1994; van Dover, 1990; 1994; 1995). The interaction between these organisms and hydrothermal geochemical processes (Lonsdale, 1977) has since been confirmed by workers such as Karl (1980; 1988; 1995), Jannasch (1993; 1995), Jorgensen *et al.* (1992) and Juniper *et al.* (1986; 1995; 1996). Free-living and symbiotic bacteria form the basis of the food web in

hydrothermal vent systems. Vent bacteria derive energy from the oxidation of hydrogen sulphide and other reduced inorganic solutes found in hydrothermal plumes, a process known as the Calvin-Benson cycle (Jannasch, 1996). Bacteria form the lowest trophic level in all presently known hydrothermal environments. The concentration of bacteria in hydrothermal plumes may vary greatly. Concentrations of microbial cells ranging from 5 x 10^5-10^6 ml-1 were measured by Karl *et al.* (1980) for venting fluids at the Galapagos Rift, and 1 x 10^9 by Corliss *et al.* (1979) for the same location. Where concentrations of bacteria are highest they may form mats composed of aggregations of living and non-living cells and inorganic matter. These can often be found growing on the surfaces of basalt, sediments, macrofauna, sulphide deposits and chimneys (van Dover & Fry, 1994).

Chemolithoautotropy, the process of microbial chemosynthesis which produces free energy from an inorganic electron donor (principally hydrogen sulphide (H_2S)), and an inorganic carbon source, has been well studied microbiologically (Jannasch, 1995). The process of chemosynthesis can proceed either aerobically, or anaerobically. Aerobic chemosynthetic processes depend on free oxygen within the system, to enzymatically oxidise an electron donor (primarily H_2S, or a form of reduced sulphide), which produces enough energy, to drive the endogenic reduction of carbon dioxide (CO_2). These reactions are biologically coupled (Equations 2a & 2b):

$$H_2S + 2O_2 \rightarrow H_2SO_4 \quad (2a)$$

$$CO_2 + H_2S + H_2O + O_2 \rightarrow [CH_2O] + H_2SO_4 \quad (2b)$$

The process of sulphide oxidation can be intensely competitive at hydrothermal vent sites, and bacteria have developed interesting biochemical adaptations for survival in such environments. In addition to H_2S, both elemental sulphur and thiosulphate compounds can be used in oxidation reactions by microbes (Kuenen & Beudeker, 1982). A variety of other reduced chemical compounds may be used in place of sulphide as electron donors (reduced iron (Fe^{2+}) and manganese (Mn^{2+}), methane (CH_4), ammonia (NH_4^+), and even hydrogen (H_2)). However, these are insignificant in terms of biomass when compared to sulphur utilising chemolithoautotrophs (Jannasch, 1995).

Chemoautolithotrophic microbes dwell suspended within vent fluid either symbiotically within or on the surfaces of vent animals. They coat rocky, basaltic outcroppings, and are present deep in the hydrothermal plumbing system. Bacterial cells often occur in such abundances within the waters of hydrothermal effluent that the water may be coloured a milky blue (Hessler & Kaharl, 1995) or form flocculent precipitates on the seafloor. The occurrence of white flocculent material is thought to denote the first exchanges between microbial communities and hydrothermal vent fluids in the early development of a vent chimney system (Haymon *et al.,* 1991). Massive amounts of white, flocculent material were observed emanating from the seafloor at three new eruption sites (9°N EPR, CoAxial, and Axial: Baross *et al.*, 1997). The material was referred to as "snow," and the vents it was discharging from were termed "snowblowers" (e.g. Haymon et al., 1993). Analyses indicate that the flocculent material is mainly composed of elemental sulphur (Juniper *et al.*, 1995), though it had a stringy texture similar to microbial mats. Further studies by Taylor & Wirsen (1997) showed that very similar sulphur flocs could be produced by a sulphide-oxidizing vibroid bacterium, in flowing, chemically enriched fluids. Haymon *et al.* (1993) have hypothesized that the white floccs observed at the seafloor are a result of subsurface microbial production, stimulated by eruptive events.

Studies concerning the nature of regeneration of the bacterial ecosystem at hydrothermal vent sites, after eruptive events, show that the consequent venting is often associated with the production of bacterial floccs, and extensive microbial mats which over-grow the fresh lava surfaces (Haymon *et al.*, 1993; Juniper *et al.*, 1995). Summit & Baross (1998) have suggested that the detection of anaerobic, thermophillic bacteria in the initial plume of a new eruption on the Gorda Ridge in 1996, is strong evidence for the existence of a subsurface biosphere.

There is also some evidence that microbes may live on, and within, basalt rock. Recovered samples of basaltic glass show microscale etching (Fisk *et al.*, 1994; Thorseth *et al.,* 1995b; Staudigel *et al.*, 1998) similar to that seen in laboratory studies of microbes and basalt (Thorseth *et al.*, 1995a), whereas the recovered samples also show enrichment of biogenically concentrated elements, including carbon, and sulphur. Basalt is known to

contain many iron-bearing minerals (such as olivine and pyroxene) that may be sources of energy for the microbes.

Special adaptations are required to grow slowly and live under low nutrient conditions. Fluctuating conditions should select for organisms that are adapted to a particularly wide range of conditions, or at least are able to survive otherwise uninhabitable conditions. The growth range of organisms generally spans 20-35°C in temperature and pH 2-3 units, but fluctuating conditions might select for particularly wide tolerances. The growth range of the microbial organisms must overlap the pH and temperatures specified for any given habitat. Under conditions of moderate fluid flow, organisms would be expected to exhibit attachment strategies and biofilm formation.

2.5 – Hydrothermal vent communities

Numerous invertebrate suspension-feeding, deposit-feeding and grazing species have direct access to the bacterial mats and free-living bacteria, and can often be seen 'intergrown' within bacterial aggregations. Hydrothermal communities are characterised by a remarkably high biomass, low species diversity and large individual organisms.. Fauna at vents are dominated by polychaetes, molluscs and arthropods (accounting for 93% of the known species), with the fourteen new families discovered constituting 13% of all the families recorded at vent sites (Tunnicliffe & Fowler, 1996). Of the 375 recorded species of vent animals only 7% are known to exist outside of this habitat (Table 2.1). The different faunal characteristics between Pacific and Mid-Atlantic vent sites have been well documented (Rona *et al.*, 1986; Tunnicliffe & Fowler, 1987). Mid-Atlantic Ridge communities tend to be dominated by extensive anemone beds, and dense swarms of shrimp around venting chimneys, very different to the vent fields of the Pacific which are dominated by vestimentiferan and pogonophoran tubeworms, alvinellid polychaetes, vesicomyid clams and mytilid mussels.

Provenance	Site	Species	Genera	Families	Phyla
Eastern Pacific	Galapagos	74	57	38	7
Eastern Pacific	13°N EPR	100	79	48	8
Eastern Pacific	21°N EPR	88	61	37	5
Eastern Pacific	Guaymas Basin	41	35	25	4
Northeast Pacific	Juan de Fuca	73	64	45	6
Western Pacific	Marianas Trench	37	35	25	6
Western Pacific	Lau, Fiji, Manus	76	58	41	4
Atlantic	Mid-Atlantic Ridge	34	27	24	6
Total Fauna	All Sites	464	240	119	9
Vent endemic	All Sites	381	107	18	-
fauna	(% endemic)	(82.1%)	(44.6%)	(15.1%)	

Table 2.1. Numbers of taxa recorded at sampled vent sites and percentage endemicity. *Data from*: Tunnicilffe & Fowler (1996); McAurthur & Tunnicliffe (1998).

The animal communities of hydrothermal vent fields show distinct zonation. This is caused by chemical and hydrothermal fluid temperature gradients. The three main zones are the vent opening, the near-field, and the periphery. These zones are not static, exhibiting various degrees of temporal and spatial variability, due to the variable nature of the hydrothermal vents themselves (Tunnicliffe, 1992). The flow of vent fluids fluctuates almost constantly, with activity and chemistry changing on time scales which range from hourly (von Damm, 1995), to millennial (Lalou *et al.*, 1993). Where the generation, or cessation of a hydrothermal vent occurs in a vent field, the entire ecosystem can be drastically affected (Tunnicliffe, 1991).

The nutrients contained within a hydrothermal vent plume (bacteria, planktonic larvae, and organic molecules) are probably attractive to non-vent deep-sea animals, and may initially attract some towards hydrothermally active areas. The community which inhabits the peripheral areas of the vent environment tend to be made up of non-vent animals. These presumably live close enough to the vent to utilize the increased nutrients, but far enough away so as not to be poisoned. Hydrothermal effluent is poisonous to most organisms, even when highly diluted (Somero *et al.*, 1989). Sulphide is a poison even in micromolecular concentrations, acting primarily as cyanide would, it poisons aerobic metabolism and interferes with haemoglobin function (van Dover, 2000). As such, non-vent animals do not generally venture into the areas which are hydrotheramally active.

The peripheal community is dominated by polychaete worms (including serpulids), enteropneust worms (acorn or spaghetti worms), large protozoan xenophyophores, and sea cucumbers, and dandelion siphonophores (Hessler & Kaharl, 1995). More motile animals such as ratail fish and spider crabs may penetrate into the near-field environment, and can probably tolerate increased levels of sulphide for short periods of time (Tunnicliffe & Jensen, 1987)

The near-field zone is dominated by sessile suspension feeding animals. Barnacles, anemones, serpulid polychaetes, and molluscs filter the nutrient-rich waters around the vent field, and absorb the copious bacterial biomass that is suspended within the effluent-mixed seawater. Suspension feeders attach themselves to basalt talus and massive sulphide blocks on unsedimented sites. Motile fauna such as galatheid crabs, rattail fish, whelks, eels, gastropods, and some polychaetes (Hessler & Kaharl, 1995; van Dover, 1996) are observed to prey on the primary consumers (and one another).

The majority of the vent fauna (both in terms of individual numbers, and biomass) dwell around the vent openings and in the areas of diffuse fluid flow (Tunnicliffe 1991). Diffuse-flow venting accounts for 80 – 90% of the vent field fluid flux, with focused flow comprising the other 10 – 20% (Elderfield & Schulzt, 1996), Although macro-fauna are limited to the seabed and sulphide surfaces of chimneys, microbial habitats may be less constrained, with inhabitable niches extending into the chimney walls (Jannasch, 1995), or deep into the sub-surface (Summit & Baross, 1998). Space, rather than nutrients, would appear to be the principle limiting factor controlling population size around hydrothermal vent openings (Hessler *et al.*, 1985). Bresiliid shrimp (e.g. *Rimicaris exocularis*) surround smokers at the Mid-Atlantic Ridge sites, jostling for position, filling venting fissues, and swarming over any hot surfaces where venting emanates (Thompson *et al.*, 1988; van Dover *et al.*, 1988). A similar, if less dynamic, scene is witnessed at the EPR vents where vestimentifera, clams and mussels clump together around the base of vent chimneys and within the diffuse flow of cracks and fissues (Hessler *et al.*, 1985; Tunnicliffe, 1991). Large individuals are not uncommon: *Riftia pachyptila* tubes have been observed up to 3 metres in length (Gaill *et al.* 1997), and vesicomyid clams such as *Calyptogena magnifica* can reach length of over 30cm (Hessler *et al.*, 1985). The clustered tubes and shells of the larger organisms also provide sheltered habitats for many other smaller animals:

alvinellid, ampharetid, amphisamythid, and maldanid polychaetes. A variety of protistans, gastropods and limpet species attach themselves to the outer surfaces of larger fauna. Those organisms that play host to endosymbionts must remain close to the interface between venting fluids and oxygenated seawater in order to survive (Childress *et al.*, 1987). Because the fluid which bathes vent organisms is constantly fluctuating with respect to chemical content and temperature, physiological adaptations have been evolved to cope with survival at hydrothermal vents.

2.6 - Physiological ecology of major vent fauna

Hydrothermal vent fauna have evolved many physiological adaptations designed to enable them to utilise both sulphide and oxygen from the surrounding waters. Sulphide and many of the heavy metals found in vent effluent are highly toxic to most animals and animals living within in the hydrothermal vent environment have developed mechanisms to tolerate and deal with these toxins. Most vent fauna have evolved strategies to prevent sulphur compounds from entering their bodies (Somero *et al.*, 1989). However, those fauna which host symbiotic bacteria must, by necessity, allow for the permeation of sulphide into their blood stream, or even actively facilitate the process (Fisher, 1995). Sulphide is toxic to aerobic organisms due to the inhibitory actions on vital enzymes required for anerobic respiration reactions. Physiological and behavioural adaptations to cope with high sulphide levels include avoidance, detoxification, immobilisation of sulphide, and the importation of oxygen (McAurthr & Tunnicliffe, 1998). Elevated levels of sulphide are reported in the tissues of practically all vent macro-fauna. In addition, high heavy metal concentrations (e.g. cadmium, zinc, silver, arsenic, copper, molybdenum, and mercury) have been found within the tissues of many of the major faunal groups (e.g. vestimentiferan and alvinellid worms: Cosson-Mannevy, 1988; vent mussels: Chassard-Bouchaud *et al.*, 1986; and vent clams: Chassard-Bouchaud *et al.*, 1988). Many mechanisms have been proposed which suggest how vent fauna could possibly be able to mediate and excrete heavy metal toxins and sulphur compounds effectively (e.g. Somero *et al.*, 1989; Cosson-Mannevy, 1988; Cosson-Mannevy *et al.*, 1986; Juniper *et al.*, 1986; Juniper, 1988; Gaill & Hunt 1988; 1991) Mechanisms may include the accumulation of toxins into granules by specific cells, and consequent excretion, the capture and accumulation of toxins by bacteria, the binding of heavy metals by metallothionien-like

proteins, and exclusion and incorporation of toxins into mucus and tube-building material by mucosite glands. In vent animals where a wholly symbiotic existence is evident, the removal of unspecifically absorbed chemical components by incorporation into tube building materials or by mucus production is highly favourable.

The half-life of sulphide in oxygenated water is in the order of only tens of minutes (Millero, 1986). Due to their size, mobility, and highly developed organs, vent macro-fauna have distinct advantages over micro-fauna in obtaining the sulphide and oxygen compounds required for respiratory processes. Where free-living sulphide-oxidising bacteria are limited to interfacial niches, metazoans can thrive in a much wider variety of habitats. Strategies for gaining access to sulphide and oxygen-rich fluids are summarised as follows:

- Animals can physically bridge the interface between their oxygen and sulphide sources, therefore spatially separating the acquisition of oxygen and sulphide.
- Animals can live in an environment where oxygen and sulphide sources are both present, but at different times, therefore temporally separating the acquisition of oxygen and sulphide.
- Animals can situate themselves in areas which are located about an interface between oxygen and sulphide sources, allowing themselves to be bathed in both oxygenated and reduced fluid types. In turn, this allows for gas exchange with both fluid types.
- Animals can move between the two sources of oxygen and sulphide, therefore behaviourally (and temporally) separating the acquisition of oxygen and sulphide.

Vestimentiferan tube worms have a large holding capacity for oxygen and sulphide (Sanders & Childress, 1993; Zal, 1998). Since their symbiotic bacteria are isolated from the outside environment within their tissues, their blood has evolved unique haemoglobins which can bind both oxygen and sulphide, in relatively large amounts, to allow transport to the bacteriocyte-laden trypanosomal tissues (Arp & Childress, 1981; 1983). Vestimentiferans are able to utilize oxygen and sulphide from their immediate environment by the separate acquisition of the two dissolved chemical species from fluids. This is achieved by moving their highly specialised protruding vascular plume,

which is located at the anterior end of the worm, into and between fluids rich in either sulphide or oxygen. Many vestimentiferan species live in regions of intense mixing between diffuse hydrothermal fluids and seawater. Temperature gradients of over 30°C across the length of an individual's body are not uncommon, and constant exposure to high levels of sulphides serve to enable the organism to thrive, rather than just survive. The interface between diffuse high temperature fluids and seawater provide ideal living conditions for vestimentiferans because they are able to transport the abundant supply of CO_2, O_2, and S^{2-} to the bacteriocytes in their bodies. In turn, this allows for phenomenal rates of carbon fixation (Childress *et al.*, 1991a; Fisher *et al.*, 1989; Scott *et al.*, 1994). In such conditions, vestimentifera can grow exceedingly fast. Growth rates of up to 50cm y^{-1} have been recorded, for *Ridgea piscesae*, located on the Juan de Fuca Ridge (Tunnicliffe and Juniper 1990).

In contrast to vestimentiferan worms, bathymodiolid mussels have no specialised hemoglobin for the uptake and transport of sulphide or other reduced chemical reactants (Tunnicliffe *et al.*, 1987). *Bathymodiolus* sp. mussels have been sampled from practically every active hydrothermal vent site in the Pacific and Atlantic regions, and are thought to be the most widely distributed genus of symbiont-contaning organism (Fisher 1988b; Fustec *et al.*, 1987). *Bathymodiolus thermophilus* Kent & Wilson, 1985 was the first species to be formally described, but numerous species are thought to exist, and have a much wider geographical range than other species in the genus which, so far, have only been reported at Western Pacific, and Atlantic vent sites (Nelson & Fisher, 1995). *Bathymodiolus* spp. has endosymbionts within their gill tissues, which they allow to be bathed in ephemeral diffuse fluid flow. Their symbiotic mechanism of respiration would suggest that these animals are tolerent to hydrogen sulphide. *B. thermophillus* is able to oxidise sulphide to (non-toxic) thiosuphate, which is then transported to the symbionts for the purpose of respiration (Childress & Fisher, 1992; Nelson & Fisher 1995). *Bathymodiolus* spp. are know to harbour many different types of symbiotic bacteria, some containing chemoautotrophic bacteria, some methanogenic bacteria, and some a combination of both (Nelson & Fisher, 1995). All species can also filter feed, which may account, at least in part, for their wide geographical dominance (Fisher *et a.l*, 1988b).

Allvinellid polychaetes are a major faunistic component, in terms of both numbers of individuals and biomass, at Pacific vent sites between 23°S to 21°N EPR (Jollivet *et al.*, 1998). Many alivinellid species are know to be able to exchange gases and dissolved organic material with seawater via active gaseous exchange along the length of their bodies (Stephens, 1975). However, *Alivinella pompejana* is associated with a unique epibiotic bacterial assemblage located within the worms' integumemt (Cary *et al.*, 1997). The epibiotic bacteria include not only sulphur oxidisers, but sulphate reducers, nitrate respirers, nitrifiers, denitrifiers, and nitrogen fixers, many of which are tolerant of, or resistant to, high levels of heavy metals. The relationship between the polychaete worm and its multitude of bacteria is symbiotic, but the exact nature of symbiosis not fully understood (Cary *et al.,* 1997). The tube microenvironment favours chemosynthetic growth by combining a good oxygen supply with a continuous supply of sulphides, and a temperature range of between 20 – 40°C (Desbruyéres *et al.*, 1985). In turn bacteria excrete amino acids, sugars, and other organic products beneficial to the worm, and may be responsible for the detoxification of the worms' immediate environment (Alayse-Dannet, *et al.,* 1987). However, the worm also feeds using retractable tentacles located on the anterior portion of their body. These grasp food particles, bacteria and mineral grains, and move them towards the mouth, and into the gut, where they become embedded in mucus (Desbruyéres *et al.*, 1985). Whether or not the worms' nutritional requirements are fulfilled by ingested bacteria or uptake of dissolved organics from interstitial waters, or possibly even chemosynthetic activity in the gut, is yet to be fully explained.

The physiology of deep-sea organisms means that most metazoans are incapable of inhabiting even the peripheral regions of vent sites. This prevents some deep-sea animal groups from invading hydrothermal habitats, and thwarts others from seeking refuge from non-vent environments. Those that do inhabit hydrothermally active environments are either highly specialised, such as vestimentiferans (e.g. *Riftia pachyptila*), or have pre-developed tolerancies to high sulphide concentrations, such as certain polychaete worms. Most vent animals possess physical barriers such as a mucus coating, or a mucus-rich shell, cuticle or carapace to prevent the interaction of soft tissue with sulphides and other toxic chemicals (McAurthur & Tunnicliffe, 1998).

2.7 - Interaction of vent fauna and hydrothermal deposits.

Deep-sea hydrothermal deposits may form substantial sulphide and oxide deposits. These range in size from only a few square metres to hundreds of square metres. The largest active deposits are frequently formed in sediment-hosted locales, where percolation of the venting fluids through the sediment effectively removes metals from solution (Scott, 1987). Investigations by workers such as Tunnicliffe & Fontaine (1987), Juniper *et al.* (1986), and Juniper & Sarazin (1995) have revealed that there are several mechanisms by which individual vent organisms can influence the primary deposition of minerals and traces elements. Organic and inorganic surface encrustations, microbial processes, bacterial overgrowth and biogenic mucus production can all serve to enhance geochemical processes at hydrothermal vent sites, possibly acting as the precursors to the formation of larger mineral deposits. Because biological and mineral 'growth' can take place at the same time, the potential for interaction between the two processes is considerable. The influence of vent organisms on geochemical processes is probably very significant (Juniper *et al.*, 1995). Therefore, it is paramount to understand the effect of biological influence on geochemical fluxes in this environment.

The widespread overprinting by successive hydrothermal events and extensive recrystallisation within a hydrothermal mound is one of the reasons that chimney structures and fossils of vent organisms are rarely preserved in ancient deposits (Oudin, 1983; Oudin & Constantinou, 1984). It has been well recognized that the decomposion of unoccupied worm tubes occurs within a few years at modern hydrothermal vent sites, unless they are mineralised (essentially either pyritised or silicified: Tunnicliffe & Fontaine, 1987; Juniper & Sarrazin, 1995). Tubes of vestimentiferans and alvinellids are commonly over-grown or replaced by barite and silica when in life position, or incorporated into the sulphide chimney structure and (re)mineralised (Haymon *et al.*, 1984; Haymon & Kastner, 1985; Cook & Stakes, 1995; Hannington *et al.*, 1988). The tubes they contain can then act as conduits for fluid flow, and become an intergral part of the chimney structure. This allows chimney mineralisation processes to overprint biogenic and/or biomineralisation processes.

2.8 - Biomineralisation

Two biomineralisation processes, one active and one passive, have been described by Lowenstam (1981). 'Active biomineralisation' (termed 'boundary organised biomineralisation' by Lowenstam (1989)) is distinguished by the formation of an organic matrix, which may be formed intra- or extra-cellularly, onto which specific ions are actively introduced, then induced to crystallise, producing specific minerals or mineral complexes. This process is regulated by the cell, where the mineral type, the orientation of the crystal axes, and microarchitectures are controlled by cellular genetics and is therefore under complete biological control (Lowenstam, 1981). This allows the organism to produce physiologically essential minerals in isolation from the external environment (Mann, 1983), through separation by the cellular barrier (i.e. a selectively permeable cell wall or membrane). This cellular isolation allows mineralisation within the cell to proceed under external conditions that are normally thermodynamically detrimental to mineral growth (Konhauser, 1998). Actively biomineralised precipitates often exhibit distinctive crystal forms and habits, which identify them from inorganically produced mineralisation. It is not uncommon for biomineralised minerals to be produced via a 'mineralogical stepping stone' or a precursor mineral of some kind. For instance the formation of magnetite by magnetotactic bacteria requires the presence of an as yet unidentified ferric iron oxide-bearing compound (Lowenstam, 1981). Magnetotactic bacteria use magnetosomes (elongate organic sheathes) to produce single chains of intracellular magnetite crystals.

'Passive biomineralisation' (termed 'biologically induced mineralisation' by Lowenstam, 1989) is the second form of mineralisation associated with organisms. This type of mineralisation process can be seen in bacterial and some algal species (Lowenstam, 1981). Passive biomineralisation does not use organic matrices, but instead relies on charged particles nucleating on to the cell surface, or interacting with cellular by-products to precipitate out of solution. Precipitates may be produced both intracellularly and extracellularly. This type of biomineralisation is a two step process (Konhauser, 1998). Metals are initially electrostatically bound to the anionic surfaces of the cell membrane or any other available organic polymers. These subsequently act as nucleation sites for mineral precipitation. This type of mineralisation is similar to inorganic

mineralisation in as much as it is regulated by the same equilibrium principles that control inorganic mineral precipitation. Therefore it may produce similar crystal habits and have similar chemical compositions to inorganically produced minerals (Lowenstam, 1981). The microbes involved essentially provide a favourable substrate for mineralisation, which may then be used as a nucleation site by cations coming out of solution if the extracellular environmental conditions favour mineral precipitation.

Bacteria that produce mineral phases by biologically induced mineralisation do not strictly control the crystallisation process. The resulting particles have no unique morphology and a broad particle size distribution. Non-magnetotactic dissimilatory iron-reducing and sulphate-reducing bacteria produce magnetite, siderite, vivianite, and iron-sulphides by biologically induced mineralisation processes (Lovley, 1990; Bazylinski & Frankel, 1992). For example, the iron-reducing bacterium *Geobacter metallireducens* is a non-magnetotactic anaerobe that couples the oxidation of organic matter to the reduction of ferric iron, inducing the extracellular precipitation of fine grained magnetite as a byproduct (Lovely, 1990).

2.9 - Fossilisation at vent sites

Most fossils found within ancient vent deposits are mouldic. Often the hard parts of vent organisms (shells, tubes, etc.) are composed of materials which have a limited residence time in the aggressive hydrothermal environment. Carbonate shells are particularly sensitive to the low pH conditions that abound at vent sites, and have relatively high dissolution rates (40μm y^{-1} for calcite shells, 140m y^{-1} for aragonite shells: Lutz *et al.*, 1994). Comparisons between the residence of dead clam shells show that those which remain in active hydrothermal areas decay within 15 – 25 years (Killingley *et al.*, 1980; Lutz *et al.*, 1988), whereas those shells that are away from the influence of hydrothermal fluids may remain intact for several centuries. Also, many vent sites are located below the carbonate compensation depth (Atlantic Ocean: ~ 4,000 m Pacific: ~ 500 - 1,500 m), which probably accelerates the dissolution processes (Little *et al.*, 1998). The formation of mineral coatings and/or mineralised biogenic mucus and filaments may contribute greatly to the fossilisation potential of hydrothermal crustacea

and gastropoda. Mineral veneers probably delay the dissolution process (Little *et al.*, 1998), and allow for further mineral nucleation.

The fossilisation of vent tube structures has been briefly touched on in this Chapter, and will be examined in much greater depth in the following Chapters. In particular, marcasite and pyrite mineralisation at low temperatures (below 100°C) is discussed in Chapter 4.1.6, pyrite and chalcopyrite mineralisation and low to intermediate temperatures (100- 300°C) is discussed in Chapter 5.1.6, and silica and barite mineralisation at low temperatures (below 100°C) is discussed in Chapter 6.1.2.

2.10 - Distribution of fossilised hydrothermal vent faunal assemblages

Despite the wide variety of interactions between hydrothermal vent fauna and mineral deposits, fossilised hydrothermal vent communities are very rare (McAurthur & Tunnicliffe, 1998). A compilation of the known fossil vent communities of the Paleozoic Era is documented by Little *et al.* (1998). So far most of the instances of fossilised hydrothermal communities are from the Urals, Russia, and are Silurian or Devonian in age (Kuznetsov *et al.*, 1988, 1993; Little *et al.*, 1997, 1999a). Early Carboniferous communities from Newfoundland were interpreted to have been related to hydrothermal vents (von Bitter *et al.*, 1990, 1992). A Carboniferous hydrothermal worm assemblage has been reported from Ireland (Banks, 1985). Worm tubes are the dominant taxonomic component of the fossilised assemblages, with presumed alvinellid and vestimentiferan tubes being identified in Silurian to Recent sulphide deposits (Figure 2.3: Little *et al.*, 1998).

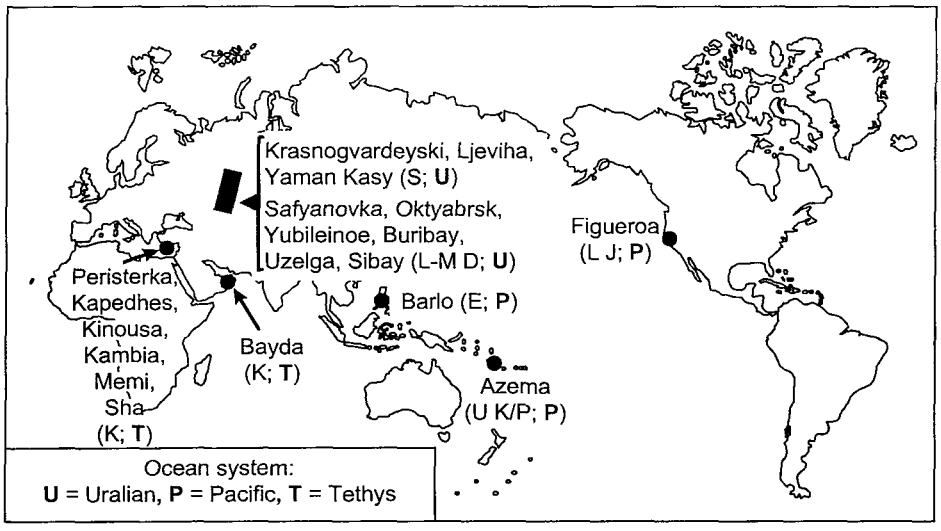

Figure 2.2 – The global distribution of fossiliferous VMS deposits. (from Little *et al.*, 1998). Key : L = Lower, M = Middle, U = Upper, P = Paleocene, E = Eocene, K = Cretaceous, J = Jurassic, D = Devonian, S = Silurian

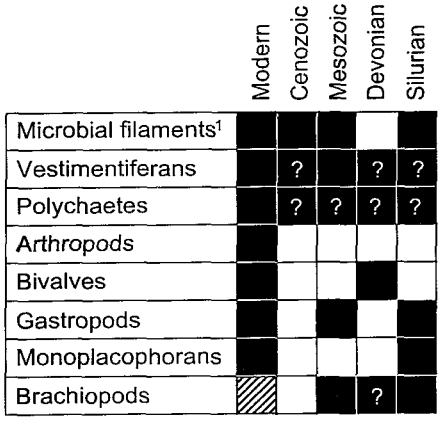

Figure 2.3 – Taxonomic contrast between grouped hydrothermal communities, and fossil vent assemblages. (from Little *et al.*, 1998: data from Little *et al*, 1998 and references therein)

A number of different taxonomic groups have been found in ancient hydrothermal deposits. However, the small number of fossiliferous vent sites discovered to date makes it difficult to draw accurate analogies with modern vent assemblages. It is not known whether ancient vent communities were spatially, temporally, geographically, or taxonomically similar to moden vent communities. There is presently an ongoing debate within the scientific litterature over the nature of the new species of hydrothermal fauna discovered in recent years, and whether or not they are evolutionary novelties, or relict taxa from a distant geological past (McAurthur & Tunnicliffe, 1996).

2.11 – Identification of fossil vent fauna

The fossil record is distinctly biased towards animals with hard parts (Wilby *et al.*, 1996). Although numerous occurrences of the preservation of 'soft bodied' fossils have been documented (e.g. Wilby & Whyte, 1995; Briggs, 1991 Briggs *et al.*, 1991; Martill, 1998), only one fossilised assemblage (Tynagh) is reported from a sub-marine hydrothermal-type deposit (Banks, 1985). In the absence of soft body parts of vent fossils the taxonomic identification of vent bivalves and brachiopods, relies on hard part morphology, such as muscle scars, hinge structures, crenulations, etc.. Similarly the identification of fossil tube structures draws closely on analogies with modern tubeworm morphologies.

Identification of tube structures built by hydrothermal organisms is further complicated by to the fact that many tubiculous species exhibit intraspecific tube variation (Tunnicliffe *et* al., 1988; Little *et al.*, 1998), and that the gross tube morphology of different species can be remarkably similar. So far, identification of fossilised vent fauna from ancient hydrothermal and VMS deposits, has used the principle of uniformitarianism to associate and compare fossilised vent fauna with modern analogues. Therefore studying the mechanisms involved in the early mineralisation and later fossilisation of modern hydrothermal vent fauna may be key to understanding the fossilisation proceswhich have acted on, and consequently preserved ancient vent faunas.

Chapter 3

Geological setting and analytical methods

3.1 – The location of hydrothermal systems and massive sulphide deposits in the modern ocean

Figure 3.1 shows the location of the global mid-oceanic ridge system, and associated hydrothermnal systems and seafloor massive sulphide deposits.

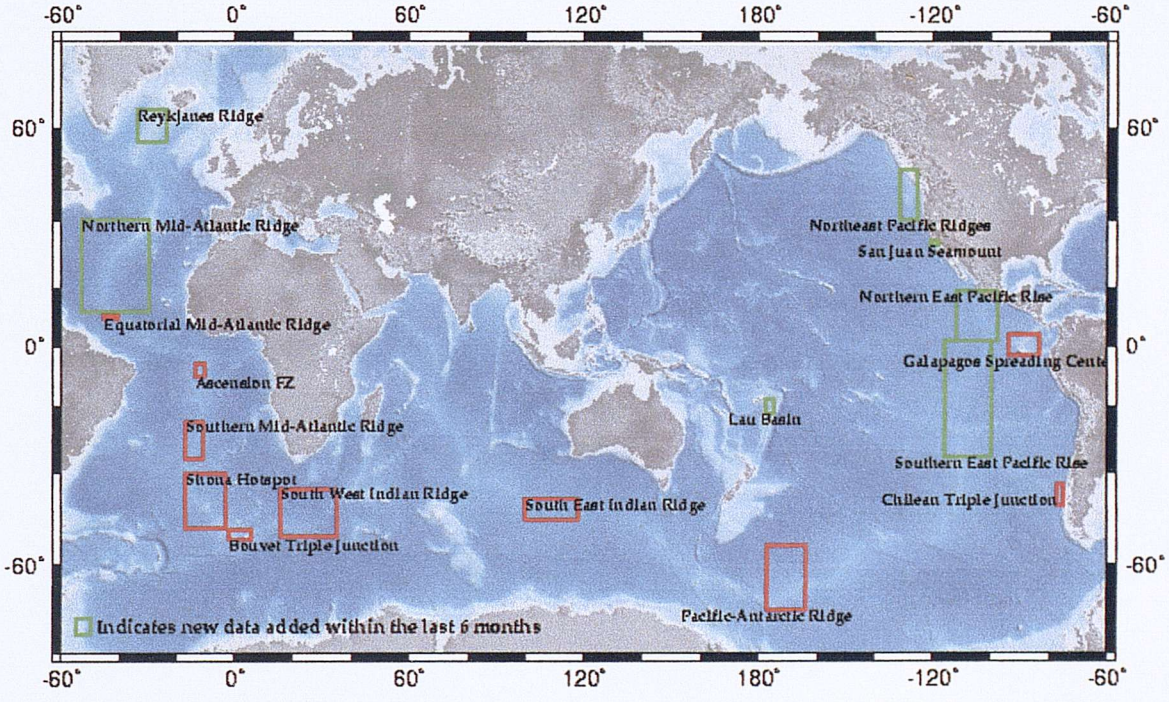

Figure 3.1 - The location of hydrothermal sites and massive sulphide deposits in the modern ocean (from Herzig & Hannington 2000).

3.1.1 -Geological setting of the East Pacific Rise (11 - 13°N)

Sulphide deposits at 11°N, 13°N and 21°N East Pacific Rise (EPR), and along the Juan de Fuca Ridge have similar geological settings (Ballard *et al.*, 1984; Hekinian *et al.*, 1980; 1983; Koski *et al.*, 1983; Baker *et al.*, 1995; Hannington & Scott, 1989). However, the spreading rate of 11 – 13°N is considerably faster than any other site on the Northern EPR at around 100 - 120cm y^{-1} (Fornari & Embley, 1995). Along the 35km of ridge crest which lies between 12°37'N and 12°54'N 149 individual sulphide hosted sites have been identified, with the active vents and smokers being restricted to the central part of the graben (Fouquet *et al.*, 1996). The axial graben varies between 20 – 50m in depth, and 200m – 600m in width, and extends unbroken for 35km bounded by an overlapping spreading center at each end (Fouquet *et al.*, 1996). Four distinct regions form the sulphidised areas of 11 – 13°N EPR, these are: active vents related to recent lava lakes along the central graben; active vents and sulphide mounds on the marginal topographic highs; inactive and tectonised vents along the top of the graben walls; and two inactive sulphide mounds on the Eastern side of the axial graben (Fouquet *et al.*, 1996; Lallier *et al.*, 1999).

A number of active sites are present in the ridge section between 12°48'N – 12°49'N EPR, such as Genesis, Elsa, and Pargo (Lallier *et al.*, 1999). These sites have dense populations of endemic vent fauna *Alvinella* sp. and *Riftia* sp. tube worms, as well as large numbers of non-endemic fauna such as octopi and serpulid worms (Lallier *et al.*, 1999). A single *Alvinella pompejana* worm tube was recovered from a vent site located between 12°48'N – 12°49'N EPR during the 'HERO' cruise expeditions (Figure 3.2). A full description of the sample site, recovery methods and description of the worm tube are described in Chapter 4.2.

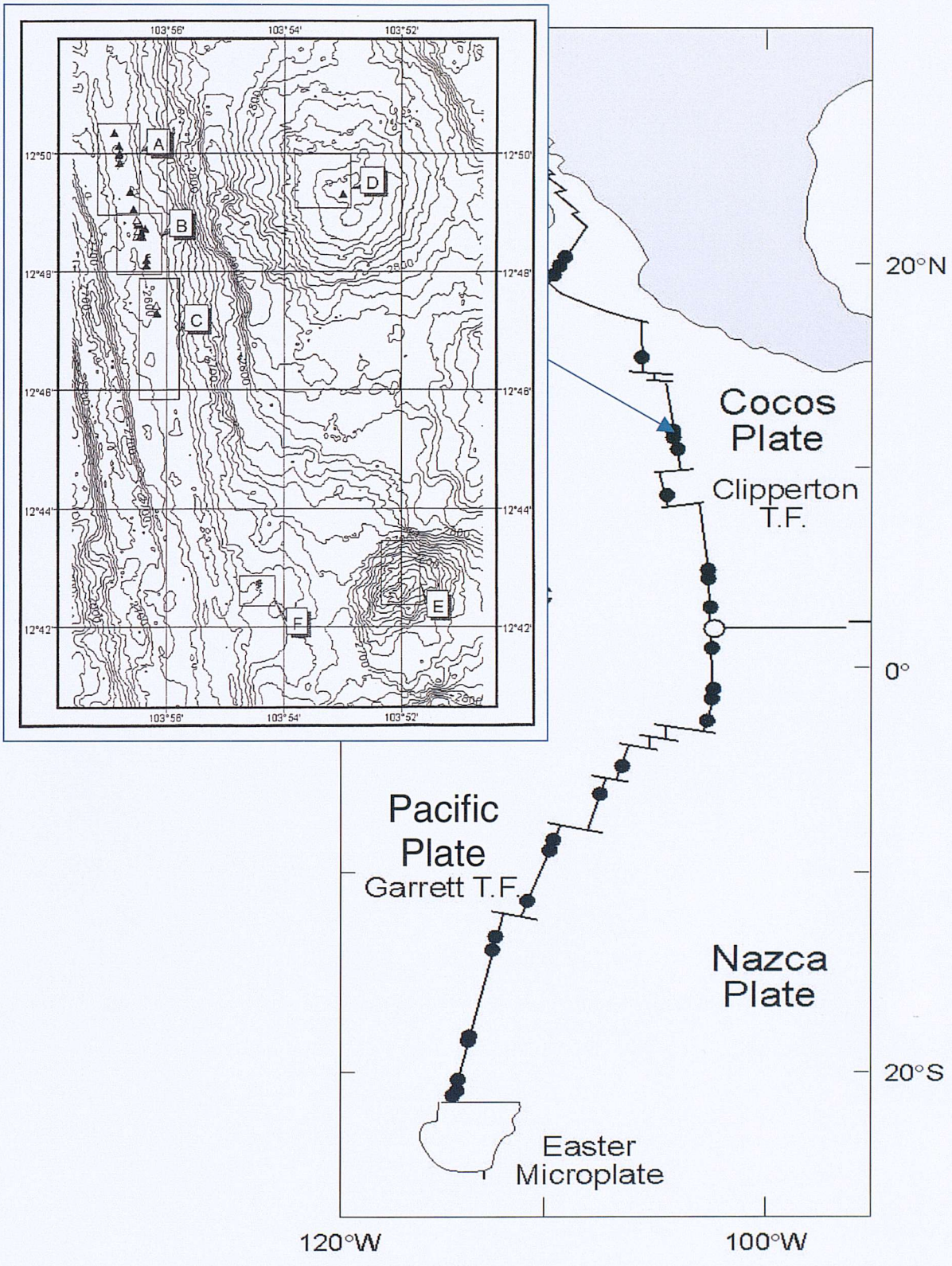

Figure 3.2 – A map of the Northern and Southern East Pacific Rise. Figure adapted from Haymon *et al.*,1991. Insert: bathymetric map of the 13°N EPR segment. Sites A, B, C & F are situated along the central axial graben, Sites D & E and outlying seamounts. 'B' represents the sample site for Chapter 4. From Lallier *et al.*, 1999

3.1.2 -Geological setting of the Southern East Pacific Rise (7°24'S)

The Southern East Pacific Rise (SEPR) is a fast spreading ridge system (12cm y^{-1}: 2°N), which grades, linearly with dereasing latitude, to an ultra-fast spreading system (16 cm y^{-1}: 23°S) towards the southern segment of the ridge (Londale, 1989). The entire length of the Southern EPR is associated with strong, cyclic volcanic activity, sporadic hydrothermal discharge, and sulphide deposition. Sulphide deposition occurs mainly in the form of massive sulphide chimneys dominantly composed of (in decreasing order of abundance) pyrite, chalcopyrite, and sphalerite (Marchig, 2000). Although fields consiting of chimneys and sulphide deposits are numerous on the SEPR, neither the fields nor the chimneys themselves have been reported to reach the large dimensions of those formed on slow spreading ridges.

The hydrothermal field at 7°24'S EPR is composed of several inactive massive sulphide chimney structures, all measuring less than 3m in height, and located at 2,740m depth (Figure 3.3). The Field is positioned on a well-defined central graben, developed on a tectonically developed ridge crest (Marchig *et al.*, 1997). The tectonic episode responsible for the crest formation is at an advanced stage, as indicated by the extensive sulphide talus which obscures around 35% of the central graben floor. The central graben itself is dominantly composed of erupted sheet lavas (Marchig *et al.*, 1997). Many of the individual talus blocks and basalt fragments within the field are encrusted with sulphides, or coated with a suite of alteration minerals, which typify inactive vent sites. The associated vent biocommunity is sparse, and indicates the wanning stages of hydrothermal activity being played out (Marchig *et al.*, 1997).

The strong hydrothermalism present at many SEPR sites has lead some researchers to infer that the significant sulphide deposits present have been formed over a much shorter time-scale than similar deposits on slower spreading ridges (e.g. the TAG deposit: Lalou *et al.*, 1993). A time scale of 80 yeras has been estimated by Marchig *et al* (1988) for the growth of a single chimney structure on the EPR at 18°25'S. Attempts to date the age of the massive sulphide chimneys and have concluded that ages of 200 years

(3 chimneys), >300 years, and >2000 years (1 chimney) (Lalou, 1992; Oudin *et al.*, 1990).

A mineralised worm tube grab sample was recovered from a location approximately 7°S East Pacific Rise during the GEOMETEP-5 (SO-62) cruise. The grab sample was taken remotely from the side of an inactive chimney. Full details of the sample site, recovery methods and description of the sample obtained are described in Chapter 5.2.

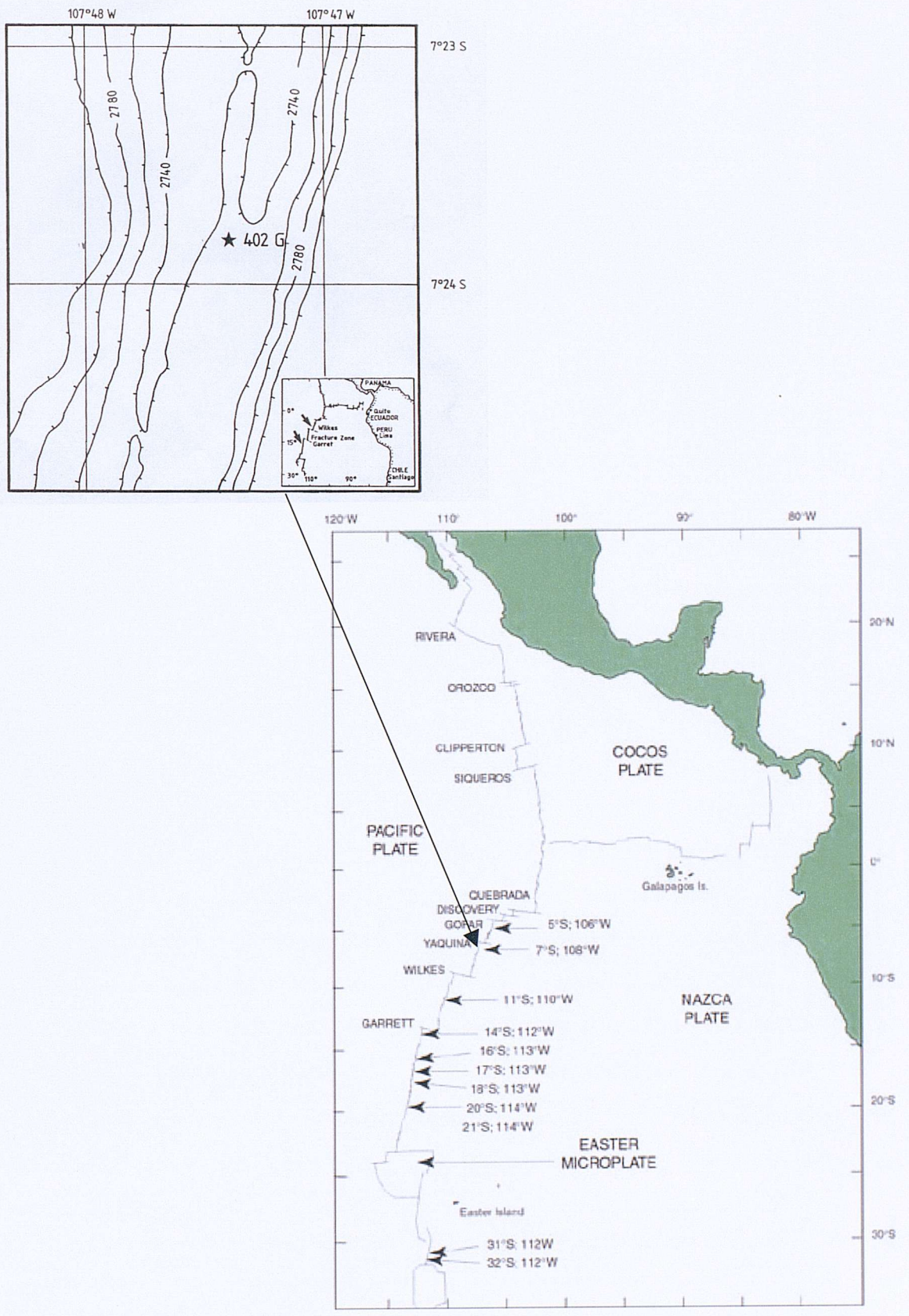

Figure 3.3 – A map to show the location of station 402G, and the Southern East Pacific Rise. Figures adapted. From Marchig *et al.,* 1988 & Wright *et al.*,2002

3.1.3 – Geological setting of the Juan de Fuca Ridge

The Juan de Fuca Ridge is located between 44°N and 48°N in the East Pacific Ocean, off the coast of Washington, Oregon and British Columbia (Figure 2.1), and is one of the most comprehensively studied ridge systems. Extensive research has been conducted in many fields, such as geology (Morton *et al.*, 1987), biology (Tunnicliffe *et al.*, 1990), ecology (Tunnicliffe *et al.*, 1991), and geochemistry (Hannington & Scott, 1988). The Juan de Fuca Ridge structure and morphology is split into three sections. The Axial Ridge trends roughly East – West, and is characterised by a volcanically active zone. This section is elevated with respect to the Northern and Southern zones. The Northern and Southern sections display cross-axial magnetic and bathymetric symmetry, and a central graben (Morton *et al,* 1987). The ridge axis is dissected by normal faults and fractures, that are thought to be the main ducts for venting fluids. The Endeavour segment of Juan de Fuca contains three main hydrothermal sites, the Main Field Site, the Clam Bed Site, and the High Rise Site. The High Rise Site, is split into a further seven active vent fields (Figure 3.4) van Dover, 1995; *cited in High Rise Expedition – Cruise Report*).

Recent high-resolution geological and hydrothermal studies along the intermediate spreading Juan de Fuca Ridge (full spreading rate of 5-6 cm/yr) in the northeast Pacific have indicated that individual segments are at different stages of magmatic and tectonic evolution, resulting in differences in the observed hydrothermal activity. Studies have focused on three areas: the Endeavour segment, Axial Seamount, and the northern part of the Cleft Segment. The Endeavour hydrothermal site is located at the along-axis high within the wide (0.5-1 km) axial valley of the Endeavour segment, which appears to be in an extensional rather than volcanic phase of spreading. Submersible studies have confirmed earlier suggestions that the boundary fault network at the base of the western wall of the axial valley is the primary control on the locations of active and relict vent sites (Delaney *et al.*, 1992). The main active vent field (180 m wide and 350 m long), which is in a region of older basaltic pillow and lobate flows, includes more than 15 large (up to 30 m in diameter and >20 m in height), actively venting structures and numerous smaller, less active or inactive structures. This within-field variation in size and level of activity of the structures argues for a secondary control on the distribution of hydrothermal flow channels. Delaney *et al.*, (1992)

suggest that localization of mineral deposition sufficient to build the large structures involves intersecting ridge-parallel normal faults and other fractures and fissures trending oblique or perpendicular to the ridge.

At Axial Seamount, a large, axial volcano located on the central part of the Juan de Fuca Ridge, the distribution and style of venting is controlled by a combination of localized fissuring and faulting and lava morphology. Although there are a number of low temperature vents within the caldera, the major sites of venting are associated with fractures and fissures along the margin of the caldera Embley *et al.*, 1990; Johnson & Embley, 1990). The location of the ASHES vent field, which contains the only high temperature vents in the caldera, is controlled by a fault zone that defines the western boundary of the summit caldera (Hammond, 1990). Compared to the Endeavour structures, the actively venting chimneys in the ASHES vent field are small (several meters in diameter and 4-5 m in height) and are confined to an 80 m x 80 m area. Diffuse venting is more widespread. Areas of focused venting appear to correlate with flow surface roughness and tend to be concentrated within smooth sheet and lobate flows, suggesting that, on a local scale, the effective permeabilities of lavas of different morphologies determine where conduits can be formed (Hammond, 1990).

A number of mineralised worm tube grab samples were recovered from the High Rise Field, Juan de Fuca Ridge during the 'High Rise Expedition' cruise, Legs 1 and 2. A full description of the sample site, recovery methods and description of the samples obtained are described in Chapter 6.2.

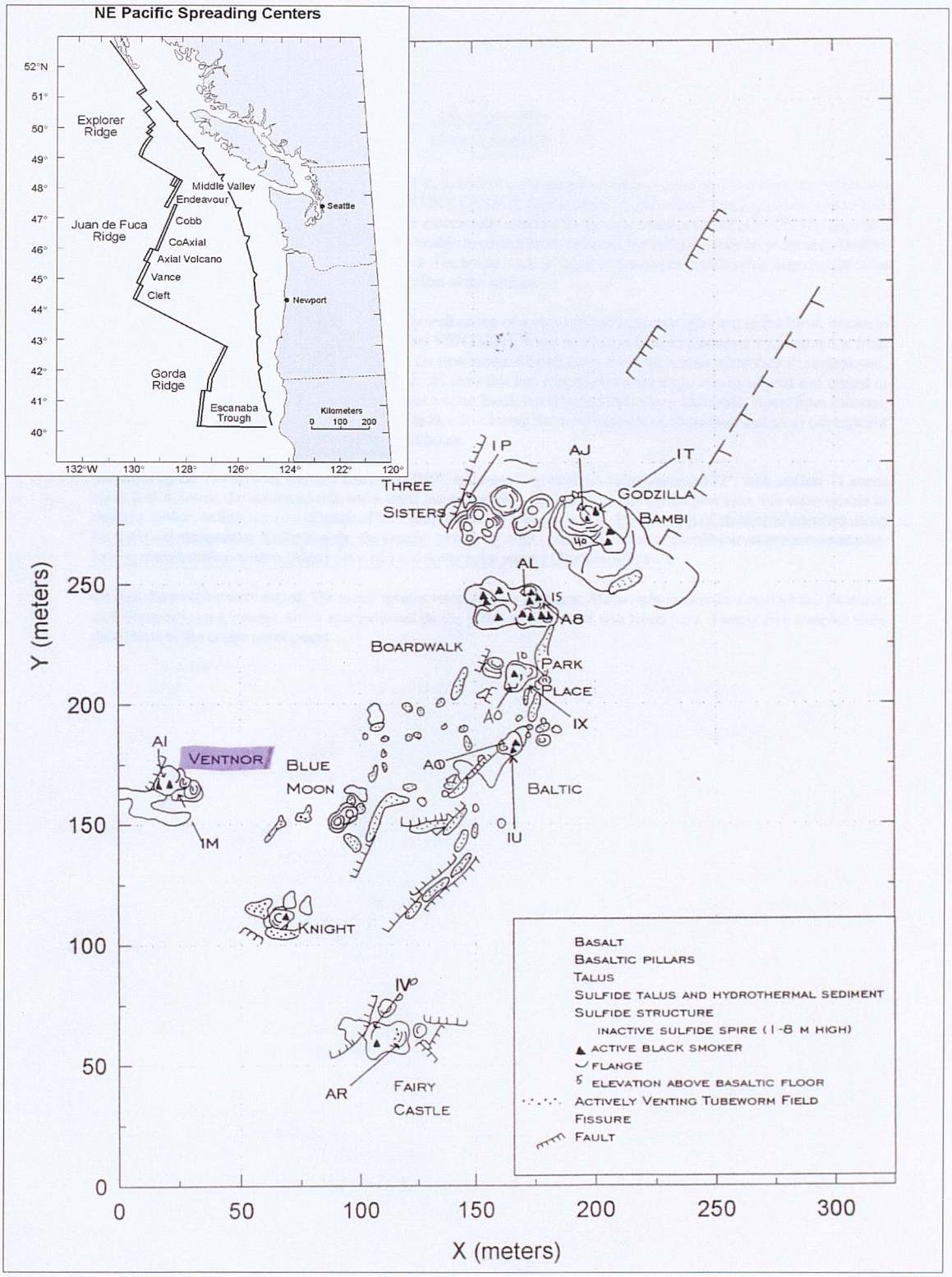

Figure 3.4 - The location of the Endeavour Segment of the Juan de Fuca Ridge (insert).,; and the High Rise Field and its associsted vents. From van Dover (1995)

3.2 – Analytical and investigational techniques.

3.2.1 - Light microscopy (LM)

Preliminary light microscopy investigations were undertaken using a WILD M32 binocular microscope. Transmitted light (TL) and reflected light (RL) photo-microscopy was undertaken using Olympus BX2M series polarising microscopes. The light microscopy studies undertaken here were particularly useful as a pre-analysis technique, allowing examination, sketches, and photo-mosiacs to be made before analysis under the Electron Micro-probe (EMP) or Scanning Electron Microscope (SEM) were carried out. Polished sections could then be marked around areas of interest, enabling faster and more accurate orientation around the specimen under observation. Photomicrographs were taken using an Olympus OM series camera, and processed and developed commercially.

The polarized light microscope is designed to observe and photograph specimens that are visible primarily due to their optically anisotropic character. Polarized light is a contrast-enhancing procedure which improves the obtained image quality with birefringent materials when compared to other techniques such as darkfield and brightfield illumination, differential interference contrast (DIC), phase contrast, and fluorescence, etc..

The Olympus BX2M series microscope is equipped with a polariser, positioned in the light path somewhere before the specimen, and an analyser (a second polarizer), placed in the optical pathway between the objective rear aperture and the observation tubes or camera port. Image contrast arises from the interaction of plane-polarized light with a bi-refringent specimen to produce two individual wave components that are each polarized normal to one another. The velocities of these light components are different and vary with the transmission direction through the specimen. After exiting the specimen, the light components become out of phase, but are reassembled with constructive and destructive interference when they pass through the analyzer.

3.2.2 - Florescence microscopy (FM)

Epi-florescence microscopy was undertaken using a Zeiss Z100 microscope with an attached ultra-violet reflected light source, and Canon A1-SLR camera.

Photoluminescence is a process described when material specimens (organic or inorganic) absorb and subsequently re-radiate light. If the light emission continues for up to a few seconds after the excitation light is withdrawn, the phenomenon is known as phosphorescence. Fluorescence, on the other hand, describes light emission which continues only during the absorption of the excitation light. The time interval between absorption of excitation light and emission of re-radiated light in fluorescence is of extraordinarily short duration, usually less than a nano-second. It is observed that the fluorescing light generates longer wavelengths than those of the excitation light.

Fluorescence microscopy can be used where the object material which can be made to fluoresce, either in its natural form (primary or autofluorescence) or when treated with chemicals capable of fluorescing (secondary fluorescence). The basic task of the fluorescence microscope is to permit excitation light to irradiate the specimen and then to separate the much weaker re-radiating fluorescent light from the brighter excitation light. Thus, only the discharge light reaches the eye or other detector. The resulting fluorescing areas shine against a dark background with sufficient contrast to permit detection. The darker the background of the non-fluorescing material, the more efficient the instrument.

Ultraviolet (UV) light of a specific wavelength or set of wavelengths is produced by passing light from a UV-emitting source through the exciter filter. The filtered UV light illuminates the specimen which emits fluorescent light when illuminated with ultraviolet light. Visible light emitted from the specimen, is then filtered through a barrier filter that does not allow reflected UV light to pass.

Many organic components, such as the outer sheaths of bacterial cells, fluoresce under UV light. Florescence microscopy was employed in this study in order to determine whether an organic component was present in the mineralised areas assosicated with the microbial structures within the studied samples. The samples were prepared from worm

tube fragments impregnated in resin, and mounted on glass as polished thin-sections of 60 – 80μm thickness.

3.2.3 - Scanning electron microscopy (SEM) & energy dispersive X-ray (EDS) analysis

Scanning electron microscopy (SEM) observations were made using a JEOL JSM-6400 SEM. Both Secondary Electron Imaging (SEI) and Back-scattered Electron Imaging (BSEI) can be performed, as well as quantitative and qualitative Energy Dispersive Spectroscopy (EDS) point microanalysis and element distribution mapping. SEI mode is effective in topographical studies, and can resolve down to 3.5nm. BSEI mode is used to differentiate compositional contrasts on plane surfaces, and can resolve to around 10nm.

For elemental mapping investigation the SEM is fitted with a PGT (Princeton Gamma-Tech) energy dispersive X-ray micro-analytical system. Which incorporates a PGT digital spectrometer, a PGT signal processor system, and a Sun Workstation computer processor loaded with PGT IMAGIST (v.8) software.

An SEM/EDS system permits the detection and identification of the X-rays produced by the impact of the electron beam on the sample thereby allowing qualitative and quantitative elemental analysis. The electron beam of an SEM is the source used to excite the atoms in the surface of the target sample. These excited atoms produce characteristic X-rays which are detected and analysed by a linked computer system. The scanning feature of the SEM, allows the spatial distribution of elements to be obtained. For flat, polished homogeneous samples, quantitative analysis can provide relative accuracy of 1-3% for compositional data, when appropriate standards are available.

Elemental mapping can be undertaken at various acceleration voltages (15 – 20kV) and through a range of magnifications. In general, higher magnifications require a higher acceleration voltage to produce sufficiently high counts, which in turn produce a visible elemental map. The count time required for elemental point analysis and elemental mapping procedures can vary greatly. Point analysis can be adequately achieved with

count times of between 60 – 120 seconds, depending on the relative abundance of the elements being analysed. A working distance of 15mm gives the optimum X-ray back-scatter for elemental analysis. The analysing spot size (X-ray spatial resolution) can vary depending on accelerating voltage and material density. Elemental mapping requires a longer count time as there are effectively many 'spots' to analyse. Count times used in this study ranged from 3600 – 36000 seconds (1 – 10 hours), depending on the magnification used, desired resolution, and relative elemental abundance.

3.2.4 - Field emission-scanning electron microscopy (FE-SEM)

The Field Emission Scanning Electron Microscope (FE-SEM) is similarly configured to a conventional SEM, except that a cold field emission electron source is used, which permits higher image resolution to be attained, increased signal to noise ratio, and increased depth of field.

The unique advantages of FE-SEM over conventional SEM techniques are summarised below:

- High resolution at low accelerating voltages
- Large depth of field technique compatible with rough samples
- High resolution with little sample preparation.

Samples were prepared as 3D fragments of tube sample and/or mineral stockwork, which were mounted on 10mm stubs, and sputter coated in gold. Observations were carried out at the Natural History Museum, London using an 'Hitachi S-4300' FE-SEM, with 'Quartz PCI' data management system, with a full digital imaging, image processing, and archiving system.

3.2.5 - Electron micro-probe (EMP) analysis

Electron probe microanalysis was undertaken at the Natural History Museum using a Cameca SX50 electron microprobe. The SX50 is a dedicated wavelength dispersive electron microprobe, capable of qualitative and quantitative element characterisation. Detection limits are within the order of 0.01 – 0.05 At%, and one

standard is used per element (up to 8 individual elements can be mapped at any one time). The Cameca SX50 operates at 15kV at 20nA and 2μm spot size. A count time of 15 seconds per point is implemented for scan-line profiles, whereas a 4 hour count time is used for the production of elemental maps.

Electron micro-probe (EMP) is an elemental analysis technique which uses a focused beam of high energy electrons (5 - 30 KeV) to non-destructively ionize a solid specimen surface (including thin films and particles) for inducing emission of characteristic X-rays (0.1 - 15 KeV). The spatial resolution of X-ray microanalysis of thick specimens is limited to a volume with dimensions of approximately 1 micrometer due to electron scattering effects. This volume may be even larger for low energy emission lines that can still be excited by lower energy electrons that have been highly scattered a significant distance from the impinging beam on the specimen surface.

Quantitative matrix (inter-element) correction procedures based on first principle physical models provide great flexibility and accuracy in analyzing unknown samples of arbitrary composition. Spatial distribution of elemental constituents can be visualized quantitatively by digital composition maps and displayed in grey scale or false colour.

These quantitative procedures have been demonstrated to produce error distributions characterized by a standard deviation of less than 3% relative when the samples are in the ideal form of a metallographically polished bulk solid. Standards utilized in these analyses are in the form of pure elements or simple compounds (e.g. MgO or GaP). This analytical approach provides great versatility in the analysis of multi-element unknowns of virtually any composition, where the atomic number of the element is greater than 5 (boron).. Detection limits are of the order of 100 ppm with wavelength dispersive spectrometry and 1000 ppm with energy dispersive spectrometry.

Advantages of EMP analytical technique:

- high intensity electron beam (tungsten preferred for stability) of approx.1 - 200 nanoamps
- coaxial light optics (reflected and transmitted) of up to 400 x magnification

- Energy Dispersive Spectrometry (EDS) for qualitative point analysis
- multiple wavelength dispersive spectrometers (WDS) for quantitative analysis
- high (> 40 degrees) x-ray take off angle for detectors.

3.2.6 - X-Ray diffraction (XRD) analysis

Bulk geochemical data was obtained from X-ray diffraction patterns from powdered worm-tube samples. Dry powder mounts were scanned between 0° & 60° at 1.2° 2θ/min, on a Phillips EW 1730 automated powder diffractometer using Co-K_α radiation.

3.2.7 - Stable isotope ratio mass spectrometry

Sulphur isotope analyses were carried out in the stable isotope laboratory at the Scottish Universities Research and Reactor Center (SURRC). All of the samples were analysed by *in situ* laser combustion from standard polished blocks. The polished blocks were inserted into a sample chamber, which was evacuated and subsequently filled with an excess of oxygen gas (Fallick *et al.,* 1992). The spatial resolution is determined by the minimum volume of SO_2 gas required for analysis (0.05–0.10 μmol), resulting in minimum spot sizes of approximately 50–100 μm. Typically, samples were rastered under the laser beam to combust individual zones extending around 500 μm by 100μm. The laser beam was a SPECTRON LASERS 902Q CW Nd:YAG laser (1 W power), operating in TEM_{00} mode. The liberated SO_2 gas was purified in a vacuum line, which is operated similar to a conventional sulphur extraction line such as that described by Kelley & Fallick (1990). The laser extraction method results in a mineral-specific sulphur isotope fractionation between the host mineral and the SO_2 gas produced via combustion (Kelley & Fallick 1990). Experimentally determined fractionation factors are currently available in the SURRC system to apply correction to several sulphide/sulphosalt minerals, including pyrite (+0.8 ‰) and chalcopyrite (+0.7‰). Further discussion of the laser-induced fractionation is given in Wagner *et al.* (*in press*). Reproducibility of the analytical

results was monitored through replicate measurements of international standards NBS-123 (+17.1 ‰) and IAEA-S-3 (–31 ‰), as well as SURRC's internal lab standard CP-1 (–4.6 ‰). The analytical precision, based on replicate analyses of the standards, was around ± 0.2 ‰ for both conventional and laser data. All sulphur isotope compositions were calculated relative to Vienna Cañon Diablo Troilite (V-CDT), and are reported in standard notation.

3.2.8 - Fourier transform infer-red (FT-IR) micro-spectroscopy

When monochromatic light passes through a glass prism, certain wavelengths are absorbed by the prism leaving the unabsorbed wavelengths to be transmitted. These transmitted wavelengths, which are complimentary to those absorbed by the prism, are identified as the colours of the rainbow. In a similar manner, apparently opaque objects such as minerals will absorb certain infrared wavelengths leaving residual radiation to be reflected and 'seen' by the infrared spectrometer. During an experiment, infrared radiation may pass through the sample where some of the radiation will be absorbed by the sample and some of it passed through (transmitted). The resulting spectrum represents the molecular absorption and transmission, creating a molecular fingerprint of the sample. No two unique molecular structures produce the same infrared spectrum which makes the technique useful for several types of analysis.

Individual chemical bonds, as well as groups of bonds, vibrate at characteristic frequencies. When exposed to infrared (IR) radiation, molecules selectively absorb radiation at frequencies that match those of their allowed vibrational modes. Measurement of the absorption of IR radiation by the sample as a function of frequency produces a spectrum that can be used to identify functional groups and consequently structure. However, vibrations that do not yield a change in dipole moment do not absorb IR radiation. For example, O_2 and N_2 do not absorb IR radiation. Consequently, IR spectra can be obtained in air. FT-IR provides specific information about chemical bonding and molecular structure, making it useful for analyzing organic materials and certain inorganic materials. FT-IR is normally a bulk analysis technique. However, using Attenuated Total Reflectance (ATR), FT-IR can acquire a spectrum from the top

1-2 mm of material. Where FT-IR analysis is used for bulk analysis, detection limits are in the order of 0.1 – 1wt%.

Profiles of the molecular structures in the sample were obtained at room temperature on a Nicolet™ *protégé* 460 Fourier Transform infrared spectrometer coupled with a Nic-plan infrared microscope. IR light is passed via a KBr beamsplitter and focused through the sample onto a liquid nitrogen cooled mercury-cadmium-telluride (MCT) detector. The data were aquired and processed using Omnic software. One hundred and twenty eight scans were accumulated for each analytical point at a resolution of $4cm^{-1}$. The sample was mounted on a motorized sample stage allowing movement in an X-Y direction. Altμs™ software permits analytical traverses to be programmed into the computer whilst observing the sample using optical light and the routine analysis of a sequence of points across the tube using infrared. To obtain spatial resolution of mineral species across the worm tube structures, a rectangular aperture, measuring 30μm perpendicular to and 10μm parallel to the traverse-line, was programmed into the computer.

The relative amounts of hydrogen species were determined by subtracting the sample spectrum from a reference spectrum taken in through air. The absorptions at 3440, 3380 and $3480cm^{-1}$ were then subtracted using baseline correction and the heights of the individual absorptions established. The Beer-Lambert law forms the basis for the quantitative relationship between species concentration and the height of the absorption peak:

$$A \text{ (Absorbance)} = \varepsilon d c \qquad [3a]$$

Where, Absorbance is the height of the absorbance peak, d is the thickness of the sample in cm, ε is the molar absorptivity in litres/mol-cm and c is the concentration of the water species (mol^{-1}). Accordingly, the intensity of an absorption, determined following baseline subtraction, is intimately associated with the absolute concentration of the absorbing species.

Chapter 4

Sulphide mineralisation in the hydrothermal vent polycheate, *Alvinella pompejana*: implications for fossil preservation.

Abstract

Hydrothermal vent fauna, particularly vestimentiferan and polychaete worm tubes, are occasionally preserved in the geological record. The early stages of mineralisation are particularly important in defining whether or not preservation will occur, and they are poorly understood. Tube samples of the polychaete worm Alvinella pompejana *collected from 13°N on the East Pacific Rise have been studied to identify the processes occurring during early pyrite / marcasite mineralisation. Iron sulphide mineralisation is present within the walls of the organic dwelling tube, and is induced by microbial flora preserved within the tube micro-layers. Various microorganisms were observed coating the inner tube surfaces, together with 10-100 μm sized Fe- and Zn-sulphide particles precipitated from vent fluids. The microbes and particulate sulphides become entombed within the tube wall as further layers of organic material are secreted by the worm, during tube-building episodes. This results in a laminated tube structure being formed, composed of alternating layers of tube material and microbially templated iron sulphide-rich interlayers. The microbial/sulphide layers provide a template for further mineralisation and replacement of the microbes with pyrite while degradation of the organic components occurs. The iron monosulphides mackinawite and greigite, have been identified as intermediatey phases that occur as precursor minerals during the formation of pyrite. Later marcasite mineralisation is observed to form over some of the pyritised organic layers. Once mineralisation has replaced most of the organic tube material, the structure will then be preserved along with the host sulphide body. These observations enhance our understanding of the mechanisms of fossil pyritisation in fine-scaled organic structures throughout the geological record.*

Abstract modified from: Maginn *et al.*, 2002 Sulphide mineralisation in the deep sea hydrothermal Vent Polychaete, *Alvinella pompejana*: implications for fossil preservation. *Marine Geology*, **181/4**, 337-356.

4.1 - Introduction.

4.1.1 – *Alvinella* sp. polychaetes at hydrothermal vent sites

There are eleven species of polychaetous annelid known from the family Alvinellidae, which includes the species *Alvinella pompejana* (Desbruyères & Laubier, 1980) (Figure 4.1), as well as two other genera, and ten other species (Table 4.1.) The family Alvinellidae has a patchy distribution throughout the Pacific rim, and flourishes at active vent sites, in a variety of species of specific niches. The geographical distribution of the Alvinellidae can be seen in Table 4.2. Differentiation between the genera *Alvinella* and *Paralvinella* relies on the production of a tube structure. *A. pompejana* and *A. caudata* both build biogenic dwelling tubes, whereas the genus *Paralvinella* secretes relatively large volumes of mucus, which serves a similar protective purpose (Gaill & Hunt, 1991). Polychaete annelids have a close affinity to the other dominant tube worm species that are found at hydrothermal vent sites such as the Vestimentifera and the Pogonophora, which are often found in close geographical (Gaill & Hunt, 1991), and geological (Little *et al.*, 1998) proximity to each other.

Species	*Reported by*	*Notes*
Alvinella pompejana	Desbruyeres & Laubier, 1980	Figure 4.1
Paralvinella bactericola	Desbruyeres &Laubier, 1982	
Paralvinella (Paralvinella) grasslei	Desbruyeres &Laubier, 1982	Figure 4.2a
Alvinella caudata	Desbruyeres &Laubier, 1986	Figure 4.2b
Paralvinella (Paralvinella) palmiformis	Desbruyeres &Laubier, 1986)	
Paralvinella (Nautalvinella) pandorae	Desbruyeres &Laubier, 1986	two sub-species P. p. pandorae, and P. p. irlandei.
Paralvinella hessleri	Desbruyeres &Laubier, 1989	
Paralvinella dela	Detinova, 1991	
Paralvinella (Paralvinella) fijiensis	Desbruyeres &Laubier, 1993	Figure 4.2c
Paralvinella (Paralvinella) sulfinicola	Desbruyeres &Laubier, 1993	
Paralvinella unidentata	Desbruyeres &Laubier, 1993	

Table 4.1 - Polychaetous annelids of the family Alvinellidae.

Name	*Location*	*Type*	*Depth (m)*	*Dominant Fauna*
Galapagos	East Pacific	Oceanic Ridge	2450 – 2700	Vestimentifera, Mytilidae, Vesicomyidea, **Alvinellidae**, Bythograedae, enteropneusts
North EPR	East Pacific	Oceanic Ridge	2000 – 2620	Vestimentifera, Mytilidae, Vesicomyidea, **Alvinellidae**, Bythograedae, Zoarcidae
South EPR	East Pacific	Oceanic Ridge	2600 – 3100	Vestimentifera, Mytilidae, Vesicomyidea, **Alvinellidae**, Bythograedae, Zoarcidae, Cirripedia,
Guaymas	East Pacific	Oceanic Ridge	2000 – 2050	Vestimentifera, Vesicomyidea, **Alvinellidae**, Bythograedae, Nuculana
Explorer	Northeast Pacific	Oceanic Ridge	1800 – 1870	Vestimentifera, actinians, gastropods, Ampharetidae, **Alvinellidae**
Juan de Fuca	Northeast Pacific	Oceanic Ridge	1540 – 2950	Vestimentifera, actinians, gastropods, Ampharetidae, pycnogonids, Vesicomyidea, **Alvinellidae**
Gorda	Northeast Pacific	Oceanic Ridge	2700 – 3300	Vestimentifera, actinians, gastropods, Ampharetidae, pycnogonids, Vesicomyidea, **Alvinellidae**
Fiji	West Pacific	Back-arc basin	2000 – 3000	Alvinoconcha, Ifremeria, Mytilidae, **Alvinellidae,** Bythograedae, Cirripedia, holothurians, Lithodidae
Manus	West Pacific	Back-arc basin	1630 – 2500	Alvinoconcha, Ifremeria, Mytilidae, **Alvinellidae**, Bythograedae, Cirripedia, holothurians, Vestimentifera
Mariana	West Pacific	Back-arc basin	2500 – 3750	Alvinoconcha, Mytilidae, **Alvinellidae,** Bythograedae, Alvinocarididae, Marinactis
Okinawa	West Pacific	Back-arc basin	680 – 1550	Vestimentifera, Mytilidae, Vesicomyidea, **Alvinellidae,** Zoarcidae, Alvinocarididae

Table 4.2 - Hydrothermal zones known to contain faunal assemblages that include polychaete worms for the family *Alvinellidae*. Adapted from Desbruyeres & Segonzac (1997)

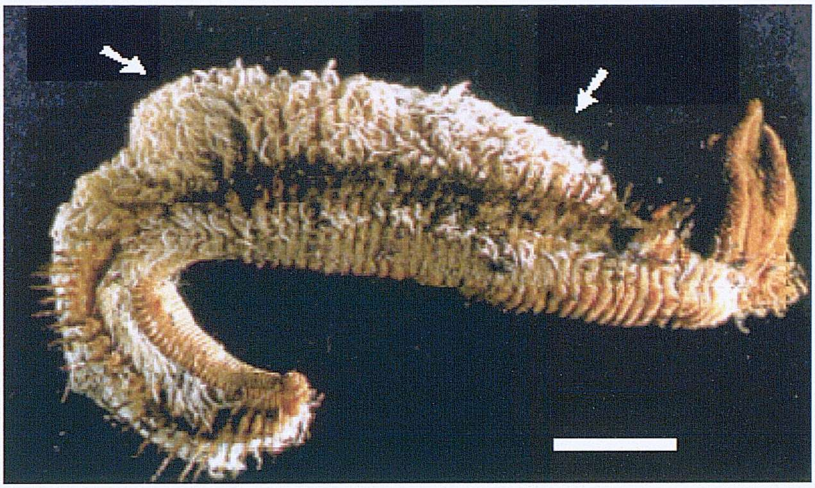

Figure 4.1 - The hydrothermal polychaete worm *Alvinella pompejana.* Anterior (right) posterior (left). Note filamentous bacteria associated with dorsal integument (arrows). Scale = 1cm. Image adapted from Desbruyeres & Segozac (1997).

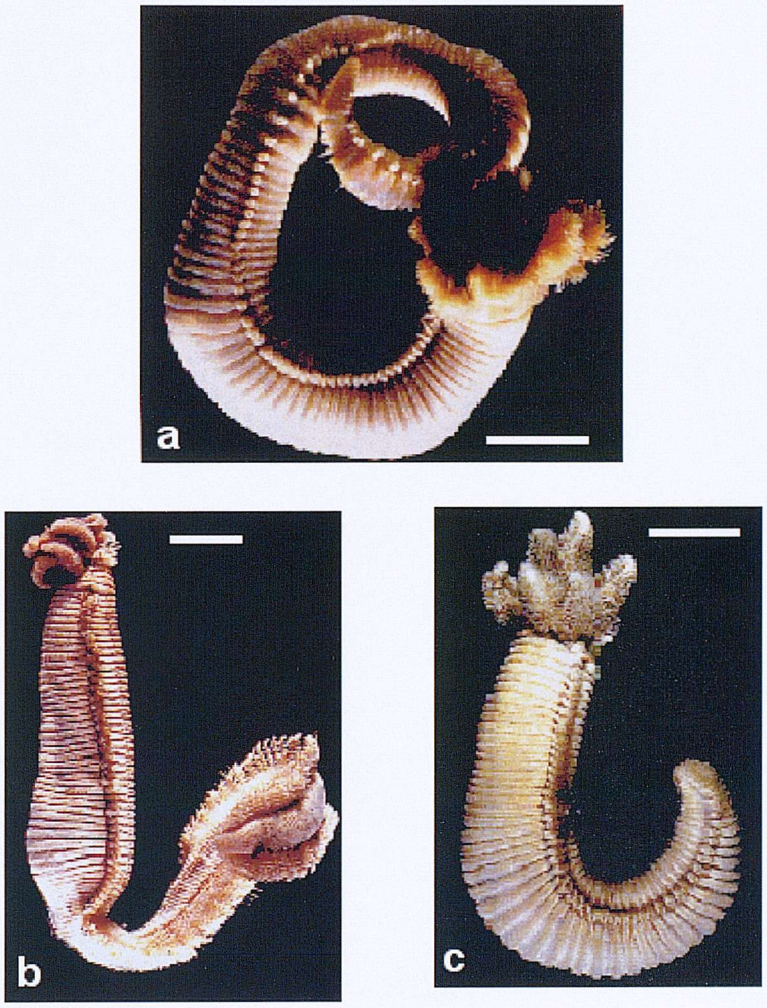

Figure 4.2 - (a) (top) *Paralvinella (Paralvinella) grasslei* Desbruyeres & Laubier, 1982. (b) (bottom left) *Alvinella caudata* Desbruyeres & Laubier, 1986. (c) (bottom right) *Paralvinella fijiensis* Desbruyeres & Laubier, 1993.

4.1.2 – Ecology and physiology of Alvinella pompejana

The polycheate worm *Alvinella pompejana* or 'Pompeii' worm was first discovered at an active hydrothermal vent site at 21°N on the East Pacific Rise. This species of alvinellid worm is exclusive to the East Pacific Rise, and has a wide geographical distribution ranging from 23°S to 21°N, although curiously it is absent from biocommunities in the Guaymas Basin and the Galapagos Spreading Centre. Individual worms may grow up to 150mm (Desbruyères & Segonzac, 1997), and are characterised by four pairs of lamellated branchiae (feeding appendages) which are retractile and filamentous; two transformed setigerous segments; a posteriorly tapering body; and an

epibiotic fauna which may be associated symbiotically or parasitically (Storch & Gaill, 1987). *A. pompejana* has a functioning gut and extendable feeding tentacles. An atypical, possibly bacterially derived form of nutrition has been postulated, and discussed extensively by Desbruyères *et al.*. Individual worms live in organically produced tubes, which form large colonies that penetrate active chimney walls.

A. pompejana secrete thin dwelling tubes directly on to the outer walls of active vents, and are often found associated with intermediate temperature venting (150 - 250°C) (Desbruyères *et al.*, 1983), and less commonly, with high temperature venting (250 - 400°C) (Prieur *et al.*, 1990). *Alvinella* sp. tubes are often the main biogenic construction seen associated with medium and high temperature hydrothermal vents (Desbruyères & Laubier, 1980), and may cover entire chimney walls. Desbruyères *et al.* (1983) reported that the tubes can often be observed to penetrate the walls of hydrothermal chimneys sufficiently deep so that they are in constant contact with the hot venting fluids (due to the growth of the chimney around the dwelling tube, as opposed to any burrowing action of the worm itself). The maximum temperature which the alvinellid worms can withstand is presently thought to be 105°C (Chevaldonne *et al.*, 1992), however, this was observed when the worm was out of its tube, and wrapped around the temperature probe of the submersible *Alvin*,and is therefore a rather ambiguous estimation. Less questionable data concerning the thermal tolerance of the Pompeii worm was demonstrated by Cary *et al.* (1998), who ascertained *in situ* temperature profiles from deep inside and from the mouth of Pompeii worm dwelling tubes over a recorded time period. Frequent temperature spikes of over 81°C were recorded deep (6 - 8cm) inside the tube, compared with a near constant 20°C at the mouth of the tube. This data unambiguously demonstrates that this particular alvinellid worm is able to tolerate thermal gradients of over 60°C across the length of its body, for short periods of time.

Contrary to research carried out by Sieburth (1975), whose studies indicated that populations of epibiotic fauna are usually lacking in polychaetous annelids, *Alvinella pompejana* is associated with specific populations of endosymbiotic microorganisms. The microenvironment within the dwelling tube would appear to be especially favourable to microbial floral growth (Juniper & Tebo, 1995). A multitude of various microbes including filamentous, sheathed, unsheathed, rod-like, and coccoid bacteria can be found

within the epidermis of the worm, between the inter-segmentary spaces, and covering the dorsal integument (Gaill & Hunt, 1991). The epibiotic bacterial species associated with *Alvinella pompejana* are both heavy metal tolerant (Jeanthon & Prieur, 1990), and diverse. The dense, fleece-like covering on the dorsal integument may exhibit a variety of chemotrophic bacteria, and often include sulphur oxidisers, sulphate reducers, nitrate respirers, nitrifiers, denitrifiers, and nitrogen fixers (Cary *et al.*, 1997). Little is known about the relationship between these symbiotic bacterial colonies and the host worm, however it is possible that the bacteria could fulfil a nutritional role (Desbruyères *et al.*, 1983), serve to detoxify the worm's immediate environment (Alayse-Danet *et al.*,1987) or transfer metabolites to the worm (Desbruyères *et al.*, 1983). Pompeii worms spend the greater part of their life within the dwelling tube, often with only the gills protruding. However, individual worms have been known to leave the protection of the dwelling tube for the purpose of grazing. In fact, Cary *et al.* (1988), reported that individual alvinellid worms regularly make excursions of up to 1m away from the tube to feed on free-living filamentous chemoautotrophs.

4.1.3 – *Alvinella pompejana* dwelling tubes

The dwelling tube of *A. pompejana* is a complex organic mix of secreted proteins and minerals. The worm uses glands located within the anterior part of its body (the anteriorventral glandular shield) to secrete proteinaceous granules, which, when mixed with sulphated glycosaminoglycans produced by the body's mucocytes, form the basis of the tube material (Gaill & Hunt, 1991). All polychaete tubes contain proteins, and often carbohydrates in the form of polysaccharides (Gaill & Hunt, 1988). Specific to the tubes of *A. pompejana* is the high concentration of natural hexose, and the amino acids serine, glycine, and alanine. These proteins are strongly self-interactive *via* either covalent bonding, or multiple weak interactions (namely di-polar bonding:Gaill & Hunt, 1988), allowing for swelling and minimal disruption of the tube wall, which in turn renders the tubes chemically and thermally stable. In fact older, mineralised tubes are generally thicker than younger tubes, attesting to the durable nature of the tube material. The tube material itself is fibrous, and composed of sub-layers of sigmoidal and parabolic fibrils, which are laid down normal to the direction of the previous sub-layer, forming a 'ply-wood' like structure (Gaill & Hunt, 1991). The numerous sub-layers are bound by

microbial horizons, which are formed by the trapping of microbes which had previously adhered to the inner surface of the tube (Gaill & Hunt, 1988). The number of individual layers and sub-layers varies from tube to tube, and along the length of individual tubes also. Elements such as sulphur, calcium and phosphorus are the major constituents of the tube material, whereas iron, zinc and magnesium form only minor constituents (Gaill & Hunt, 1986). The elemental sulphur content is high, and may vary from 12 - 25% (Gaill & Hunt, 1991). Elemental sulphur has been observed within bacterial cells, and associated with the bacteria on the inner surface of the tube. Chitin is not observed to be present in alvinellid tubes, as it is in vestimentiferan worm tubes.

The preferred habitat of the Pompeii worm is the zone of early sulphide mineralisation on actively growing chimneys (Desbruyeres *et al.,* 1985), which is also the zone of most vigorous mineral precipitation, and the steepest physicochemical gradients (Juniper *et al.*, 1992). Studies of the mineralogy of hydrothermal vents colonised by alvinellid worms, has revealed that the biomineralisation initiated by a mature colony of worms can cause macro-scale cementation over large areas of the host chimney. Mineral precipitation on this scale is known to affect wall porosity, fluid flow, hydrothermal mineralisation and local geochemistry and can therefore greatly affect the rest of the adjacent hydrothermal biocommunity.

4.1.4 – Microbial processes associated with *Alvinella pompejana*

The bacterial mediation, manipulation and uptake of metal ions, and the consequent production of biomineralised mineral deposits is a well documented phenomena, which has been discussed by workers such as Beveridge (1978); Beveridge & Fife (1985); Clarke *et al.* (1997); Ferris *et al.* (1987); (1988); Ghiorse (1984); Juniper & Forquet (1988); Juniper & Tebo (1995); Konhauser & Ferris (1996); Konhauser, (1997); Konhauser *et al.* (1998); Ohmoto (1993); and Urrutia & Beveridge (1993a); (1994). A number of studies have shown that dissolved metals in substantial quantities can be complexed into metal cations by bacteria and their respiration/metabolisation products (e.g. Beveridge & Murray, 1976; Beveridge & Fyfe, 1985). The binding of metallic ions into cellular walls and external sheaths is facilitated by electrostatic attractions with bound anionic carboxyl, hydroxyl and phosphoryl groups, which form the structural polymers of

the microbial cell wall structure (Beveridge & Murray, 1980). The molecular components present in the cell walls of bacteria are particularly reactive and therefore can accumulate metals in large quantities on their cellular surfaces. This is enhanced by the fact that, due to their small size, bacteria have the largest surface area to volume ratio of any cellular life forms: surface area to volume ratios vary depending on cell type, but may range from 10 : 1 for rod-shaped cells to 16 : 1 for spiral-shaped cells (Beveridge, 1989b), offering good surface adsorption capabilities. In fact, the external sheaths and cell walls of degraded microbes are the most abundant microbial remains preserved as microfossils (Knoll, 1985). Transition metals show an exceptional affinity for bonding with the microbial polymeric cell components, due to very compatible electronegativities, valences, hydrated radii, and hydration energies (Ferris *et al.*, 1986). However, some bacteria show extreme selectivity, and may incorporate only one cation in a solution of competing metal ions, whereas other bacteria are totally unspecific, and may scavenge all available cations (Williams, 1981).

The method by which microbes become trapped and incorporated into the Pompeii worm dwelling tube structure is fairly well understood and has been extensively discussed by workers such as Gaill & Hunt (1991). There is no doubt that when the microbes become buried within the tube, they will effectively cease to metabolise and die. However, this does not, by any means, suggest that the mineralisation potential of the microbial cells is inhibited. Ferris *et al.* (1988) suggested two reasons why the binding capability of dead microbial cells, could be greater than living cells. The first is that the cellular degradation that occurs after death increases the availability of organic functional groups which are capable of binding metal ions from solution. The second reason is that the protons generated by cellular respiration are not available to compete with the aqueous metallic ions, and therefore this increases the accessibility of binding sites. The production of polysulphide ions due to cellular degradation could also enhance metal sulphide precipitation within the immediate environment of the degrading cell.

4.1.5 Mineralisation associated with *Alvinella pompejana* dwelling tubes

It has been convincingly demonstrated that vent biota can influence mineralisation processes at modern hydrothermal sites (Juniper et al., 1992). For

example, bacterial mats growing on animal and sulphide mineral surfaces can act as loci for metal crust formation (Jannasch & Wirsen, 1979; Tunnicliffe & Fontaine, 1987), and alvinellid polychaetes are known to alter black smoker chimney morphology, porosity, and mineralogical composition (Haymon & Koski, 1985); Juniper & Sarrazin, 1995). The same mineralisation processes sometimes lead to fine-scale replacement of vent animal shells and organic tubes, and their subsequent incorporation into the growing massive sulphide deposits. Examples include the alvinellid polychaete *Alvinella* sp. tubes on the East Pacific Rise being replaced by layers of silica and pyrite (Haymon & Koski, 1985); tubes of the vestimentiferan *Ridgeia piscesae* on the Juan de Fuca Ridge being replaced by barite, amorphous silica and later Fe, Zn and Cu sulphides (Cook & Stakes, 1995); and shells of the gastropod mollusc *Ifremeria nautilei* being replaced by Zn-rich sulphides in the Manus Basin (Tufar, 1990). The process of mineralisation and preservation has been inferred from observations of a range of tube replacement mineralogy (e.g. Little *et al.* 1998) and the role of microorganisms has been debated (Juniper & Tebo, 1995a). Late stage sulphide replacement of vent tubeworms has been investigated by Cook and Stakes (1995). However, early mineralisation processes are particularly poorly understood, and are of importance in understanding the presence of fossils in ancient vent deposits. The processes involved are likely to be different from soft tissue preservation by sulphides described in sedimentary systems (e.g. Briggs *et al.*, 1991; Canfield, 1991; Raiswell *et al.,* 1993; Wilby *et al.*, 1996; Raiswell, 1997).

Hydrothermal vent fossils have been found in at least 25 ancient massive sulphide deposits ranging in age from the Silurian to the Eocene (Oudin & Constantinou, 1984; Haymon *et al.*, 1984; Haymon & R.A., 1985; Little *et al.*, 1997; Little *et al.*, 1998;Little *et al.*, 1999a; Little *et al.*, 1999b; Little *et al.*, 1999c). The majority of these fossils are vestimentiferan, polychaete and other unidentified, tubeworms, but brachiopods, and monoplacophoran, bivalve and gastropod molluscs are also present. All of these fossils are preserved as pyrite or marcasite moulds and there are no remaining shells or organic tube walls (Little *et al.*, 1998). The sulphide mineralisation process is thought to have taken place rapidly, but the exact mechanisms are unknown and will be investigated further in this Chapter, with a discussion of the formation of iron sulphides in aqueous systems below 100°C.

4.1.6 - Reactions forming pyrite & marcasite below 100°C.

Authigenic sulphide minerals occur in marine sediments primarily as the result of either marine hydrothermal activity or biological processes (Morse *et al.*, 1987). Pyrite formation is also associated with fossils where organic material decays by sulphate reduction, or where the carbonate material in the skeleton either acts as a nucleation substrate for pyrite or induces precipitation by dissolution (Raiswell, 1997). The wide range of industrial applications for pyrite, and the control that the formation of authigenic iron has on the global O_2 and H_2S / SO_4^{2-} cycles, has led to research into the physical properties of iron sulphides, together with investigation into the chemical properties, reaction kinetics, and mechanisms of formation (e.g. Morse *et al.*, 1987; Rickard 1997; Rickard & Luther, 1997).

Despite being extensively researched over many years, the mechanisms for the formation of pyrite and its orthorhombic dimorph marcasite (FeS_2), are still not completely understood (e.g. Allen *et al.*, 1912; Berner 1970, 1972, 1984, 1985; Gardener, 1973, 1974, 1979; Sweeney & Kaplan, 1973; Goldhaber & Kaplin, 1974; Berner & Westrich, 1985; Fyfe, 1987; Morse *et al.*, 1987; Luther, 1991; Schoonen & Barnes 1991a, 1991b; Wilkin & Barnes, 1996; Vaughan & Craig, 1997; Benning *et al.*, 2000). Formation mechanisms for the Fe-S system at temperatures over 350°C are relatively well constrained, and the phase relations are well understood (refer to section later in this Chapter). However, although well studied, the reaction pathways and mechanisms associated with pyrite formation in aqueous solutions at low temperatures (<100°C) remain controversial, with the reaction rates being poorly constrained (Benning *et al.*, 2000).

Pyrite formation below 100°C can potentially proceed by two methods: replacement of an iron monosulphide precursor mineral, or the direct nucleation and subsequent growth of FeS_2 from solution (Morse *et al.*, 1987). Although neither pathway has been indisputably verified in any environment (Schoonen & Barnes, 1991a) those environments where undersaturation of metastable iron monosulphide within the pore waters occurs may be more biased towards direct nucleation (e.g. Raiswell, 1982; Giblin & Howarth, 1984; Weise and Fyfe, 1986). Laboratory experiments have reported some

evidence for the precipitation of FeS_2 *via* nucleation (e.g. Farrand, 1970; Rickard, 1975; Murrowchick & Barnes, 1986; Schoonen & Barnes, 1991a). The rate at which the direct nucleation of FeS_2 proceeds in acidic solutions (pH <4.88) is insignificant when compared to FeS_2 formation *via* replacement of FeS (Schoonen & Barnes, 1991a). The reaction between ferrous and polysulphide species, to nucleate FeS_2 proceeds at an insignificantly low rate in non-acidic solutions (Schoonen & Barnes, 1991a). This is attributed to a high nucleation barrier for pyrite and marcasite, which renders nucleation impotent, unless the aqueous solution is highly supersaturated. In fact, the nucleation barrier for FeS_2 is so high that in order for nucleation of FeS_2 to proceed at a significant rate the solution must first exceed saturation with respect to FeS. However, in practice, once the solution is super-saturated with iron monosulphides and iron disulphides, amorphous iron monosulphides will nucleate out of solution first, due to their lower nucleation barrier (Schoonen & Barnes, 1991a). Therefore direct precipitation of FeS_2 is not regarded as an important process in low temperature pyrite or marcasite formation, when compared to the formation of iron disulphides via a monosulphide precursor.

The most probable method of low temperature iron disulphide precipitation is by the replacement of an iron monosulphide precursor. As such, pyrite and marcasite formation can be hypothetically simplified to a 2 stage process (Schoonen & Barnes, 1991b). The formation of an iron monosulphide precursor mineral is the first step towards pyritisation. The monosulphide phase is produced by the reaction between aqueous ferrous iron species and aqueous hydrogen sulphide (4a).

$$Fe^{2+} + H_2S_{(aq)} \rightarrow FeS_{(s)} + 2H^+ \qquad (4a)$$

The iron monosulphide phase involved in this process is generally accepted to be the mineral mackinawite (Allen *et al.*,1912), this has the chemical composition Fe_9S_8, but is, in fact, variable and ranges between $Fe_{0.87}S$ to $FeS_{1.1}$ (Berner, 1964; Sweeney & Kaplan, 1973). However, it should be noted that within high-temperature vent fluid the pyrrhotite group of minerals (general formula: $Fe_{1-x}S$) are often present, and will substitute for mackinawite. The Pyrrhotite group of mineral are comprised of a number of 'magnetic pyrites' (Ineson, 1989) which are metastable in venting environments (Haymon, 1993). In addition, Benning *et al.* (2000) noted that the low temperature

conversion of mackinawite to pyrite probably progresses *via* the mixed valency (Fe^{2+} / Fe^{3+}) phase gregite (Fe_3S_4). However, for the purpose of this review, the stoichiometry for the iron monosulphide precursor can be taken to be FeS, as this is generally accepted in most mineralogical literature.

The second step of pyritisation has numerous potential reaction pathways, which depend on the mechanism of conversion: either by addition of sulphur from sulphur-containing species, or via rejection of Fe^{2+} from amorphous FeS (Schoonen & Barnes, 1991b). Conversion to FeS_2 by sulphidation of the precursor may proceed by the following reactions (4b-g), which depend on the presence or absence of aqueous sulphur species, which in turn, can be dependent on the following variables: concentration of sulphur-contributing species, acidity, redox state, and time (Schoonen & Barnes, 1991b).

$$FeS_{(s)} + S^0_{(s)} \rightarrow FeS_{2\,(s)} \quad (4b)$$

$$FeS_{(s)} + S_n^{2-} \rightarrow FeS_{2\,(s)} + S_{n-1}^{2-} \quad (4c)$$

$$FeS_{(s)} + H_2S_{(aq)} \rightarrow FeS_{2\,(s)} + H_{2\,(g)} \quad (4d)$$

$$FeS_{(s)} + HS^- + H_20_{(l)} \rightarrow FeS_{2\,(s)} + H_{2\,(g)} + OH^- \quad (4e)$$

$$FeS_{(s)} + S_2O_3^{2-} \rightarrow FeS_{2\,(s)} + SO_3^{2-} \quad (4f)$$

$$FeS_{(s)} + S_nO_6^{2-} \rightarrow FeS_{2\,(s)} + S_{n-1}O_6^{2-} \quad (4g)$$

Elemental sulphur ($S_{(s)}$) does not dissolve in water as it is extremely insoluble. However, it is rapidly converted to hydrogen sulphide ($H_2S_{(aq)}$), or bisulphide, polysulphide, or thiosulphate, depending on the pH of the solution, and could therefore be a potential sulphur contributor. Sulphate (SO_4^{2-}), on the other hand, is not seen as a sulphur contributor, mainly because it is not reduced below 250°C (unless *via* bacterial mediation).

Wilkins & Barnes (1996) demonstrated that FeS_2 formation can proceed by the loss of Fe^{2+} ions from monosulphide precursor (4h). The redox balance of the system is maintained by reducing an aqueous species at the surface of the precursor (Schoonen & Barnes, 1991b). Protons (4h) or organic species are seen as the possible reactants for conversion *via* Fe^{2+} rejection.

$$2FeS_{(s)} + 2H^{+} \rightarrow FeS_{2(s)} + Fe^{2+} + H_2 (g) \quad (4h)$$

Conclusive evidence to back many of these hypothesised reaction pathways (4f - l) is still missing (Benning *et al.*, 2000). Research by workers such as Schoonen and Barnes (1991a, 1991b), Rickard (1997) and Rickard & Luther (1997), have shown that the reaction to form FeS_2 from H_2S and FeS below 125°C can be very fast. However, these observations are generally inconsistent with the work carried out by previous researchers (e.g. Berner, 1964, 1974; Rickard 1969, 1975; Roberts *et al.*, 1969, Schoonen & Barnes 1991a, 1991b; Wilkin & Barnes, 1996), whose studies show that FeS_2 formation proceeds at fast rates only with an oxidant other than H_2S.

The importance of a zero valent sulphur source (e.g. $S^0_{(s)}$) has been clearly demonstrated by the work carried out by Schoonen & Barnes (1991b). Pyrite and marcasite were only seen to form in the presence of an intermediate sulphur species, such as polysulphide, thiosulphate, or polythionate. At a temperature of 65°C, Schoonen & Barnes (1991b) observed the rapid formation of FeS_2, from the reaction between amorphous FeS, and intermediate sulphur species (equations 4b & c). However, at the same temperature the formation of FeS_2 by the reaction between H_2S and FeS was observed to proceed at an very slow rate. Yet at slightly more elevated temperatures (at or above 100°C) the rate of reaction was measurable. The formation of FeS_2 by Fe-dismissal (equation 4h) appears to be undetectable at all temperature ranges between 65 – 300°C.

During the sulphidation of FeS, the reaction pathway is determined and controlled by the overall pH of the system. In solutions where the pH >6, marcasite is not formed, and the reaction products are entirely formed of pyrite crystals (Schoonen & Barnes, 1991a). The pyrite formed is generally small (crystals <2μm diameter), and exhibits an anhedral crystal form. The replacement sequence of FeS at pH >6 is thought to proceed by the continual sulphidation of mackinawite, which in turn replaces for greigite, and finally substitutes for pyrite (Schoonen & Barnes, 1991b). Mackinawite may substitute for pyrite directly under highly reducing conditions. However, at these low temperatures (<100°C) pyrite is not able to precipitate directly from solution. Instead the conversion of FeS to pyrite *via* greigite is able to proceed, indicating that oxidising conditions are favoured, and that therefore the rate of reaction will increase with an increase in the

oxidation state of the system. Schoonen & Barnes (1991a) attribute the influence of oxidation state to a change in sulphur speciation, indicating that intermediate sulphur species are not abundant under reducing conditions.

In acidic (pH<5) environments the dominant end-product is marcasite (Murrowchick & Barnes, 1986; Schoonen & Barnes, 1991b). This has been attributed to marcasite having a faster growth rate than pyrite below pH 5. Murrowchick & Barnes (1986) suggested that at a pH <5 the polysulphide reactants can become protonated. Protonated polysulphides (H_2Sn) are attracted to the growing surface of a marcasite crystal, but repelled from a growing pyrite surface. This hypothesis can also explain why marcasite crystals grown from the sulphidation of FeS during the reaction with polysulphide ions below pH 4 are euhedral, and exhibit larger crystal sizes, when compared to pyrite formed in the same manner at pH >6.

In this Chapter the organic tube of the alvinellid polychaete tubeworm *Alvinella pompejana* Desbruyères & Laubier, 1980 is used to explore early sulphide biomineralisation processes at vent sites. It is crucial that the biological controls on the mineralisation processes in higher temperature hydrothermal systems are understood, so that the processes responsible for mineralisation can be identified, and comparisons between modern and ancient vent faunas can be effected, allowing a better understanding of ancient hydrothermal vents and their biocommunities.

4.2. Sampling and Methods

The single *Alvinella pompejana* tube studied comes was retrieved from worm colonies inhabiting the walls of vent chimneys at an active hydrothermal vent field located between 12°48´N/103°57´W and 12°49´N/103°56´W on the East Pacific Rise (Figure 3.2). It was collected by the DSRV Alvin during the joint French-U.S. Hydrothermal Environment Research Observatory (HERO) expeditions in October 1991 (Haddad *et al.*, 1995). The sample was preserved in propanol, in a sealed container, and stored at room temperature at the Natural History Museum of London archive, following collection

The tube was first viewed with a binocular microscope to identify mineralised areas of interest. These were excised, critical-point dried, impregnated with AY 105 epoxy resin, and prepared as either polished thin sections or polished blocks. The sections and blocks were then investigated using reflected light microscopy (RL), transmitted light microscopy (TL), scanning electron microscopy (SEM), energy dispersive spectroscopy (EDS), electron microprobe analysis (EM-P), and fluorescence microscopy (FM). Elemental analysis was carried out on using a Cameca SX-50 electron microprobe fitted with a wavelength dispersive X-ray analyser. Detection limits for this method are <0.01% for elements analysed. Accuracy was monitored by calibration against well characterised standards immediately prior to analytical runs.

A full description of the analytical methods and geological setting of the study area can be found in Chapter 3.2.

4.3. Results

4.3.1. Microorganism distribution

Microorganisms were observed in two areas of the material: unevenly coating the inner tube wall surface, and forming distinct layers within the tube wall itself. No microorganisms were observed on the outer tube surfaces. The microorganisms on the inner tube surface can be separated into at least three distinct morphologies: large sheathed filaments (Figure 4.3a), branching filaments Figure 4.3b), and small rod shaped cells (Figure 4.3c). The sheathed filaments form the majority of the microorganism assemblage and occur with sulphide-rich, particulate matter (Figure 4.4). The exact identification of these microorganisms using LM and SEM techniques is not certain, and no specific molecular tests have been performed, such as those of (Cary *et al.*, 1997). However, the sheathed filaments are morphologically identical to filaments identified as epsilon proteobacteria by (Cary *et al.*, 1997) and as bacteria by Gaill and Hunt (Gaill & Hunt, 1991), as well as being reminiscent of *Thiothrix*-type filaments described by Jannasch (1984). The rods are also inferred to be bacteria because of their small size and shape.

The intra-tube microorganism layers have a maximum thickness of around 10 – 20 μm and comprise small rods or larger filaments that are generally orientated perpendicular to the layering of the tubes (Figure 4.5 & 4.6). However, a proportion of the filaments are parallel to the layers and can be up to 10-50 μm long (Figure 4.6b). In accordance with previous studies (Gaill & Hunt, 1986; Gaill & Hunt, 1991) it is thought that these microorganisms are the same as those growing on the worms' outer integument and on the inner tube wall surface. These have then become incorporated into the tube wall structure by subsequent deposition of organic layers. Each of the microbial horizons represents a layer which was once the inner surface of the tube wall, and covered with microbes, but has now been entombed by newer organic layers during the process of tube building. At some stage during the process of 'entombment', some of the larger filaments have been cropped (e.g. Figure 4.7), possibly by the feeding action of the worm itself. The microorganisms tend to retain morphological integrity after entombment in the tube wall (Gaill & Hunt, 1991) except in areas of significant sulphide mineralisation. Fluorescence microscopy (FM) has been used to demonstrate

that during the earliest stages of mineralisation, an organic component of the cell remains (figure 4.6c), even as the cellular wall of the microbe begins to become mineralised (figure 4.6b).

4.3.2. Chemistry of the tube wall

Table 4.3 shows the range in measured values for S, Si, P, Ca, Fe, Sr and Ba for unmineralised and mineralised portions of the tube wall using E M-P analysis. In the unmineralised portion of the tube, the total inorganic element content of the tube is <5%, the majority of the material being organic. This material represents tube wall material prior to mineralisation. The organic nature of the tube, combined with the porous nature of the material, explains the low total counts observed in these samples. Phosphorus maps of the tube wall show that P is associated with the organic matter (Figure 4.8a) and may be effectively used as a biomarker. A cross-section across this portion of the tube show that Fe and S also co-vary with the P content (Figure 4.8b).

The mineralised areas of the tube wall are dominated by iron sulphides, the stoichiometry of which varies across the tube wall. Phases identified include greigite and/or mackinawite (Figure 4.8e); and pyrite/marcasite (Figure 4.9d). The differentiation between these minerals is demonstrated using quantitative data collected by EMP, and qualitative XRD data (Figure 4.11). Pyrite and marcasite (FeS_2) are identified as they have an atomic ratio of sulphur to iron of 2:1, accurate to within 1.5% (Figure 4.9d). The calculated atomic ratio of S:Fe, for greigite (Fe_3S_4) is 1.333:1, and the equivalent S:Fe ratio for mackinawite (Fe_8S_9) is 1.125:1. (note that the S:Fe ratio of pyrrhotite (Fe1-xS), a mineral group commonly associated with pyrite/marcasite is 1.11:1, and it does not occur here). Figure 4.8e demonstrates that the mineralised area analysed in Figure 4.8c has a S:Fe ratio of 1.154 – 1.335, and lies between that of greigite and mackinawite, indicating that both iron sulphide species may be present. Two distinctive mineralised zones are clearly visible here (Figure 4.8c), one being porous and the other being well-crystallised, with the porous zone having a lower S:Fe ratio (Figure 4.9e). In the areas of the tube wall where greigite and/or mackinawite are present, the P content is low (Table 4.3). Generally the porous areas have very low phosphorus content (often below 0.05%), whereas the P content of the well-crystallised areas can be up to 0.2%. The phosphorus in the organic

layers adjacent to the mackinawite/greigite bands, often appears significantly enriched. For example, the layer adjacent to the well-crystallised mineralised layer in is enriched by up to 50% when compared to similar unmineralised areas.

	S	*Si*	*P*	*Ca*	*Fe*	*Sr*	*Ba*	*Total*
unmineralised tube – maximum Fe content	1.16	0.091	1.30	0.111	1.23	bdt	0.014	7.78
unmineralised tube – minimum Fe content	0.057	0.02	0.003	0.004	0.01	0.018	0.015	0.251
mineralised tube (marcasite/ greigite layer) - maximum Fe content	29.54	0.02	0.006	0.011	43.9	bdt	0.19	73.7
mineralised tube (marcasite/ greigite layer) - minimum Fe content	26.75	0.048	0.099	0.065	34.8	0.027	0.083	61.9

Table 4.3 - Maximum and minimum atomic weight % values for areas of mineralised and unmineralised alvinellid tube wall ascertained using E M-P analysis. Totals are lower than 100% due to organic phases present in the unmineralised areas and high porosity in the mineralised areas. bdt = below detection limit (detection limit in the order of 0.01 - 0.05%)

4.3.3. Sulphide mineralisation

Three distinct areas of sulphide mineralisation have been identified in the *Alvinella pompejana* tube samples: a) particles on and between the microorganisms growing on the inner surface of the tube wall, b) layers within the tube wall, and c) layers on the external surface of the tube wall. These will be described in turn.

(a) Sphalerite (ZnS) and pyrite (FeS_2) particles were observed both adhering to the outer sheaths of the filamentous microorganisms on the inner tube wall (e.g. Figure 4.12) and trapped within the network of filaments (e.g. Figure 4.4). The particles are between 10 and 100 μm diameter; small particles tend to be found on the filament sheaths, whereas the larger particles are generally found trapped between the filaments. It can be concieved that particulate matter from either the 'fall out' of black smoker plumes or by particles transported by vent fluid flow or thermal siphoning effects, could be responsible for incorporating a whole suite of metal-rich particulates within the microbial filament mass. These minerals could conceivably include sulphides such as

pyrrhotite, pyrite, sphalerite, wurtzite, bornite and covelite; sulphates such as anhydrite, barite and silca; and even native sulphur.

(b) The sulphide mineralisation within the tube wall structure occurs as discontinuous layers of iron sulphides running parallel to the organic layering and preferentially in the microorganism sub-layers (Figure 4.9a). The iron sulphide layers are generally between 10–50 μm thick, although some extensively mineralised areas are up to 200 μm thick. Although iron sulphides have replaced the organic material in the mineralised layers the phosphorus banding noted in Section 4.3.1 is still apparent. Pyrite and marcasite are both present in many of the iron sulphide horizons (Figure 4.10b), and can be observed throughout the section. These phases can be differentiated optically as a primary pyrite-rich sulphide; and a later marcasite-rich sulphide. Pyrite can be difficult to distinguish optically from marcasite when a lack of obvious crystal habit exists. Pyrite exhibits a brassy to light yellow colour under RLand weak anisotropy, whereas marcasite often shows as a lighter, paler yellow colour, usually with a hue of light green or pink, and is strongly anisotropic. Twinning and high reflectance (when polished) are also indicative (Ineson, 1989). However, marcasite is more susceptible to tarnishing than pyrite, it may appear to be darker under reflected light, or exhibit a multi-coloured tarnish. Due to the different crystal habits of pyrite and marcasite (cubic and orthorhombic, respectively) the two minerals show different X-ray diffraction patterns under XRD analysis. (Figure 4.11)

The pyrite-rich phase shows no obvious mineral textures, however, it does have a variable degree of porosity that is caused by numerous circular and sub-circular, holes 1-2 μm in diameter (e.g. Figure 4.9b). There are also a few more elongate holes up to 10-15 μm long and approximately 1-2 μm wide (Figure 4.9b). The abundance of the holes varies between individual mineral layers, and to some degree along the length of the mineralised horizons. The later, marcasite-rich sulphide phase can be seen to overgrow the pyrite-rich horizons. The degree of precipitation is variable,and marcasite-rich sulphide from adjacent layers may merge if the mineralisation is extensive enough (Figure 4.9c), with the degree of precipitation likely due to ube permeability, and therefore the availability of the aqueous ions necessary to form marcasite. When the marcasite-rich sulphide surfaces are fresh, no texture can be observed, however if the

sections are left to tarnish under atmospheric conditions a banded collomorphic texture becomes apparent (Figure 4.9e). The individual collomorphic laminae are often less than a micrometer thick, and are therefore much too thin to analyse accurately with the SEM/EDS or the EM-P. The observed mineralogical textures may reflect differences in the composition of the iron sulphides present, and the mechanism of mineral precipitation (Figure 4.9e).

The initial stages of mineralisation can be seen occurring on the cellular surfaces of individual microbes when analysed under fluorescence microscopy (FM); TL.; SEM/EDS; and RL Figure (4.6 a - d) shows an individual filament lying parallel to the organic layering. The filament has been examined under fluorescence microscopy, and clearly fluoresces under reflected ultra violet light, indicating the presence of organic material within the cell structure. In addition to this, the same microbial filament has been observed under transmitted, and reflected light microscopy: TL. shows that the filament has a dark, thickened cell wall, with fine grained opaque minerals contained within the cell wall. Under RL the same area reflects with a predominantly light grey light, with lesser areas of dark, bluish grey. Indicating the presence of sulphide minerals associated with the organic cellular material. EDS point analysis also indicates that organic and inorganic components are evident (Figure 4.6d).

(c) The external tube wall surface has a patchy, discontinuous veneer of collomorphic, laminated pyrite and marcasite up to 1.5 mm thick (Figure 4.10a). Small circular holes 1-2 μm in diameter occur in some of the pyrite-rich laminae (Figure 4.10b). However, no microbes, or microbial remains have been observed associated with the outer mineralised veneer. Minor barite, silica, sphalerite, galena and particulate iron oxide are also present. The barite occurs as small laths and 'rosettes' on the external iron sulphides and directly on the outer organic tube wall, and have been identified using EDS, and visually using SEM. Located throughout the tube wall, but more pronounced towards the outer layers are areas where the organic layers have been disrupted by the later growth of distinct sphalerite grains measuring around 100-200μm in diameter (Figure 4.12), which have precipitated inorganically by direct nucleation on to seed crystals incorporated within the microbial material (e.g. Figure 4.4). These cause disturbance of the original organic layering, and can be observed under TL and EM-P.

The numerous small voids observed in the biomineralised layers are inferred to be microbial cell moulds, occurring in greater or lesser concentrations, in all of the greigite/mackinawite or pyrite-rich sulphidised layers (Figures 4.8a; 4.9a, b, c; and 4.10a). No mineral in-fill of these moulds has been detected using any of the analytical techniques used. When viewed under secondary electron imaging the cell ghosts appear as topographical voids, an indication that any microbial remains have decayed or been scavenged away, or removed during the sample preperation process.

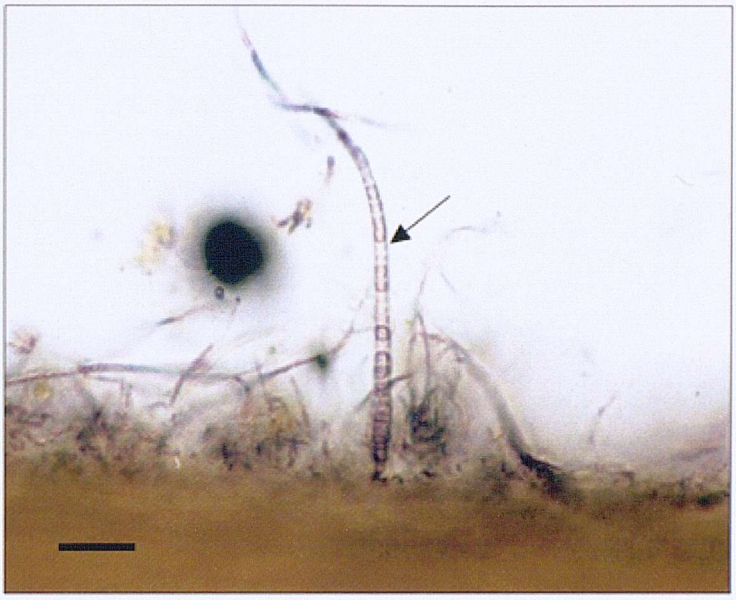

Figure 4.3a (left) Transmitted Light (TL) microscopy image of a sheathed bacterial filament (scale = 10 µm: tube wall inner surface is located towards bottom of figure).

Figure 4.3b (right) - TL microscopy image of branching filamentous microbial structures (scale = 10 µm: tube wall inner surface is located towards bottom left of figure)

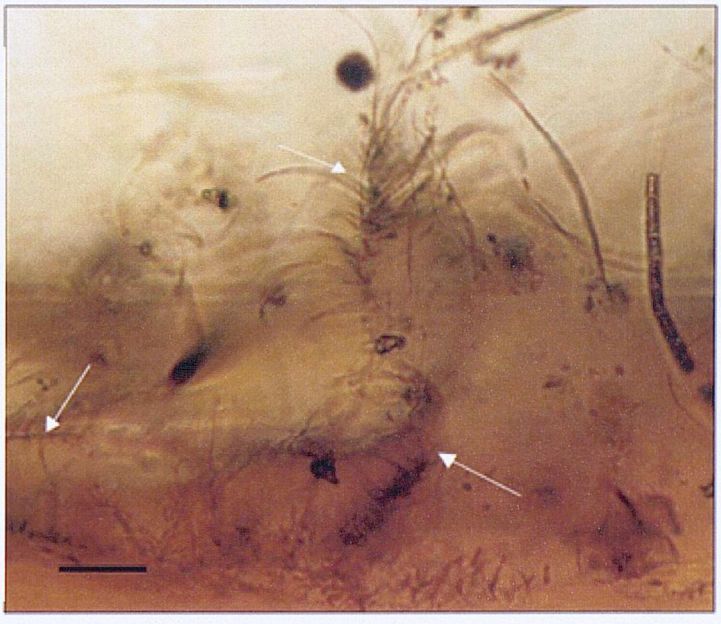

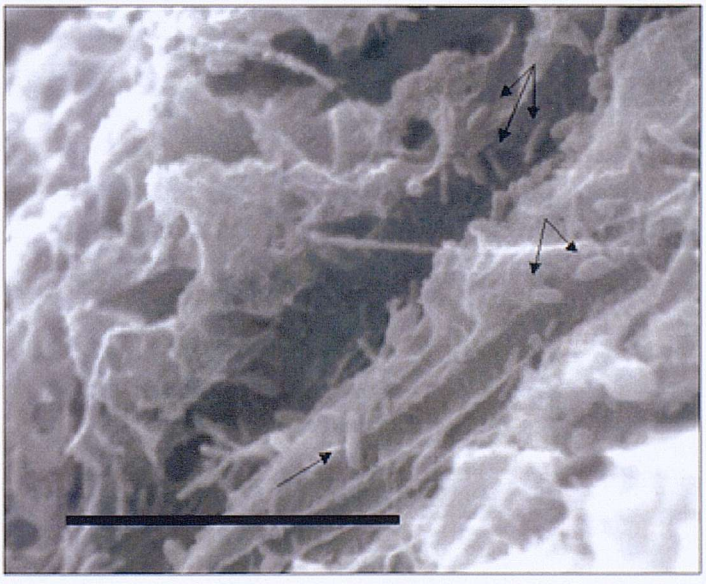

Figure 4.3c (left) – Back-scattered electron microscopy image of single celled, rod-shaped microbes observed along an obliquely cut area of tube. (scale = 10 µm: arrows indicate microbes)

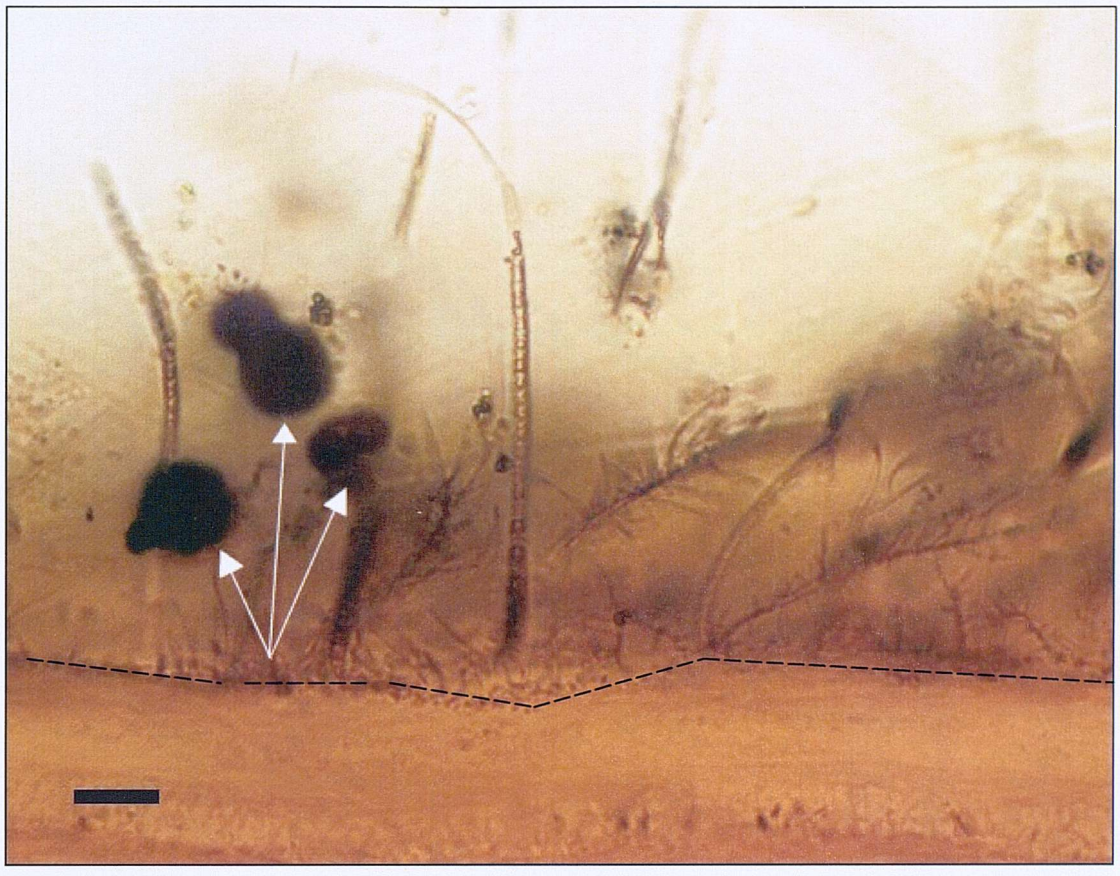

Figure 4.4 - T.L. microscopy image of a microbial assemblage of sheathed filaments and branched filaments, on inner surface of the tube wall and associated trapped sulphide particles (arrows). (Scale = 10μm: inner wall surface is located towards the bottom of the figure – indicated by dashed black line).

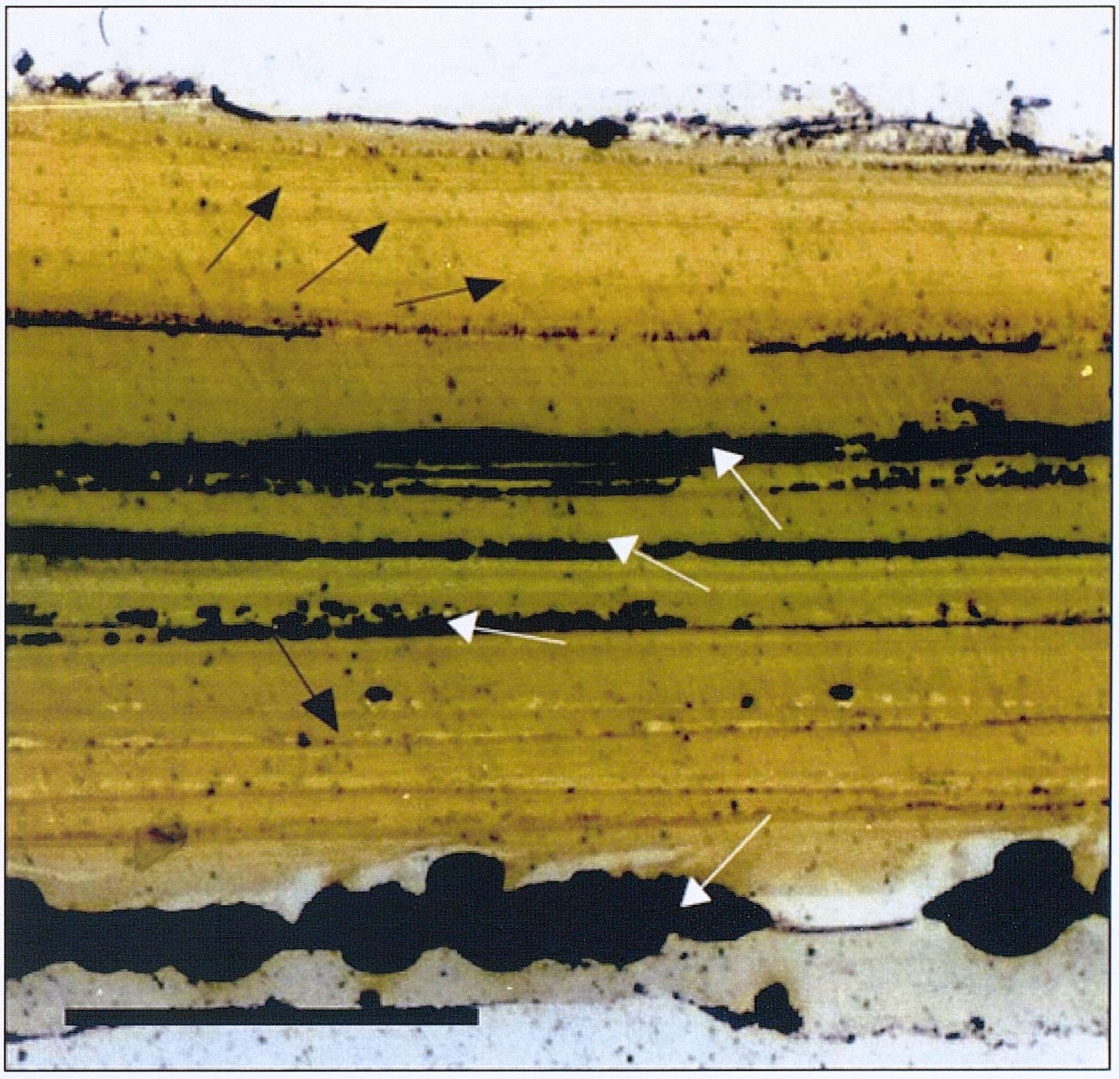

Figure 4.5 - TL microscopy images of a cross section of the tube wall, to show the nature and distribution of mineralised (white arrows) and microbial (black arrows) horizons within an area measuring approximately 1.5 mm^2. (Scale = 500 µm: inner surface of tube orientated to top of figure).

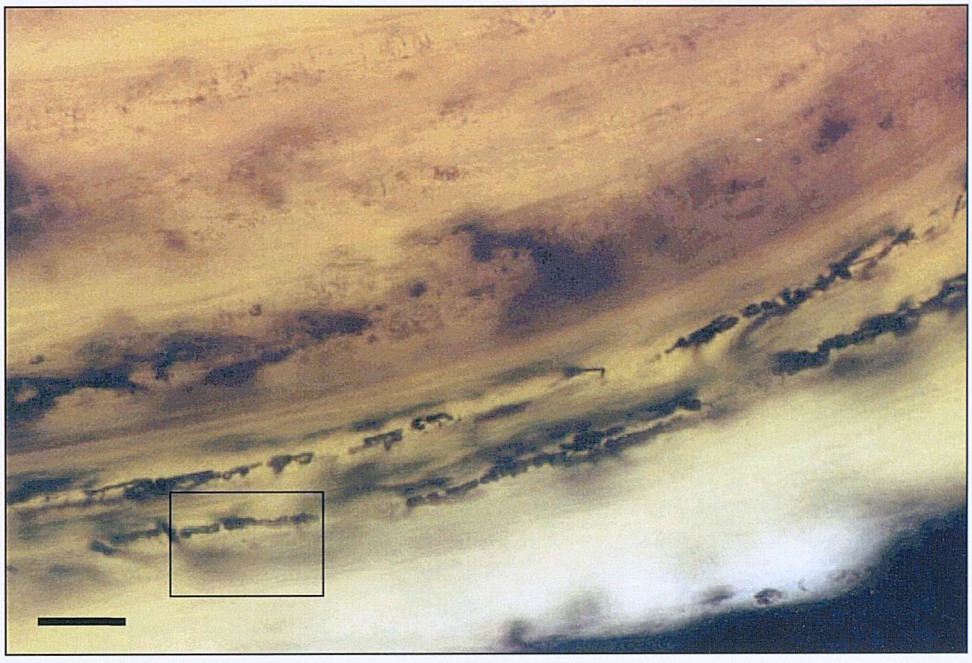

Figure 4.6a - Microbes trapped within the organic sub-layers (x100, scale bar 20µm). Microbial filaments within the tube sub-layers. These dominantly filamentous bacteria are inferred to be at the earliest stage of biomineralisation. The filaments have a thin veneer of iron sulphide electrostatically bound to the anionic surface of the cell wall which will then serve to act as a nucleation site for further crystal growth.

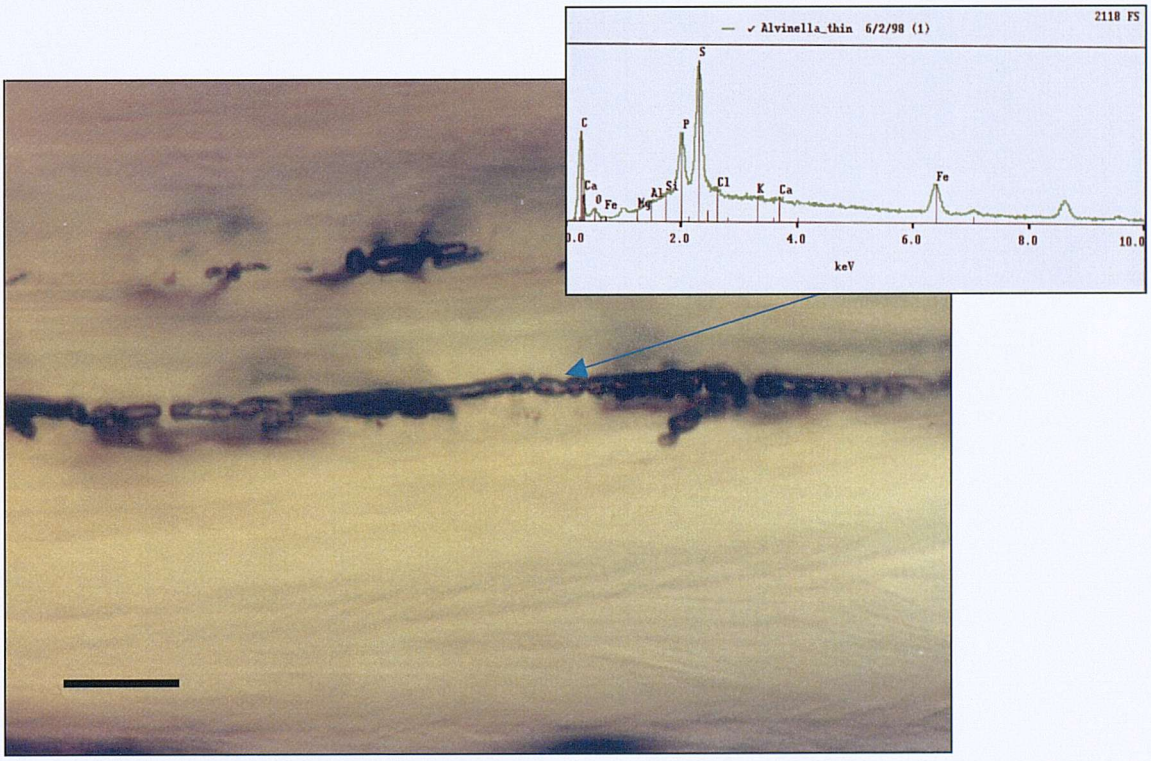

Figure 4.6b - A close-up of 4.6a, shows the cellular nature of the mineralised filaments and also shows the herring-bone structure of the organic tube wall (bottom of frame) (x400, scale bar = 10µm). EDS point analysis display (insert) demonstrates biomineralisation of the microbial cell wall (acceleration voltage = 15kV; count time = 60 seconds).

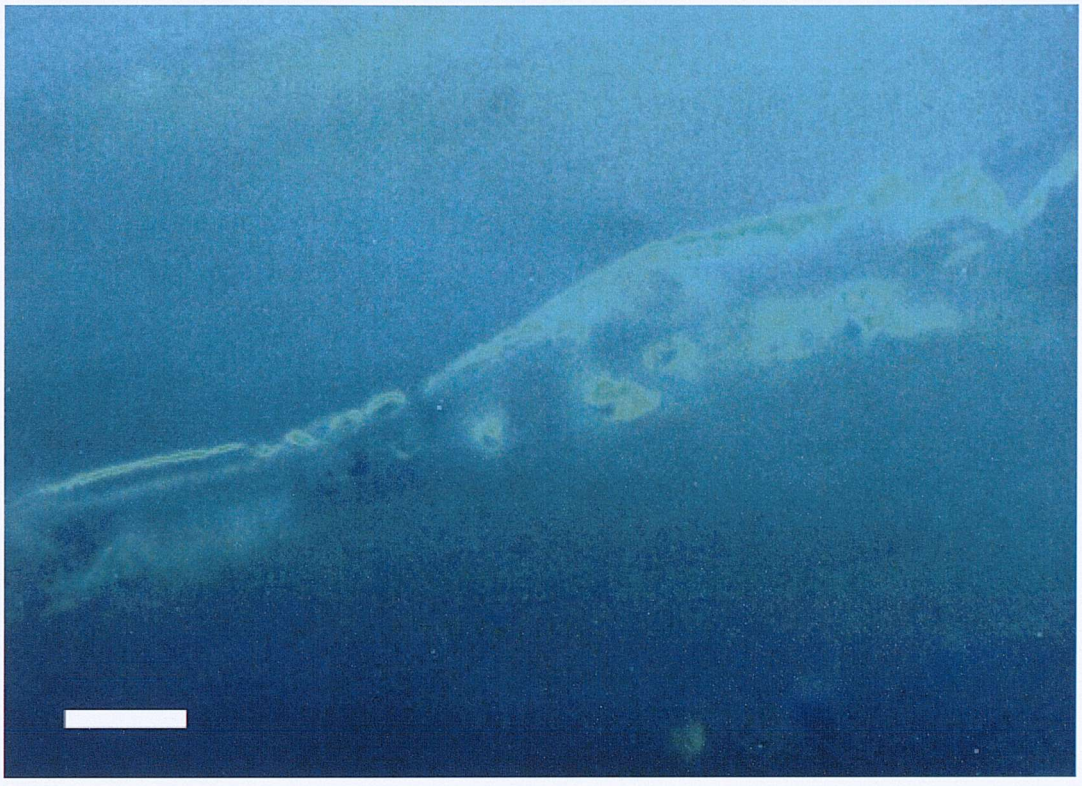

Figure 4.6c - The organic component in the cell wall of the microbes can be seen to fluoresce under reflected ultra violet light (scale bar = 10µm:inner surface of tube orientated to top of figure).

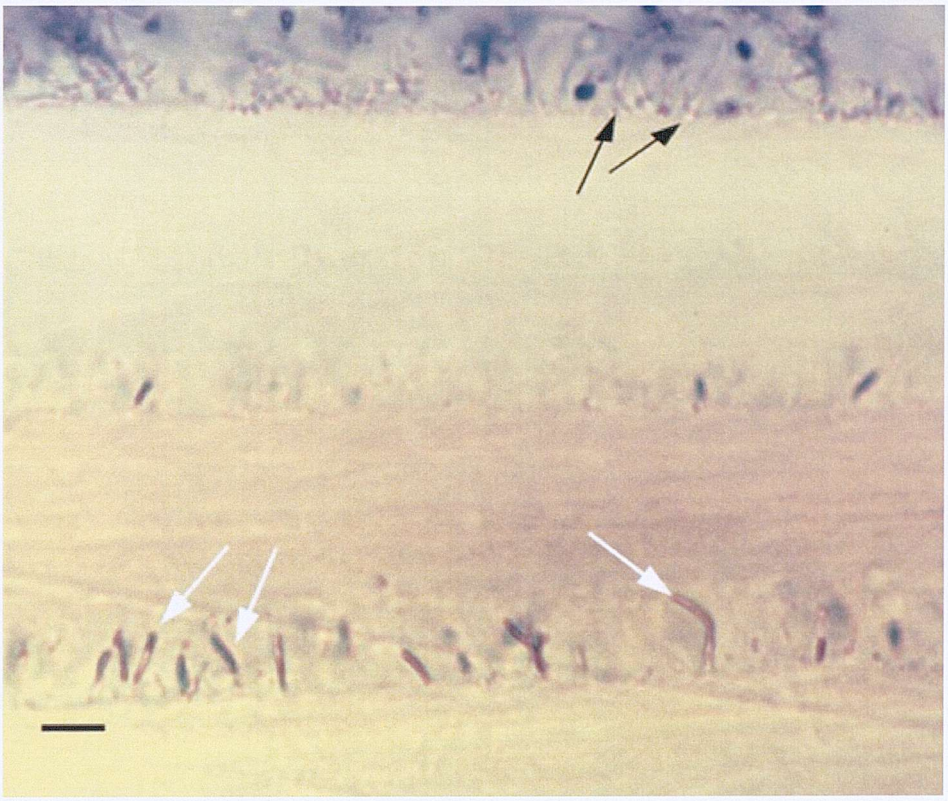

Figure 4.7 - TL microscopy image of an intact organic microbial structures observed along three microbial horizons. The inner wall surface can be seen at the top of the frame, and is covered by microbes, the two microbial horizons below (middle and bottom of frame) are entombed microbes which separate the organic tube layers, and consequently infer tube building episodes (scale = 10µm).

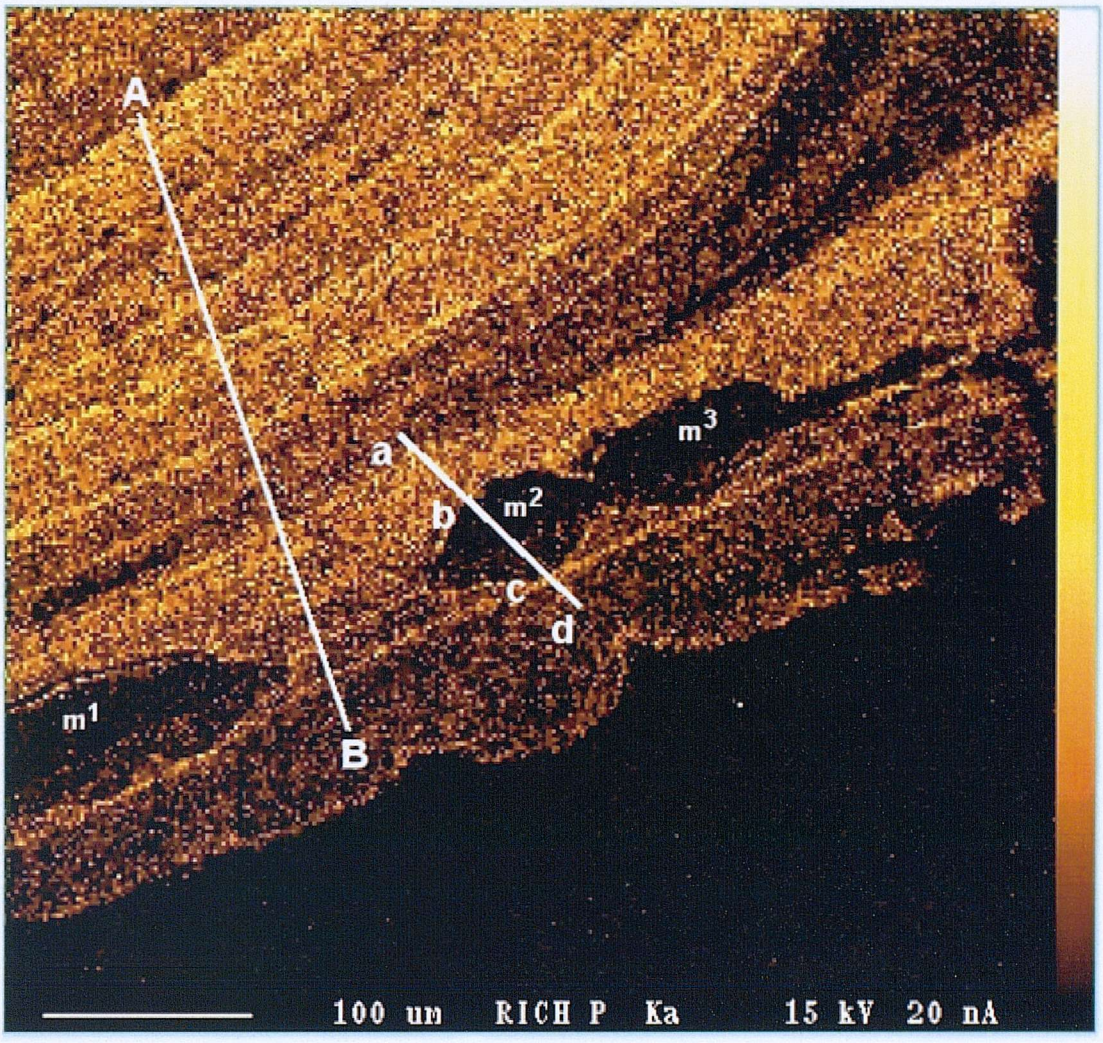

Figure 4.8a - Electron microprobe elemental map for P, about a section of the outer tube wall (external tube surface orientated towards bottom of figure). The organic sub-layers that compose the tube walls contain elevated levels of phosphorus. The labelled areas (m), are mineralised horizons.

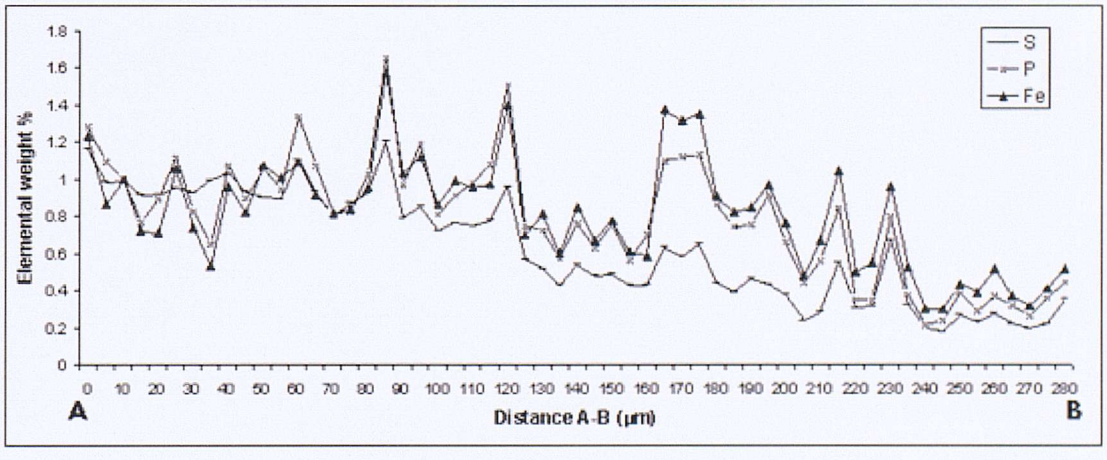

Figure 4.8b - Analysis of Fe, S and P along the unmineralised traverse A – B.

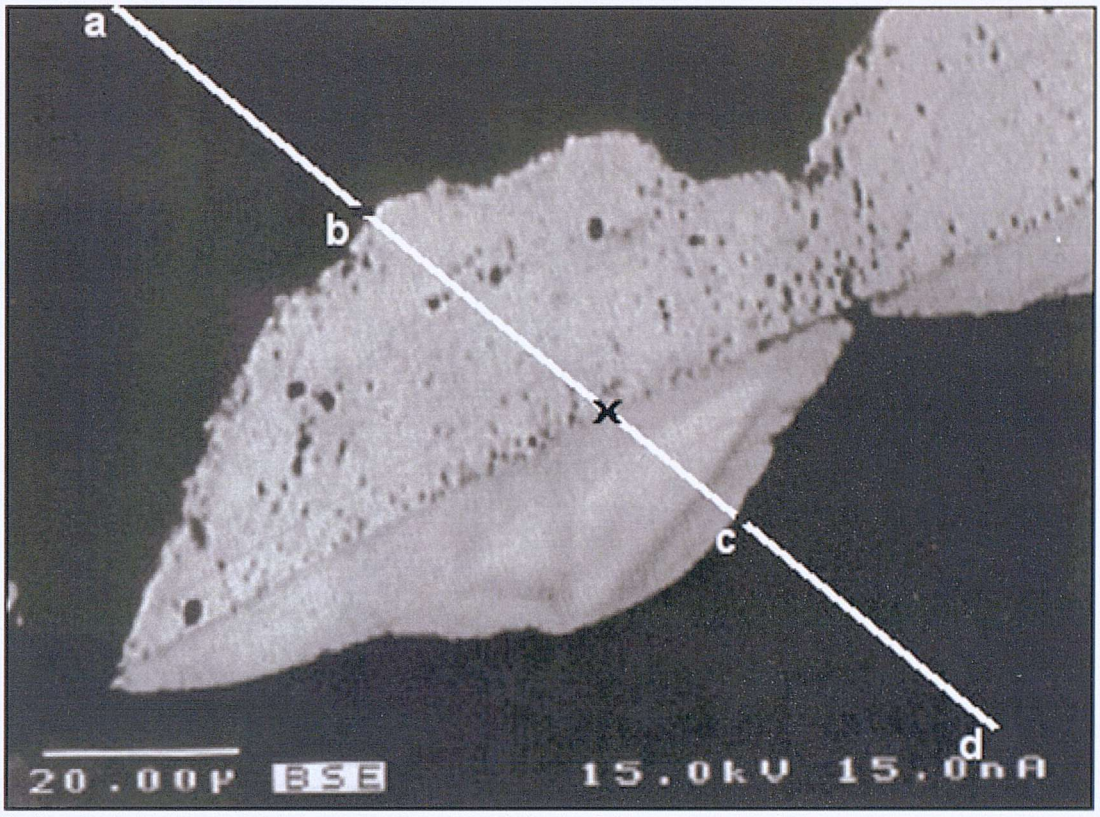

Figure 4.8c - A back-scattered electron image of the mineralised horizon a-d in Figure 4.8a, composed of porous mackinawite/greigite within the host organic tube layers. (Point 'X' indicates the transition from porous to well crystallised mineralised areas)

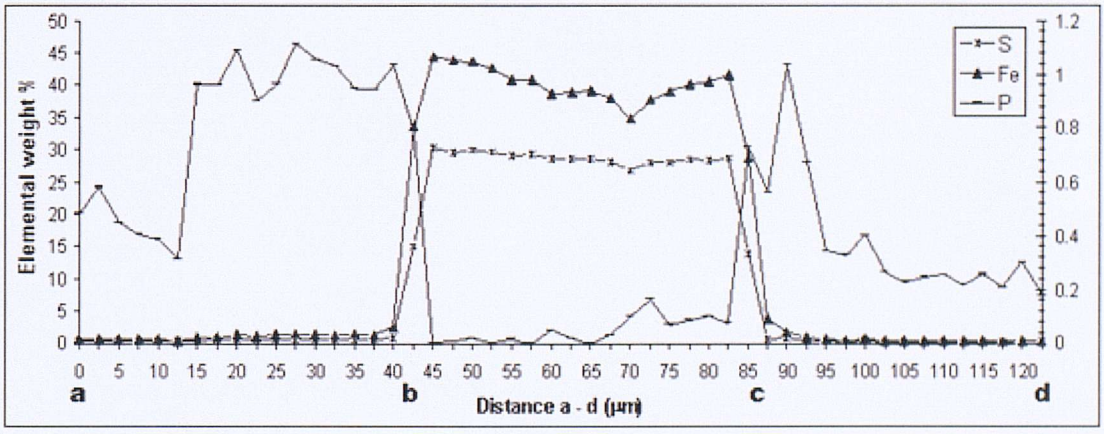

Figure 4.8d - A 50 point analysis, plotting weight % for P, Fe and S along the traverse a - d.

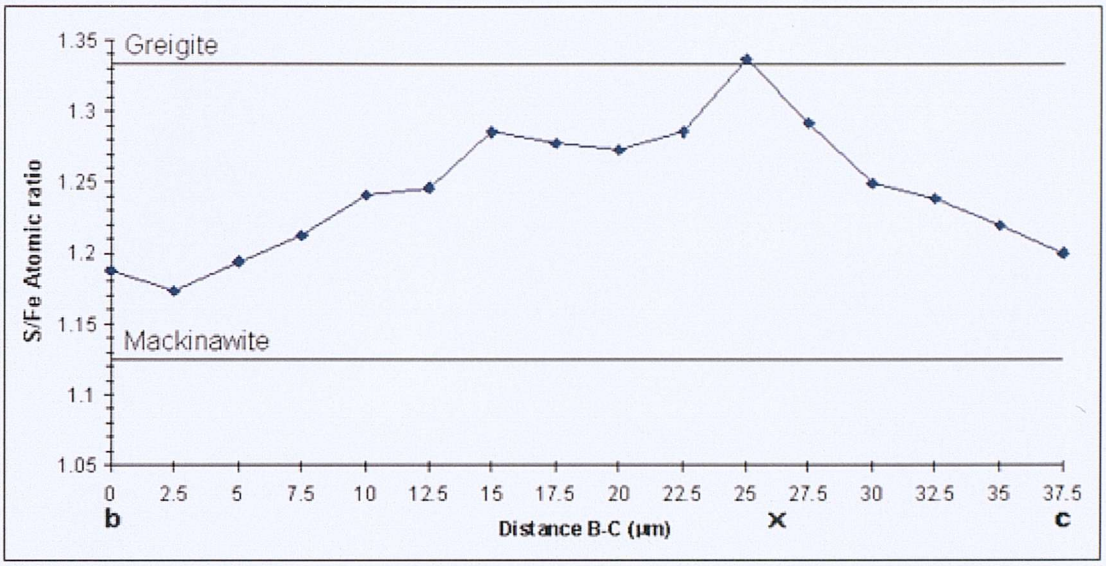

Figure 4.8e - Plot for S:Fe for the mineralised horizon along b– c, note that the mineral becomes sulphur-rich towards point 'X'

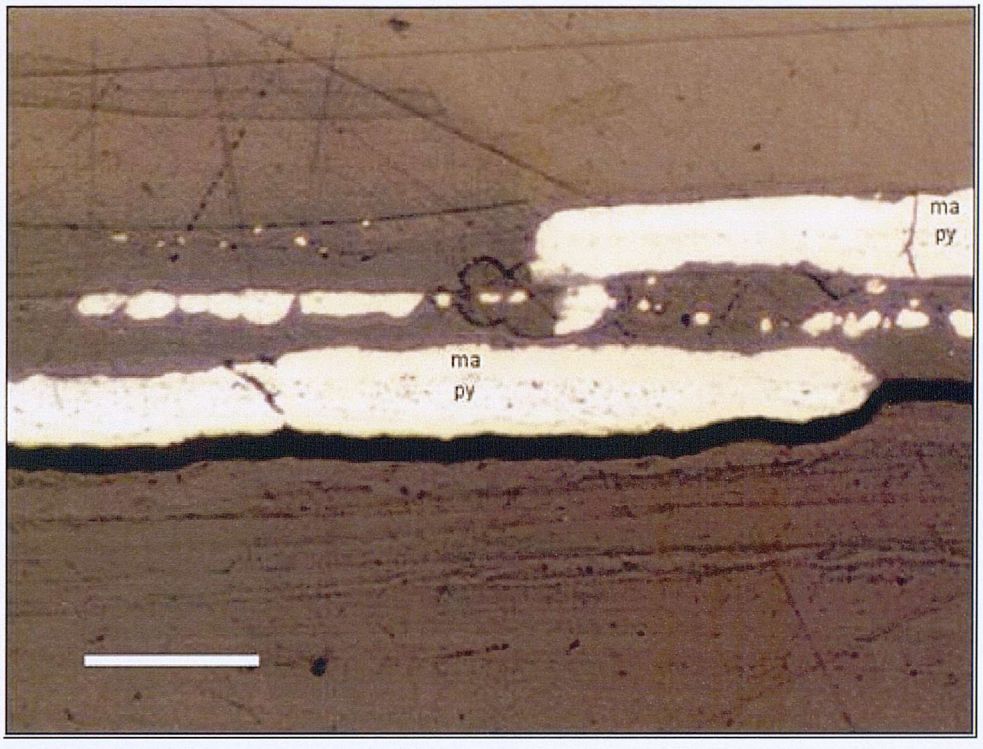

Figure 4.9 – Images of the mineralised zones of the *Alvinella pompejana* tube wall. (a) Reflected light (RL.) microscopy image of primary pyrite (py) and secondary marcasite (ma) mineralisation along separate microbial horizons. Numerous pores inferred to be microbial cell moulds are present in the pyrite layers (scale = 50 µm).

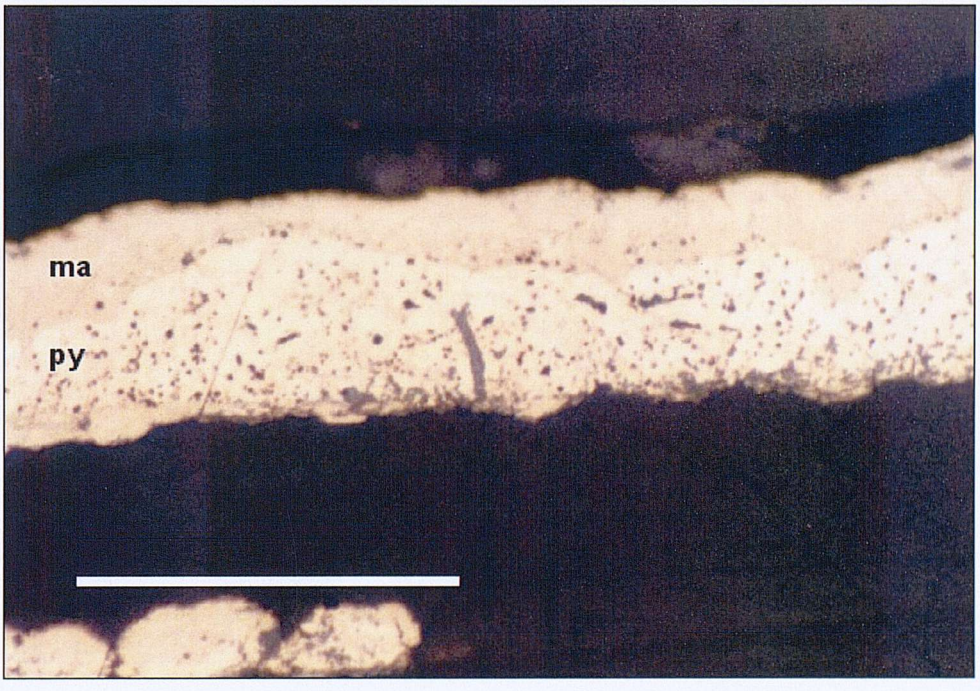

Figure 4.9b - RL microscopy image of a mineralised horizon within the tube lamina (scale = 50 µm). Note the elongate, cellular cast in the centre of the figure.

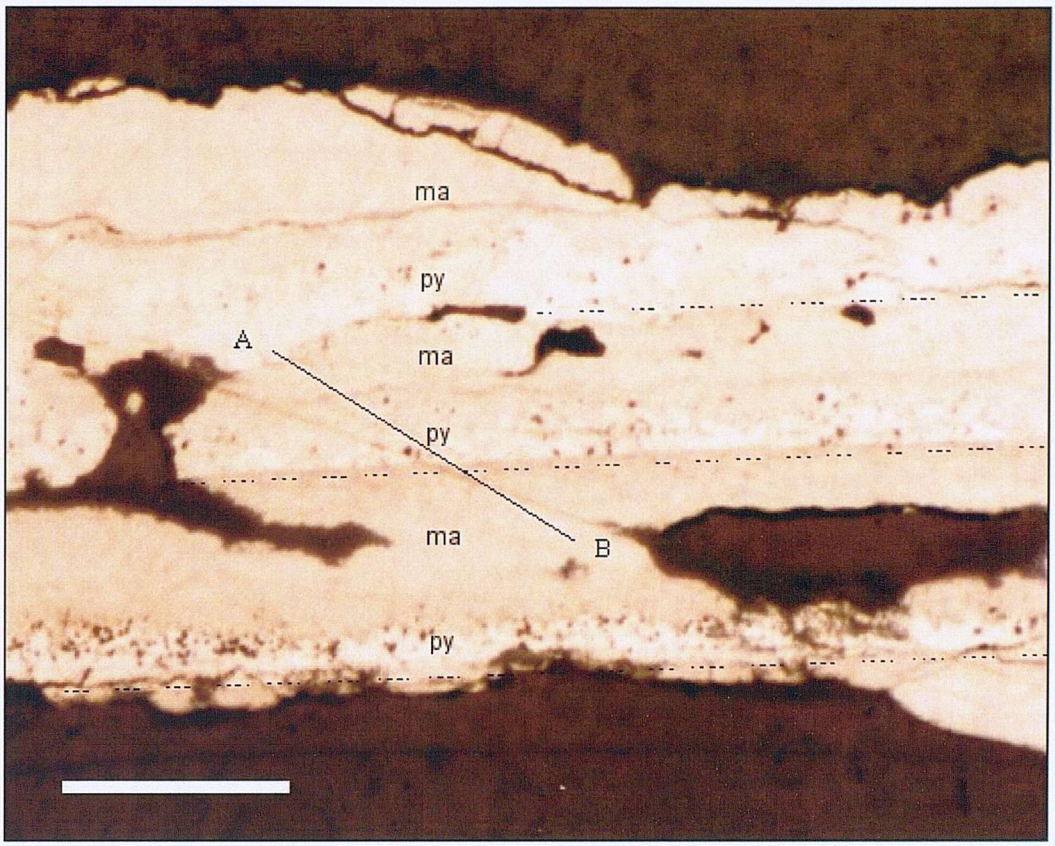

Figure 4.9c - Extensive marcasite replacement of organic wall has led to intergrowth of the mineralised horizons (scale = 50 µm: dotted lines indicate the position of the microbial horizons situated at the mineral bounderies).

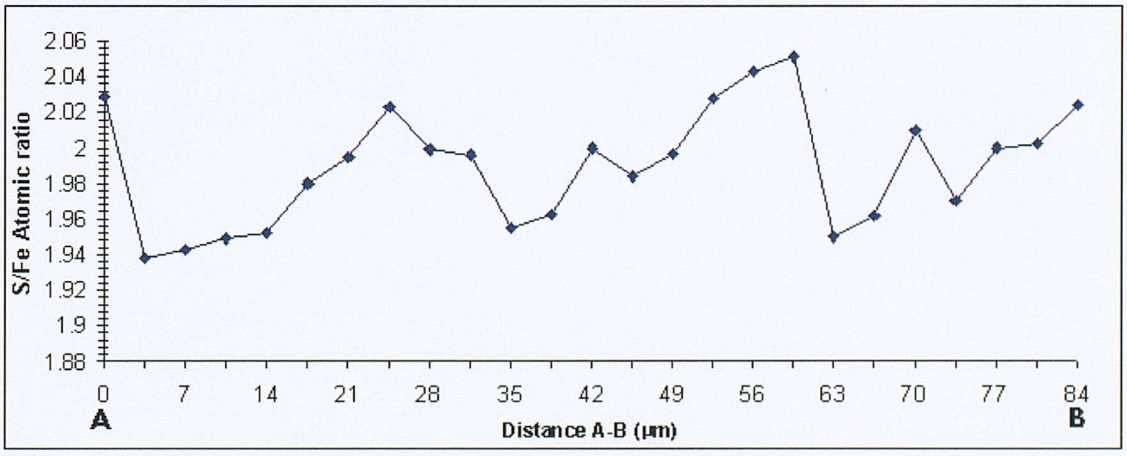

Figure 4.9d - S:Fe ratio for the traverse A – B in Figure 4.9c.

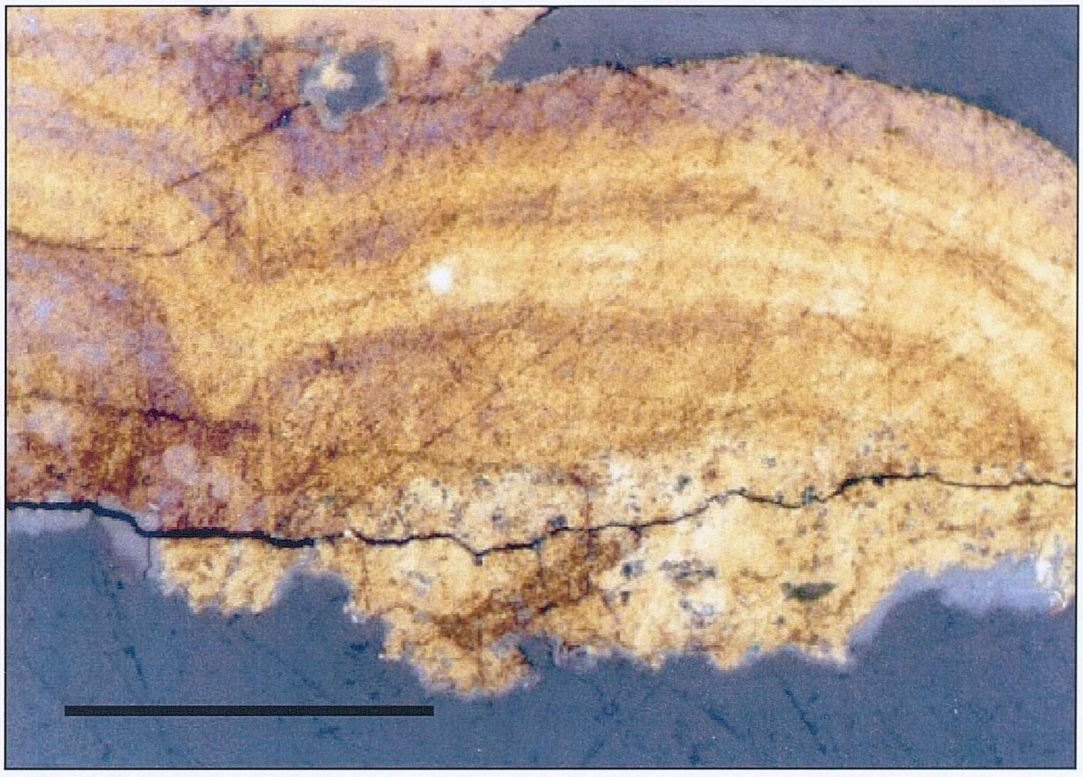

Figure 4.9e - The collomorphic habit of marcasite mineral overgrowing porous pyrite, along a fractured tube layer (scale = 10 μm).

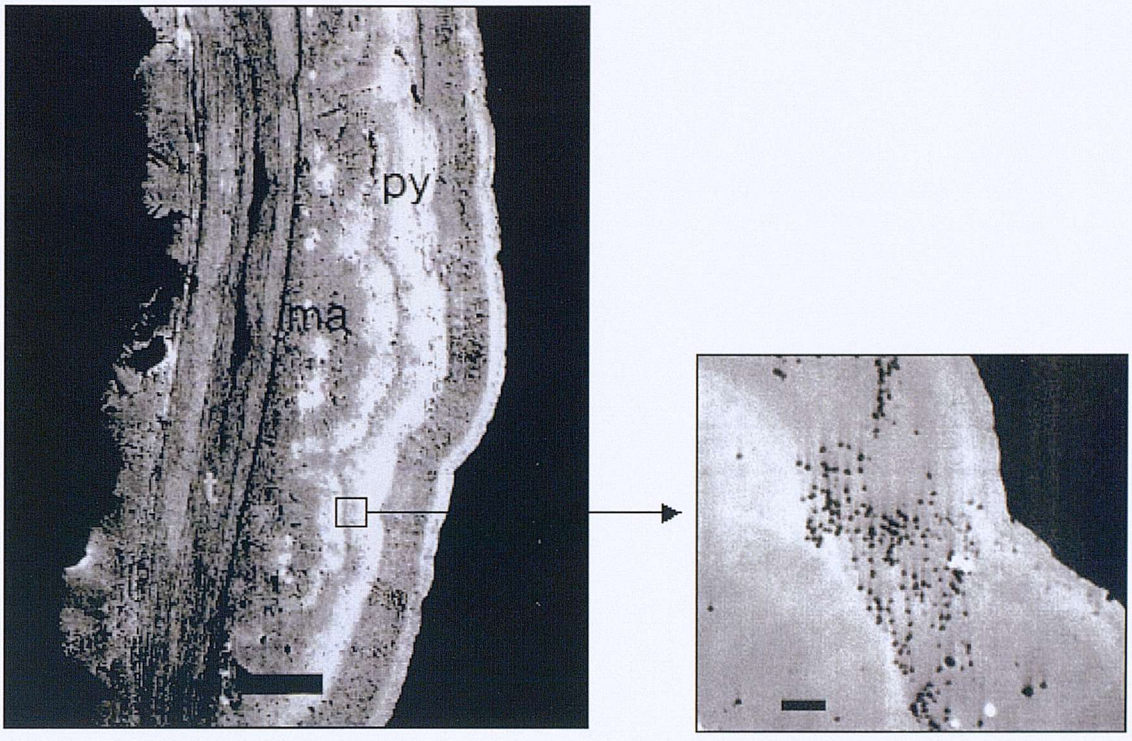

Figure 4.10 - Back-scattered electron images of (a) a transverse section through iron sulphide layer forming on the outside of the *Alvinella pompejana* tube (scale 35 μm). The organic tube (t) is being replaced by pyrite. The sulphide layer is differentiated into marcasite (ma) and pyrite (py) zones and has a collomorphic texture. (b) The pyrite zones are particularly porous and at higher magnification, the porosity is inferred to be due to the presence of microbial cell ghosts, each around 1 μm in diameter (scale 10 μm)

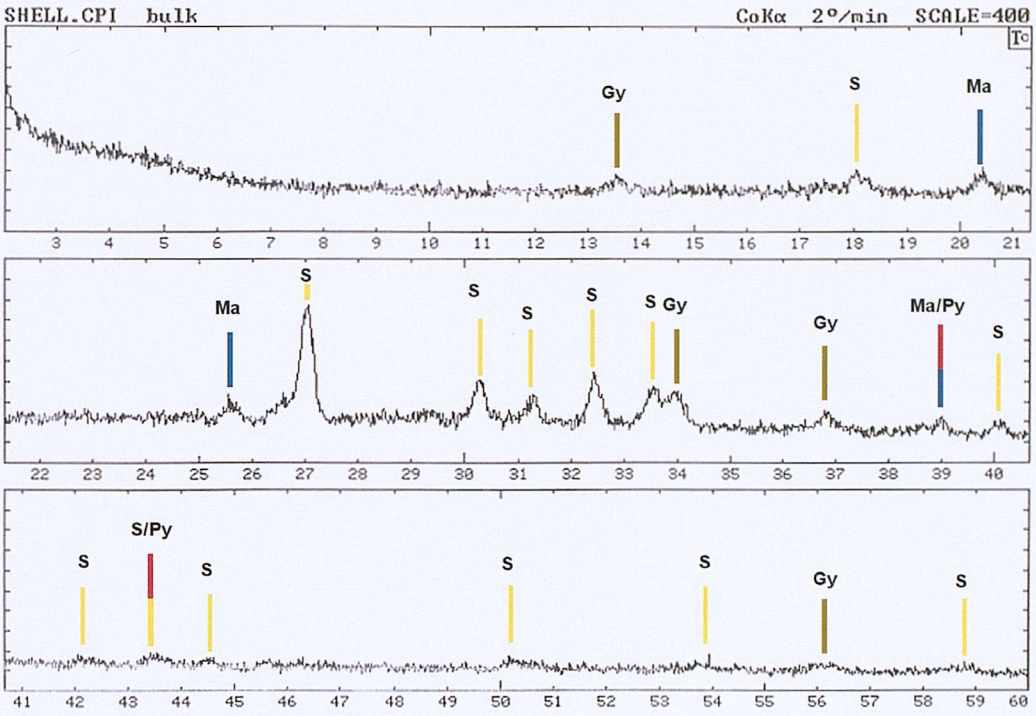

Figure 4.11 – XRD analysis of mineralised tube wall structure. py: pyrite; ma: marcasite; S: sulphur; Gy: gypsum.

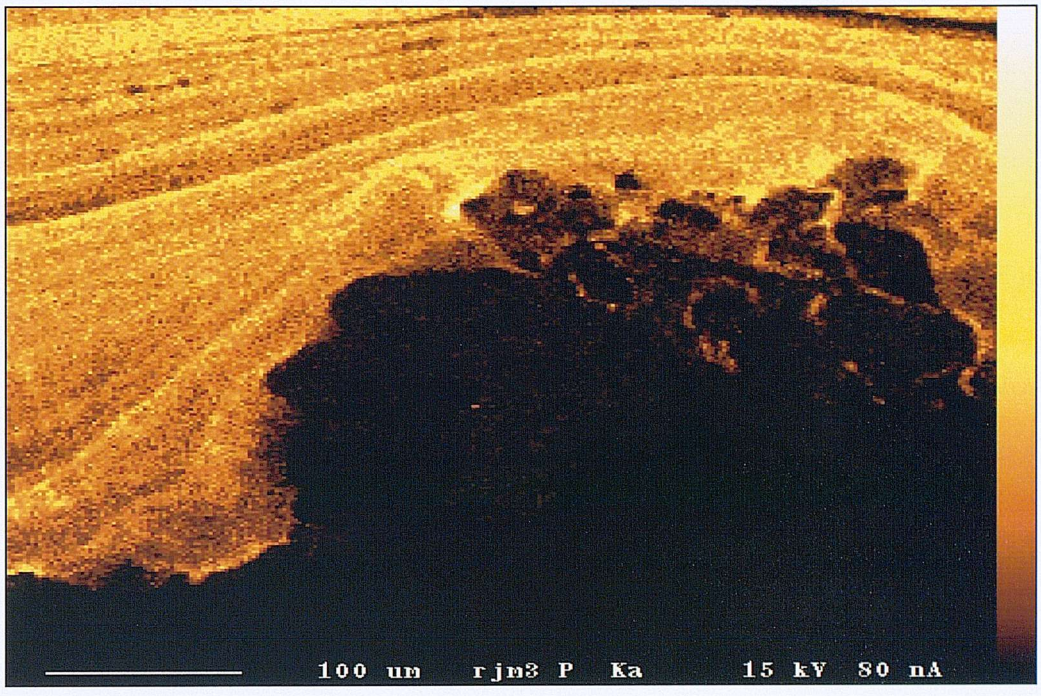

Figure 4.12 - Inorganic mineralisation within the dwelling tubes. An electron microprobe image of a sphalerite (ZnS) crystal which has grown between two organic sub-layers. The image was mapped for phosphorus which is used as an organic tracer. It can be seen that the sphalerite crystal has distorted the organic layer within the tube structure, and has therefore undergone considerable mineralisation whilst trapped. This is thought to have been a trapped particle of sphalerite which has acted as a 'seed' for mineral crystallisation

4.4. Discussion

4.4.1. Trapping of sulphide particles.

It has been shown that numerous microorganism rich horizons are present within the internal layering of the *Alvinella pompejana* dwelling tubes. The extent and style of mineralisation varies across the tube wall. Two mechanisms for introducing sulphide particles onto cellular surfaces of these microorganisms have been previously identified (a) entrainment and capture of particles from solution and (b) binding and precipitation of metals at the cell surface in response to elevated metal concentrations (e.g. Beveridge & Fyfe (1985); Beveridge & Murray (1980)). It seems most likely that the microbes on the inner tube wall die when they become trapped within the proteinaceous sub-layers, and mineralisation of the cellular surfaces is predicted to start almost immediately. The microbes will have metal ions bound to their cell membranes before they become trapped within the tube wall (e.g. Konhauser 1988; 1996), due to their continual contact with the hot hydrothermal fluid that flows through the dwelling tube (up to 80°C: Cary *et al.* 1998). Having metal ions 'pre-seeded' in the cell membrane will induce further nucleation of ions from solution, once the individual microbial cells have become entombed and begin to degrade. The formation of degradation products (polysulphide ions, anionic organic functional groups, etc.) effectively enhances the biomineralisation potential of the microbial laminae (Ferris *et al.*, 1988).

4.4.2. Microbial cell moulds.

The intra-sulphide porosity in the intra-tube greigite/mackinawite phases, and the pyrite-rich sulphide phase, is interpreted to represent the moulds of microorganisms that have subsequently decayed away. The evidence for this is that the holes are similar in size and shape to the microorganisms observed on the inner tube surface (Figures 4.3 a-c) and the juxtaposition of porous iron sulphides and microorganism sub-layers within the tube. The elongate holes (e.g. Figure 4.9b) are inferred to be the moulds of the longer sheathed filamentous microorganisms present on the inner tube wall (e.g. Figure 4.3a). Support for this interpretation comes from observations of microbial mats at vent sites on the EPR (Jannasch & Wirsen, 1981) where filamentous bacteria can clearly be seen to be encased by sulphide crusts. In addition, similar holes have been described

from a thin oxidised veneer on the surface of black smoker chimney fragments from the Pito Seamount on the Easter Island microplate (Verati *et al.*, 1999) and identified as microbial moulds by these authors. This texture has not been reported before in this context, and may prove to be important in the future identification of fossilised hydrothermal vent fauna.

The pores present within the outer-layer sulphides are also inferred to have been formed by the same mechanism of bacterial degradation and mineralisation. Alternatively these outer layer pores could possibly arise from some sort of biocorrosion phenomena, such as that reported by Verati *et al.* (1999), which has been observed to produce numerous, uniformly sized, circular pores in an iron sulphide-rich micro-layer around vent chimneys.

4.4.3. Mineralisation.

Iron sulphides (pyrite and marcasite) dominate the internal mineral assemblage, and sphalerite, barite, silica, and iron oxides are present in minor quantities (observed using LM, SEM and EMP techniques). There is evidence for both abiotic mineral precipitation and biologically induced mineral precipitation processes within this system. The thickening of the microbial cell walls (Figure 4.6) is interpreted to be the earliest stage of biologically induced mineralisation. It is hypothesised that mineral precipitation derived from the nucleation of iron and sulphide ions is initiated by electrostatic forces, caused by ions already present and bound to the outer cellular membranes of the microbes trapped within the tube layers. This results in the mineralisation of the cell wall, close to the inner tube surface. Biologically induced mineralisation of this type has been described in great detail in bacterial systems (e.g. Lowenstam, 1981; Beveridge & Fyfe, 1985; Konhauser, 1998). However, such finely preserved structure on a micro-scale (e.g. Figure 4.6) is uncharacteristic of pyrite precipitation. Pyrite, being a mineral with a well-defined crystal habit, is only rarely involved in the fine-scale preservation of soft bodied organisms (Briggs *et al.*, 1991), and less commonly in the detailed fossilisation of microbial remains. Therefore, it is proposed that a crypto-crystalline, pyrite-precursor mineral, such as mackinawite (Allen *et al.*, 1912) could be involved in the earliest stages of mineralisation. The precursor

mineral mackinawite is then replaced by pyrite, *via* a greigite intermediate phase (Benning *et al.*, 2000). A mineral phase with a S:Fe ratio similar to that of the minerals mackinawite and greigite has been identified in the tube wall (Figure 4.8). The outer areas of this precursor mineral layer have a S:Fe ratio which is sulphur deficient (and tends to that of mackinawite) when compared to the middle of the mineralised area (which tends to greigite). Therefore, we suggest that the mackinawite mineral layer is formed first, close to the microbial – tube wall interface, and then progressively re-crystallises through solid-state transformation to greigite (as suggested by Benning *et al.*, 2000). It has been shown (Schoonen & Barnes, 1991b) that mackinawite may alternatively alter to pyrite directly, under highly reducing conditions. However, the reaction rate is not as fast as for the conversion of FeS to pyrite *via* greigite.

Replacement, and subsequent pyritisation of the microbial remains, may proceed by sulphidation of the precursor mineral, by a variety of reaction pathways, depending on the precise chemical conditions (Schoonen & Barnes, 1991b), or by the loss of Fe^{2+}, in the presence of H^+ or some organic species (Wilkin & Barnes, 1996). The formation of either pyrite or marcasite is dependent on the overall pH of the aqueous hydrothermal system (Allen *et al.*, 1912). Sulphidation occurs due to electrostatic interactions between polysulphides and the growth surfaces of the pyrite and marcasite minerals (Wilkin & Barnes, 1996). In acidic solutions (pH<5), the protonated ends of polysulphides are repelled by pyrite growth sites, but not from marcasite growth sites, due to dipolar repulsion. Whereas, the negative polysulphide ions (such as HS^{2-} and S_2^{2-}) found in solutions of pH>5 are strongly attracted to pyrite growth sites (Murrowchick & Barnes, 1986). Therefore, at pH greater than 5, pyrite precipitation is favoured over marcasite precipitation, and in solutions where pH >6, pyrite is formed exclusively (Schoonen & Barnes, 1991a).

Eventually a biomineralised pyrite-rich layer of up to 40-50 μm thickness forms (Figures 4.9a, b & c), which completely replaces the associated organic-rich, microbial horizon. The precipitation of the pyrite-rich mineral layer is thought to cease when the decaying microbes become completely degraded. The microbial decay and release of degradation products into the alvinellid tube is inferred to contribute greatly to the mineral formation process. However, this is not thought to be the case where the organic tube wall

components are concerned, as the organic tube is thought to be much more resistant to decay (Gaill & Hunt, 1988) than the microbial components which degrade with relative ease (Ferris *et al.*, 1988). Studies by Berner (1980); Briggs *et al.* (1991); Raiswell *et al.* (1993) and Wilby (1996) have suggested that pyritisation will occur when sulphide dominated micro-environments formed by the degradation of organic matter are contained within iron dominated fluids. The consequent formation of pyrite will continue until the concentration of sulphide ions greatly exceeds the concentration of aqueous Fe in the local environment, or the supply of either the Fe or sulphide ions is sufficiently depleted. However, this process would not appear to be pertinent to this study, possibly because of the radically different geochemistry provided by the hydrothermal environment.

Precipitation of marcasite is inferred to occur only under local acidic conditions that may be controlled by the mucous tubes produced by the living worm (Juniper & Sarrazin, 1995). Where the marcasite layers are observed in the tube structure (e.g. Figure 4.8c and e), the most likely method of crystallisation is direct nucleation from polysulphide ions and Fe^{2+} (Paradis *et al.*, 1988), and subsequent growth, *via* diffusion limited aggregation from solution. Growth limitation by diffusion is indicated by the collomorphic (leisgang-type) banding demonstrated in Figure 4.9e. Rhythmic banding of this type occurs due to complicated osmoitic effects which manifest along the mineralising interface during mineral precipitation. Diffusion of ions within the aqueous system, and to a lesser extent, molecular adsorption effects are thought to be mechanisms for the formation of banded minerals (Stern, 1954). Precipitation of the marcasite occurs within the organic tube matrix, and replacing the organic tube material. This occurs at a much slower rate than the pyrite precipitation as is indicated by the presence of the collomorphic bands, and retains remnants of the original tube structure, therefore explaining the elevated phosphorus content of the marcasite horizon, which traces the original organic lamina.

The outer veneer of pyrite/marcasite on the exterior of the tube wall is inferred to have been produced by the same mineralisation processes that produced the internal sulphide layers. However, in this case, erosive processes acting on the outer layers of the tube wall, coupled with the growth of the internal sulphides (which act so as to

deform the internal organic lamina), are thought to have caused the original outer layers (and therefore the oldest tube material) to have been worn away. Thus, the internal sulphide layers on the outer wall are exposed, and may then be used as further nucleation sites for further mineral precipitation.

4.4.4. Model of sulphide mineralization

Based on the observations and interpretations above and the work of Little *et al.* (1998; 1999c) a model for the sulphidemineralisationin the tube *Alvinella pompejana* is presented:

- Mats of microorganisms growing on the inner surface of the *A. pompejana* tube wall trap iron and zinc sulphides, elemental sulphur and other metal-rich particles both between cells and on cellular surfaces.
- Subsequent tube wall growth entombs the microorganisms and trapped particulate sulphide particles within the laminated structure of the tube wall. The larger filaments become cropped, possibly by the worm feeding on them.
- The microorganism cellular components begin to decompose after entombment and the degradation products are released through the cell walls, to combine with trapped Fe ions, leading to the formation of a precursor iron mono-sulphide mineral, which envelopes the cell wall. Microorganism decay provides a reducing microenvironment which allows for the precipitation of mackinawite, then greigite, followed by pyrite along the internal microbial lamina. This leads to the formation of significant iron sulphide mineralisation on a biological template with the sulphide texture replacing the original organic layer. Passive biomineralisation continues until the degradation of the microorganism cells is complete. The pyrite phase observed is the recrystallisation product of an earlier, iron monosulphide precursor mineralisation stage. Complete degradation of the microorganism cells results in spherical and elongate pores within the pyrite/biomineralised layer.
- A later phase of marcasite-rich mineralisation envelops many of the pyrite-rich mineral horizons. In places the marcasite phase also replaces the organic tube wall material but preserves the gross laminated morphology of the tube as a P signature. This mineral growth is assumed to be abiogenic and diffusion limited,

which is indicated by the distinct fine-scale, rhythmic, mineral growth bands, picked out by differential tarnish of the layers. Most of the marcasite growth occurs in horizons nearer to the outer edge of the tube wall, either because the tube material is older, and mineralisation is more progressive; or because the tube layers are older and more fractured and therefore allow greater ease of vent fluid penetration.

- Once a significant portion (mm rather than μm) of the tube wall has been replaced by sulphides, it is increasing likely that the mineralised tubes will persist and become incorporated into massive sulphide deposits and thence into the fossil record.

4.5. Conclusions

This study shows how the organic living tubes of vent organisms can be rapidly replaced by sulphide minerals, and that this sulphide mineralisation does not require precursor mineralisation by silica or barite (*cf.* Cook & Stakes, 1995). The sulphide mineralisation is controlled, in part, by microorganisms that are intimately associated with the living worm. These act as loci for mackinawite/greigite, pyrite and marcasite precipitation which subsequently replaces the adjacent organic tube layers, replicating fine details of the original tube wall structure including laminae and microorganism layers. Preserved *Alvinella pompejana* tubes are only identified within the fossil record, when biologically induced mineralisation, such as that seen here, outpaces the gross chimney mineralisation. Biologically induced mineralisation allows the fine-scaled internal detail, such as, tube wall laminae and microbial cell ghosts to be preserved or replaced, rather than overprinted by bulk hydrothermal sulphide mineralisation, and therefore it is the microbial textures that are the indicators for biologically induced mineralisation.

These results are consistent with the mode of preservation of vent fossils hosted by Phanerozoic massive sulphide deposits (Little *et al.,* 1998; 1999c) where organic material is entirely absent but fine-scale details of the tube wall are retained.

Chapter 5

Fossilised dwelling tubes from the Southern East Pacific Rise, 7°24'S.

This Chapter describesmineralisationprocesses in a selection of sulphide tube structures recovered from an extinct sulphide mound on the Southern East Pacific Rise. The tube structures have been identified as fossilised dwelling tubes. The similarity to existing faunal assemblages suggests that these structures were associated with Alvinella *sp. polychaete worms.*

Tube structures are common features within seafloor hydrothermal chimney material and their occurrence has generally been attributed to abiotic chimney growth and remineralisation processes. Samples from an inactive vent site on the Southern East Pacific Rise were studied to establish the role of biomineralisation processes in chimney formation. Two generations of pyrite mineralisation were identified along with a later stage chalcopyrite phase. Only minor sulphate phases were present in the chimney material. Fine scale variability in tube wall geochemistry reflects changes in sulphide mineralogy across the wall structure. Sulphides form discrete concentric laminae around the tube structures which are embedded in a matrix of mixed sulphides. Laser combustion sulphur isotope analyses of the different sulphide phases gives a wide range in $\delta^{34}S$ values ($\delta^{34}S$ = +3.8 to +10.7‰). The highest values are observed in sulphide tube structures (+6.10 to +10.7‰). The upper end of the range is higher than any previously measured for chimney structures on a sediment-free ridge setting. Matrix sulphides are dominated by chalcopyrite phases which have significantly different values ($\delta^{34}S$ = +3.8 to +7.8 ‰). Pyrite-marcasite laminae originally laid down in association with biogenic tube structures are replaced by euhedral pyrite and later stage primary chalcopyrite precipitation, which is associated with growth of the hydrothermal chimney wall and higher temperature post-mortem environments. The high $\delta^{34}S$ values are indicative of seawater entrainment into tube features and Rayleigh type fractionation during dissimilatory sulphate reduction. This biological enhancement of mineralisation processes produces high $\delta^{34}S$ values that are preserved in the tube features embedded in seafloor sulphides. This is a previously undescribed process of potential importance in preservation of fossil vent fauna.

5.1 - Introduction.

Sulphide chimney structures often contain relict tube features within the chimney walls and mounds. The biological origin of some of these features has often been overlooked in mineralogical studies. Sulphide chimneys have been collected from the newly discovered site at 7°24'S on the EPR, and a three-stage chimney growth model has been proposed by Marchig *et al.*(1997), which differs notably from the standard model (Haymon, 1983):

- The central vent is lined with euhedral, partially porous, aggregated Fe-sulphides crystallized at high temperatures (> 300°C).
- Cementation and clogging of the central vent with late stage (150-100°C) epithermal impregnation of early precipitates by layered colloidal and laminated fine-grained sulphide species.
- Emanation of fluids at the chimney base or from secondary vents branching off the chimney; direct seawater mixing and precipitation of quenched sulphides on the outer shell of the initial central vent with partial impregnation of walls.

This model adequately explains the textural and isotopic disequilibrium assemblage of pyrite, chalcopyrite and sphalerite present in this chimney material. These chimneys differ from previous studies at other sites by the notable lack of sulphate minerals associated with the wall structures.

Sub-samples from the Marchig *et al.* (1997) sample suite were studied here. A number of mineralised tube structures were observed in hand specimen and studied in detail to determine the mode of formation of these structures. The form of the structures suggested that they are associated with worm tubes living on the outer chimney wall. The *Alvinella pompejana* tube worms are found only in the Pacific with a geographical range of at least 21°N to 32°S. The objective of this study was to test the hypothesis that these tubular structures were biogenic in origin, and if so, consider the modes of preservation involved.

5.1.1 - Sulphur isotopes

Stable isotope abundances show variations in nature due to physical, chemical, and biological processes that produce isotopic fractionation. The most commonly studied stable isotopes (H, C, N, O and S) provide useful information on sources, materials and a wide range of processes including temperature of formation and depositional environment (Faure, 1986). Sulphur isotope geochemistry has broad applications in geological and biological studies as sulphur is found in all environments at a wide range of concentrations.

There are four stable isotopes of sulphur (Table 5.1). All $\delta^{34}S$ values are reported relative to the Cañon Diablo Troilite standard (CDT: Jensen, 1962)(Equation 5a):

Isotope	Abundance (%)	Mass (amu)
^{32}S	94.941	31.97207
^{33}S	0.769	32.97146
^{34}S	4.273	33.96877
^{36}S	0.017	35.96708

Table 5.1 - Abundance and mass of the different isotopes of sulphur.

$$\delta^{34}S = \left[\left(\frac{\left(^{34}S/^{32}S\right)_{sample}}{\left(^{34}S/^{32}S\right)_{std}}\right) - 1\right] \times 10^{3} \qquad (5a)$$

Sulphur isotopes are particularly useful in hydrothermal geochemistry as indicators of sources and processes involved in sulphide mineral formation. The relative simplicity of constructive plate margin hydrothermal systems with respect to sulphur isotopes (Shanks, 1995), enables well constrained studies of the hydrothermal system to be carried out (e.g. Herzig, 1998; Gemmell, 1998; Chiba, 1998; Canfield, 1990; Bluth, 1988; Ohmoto, 1983; Ohmoto, 1986)

The residence time of reduced sulphur (H_2S) in the ocean is short (minutes), therefore the vast bulk S in the oceans occurs as sulphate. The residence time of sulphate in the modern ocean is orders of magnitude longer than the mixing time of the oceans (~103 years), leading to a constant dissolved sulphate concentration. This sulphate has a near constant isotopic composition around 20.9‰ (Rees *et al.*, 1978). Sulphate reduction occurs under reducing conditions where H_2S is produced. The H2S is either reoxidized, or reacts with available metal cations, principally Fe, forming Fe-sulphide minerals. Minor amounts reduced sulphur remain as acid-volatile sulphide, elemental sulphur and dissolved sulphide.

Sulphide deposits exhibit a wide range of $\delta^{34}S$ values depending on mode of formation (Figure 5.1). All sulphide deposits typically have $\delta^{34}S$ values << 20‰ as the lighter isotope, $\delta^{32}S$, is preferentially taken up during all reduction reactions. Sulphur isotope fractionation between coexisting phases occurs either by equilibrium-chemical exchange reactions or by kinetically controlled reactions often catalysed by microbes.

5.1.2 - Equilibrium fractionation of sulphur isotopes

Equilibrium fractionation factors between sulphur-bearing compounds and dissolved H_2S are shown in Figure 5.2. For example, sulphate is reduced to H_2S in the presence of Fe^{2+} at temperatures in excess of 250°C (Ohmoto and Rye, 1979) and the isotopic fractionation between dissolved sulphate and sulphide can be calculated using Equation 5b (Ohmoto and Rye, 1979):

$$1000 \ln \alpha_{SO_4-H_2S} = \frac{6.463 \times 10^6}{T^2} + \frac{0.56 \times 10^3}{T}$$

if T = 250° C, (5b)

$$1000 \ln \alpha_{SO_4-H_2S} = 24.7 = \delta^{34}S_{SO_4} - \delta^{34}S_{H_2S}$$

However, isotopic equilibrium between sulphate and sulphide is only achieved very slowly in typical hydrothermal systems (10^3-10^4 years, pH 3-8 and temperatures of up to 300°C).

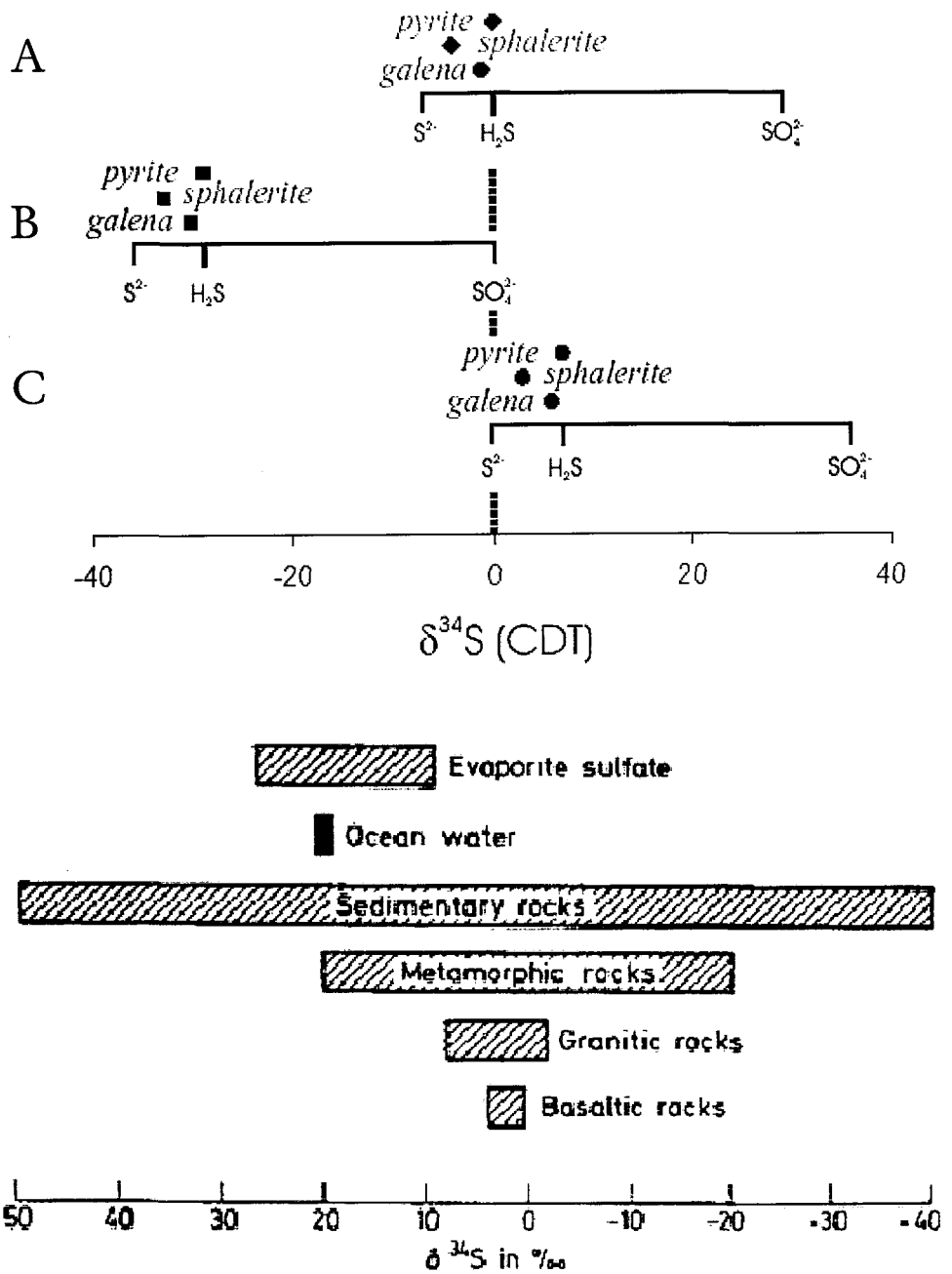

Figure 5.1 – a): Isotopic composition of minerals forming from a fluid with a $\delta_{34}S$ value of 0‰. *A*) with H_2S as dominant fluid species; *B*) SO_4^{2-} as dominant fluid species; *C*) S_2^- as dominant fluid species. Modified from Nielsen, 1979. b): Characteristic sulphur isotopic values of different geological phases. From Hoefs, 1980.

Equilibrium fractionation is observed more commonly between dissolved sulphide and precipitated sulphides in hydrothermal solutions. The offset in $\delta^{34}S$ values can be used as a geothermometer if equilibrium is established. For example, the pyrite-

chalcopyrite pair can be used to estimate temperature of formation *if* equilibrium is attained during precipitation (Equation 5c):

$$1000 \ln \alpha_{Pyrite-Chalcopyrite} = \frac{0.45 \times 10^6}{T^2}$$
$$\text{if} \delta^{34}S_{Pyrite} - \delta^{34}S_{Chalcopyrite} = 2‰ \quad (5c)$$
$$T = 200°C$$

In seafloor hydrothermal systems, sulphur isotope geothermometry of chimney material rarely generates realistic results, due to the chemical disequilibrium that exists within most vent structures (Marchig *et al.*, 1997). Isotopic disequilibrium is often observed in the initial and final periods of hydrothermal venting, due to quenching, solution mixing and remineralisation processes. If more than one mineral pair is used to give consistent estimates of temperature then the system is likely to be approaching equilibrium. Conversely calculation of unreasonable temperatures allows inferences to be made about isotopic disequilibrium in the system.

5.1.3 - Kinetic isotope fractionation

5.1.3.1 - Microbial sulphate reduction

Isotopic fractionation between dissolved sulphate and sulphides is kinetically controlled in anoxic environments where reduction is catalysed by microbial activity and there is no oxidant present for the reverse reaction performed by sulphate reducing bacteria. The resultant low-temperature biogenically controlled kinetic fractionation has the largest effect on the global sulphur isotope budget. Sulphate reduction occurs *via* two processes, assimilatory and dissimilatory reduction. The latter is by far the most important mechanism for sulphate reduction in the global biogeochemical sulphur cycle.

Assimilatory sulphate reduction occurs in autotrophic organisms where S is incorporated in proteins, particularly as S^{2-} in amino acids. Assimilatory reduction involves a valance change from +6 in SO_4 to –2. The bonding of the reduced sulphur is

similar to the dissolved sulphate ion, so isotopic fractionation ($1000\ln\alpha SO_4$-S) is small (+0.5 to –4.5‰: Kaplan, 1983; Kaplan *et al.*, 1963).

Dissimilatory sulphate reduction is performed by heterotrophic organisms, particularly *Desulfovibrio desulfuricans*. The sulphate reduction pathway consists of four steps (Goldhaber and Kaplan, 1974; Figure. 5.2a). The fractionation factor for each reaction is suggested to be inversely proportional to the rate of each step. In a reaction limited by the available reactant (nutrient) sulphate, all available sulphur will be used, and no isotopic fractionation will occur. In a sulphur reaction that is not limited by reactants, but is limited by the rate of the reaction itself, there will be isotopic fractionation. Of the four steps in dissimilatory reduction, step 2 is generally the slowest and determines the overall kinetics of the entire reaction sequence (Figure 5.2b). The fractionation factor for step 2 is large ($1000\ln\alpha$ > -30 to -40‰), and is therefore responsible for the majority of isotopic fractionation observed for sulphur in the natural environment.

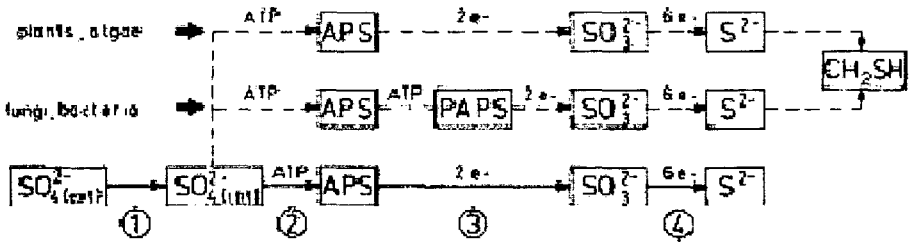

Figure 5.2a – Metabolic pathways involving sulphur compounds, of various photosynthetic and chemosynthetic organisms. (Goldhaber and Kaplan, 1974)

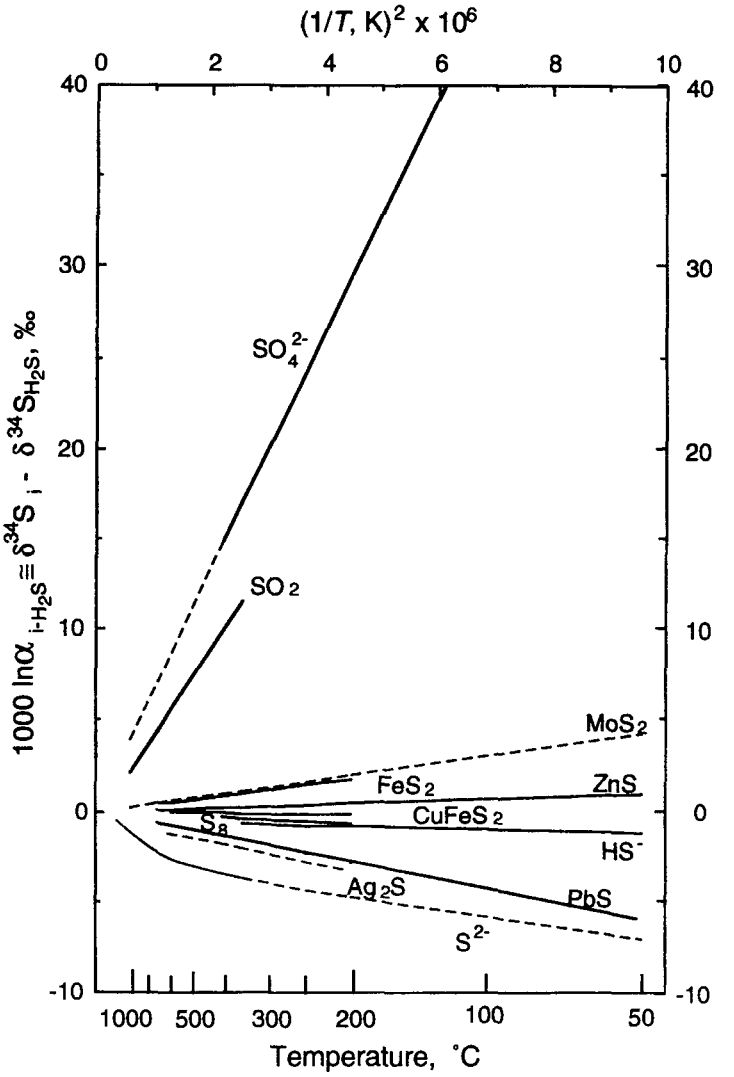

Figure 5.2b – Equilibrium fractionation factors between sulphur compounds and H_2S. Solid lines: experimental; dashed lines: theoretical. From Barnes, 1997. The isotopic fractionation of SO_4^{2-} (step 2: Figure 5.2a) has the highest gradient and therefore the highest fractionation factor when compared to other sulphur containing compounds.

The effect of kinetic fractionation during sulphate reduction is amplified when Rayleigh fractionation effects are considered in a closed system where reaction products are removed. Thus the residual reactant (SO_4) is progressively fractionated as light S is removed to form pyrite. The residual SO_4 evolves to heavier values as precipitation progresses (Equation 5d):

$$\delta^{34}S_{py} + 1000 = \alpha\left(\delta^{34}S_{(SO_4)_0} + 1000\right)f^{\alpha-1} \qquad (5d)$$

Where $(SO_4)_0$ is the initial $\delta^{34}S$ value of the SO_4, f is the fraction of SO_4 remaining and α is the fractionation factor ($a_{py\text{-}SO4}$ ~0.95). Figure 5.3 shows how the $\delta^{34}S$ composition of both the sulphate and precipitated pyrite vary in a closed system as precipitation progresses.

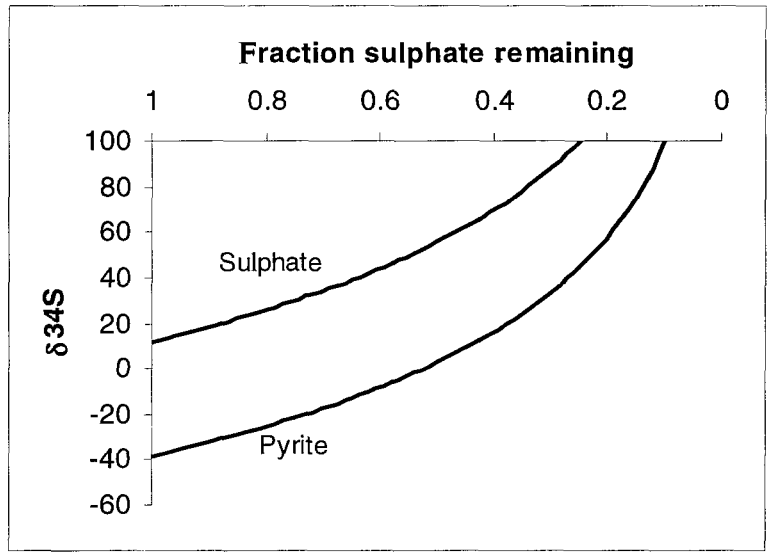

Figure 5.3 Variation in $\delta^{34}S$ as a function of fraction of remaining sulphate in a closed system. The starting product is seawater sulphate with $\delta^{34}S$ = 21.9 ‰. If α= 0.95, pyrite forms with a $\delta^{34}S$ value of –29.1 ‰. As pyrite is removed from the system, both the sulphate and pyrite evolve to heavier $\delta^{34}S$ values.

Variations in natural $\delta^{34}S$ values leading from Rayleigh fractionation processes of over 150‰ have been observed (McKibben & Eldridge, 1990; McKibben & Riciputi, 1998).

5.1.3.2. - Microbial sulphide oxidation.

Sulphide oxidation in hydrothermal systems can provide up to 99% of the energy available for primary production (Jannasch, 1995). The principal electron donor for microbial metabolism reactions is H_2S, which can be readily oxidised by thiotrophic bacteria in the presence of O_2 (and CO_2) to form free-energy (and organic carbon). Microbial sulphide oxidation is a kinetic process with a fractionation factor close to unity

($1000\ln\alpha = 0$ to -5 ‰). Thus sulphur and sulphate formed from sulphide oxidation have $\delta^{34}S$ values essensially similar to the reactant sulphide.

5.1.4 - Sulphur isotope systematics of hydrothermal vents

The sulphur isotope systematics of many seafloor hydrothermal seafloor systems have been well studied (e.g. TAG: Herzig *et al.*, 1998; Stuart *et al.*,1994; 21°N EPR: Woodruff & Shanks, 1988; Hekinian *et al.*, 1980; 11-13°N EPR: Bluth & Ohmoto, 1988; Axial Seamount: Hannington & Scott, 1988; Middle Valley: Duckworth *et al.*, 1994; Stuart *et al.*, 1994; Zierenberg, 1994: see Figure 5.4). High temperature reactions control the sulphur isotope signatures observed in hydrothermal systems, with the most intense fluid/rock interactions occurring at the cracking front, above the magma chamber (Seyfried *et al.*, 1991; 1999). H_2S is produced by the leaching of igneous sulphide from basaltic rocks during water-rock interaction (Shanks, 2001). However, no study of $\delta^{34}S$ in black smoker end-member fluids has ever shown H_2S with a purely magmatic $\delta^{34}S$ value (0 +/- 0.5‰). Values more positive than 0‰ typically call for an input of sulphide from the reduction of seawater sulphate in the hydrothermal regime before the hydrothermal fluid vents at the seafloor (Shanks 2001).

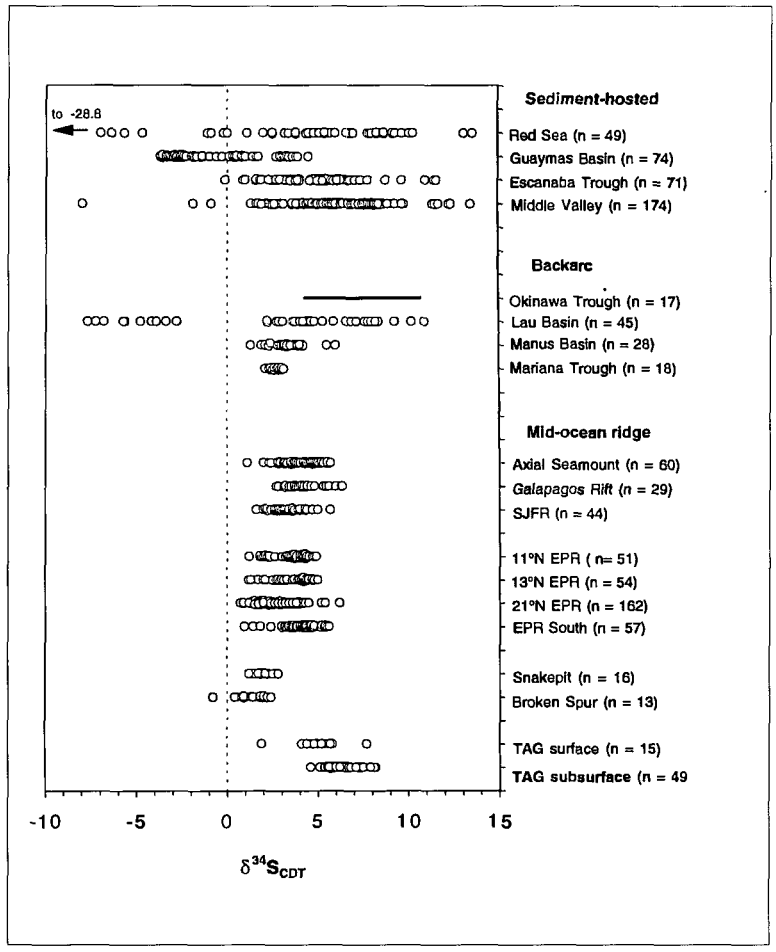

Figure 5.4 – Sulphur isotopic ratios of seafloor massive sulphide deposits, from a range of hydrothermal settings (from Herzig *et al.*,1998, and references therein).

$\delta^{34}S$ values of sulphide mineralisation observed from the East Pacific Rise at 21°N average $\delta^{34}S$ = +2.1‰ (Figure 5.5), are interpreted as having originated, predominantly from the non-equilibrium mixing of entrained, and consequently reduced, seawater ($\delta^{34}S$ = +20.9‰: Rees *et al* 1978) and S derived from mid-ocean ridge basalt (MORB, $\delta^{34}S$ = +0.1‰: Sakai *et al* 1984), in a ratio of 1:9 (Arnold and Sheppard, 1981). Herzig *et al.* (1998) have calculated that the average $\delta^{34}S$ for unsedimented ridge sites is +3.2‰ (compiled from over 500 individual sulphur isotope analyses: Figure 5.4) with the mean increase in heavier sulphur isotopes being explained by incorporation of reduced seawater sulphate during upflow from the reaction zone. Using the same principle of non-equilibrium mixing, Herzig *et al.* (1998) deduced that for a modern vent fluid to attain a $\delta^{34}S$ value of +6‰, it would require a seawater : basalt ratio of 3 : 7. However, such a simple scenario does not cover all modern hydrothermal vent sites, as is demonstrated by

the drilling of the TAG vent field (ODP Leg 158). The average $\delta^{34}S$ value for bulk samples from the TAG mound (+4.4 to +8.2) are around +3‰ heavier than the value for any other unsedimented ridge site (Figure 5.4). These heavy $\delta^{34}S$ values are attributed, in part, to subsurface mixing with seawater sulphate, and in part, to the remobilisation of sulphate from subsurface anhydrite deposits (Herzig *et al.,* 1998). The slight increase in $\delta^{34}S$ with depth within the mound, and distinct variations between early disseminated sulphides related to wallrock alteration, and massive, as well as late vein sulphides, indicates widespread entrainment of seawater deep into the system. Seawater influence on $\delta^{34}S$ values in seafloor deposits is supported by observations from δD, $\delta^{18}O$ and $^{87}Sr/^{86}Sr$ analyses of hydrothermal mineral phases (Teagle *et al.*, 1998; Mills *et al.*, 1998).

There is generally a larger range of $\delta^{34}S$ values in the sulphide minerals forming vent chimneys, than in the H_2S contained in the vent fluids expelled from the chimneys (Shanks, 2001). When bulk $\delta^{34}S$ analyses for sulphides are compared with sampled vent fluids there is a consistent negative offset (Figure. 5.5). This offset has not been fully explained to date, other than to suggest disequilibrium conditions and local reduction of seawater sulphate (Shanks, 2001). Nevertheless the observation of isotopically heavier fluids associated with lighter chimney material is a general one.

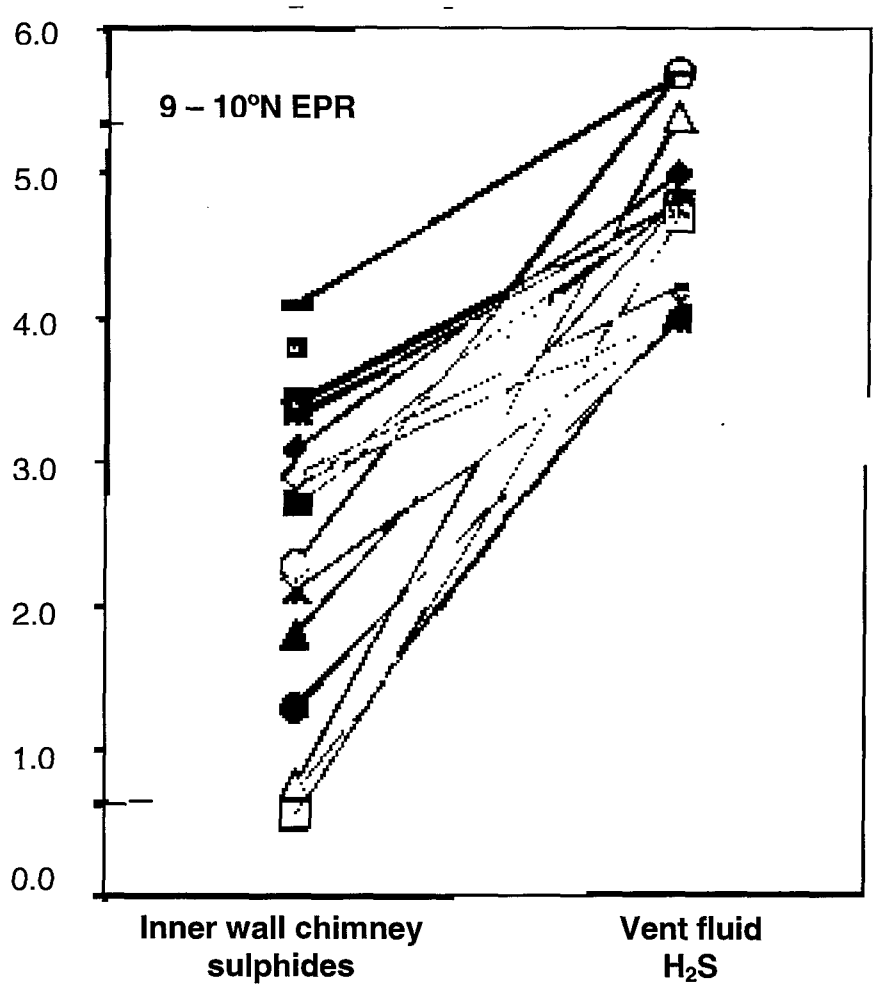

Figure 5.5 – Sulphur isotope values for hydrothermal vent fluids from 9°N EPR and their coexisting chimney sulphides (Shanks 2001).

5.1.5 Sulphur isotope systematics of vent fauna

Symbiotic relationships between thiotrophic bacteria and vent macro-fauna are common in hydrothermal settings (Fisher, 1990; Nelson & Fisher, 1995). Many fauna, such as tubeworms, shrimp anenomes and molluscs contain chemolithotrophic bacteria within their tissues, which provide a primary energy source. Vent macro-fauna can occupy a variety of temporal and spatial niches, but must remain within the interface between the venting hydrothermal fluid and ambient seawater in order to thrive. As previously discussed (in Chapter 1), hydrothermal flow rates at active vents can vary in a variety of ways, so as to drastically alter thermal and chemical components of a micro-environment, and thus alter the natural habitat of the fauna. However, data concerning the manipulation of sulphur isotopes by hydrothermal vent fauna are remarkably consistent. Vestimentifera and bivalves from 21°N EPR show $\delta^{34}S$ ranges from _4.7 - +4.7‰, and -1.7 - +0.4‰ respectively, indicating that the microbial symbionts responsible for respiratory function in these animals can buffer many of the $\delta^{34}S$ changes that might normally be observed in a dynamic hydrothermal environment. In addition, comparisons by Fry *et* al. (1983) of vent fauna, and associated conjugate vent fluids at 21°N EPR, show that the oxidation of vent-derived H_2S by symbiotic thiotrophic bacteria, and the subsequent uptake of oxidation products by the host fauna, do not change the $\delta^{34}S$ values for sulphur substantially.

In this Chapter S-isotope data for chimney samples from 7°24'S on the EPR are discussed, along with textural and geochemical data to determine the origin of mineralised tube structures found within chimney walls on an inactive hydrothermal mound.

5.1.6 - Reactions forming pyrite and chalcopyrite above 100°C.

The phase relations in the condensed Fe-S system at temperatures above 400°C have been well constrained by numerous studies (e.g. Kullerud & Yoder, 1959; Brett & Bell, 1964; 1969; Scott, 1974; Vaughan & Craig, 1978). Not withstanding numerous studies, the phase relations within the Fe-S system below 350°C are much less clearly understood (Barnes, 1997). Essentially the system made is problematic primarily by the

complex nature of pyrrhotite crystal chemistry (Kissin & Scott, 1982). The pyrrhotite group of minerals are composed of 'iron monosulphides' which have a stoichiometry which ranges from FeS (troilite) – Fe_7S_8 (monoclinic pyrrhotite), and form octahedral and trigonal prismatic crystal forms. However, the Fe – FeS and FeS_2 – S compositional regions of the system are moderately straightforward, primarily acting in a similar way to the phase relations of equivalent compositional phases above 400°C.

Pyrite has a tendency to grow as euhedral crystals, often cubic, during the cooling from initial crystallisation conditions. Such crystal growth and consequent pyrite formation is generally thought to take place due to the relative loss of sulphur from pyrrhotite, and from pyrite by either exsolution or overgrowth of pre-existing pyrite crystals (Barnes, 1997). Where large crystals are formed, isotopic zonations may be visible, with the $\delta^{34}S$ values becoming more positive towards the outer rim of the crystal (Craig *et al.*, 1991).

In aqueous hydrothermal systems at temperatures between 100 – 350°C, pyrite precipitation tends to rely heavily on the formation and continual supply of polysulphide ions from solution (Equation 5e). This causes pyrite nucleation onto pre-existing pyrite minerals, or to form *via* monosulphide precursors (as described in Chapter 4.).

$$Fe^{2+} + H_2S_2 \rightarrow FeS_2 + 2\,H^+ \qquad (5e)$$

The necessary polysulphides can be formed in a variety of ways (Equations 5f & 5g):

$$H_2S \rightarrow H_2S_2 + H_2 \qquad (5f)$$

$$7H_2S + H^+ + HSO_4^- \rightarrow 4H_2S_2 + 4H_2O \qquad (5g)$$

The formational mechanisms of chalcopyrite are further complicated due to the fact that aqueous copper in hydrothermal fluids is transported as Cu^+, where as Cu in chalcopyrite is in the Cu^{2+} valency state (e.g. Equation 5h).

$$Cu^+ + Fe^{2+} + 2H_2S \rightarrow CuFeS_2 + 3H^+ + {}^1/_2\,H_2 \qquad (5h)$$

The direct nucleation of chalcopyrite from hydrothermal solutions has been observed, where it forms dendritic crystal clusters (Morimoto & Ohmoto, 1991). If fewer nucleation points are present in the cooling hydrothermal solution, then fine crystal aggregates may form (Ineson, 1989). However, chalcopyrite commonly forms from the replacement of pre-existing sulphide phases (e.g. pyrite, sphalerite, pyrrhotite, and galena) (Eldridge *et al.*, 1983). Various reactions for the replacement of common hydrothermal sulphides by chalcopyrite are described below (Equations 5i – 5k).

$$Cu^{+} + FeS_2 + {}^{1}/_{2}\ H_2 \rightarrow CuFeS_2 + H^{+} \quad (5i)$$

$$2Cu^{+} + Fe^{2+} + FeS_2 + 2\ ZnS \rightarrow CuFeS_2 + 2\ Zn^{2+} \quad (5j)$$

$$Cu^{+} + FeS + H_2S \rightarrow CuFeS_2 + H^{+} + {}^{1}/_{2}\ H_2 \quad (5k)$$

A difference between the $\delta^{34}S$ values of the nascent chalcopyrite and the original sulphide (e.g. pyrite) would signify that the formation of chalcopyrite has involved a H_2S source, normally from hydrothermal fluid (e.g. Equations 5i & 5j). Whereas comparable $\delta^{34}S$ values between chalcopyrite and pyrite would imply a replacive mode of formation (e.g. Equation 5k) although a finite degree of isotopic re-equilibration should be expected at hydrothermal temperatures.

The objective of this study was to establish whether there is a biogenic origin for tube structures within chimney material collected from an inactive hydrothermal site on the Southern East Pacific Rise. Textural, mineralogical, geochemical and sulphur isotope studies have been combined to identify the mechanisms involved in chimney formation. Here the published explanation of chimney genesis (Marchig et al., 1997) is challenged and a previously unidentified biomineralisation process is invoked, that is potentially important for fossil preservation.

5.2 - Samples and Methods

During the GEOMETEP-5 (SO-62) cruise of the *R.V. Sonne*, massive sulphides were remotely sampled from a newly discovered vent field, located at 7°24'S on the East Pacific Rise (see Chapter 3 for location description). A mineralised worm tube grab sample (Figure 5.6) was recovered using a remotely (ship-board) operated TV grab, from the side of an inactive chimney at Station 402 G (Figure 5.7). The site lies in 2740 meters of water, at 7°23.8'S/107°47.4'W, and the sample site is composed of 5 inactive chimneys measuring between 1 – 3.5 meters high (see Marchig *et al.* 1997 for a full description and sketches of Station 402 G).

The sample used in this study measured approximately $10cm^3$ and macroscopic examination of the sample shows that it contains at least four cylindrical tube structures. The largest tube, 2cm in diameter, is located centrally, forming a conduit through the middle of the sample, and has no mineral infill. Two of the tube structures have a mineral infill, one measuring approximately 1 – 1.25cm in diameter; the other around 8mm diameter; a fourth tube has no infill, and also measures approximately 1 – 1.25cm in diameter. Tube wall thickness varies from tube to tube, and along the tube length and diameter, but is generally between 0.3 – 3mm thick.

Preparation of the sample was undertaken by cutting though the tubes in cross section, resulting in a mineralised slab of 1cm thickness, which contained three of the four mineralised tubes. The slab was then impregnated, under vacuum, with AY105 epoxy resin, and then finally prepared as two 35mm diameter polished blocks, for SEM, EM-P and LASER sulphur isotope studies. Block EPR 99 01A is a cross section through a heavily mineralised section of the sample which contains two tube structures, both of which are infilled with heavy mineralisation, similar to that of the outer stockwork (Figure 5.8). The tube structures lie adjacent to one another and both are similar in size: approximately 10mm diameter and 0.3 – 0.5mm wall thickness (EPR 99 01A was subsequently cut in half). Polished block EPR 99 02A contains one large tube cross section positioned centrally within the block. The tube structure measures approximately 25mm in diameter and the thickness of the walls is between 2 – 3mm (Figure 5.9). The

tube formed a fluid conduit, and a thin veneer of infill mineralisation can be seen to coat the inner surface of the tube (up to ~0.5mm thick). The outer stockwork mineralisation appears to be similar to that of EPR 99 01A.

For the purposes of XRD and FE-SEM, sections of the tube wall were removed under a binocular microscope, and either crushed for XRD studies, or mounted on conducting stubs and sputter coated in gold for FE-SEM observations.

A description of the investigative and analytical techniques used in this chapter can be found in Chapter 3.3.

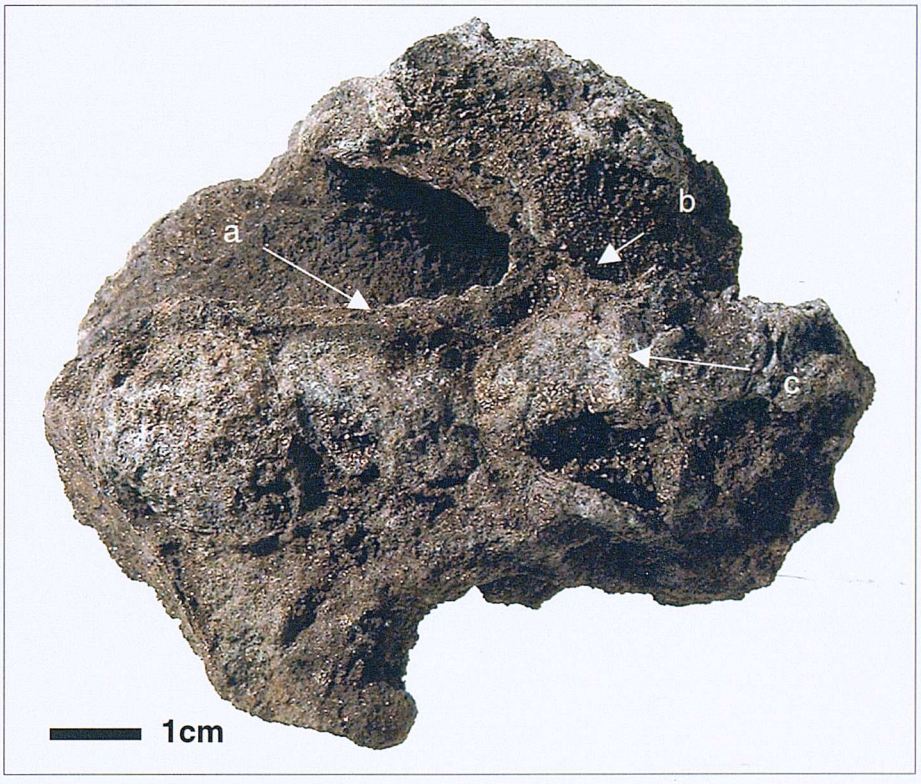

Figure 5.6 – Grab sample from Station 402G, 7°SEPR: Arrow a indicates a large tube structure (EPR 99 02A is centred about this tube structure). Arrow b indicates a smaller, partially infilled tube structure. Arrow c indicates a small infilled tube structure. (Tubes b and c form EPR 99 01A)

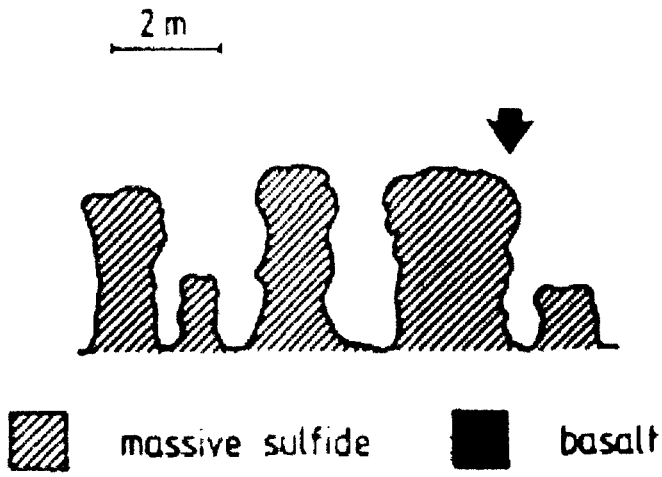

Figure 5.7 – A sketch of the chimney sampled at locatlity 402G (arrow indicates grab position). Adapted from Marchig *et al*, 1997.

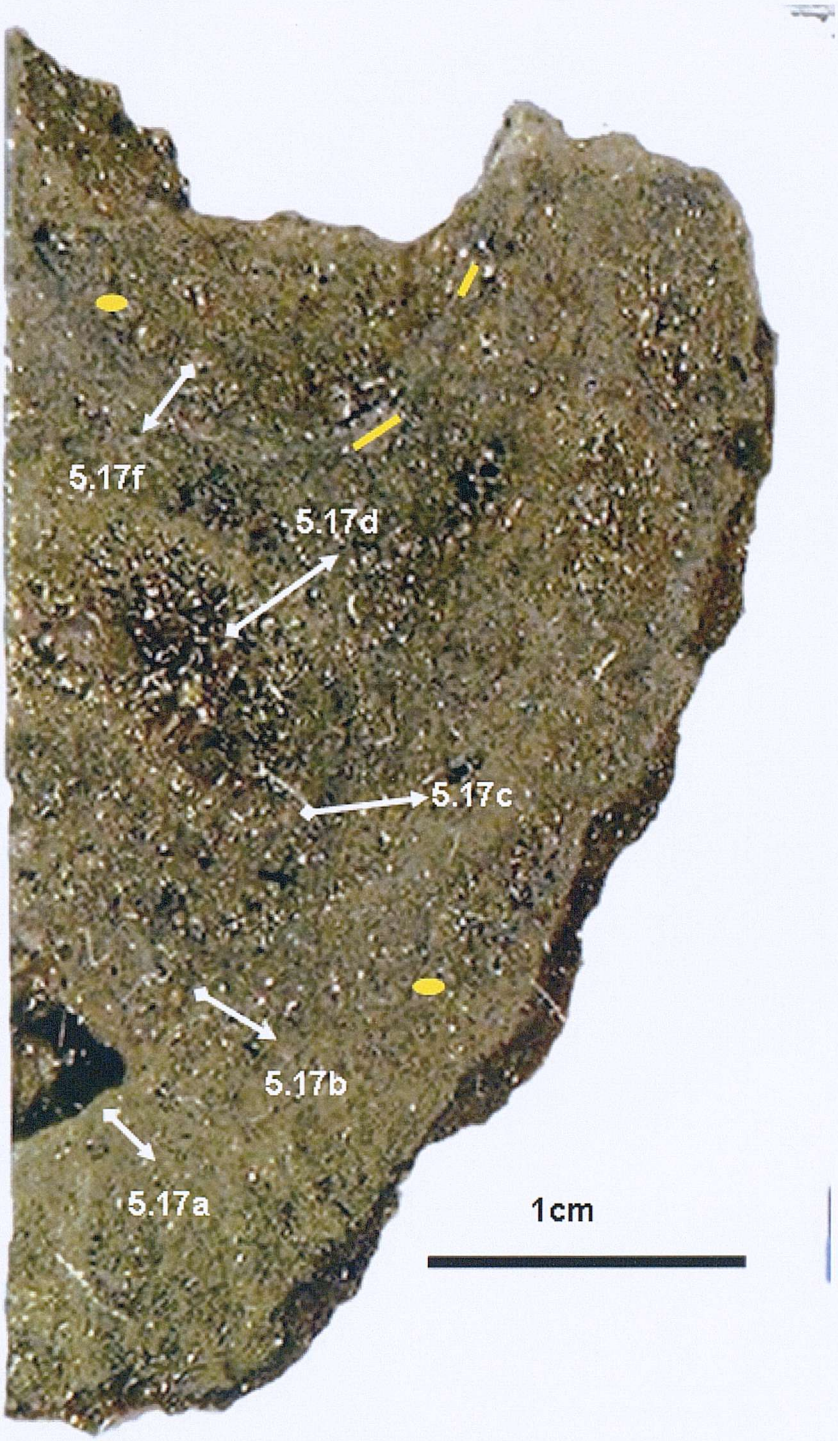

Figure 5.8 – EPR 99 01 A (partially infilled tube from figure 5.6'b' is orientated at top; infilled tube 5.6'c' is located towards mid-left) EMP scan-line traverses marked with white arrows; isotope analysis marked with yellow dots (cpy) and lines (py).

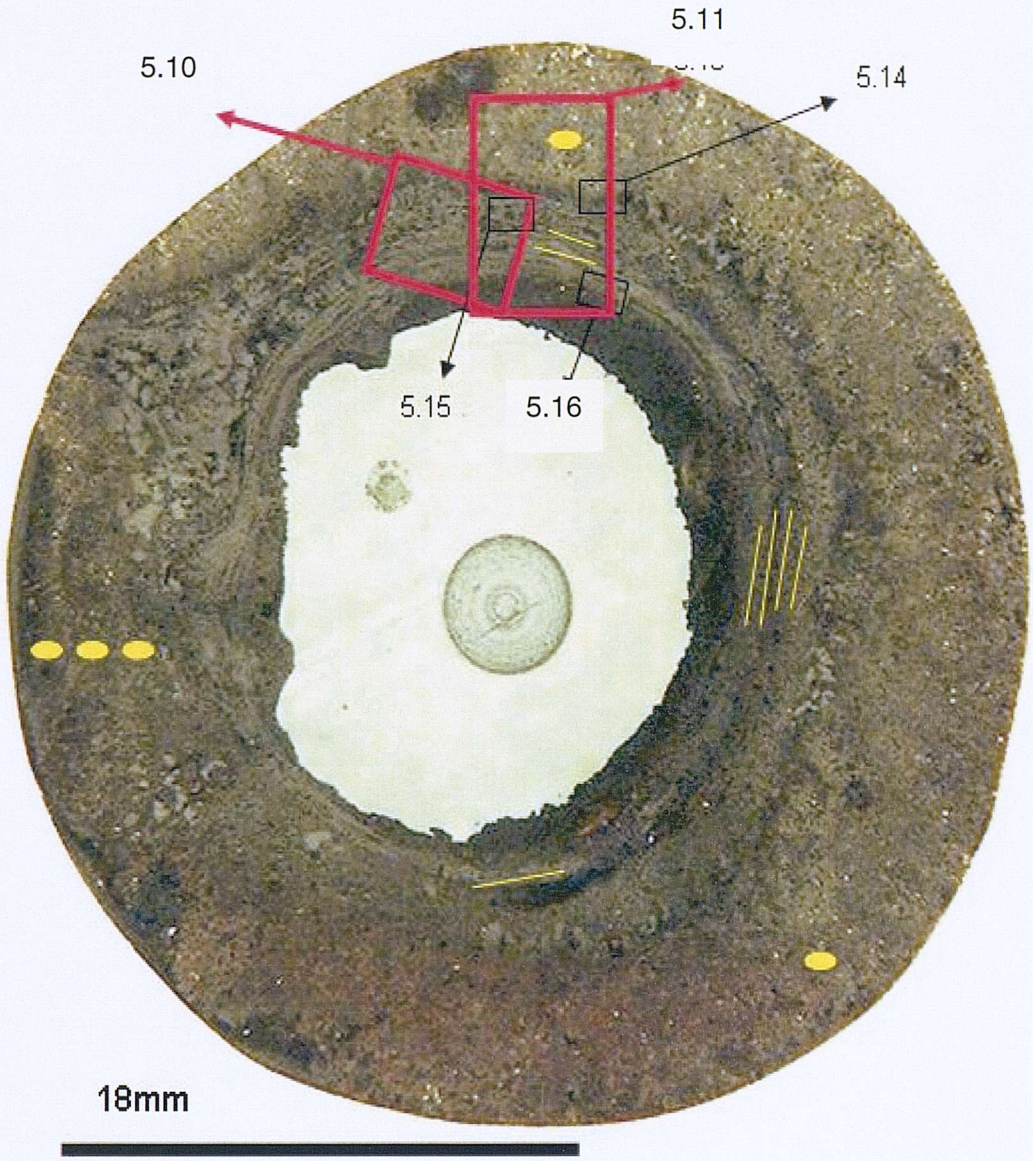

Figure 5.9 – Sample EPR 99 02A shown as a polished block. Red boxes: mark areas covered by Figures 5.10 & 5.11; black boxes mark areas mapped by EMP; yellow lines (py) and dots (cpy) represent areas analysed for sulphur isotopes.

5.3 - Results.

5.3.1 - Mineralogy.

Observation of the sample under reflected light microscopy shows subhedral – euhedral and disseminated chalcopyrite as the major mineralogical component, forming the 'stockwork' deposit around the tubes and the dominant component infilling the tubes. Observations of polished thin-sections reveal concentrically, multilayered tube wall structures which form regular circular features in cross-section indicating a biological rather inorganic origin. These tubes are similar in shape, circumference and size to organic dwelling tubes, especially *Alvinella pompejana* dwelling tubes (e.g. Gaill & Hunt, 1987, 1991, 1994; Desbruyères *et al.*, 1983, 1997) There is a striking similarity between the layered tube walls and the tubes described in Chapter 4, except that in the absence of any discernable organic material, the layered structure is predominantly composed of iron and copper sulphide minerals (e.g. Figure 5.10). Distinct, internal tube laminae are identifiable, and are often texturally similar to the mineralised horizons described in Chapter 4 (Figure 5.11a & b).

Three sulphide minerals have been identified petrographically: chalcopyrite, pyrite and sphalerite, the latter being present in only minor quantities. These have been further distinguished on the basis of their textural differences, such as crystal size and shape; porosity and crystal habit with other sulphides (Figures 5.12 a – f : and summarised in Table 5.2).

Mineral Type	Morphology / description	Crystal size	Colour under R.L.	Estimated percentage of tube	Percentage of stockwork zone	Replacement by
PYRITE – 1	Fine grained. Porous. Often colloform.	< 5μm	Dirty white (green / brown tinge)	<15%	0%	PY - 2
PYRITE – 2	Sub-euhedral, cubic.	5 – 150μm	White (yellow white)	50%	<10%	CPY - 2
SPHALERITE – 1	Anhedral, disseminated	<5μm	Light – medium grey	<1%	<2%	CPY – 2
CHALCOPYRITE - 1	Colloform / banded	<5μm	Light greenish yellow	<2%	<5%	CPY - 2
CHALCOPYRITE – 2	Sub – euhedral	25 – 150μm	Light brassy yellow	30%	50%	-
CHALCOPYRITE - 3	Sub – anhedral. Often massive/ disseminated	5 – 25 μm	Pale brassy yellow – light yellow brown	<5%	35%	-

Table 5.2 – Textural characteristics of sulphides in mineralised tube sample EPR 99 02A.

An initial investigation using XRD techniques to reveal the bulk mineralogy of the tube material, indicates the presence of pyrite, chalcopyrite, and minor marcasite (Figure 5.13). There is no discernable sphalerite present in the tube wall material sampled, which is likely due to patchy distribution of sphalerite throughout the tube wall.

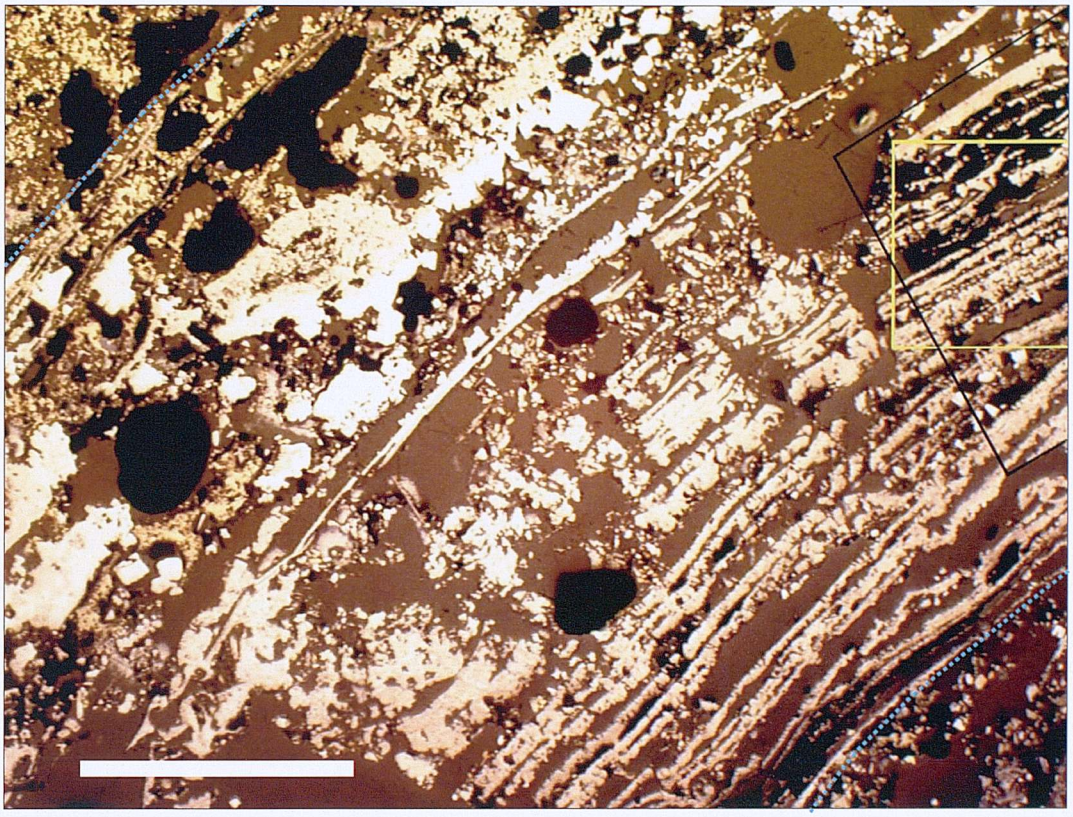

Figure 5.10 – The layered texture within the tube wall of a preserved worm tube structure from sample EPR 99 02A, viewed under reflected light. Inner surface is orientated towards bottom right of frame (blue dotted line); outer tube surface is located towards upper left of frame (blue dotted line); the black box marks the area mapped in Figure 5.16; the yellow box marks the area observed in Figure 5.12a; the brown areas are the mounting medium (resin); the black areas are polish residue from the preparation process. Scale bar = 1mm.

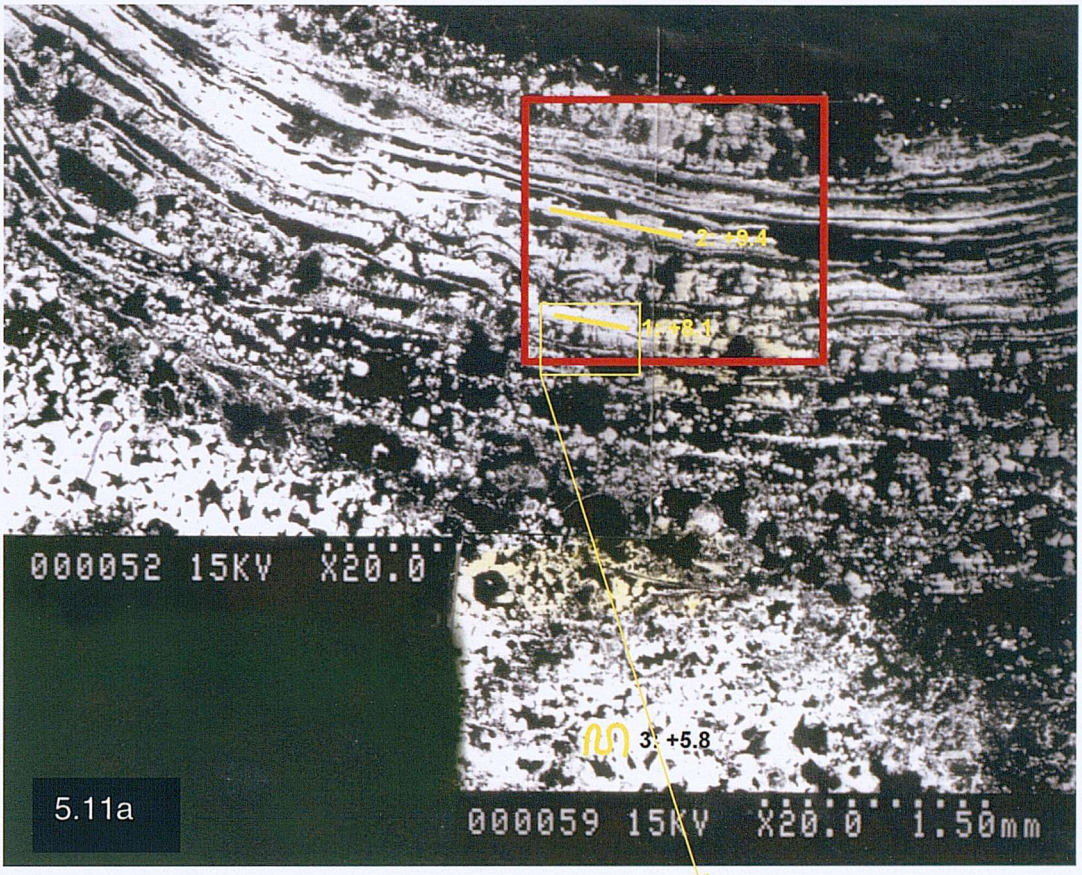

Orientation:
Inner surface

Figure 5.11a - SEM image of the sulphidised tube inter-layers, and outer stockwork zone. Red box shows the area observed in figure 5.12a ; yellow lines represent various LASER ablation traces and corresponding $\delta^{34}S$ values. Yellow box shows the position of (5.11b).

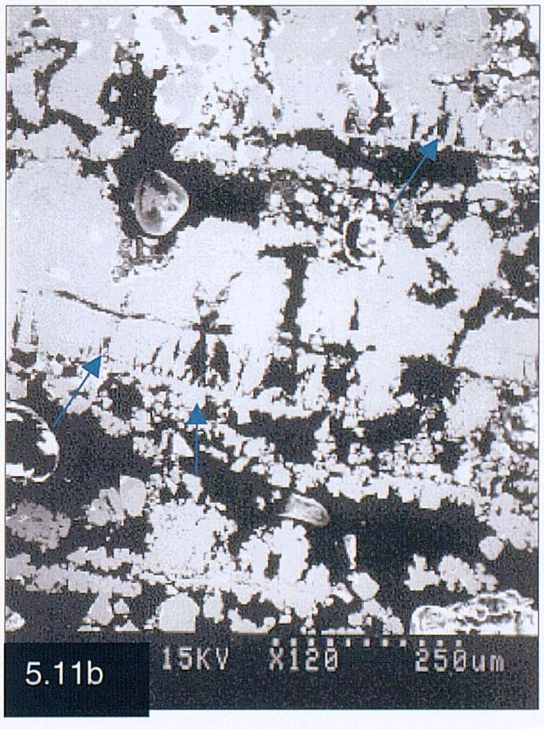

Figure 5.11b - The texture of an individual sulphidised inter-layer indicates the presence of preserved microbial horizons (shown by blue arrows) which branch towards the inner surface

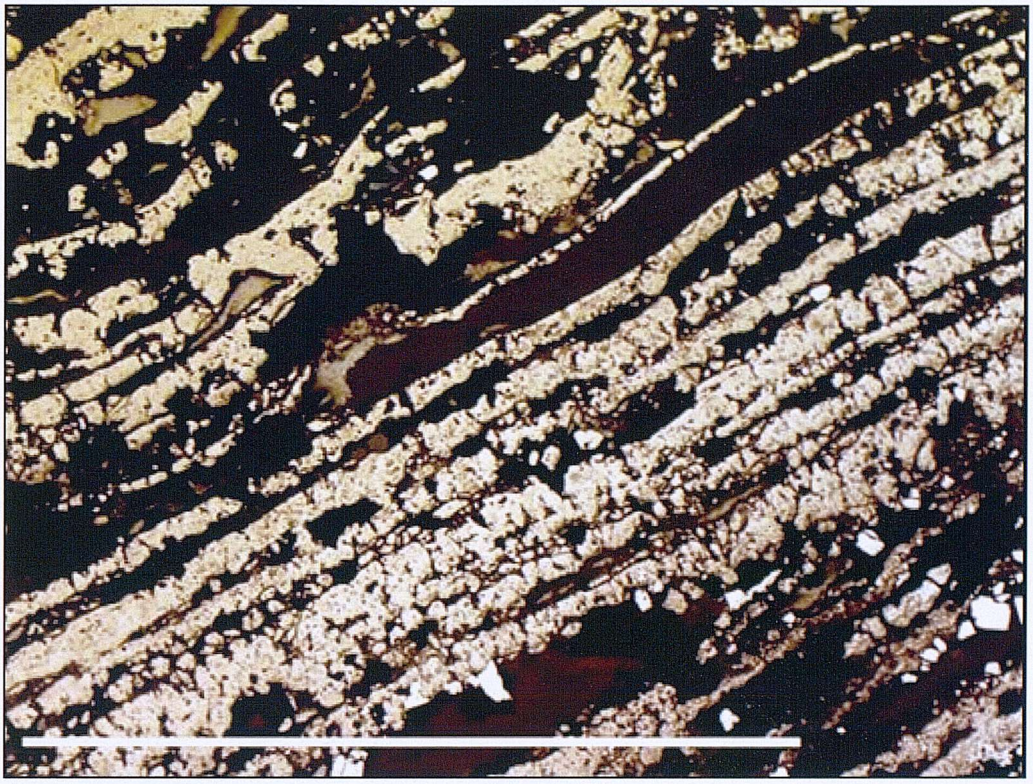

Figure 5.12a – A magnified, reflected light image of the multiple internal tube layers within the tube wall structure. Inner layer is orientated towards the bottom left of the frame. Scale bar = 1mm.

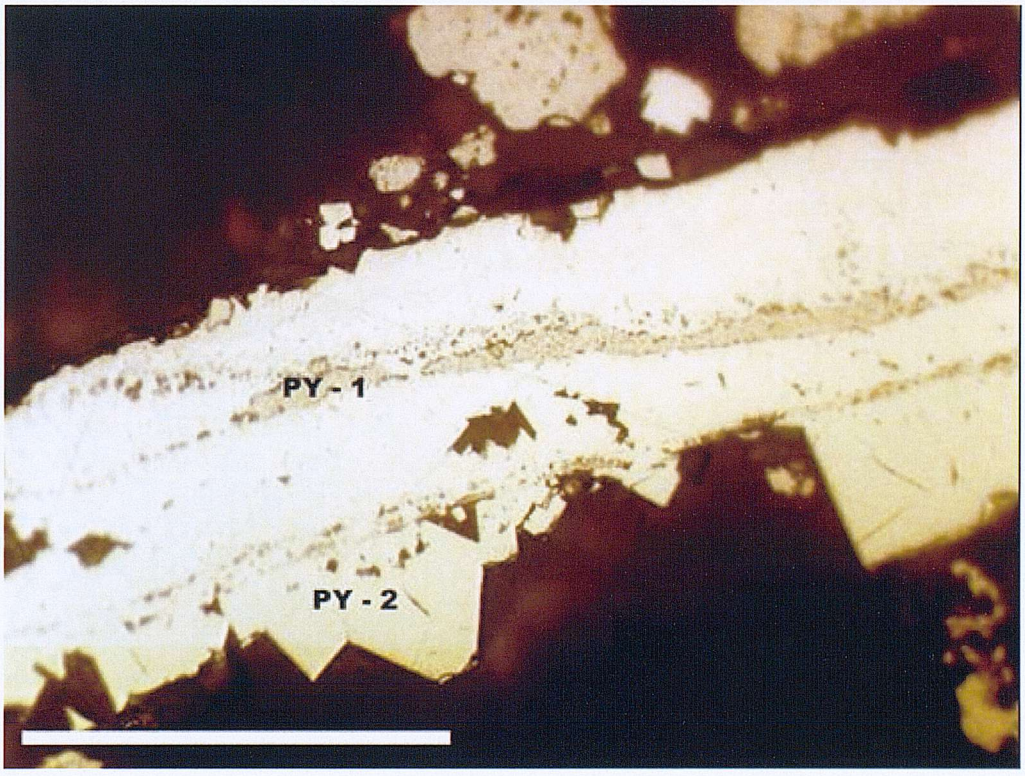

Figure 5.12b – Two pyritised microbial layers consisting of a primary pyrite/marcasite mineral layer (PY-1), which is being replaced by a secondary, more crystalline pyrite (PY-2). Scale bar = 50μm.

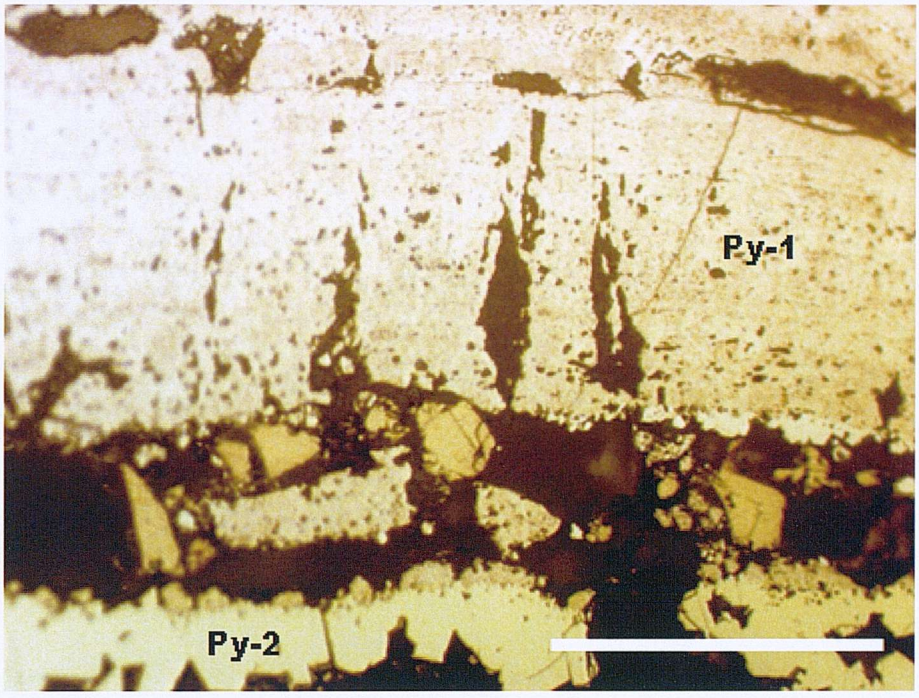

Figure 5.12c – Primary pyrite/marcasite (Py-1) texture is porous and contains remnant microbial structures, and may exhibit a collomorphic texture under reflected light. Towards the bottom of the frame, secondary pyrite (Py-2) can be observed to replace Py-1. Py-2 is crystalline and tends to be devoid of porosity, except near the PY-1/Py2 interface, where elements of the PY-1 porous texture can be observed, indicating replacement of PY-1 by Py-2. Scale = 50μm.

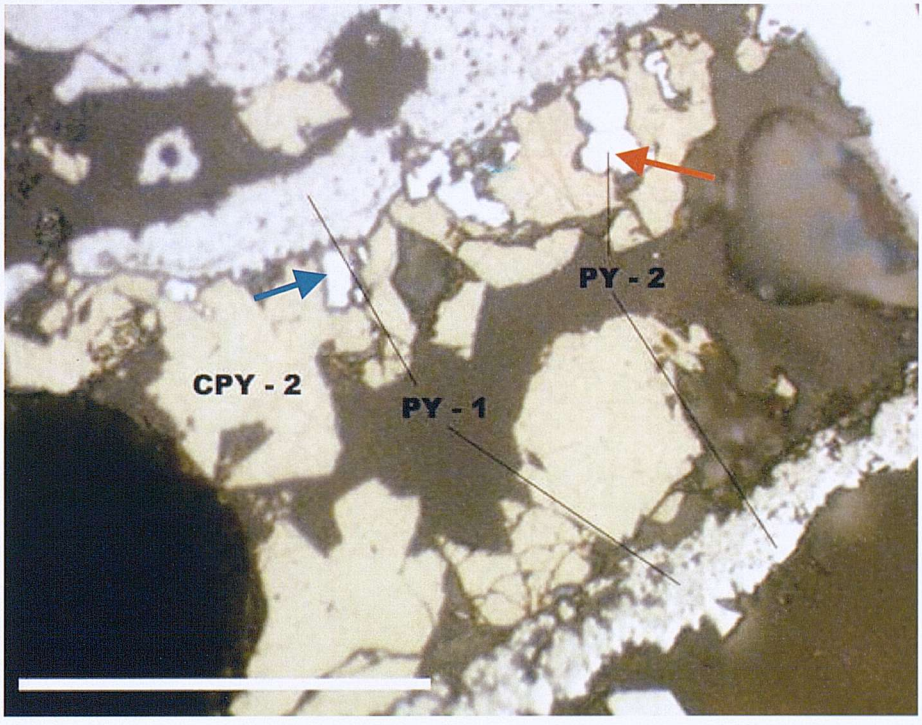

Figure 5.12d – Replacement of PY-1 by PY-2 is succeeded by further replacement of PY-2 by CPY-2, a non-porous, crystalline chalcopyrite phase. Replacement of PY-2 by CPY-2 causes the evolution of corroded 'caries' structures (blue arrow) and 'atoll' structures (red arrow). Scale bar = 20μm.

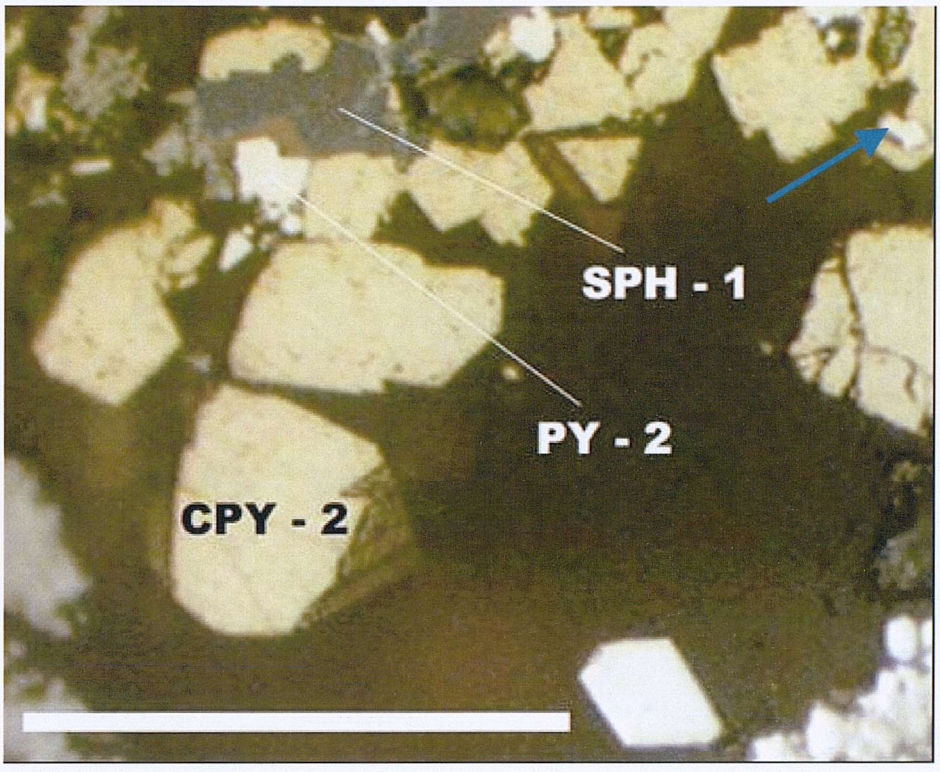

Figure 5.12e – Intergrown sphalerite (SPH-1) and PY-2, are selectively replaced by CPY-2. Corrosion structures such as 'caries' structures (blue arrow) are evident. Scale bar = 50μm.

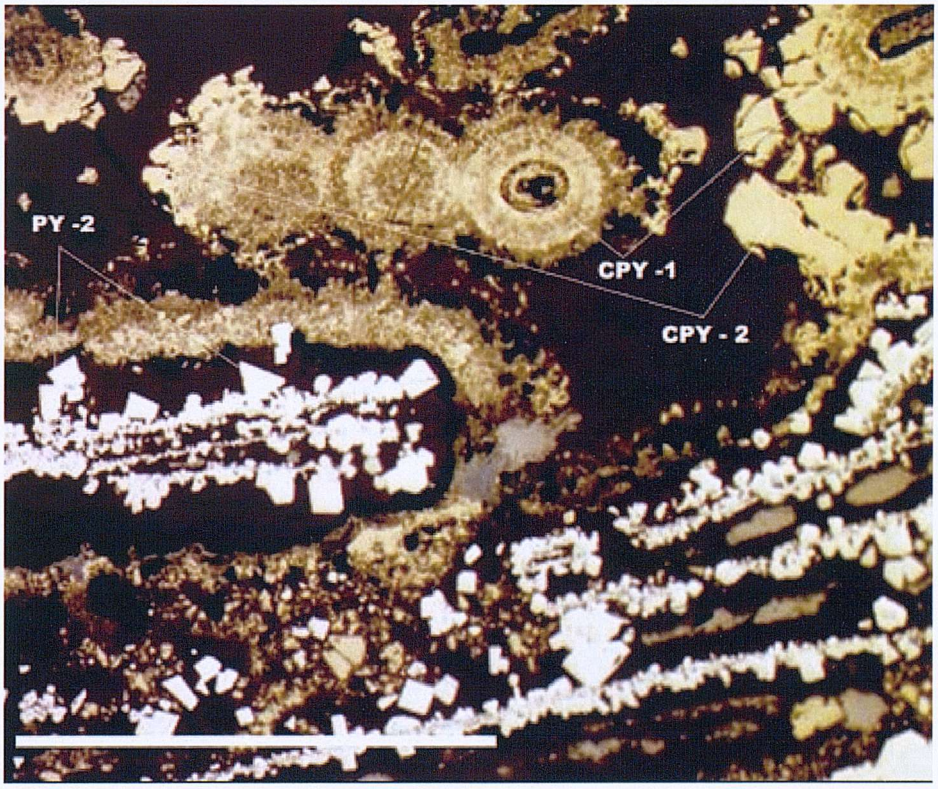

Figure 5.12f – Supergene alteration forming 'bird's eye' textures of colloform CPY-1 nucleated around central pyrrhotite crystals, and remnant PY-1 phases. Later CPY-2 replacement and/or overgrowth of CPY-1 can also be observed. Scale bar = 60μm.

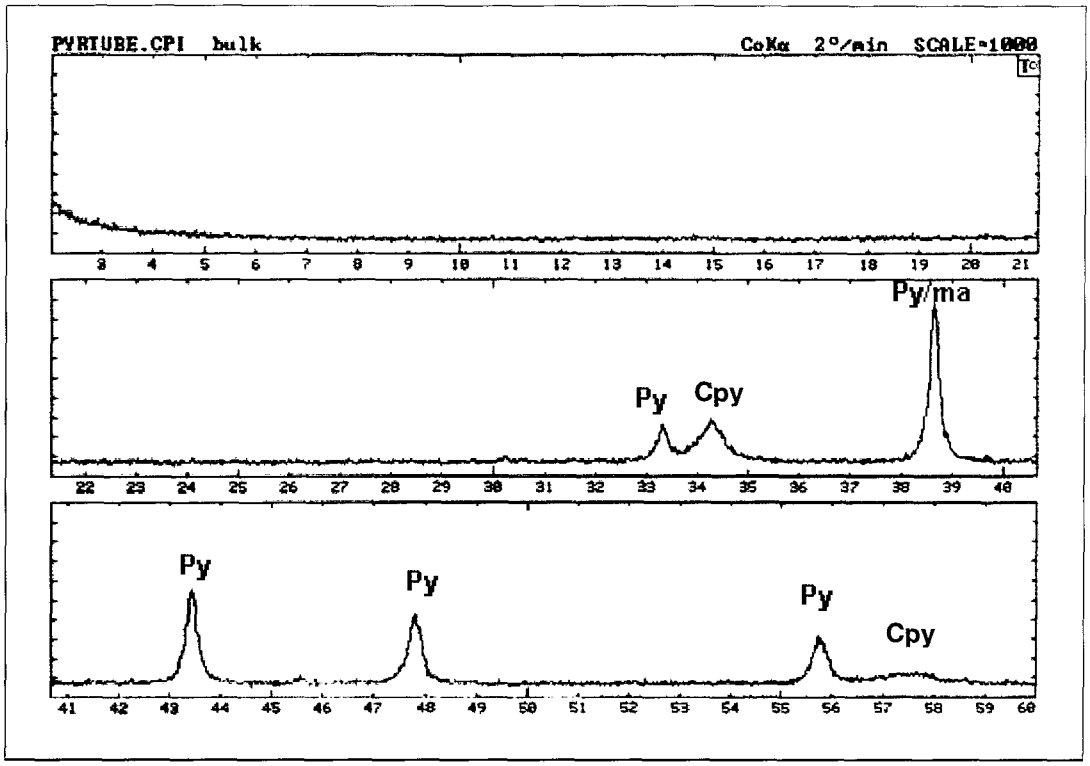

Figure 5.13 – XRD analysis of mineralised tube wall structure. Py: pyrite; Cpy: chalcopyrite; Ma: marcasite.

5.3.2 Geochemistry

SEM – EDS analysis and EMP analysis confirm the presence of S, Fe and Cu as the dominant elements within the tube material, as well as signifying extremely low abundances of other chemical elements usually associated with hydrothermal vent mineralisation (such as Zn, Si, Ca (anhydrite), Ba (barite)). Quantitative EMP point analysis of various mineralised horizons forming the tube layers, and the outer stockwork zone (Table 5.3), are compared with geochemical analyses carried out by Marchig *et al.* (1997) using a combination of atomic absorption spectroscopy (AAS) and neutron activation (INAA) techniques (Table 5.4).

Trends in spatial mineralogical relationships (for the tube wall in sample EPR 99 02 A: Figure 5.9) can be observed using elemental mapping and scan line traverses compiled on the EMP. Figures 5.14, 5.15 and 5.16 show elemental maps for S, Fe, Cu and (Fe + Cu), covering different areas of the tube wall. The (Fe + Cu) maps (Figures 5.14d, 5.15d & 5.16d), clearly show the extent of chalcopyrite mineralisation. Figure 5.14 is centred about the interface between the inner tube wall layers and the mineral infill which coats the inner surface. Chalcopyrite mineralisation can be seen to form the major fraction of the mineral infill, and pyrite to form the layered tube structure. However, within the first 200μm of the inner tube wall, chalcopyrite can be seen infiltrating the layered structure, forming intergrowths, and replacing the pyrite. A similar relationship can be seen at the outer wall interface of EPR 99 02A (Figure 5.15) where the overgrowth, intergrowth, and replacement of the outer pyrite layers is extensive. Pyrite is abundant in the stockwork mineralisation. Figure 5.16 shows a 1500μm^2 mapped area of EPR 99 02A which centres around the middle section of the tube structure (see boxed area in Figure 5.11). The layers towards the outer surface of the tube (top of frame) show Cu-rich mineral precipitation, dominantly overgrowth of the pyrite mineral layers, and intergrowth within the gaps and pore spaces, as opposed to replacement of the pyrite layers.

Figure 5.8 shows sample EPR 99 01 A, which includes 5 EMP scan line traverses, also plotted for S, Fe and Cu, through the mineralised wall, of two of the smaller tubes

lying adjacent to one another, and the areas of sulphur isotope analyses (it should be noted that plots 5.17a – d are all from different areas of the same tube, and 5.17e is from a different tube). Plots 5.17 a – d all show that the tube is composed of distinct mineralised bands of pyrite and chalcopyrite. Figure 5.17a is dissimilar in that it has alternating layers of Cu-rich and Fe-rich sulphides, whereas plots 5.17 b – d only have significant amounts of Cu-rich sulphide in the outer 25 – 40% of the tube layers. Figure 5.17e contains only a thin (25μm) layer of chalcopyrite located towards the inner surface (~175μm).

chimney	sample	Si (%/wt)	Fe (%/wt)	Cu (%/wt)	Zn (%/wt)	Ca (%wt)	P (%wt)	S total (%/wt)	Total (%/wt)
402 G	EPR 99 01 A / stockwork	0.01	30.95	33.35	0.08	0.01	0.11	34.18	98.77
402 G	EPR 99 01 A / stockwork	0.00	30.28	33.90	0.05	0.00	0.10	35.04	99.46
402 G	EPR 99 01 A / stockwork	0.01	46.00	0.41	0.05	0.04	0.00	53.28	100.03
402 G	EPR 99 01 A / stockwork	0.01	46.46	0.28	0.00	0.00	0.00	53.97	100.92
402 G	EPR 99 01 A / stockwork	0.00	30.40	33.50	0.00	0.00	0.08	34.58	98.69
402 G	EPR 99 01 A / stockwork	0.02	28.79	30.02	0.08	0.05	0.08	30.00	89.26
402 G	EPR 99 01 A / tube	0.01	47.09	0.04	0.04	0.00	0.00	52.90	100.23
402 G	EPR 99 01 A / tube	0.00	44.82	0.37	0.13	0.02	0.03	51.64	97.15
402 G	EPR 99 01 A / tube	0.00	45.71	0.34	0.00	0.00	0.04	51.94	98.07
402 G	EPR 99 01 A / tube	0.00	30.77	33.73	0.00	0.02	0.12	35.20	99.95
402 G	EPR 99 01 A / tube	0.02	45.58	0.29	0.01	0.03	0.00	52.26	98.31
402 G	EPR 99 01 A / tube	0.00	44.96	0.24	0.00	0.00	0.00	53.00	98.48
402 G	EPR 99 02 / stockwork	0.02	30.60	33.81	0.10	0.00	0.06	34.73	99.41
402 G	EPR 99 02 / stockwork	0.00	30.21	33.59	0.06	0.02	0.06	34.89	98.94
402 G	EPR 99 02 / stockwork	0.03	30.39	33.61	0.09	0.00	0.08	35.55	99.77
402 G	EPR 99 02 / stockwork	0.04	45.41	0.41	0.00	0.00	0.00	51.38	97.53
402 G	EPR 99 02 / stockwork	0.00	30.99	34.27	0.00	0.01	0.10	34.75	100.19
402 G	EPR 99 02 / stockwork	0.05	47.44	0.18	0.00	0.01	0.00	53.20	101.03
402 G	EPR 99 02 / tube	0.00	45.25	0.39	0.05	0.00	0.00	53.34	99.31
402 G	EPR 99 02 / tube	0.02	45.58	0.29	0.01	0.03	0.00	52.26	98.31
402 G	EPR 99 02 / tube	0.00	44.96	0.24	0.00	0.00	0.00	53.00	98.48
402 G	EPR 99 02 / tube	0.01	46.05	0.21	0.66	0.00	0.00	53.09	100.21
402 G	EPR 99 02 / tube	0.01	46.46	0.28	0.00	0.00	0.00	53.97	100.92
402 G	EPR 99 02 / tube	0.00	33.42	22.60	0.01	0.02	0.11	38.70	95.06

Table 5.3 - Chemical composition of massive sulphide tube structures from 7°24'S EPR.

chimney	sample no	Si (%/wt)	Fe (%/wt)	Cu (%/wt)	Zn (%/wt)	C total (%/wt)	C organic (%/wt)	S total (%/wt)	Total (%/wt)
402 G	2d/A	4.70	32.55	0.81	8.75	0.14	0.11	47.56	94.62
402 G	2d/B	7.30	33.83	2.45	5.25	0.13	0.09	48.08	97.13
402 G	2d/C	6.60	33.14	6.00	4.00	0.08	0.07	48.28	98.17
402 G	2d/D	7.30	34.55	6.38	2.63	0.08	3.10	43.10	94.14
402 G	2d/E	6.70	34.75	8.75	0.24	0.09	0.06	48.55	99.14
402 G	2d/F	1.50	39.02	5.13	0.65	0.12	0.08	57.44	103.94
402 G	2d/G	2.90	38.88	5.75	1.13	0.10	0.07	47.13	95.96
402 G	2d/H	7.90	36.56	6.50	0.50	0.10	0.09	52.44	104.09
402 G	3d/A	0.10	40.34	0.33	2.85	0.22	0.16	45.84	89.84
402 G	3d/B	0.50	37.73	9.50	0.26	0.13	0.13	52.59	100.84
402 G	3d/C	1.90	30.86	9.63	3.20	0.12	0.06	45.37	101.14
402 G	3d/D	0.40	31.46	6.50	0.11	0.12	0.08	39.13	97.80
402 G	3d/E	0.40	30.21	9.00	0.09	0.13	0.07	45.13	105.03
402 G	3d/F	0.05	30.98	9.25	0.12	0.09	0.10	44.40	104.99

Table 5.4 - Chemical composition of massive sulphide chimney samples from 7°24'S EPR (data from Marchig *et al.*, 1997).

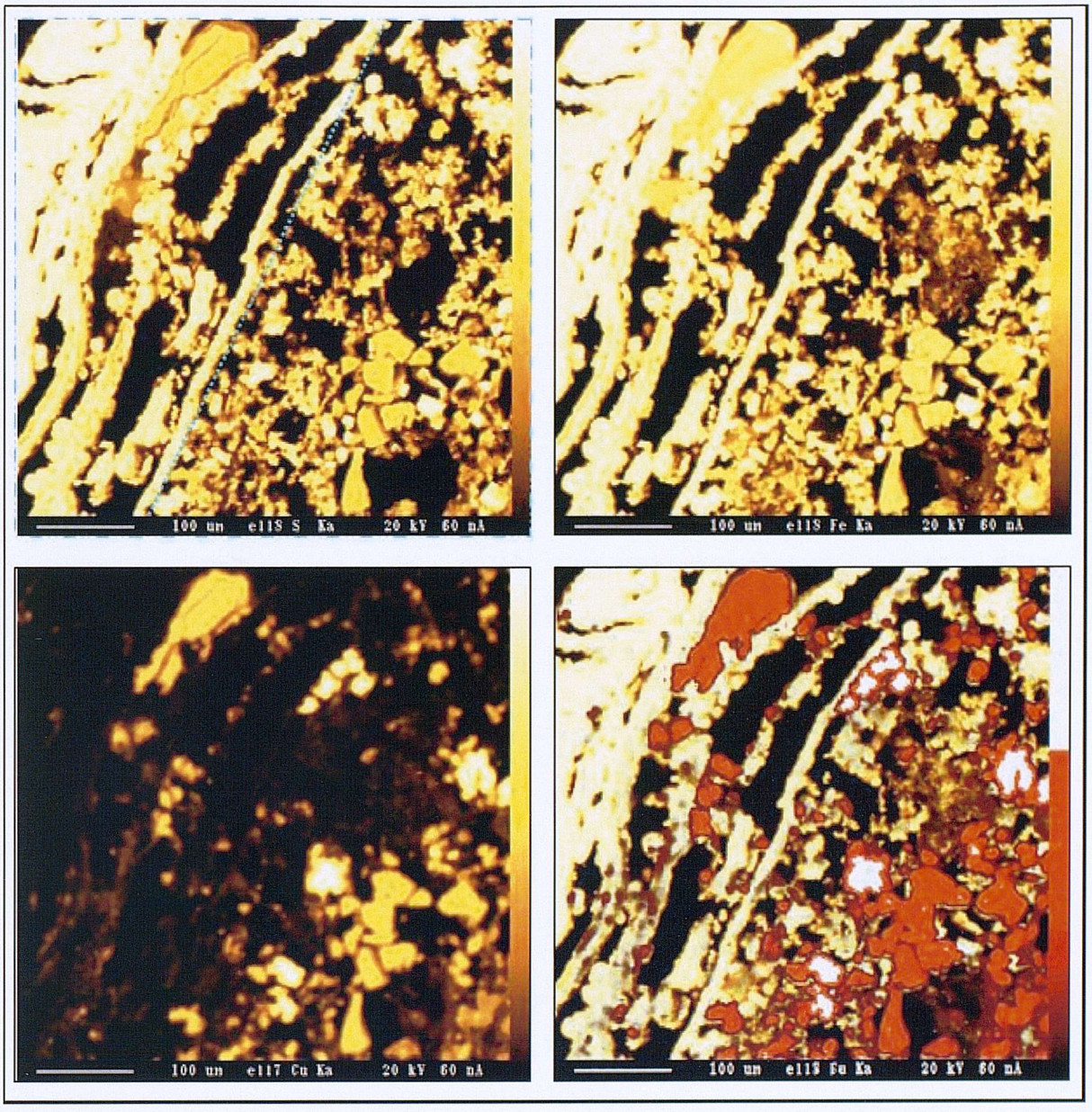

Figure 5.14 – Elemental maps of the inner wall of an area of *Alvinella* tube (location of mapped area shown on Figure 5.9). Top left: S ; Top right: Fe; Bottom left: Cu; Bottom right Cu (red) overlying Fe (yellow).

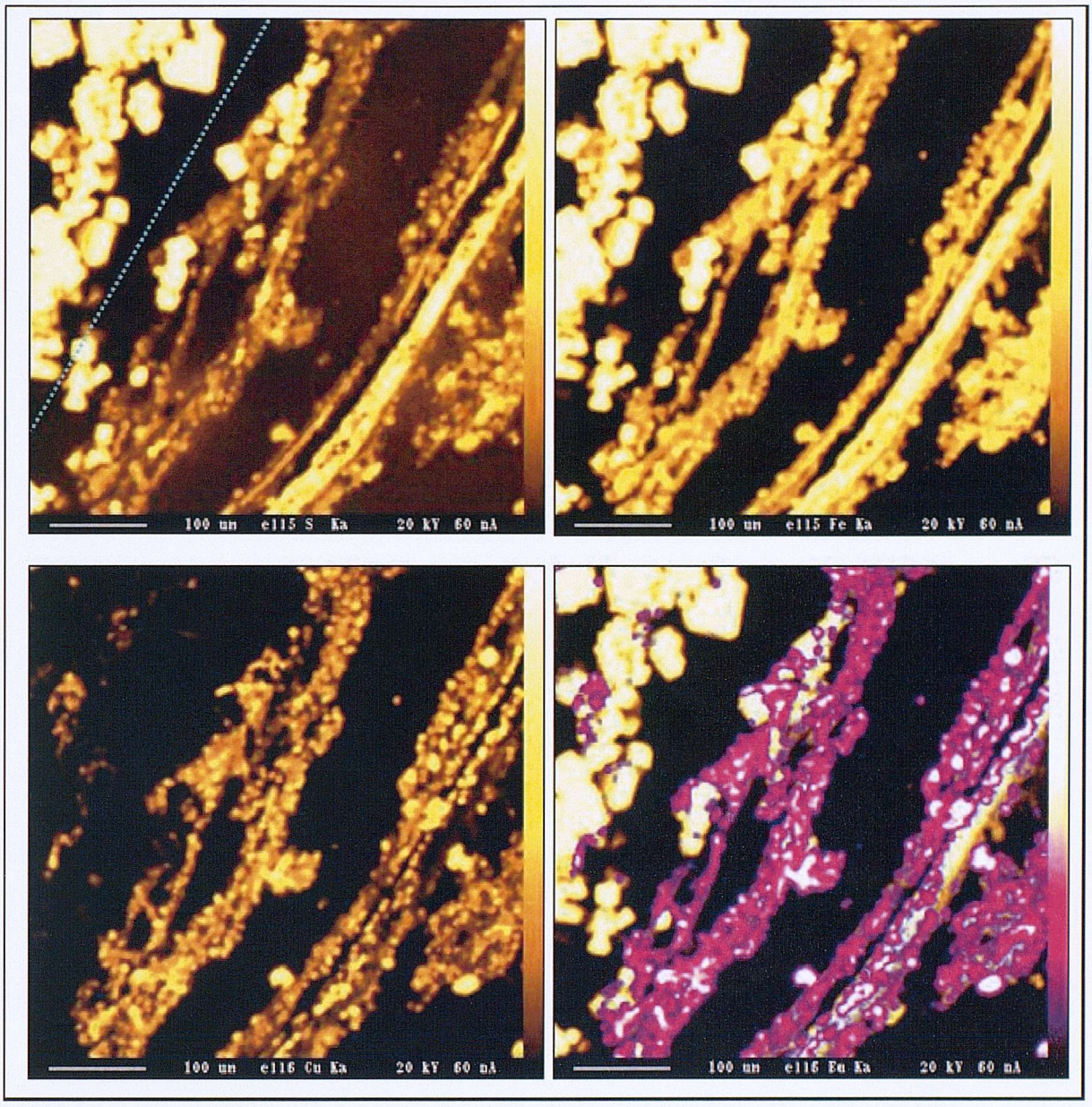

Figure 5.15 – Elemental map of outer wall area of *Alvinella* tube tube (location of mapped area shown on Figure 5.9). Top left: S ; Top right: Fe; Bottom left: Cu; Bottom right: Cu (purple) overlying Fe (yellow).

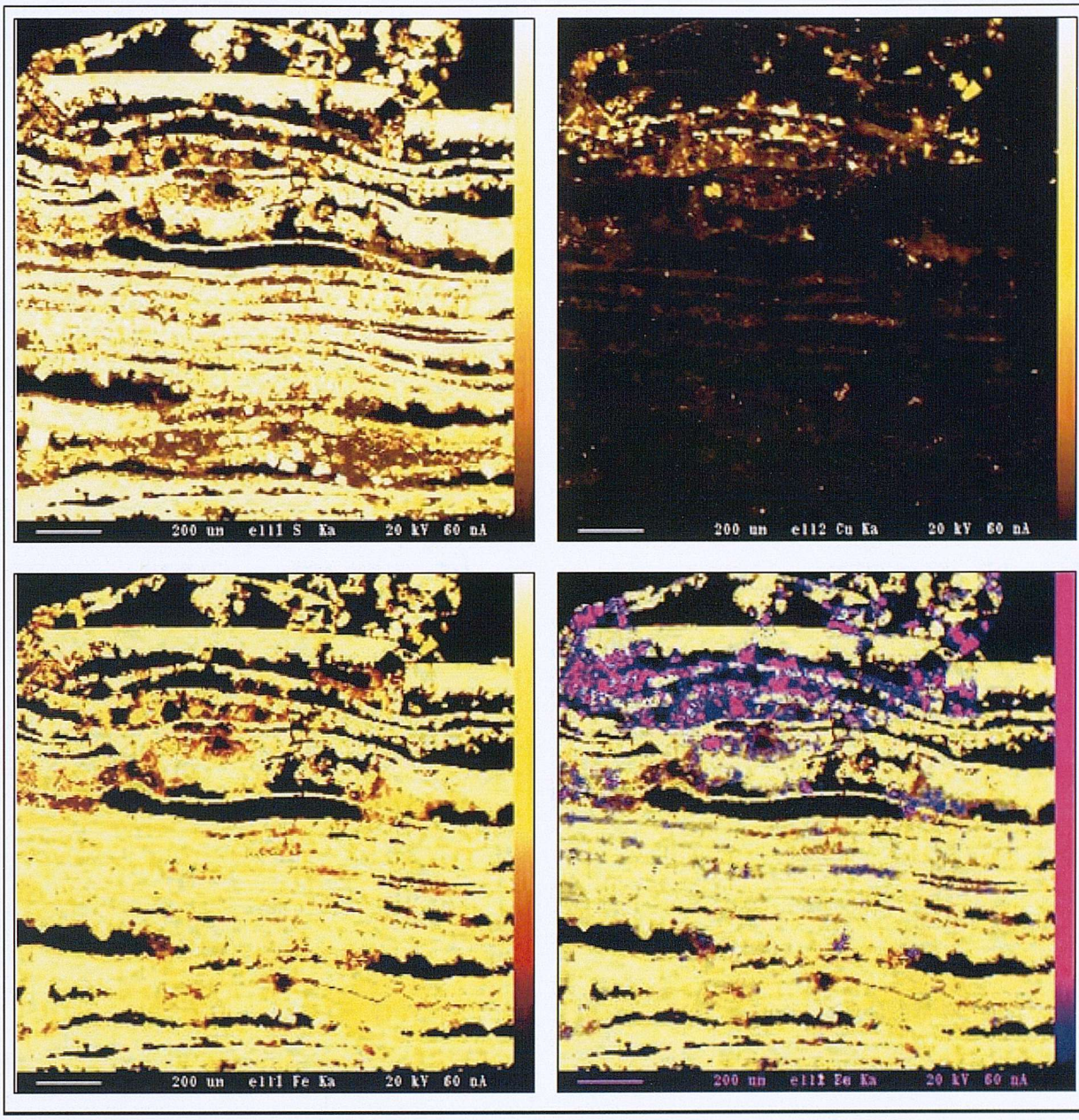

Figure 5.16 – Elemental map of outer wall area of *Alvinella* tube tube (location of mapped area shown on Figure 5.9). Top left: S ; Top right: Fe; Bottom left: Cu; Bottom right: Cu (purple) overlying Fe (yellow).

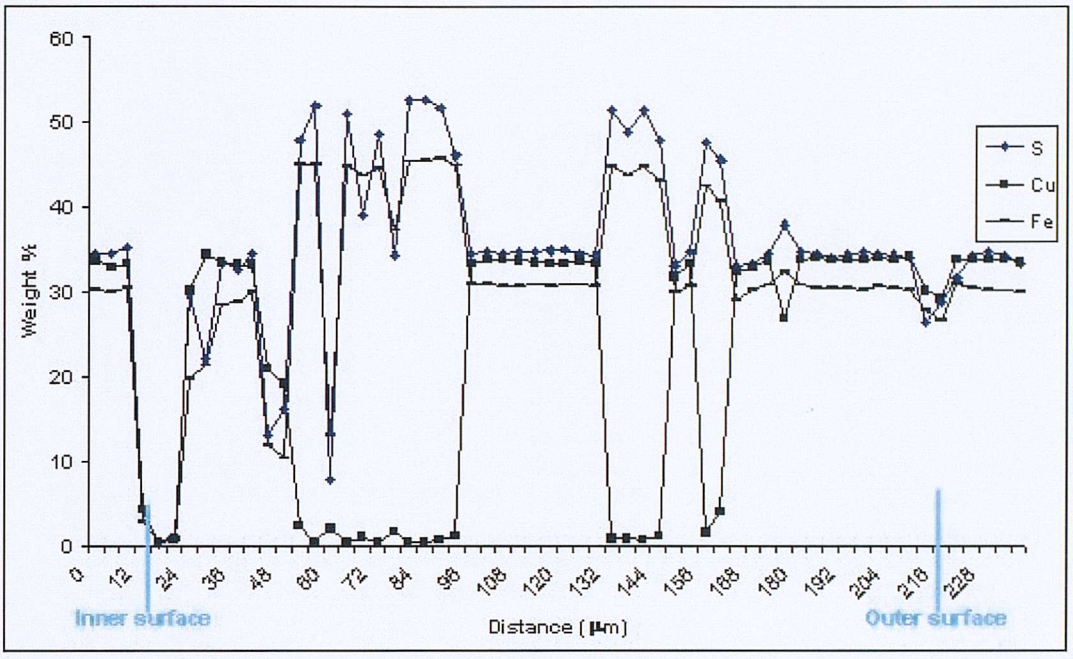

Figure 5.17a – EMP scan line traverse showing weight percent of selected elements vs. distance of scan line.

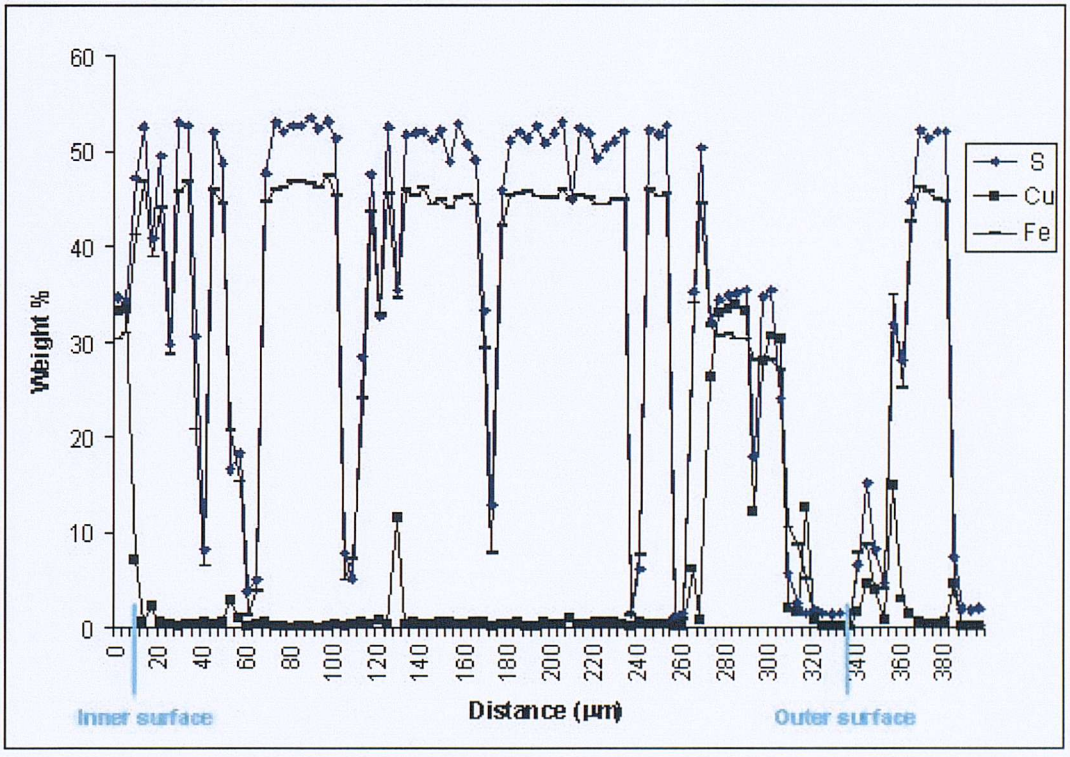

Figure 5.17b – EMP scan line traverse showing weight percent of selected elements vs. distance of scan line.

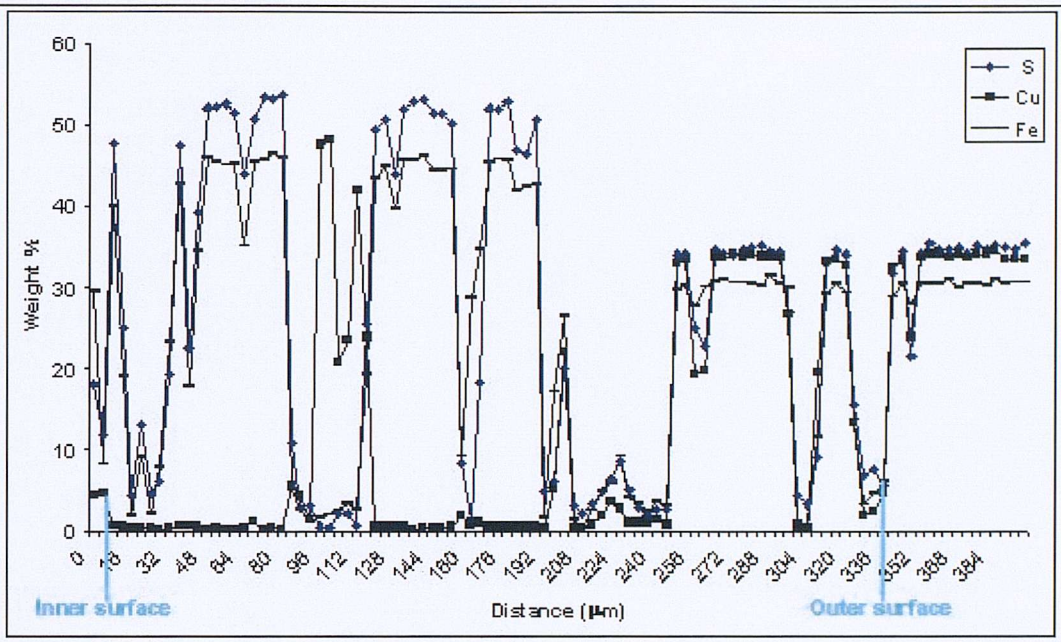

Figure 5.17c – EMP scan line traverse showing weight percent of selected elements vs. distance of scan line.

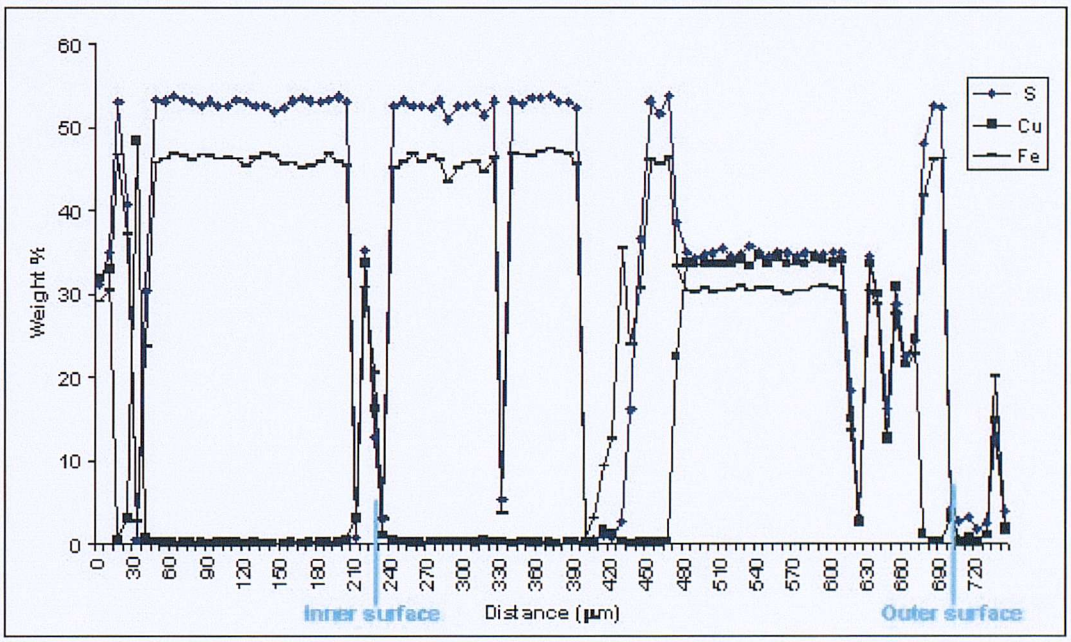

Figure 5.17d – EMP scan line traverse showing weight percent of selected elements vs. distance of scan line.

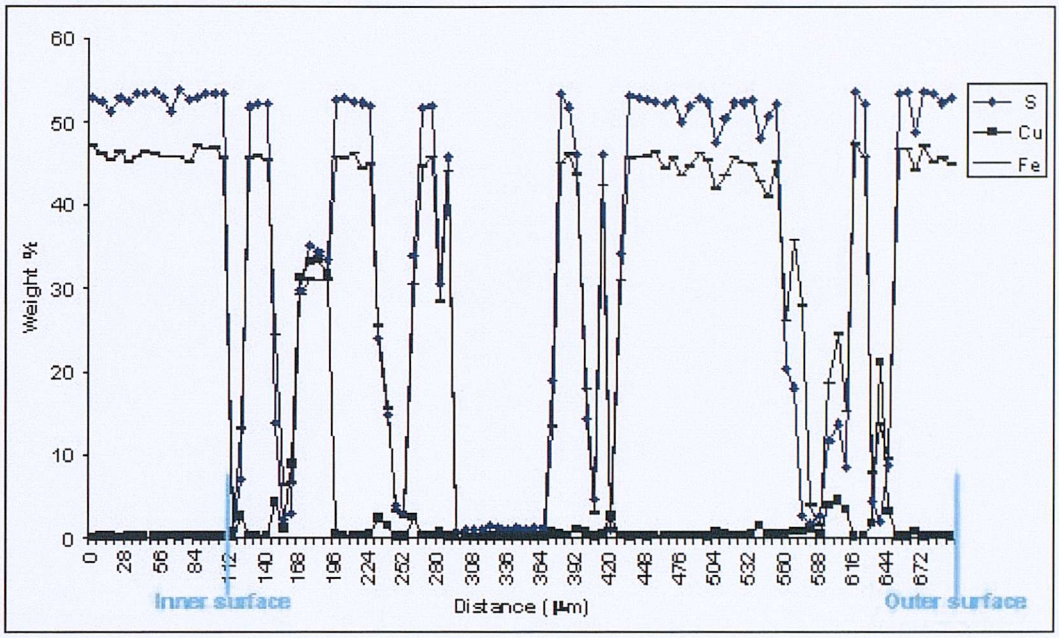

Figure 5.17e – EMP scan line traverse showing weight percent of selected elements vs. distance of scan line.

5.3.3 - Textural observations using High-Field Scanning Electron Microscopy.

High-field scanning electron microscopy (HFSEM) allows for remarkably detailed textural observations at very high magnification, and the ability to manipulate three dimensional samples to attain different view points. HFSEM was carried out on a sample of tube material removed from tube 'a' (Figure 5.6). Figure 5.18a displays a highly magnified view of a single sulphidised mineral lamina in cross-section. Here it can be seen that the crystalline outer sections appear to have either grown out from the porous, micro-crystalline central layer, or have crystallographically reorganised inwards from the outer boundaries towards the central margin. At higher magnification still (Figure 5.18b) the individual crystals which form the outer margins of the lamina, can be seen to exhibit good euhedral crystal shape, markedly different from the massive, poorly-crystalline, and porous inner margin (Figure 5.19a). Also noticeable within Figure 5.19a is what appears to be a sinusoidal 'herringbone' texture analogous to that seen in the mineralised tube wall of *Alvinella pompejana* tubes (Gaill & Hunt, 1987). This type of sinusoidal patterning can be observed frequently under HFSEM. In Figure 5.19 b small area displaying the 'herringbone' texture can be seen to be replaced by a crystalline mineral with euhedral shape.

Figure 5.20a shows a small assemblage of filamentous crystals which have been preserved within the tube layers. Several of the filaments have branching junctions which may be indicative of organic origins. An amorphous mineral intergrowth can be seen between the individual filaments, and areas of anhedral – sub-cubic mineral growth at the proximal ends of some of the filaments. Figure 5.20b shows a diatom embedded within the tube wall structure which shows outstanding preservation.

Throughout the tube sample, euhedral rhombic crystals of pyrite can be seen to form complex patterns (Figure 5.21a) which often appear to grow out into open space which are probably the pore spaces, gaps and fractures that form within and between the tube layers. Figure 5.21b shows a small assemblage of barite crystals located within the stockwork chalcopyrite, these too have precipitated into open space and have good crystal habit. Barite and other sulphide minerals are infrequently observed within the stockwork zone of the sample, but are as yet not seen at all within the tube structure itself. Another

unusual texture seen within the stockwork mineralisation is a type of sulphidised filamentous encrustation (Figure 6.22a), which form localised dendritic networks. On closer observation (Figure 6.22b), the filaments appear to be formed of subhedral rhombic crystals and a poorly-crystalline, massive type of precipitate.

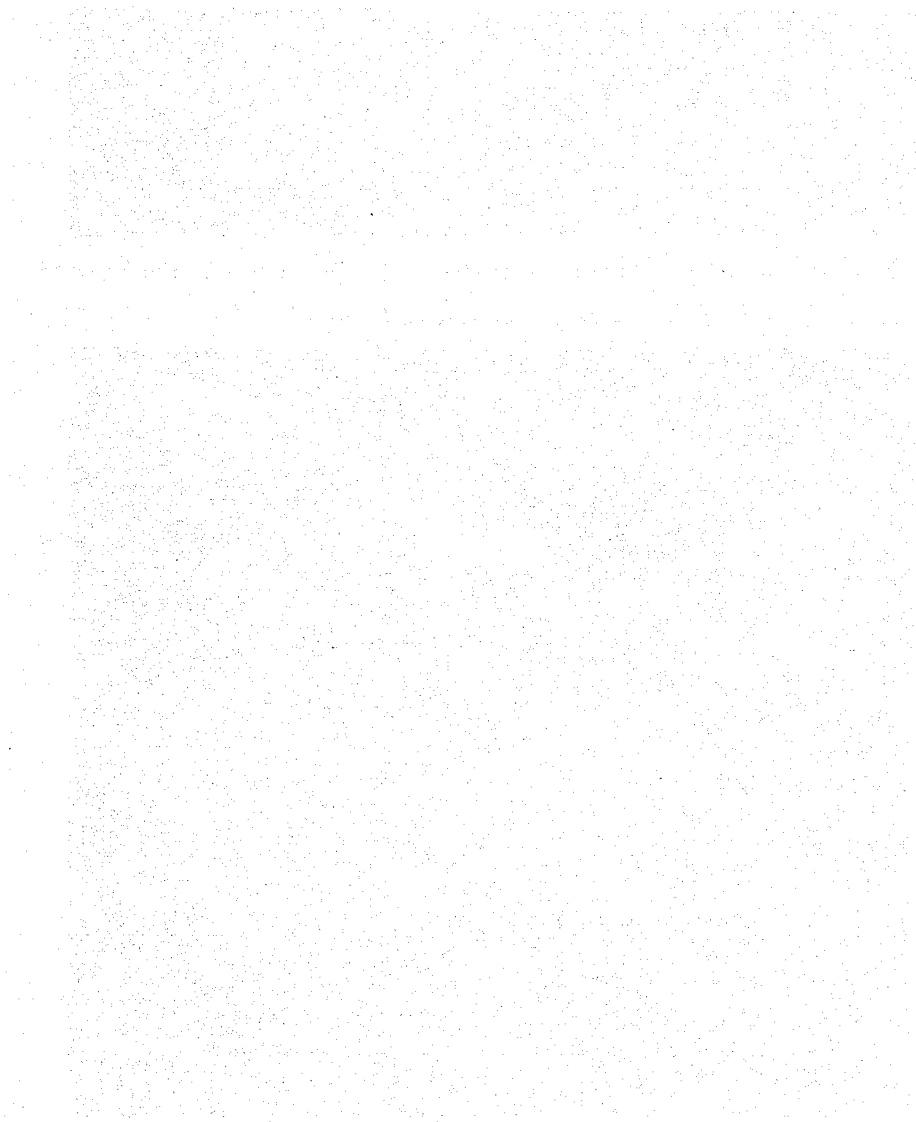

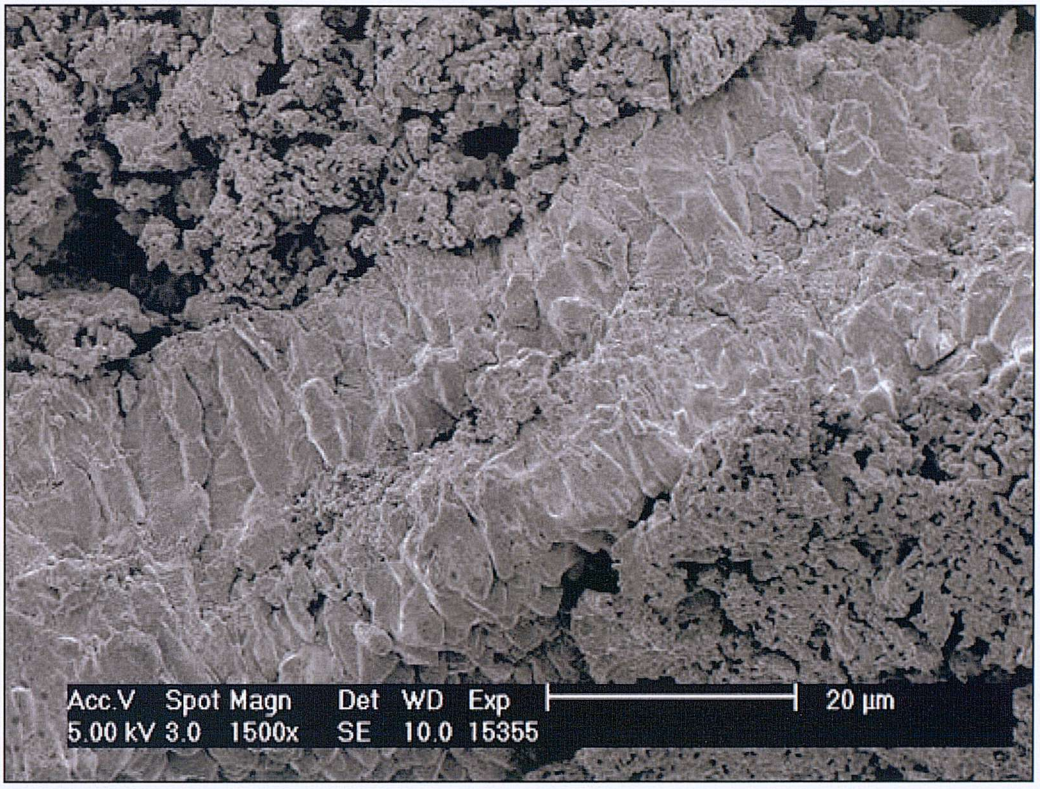

Figure 5.18a – A crystalline, sulphidised mineral layer adjacent to a porous, poorly crystalline (possibly microbial?) horizon, and set within a porous mineral matrix.

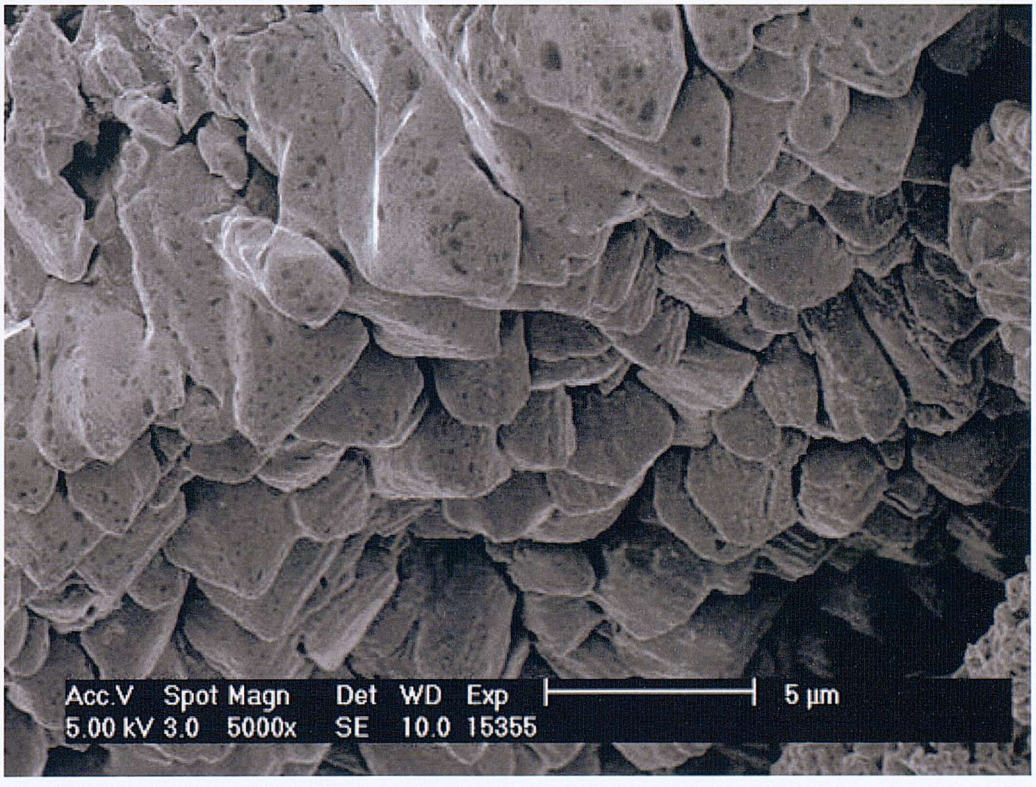

Figure 5.18b – At high magnification the crystallised layer seen in Figure 5.19a, can be seen to be formed of euhedral crystals of a regular size.

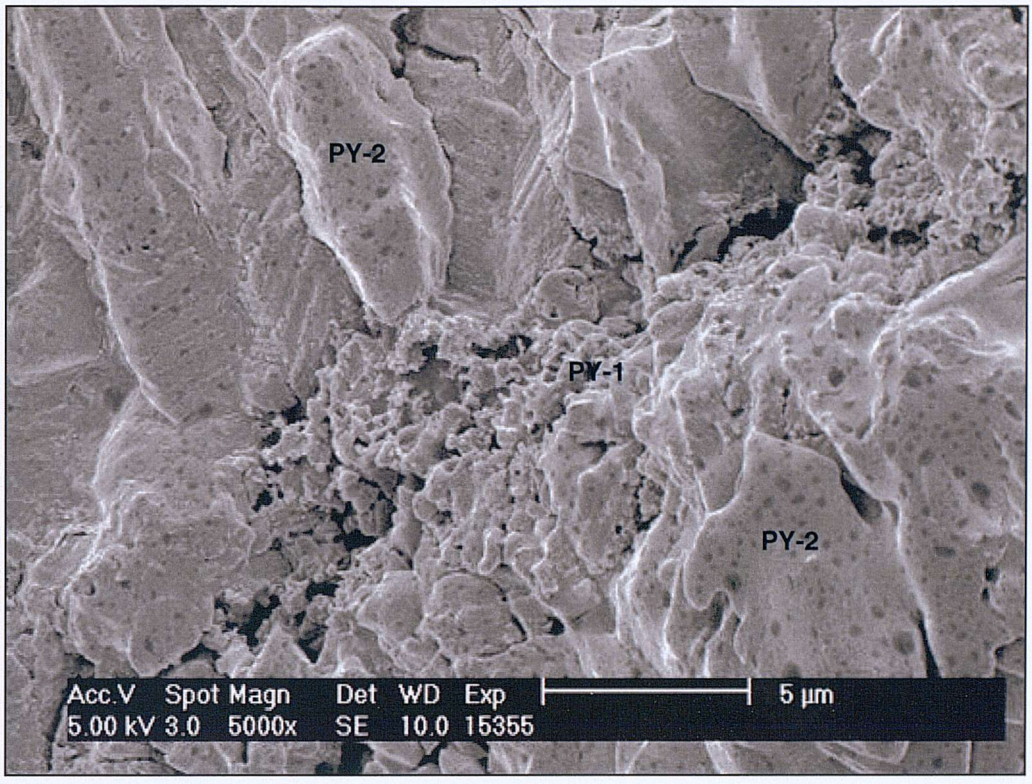

Figure 5.19a – High magnification image of the porous, poorly-crystalline PY-1 mineral phase, and replacement by the crystalline PY-2 phase. Note the herringbone texture preserved along the faces of the crystals in the upper section of the frame.

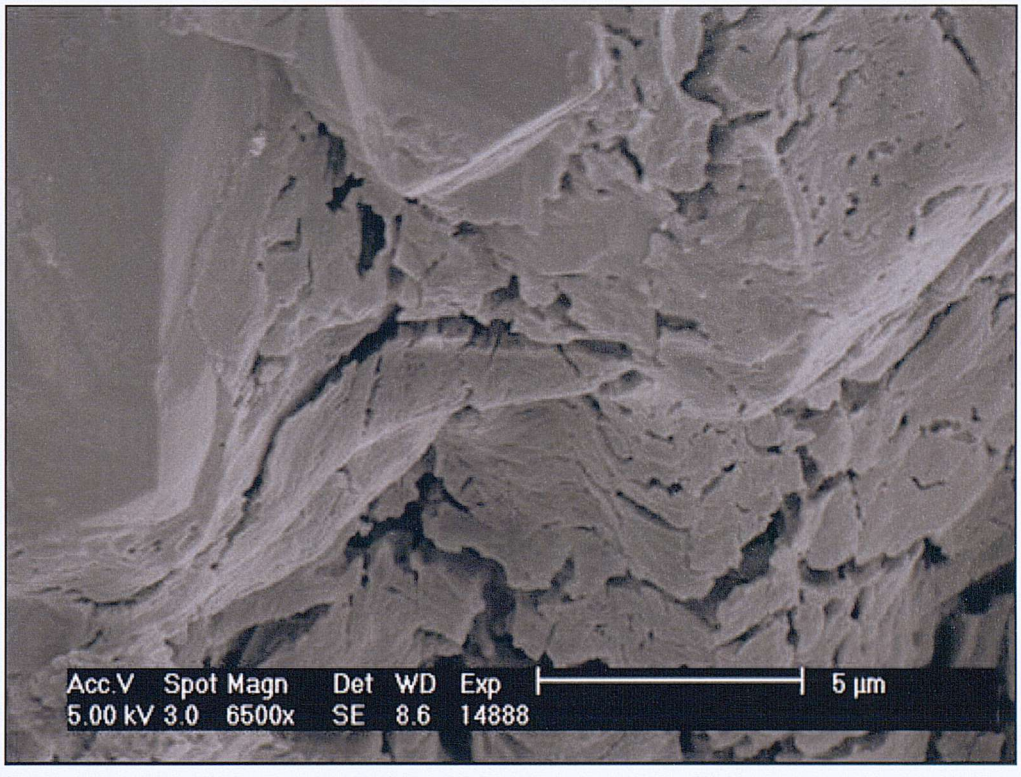

Figure 5.19b – A sinusoidal texture is preserved in the tube wall material, which is inferred to be formed from desiccated organic material, which is being replaced by a progressive mineralisation front.

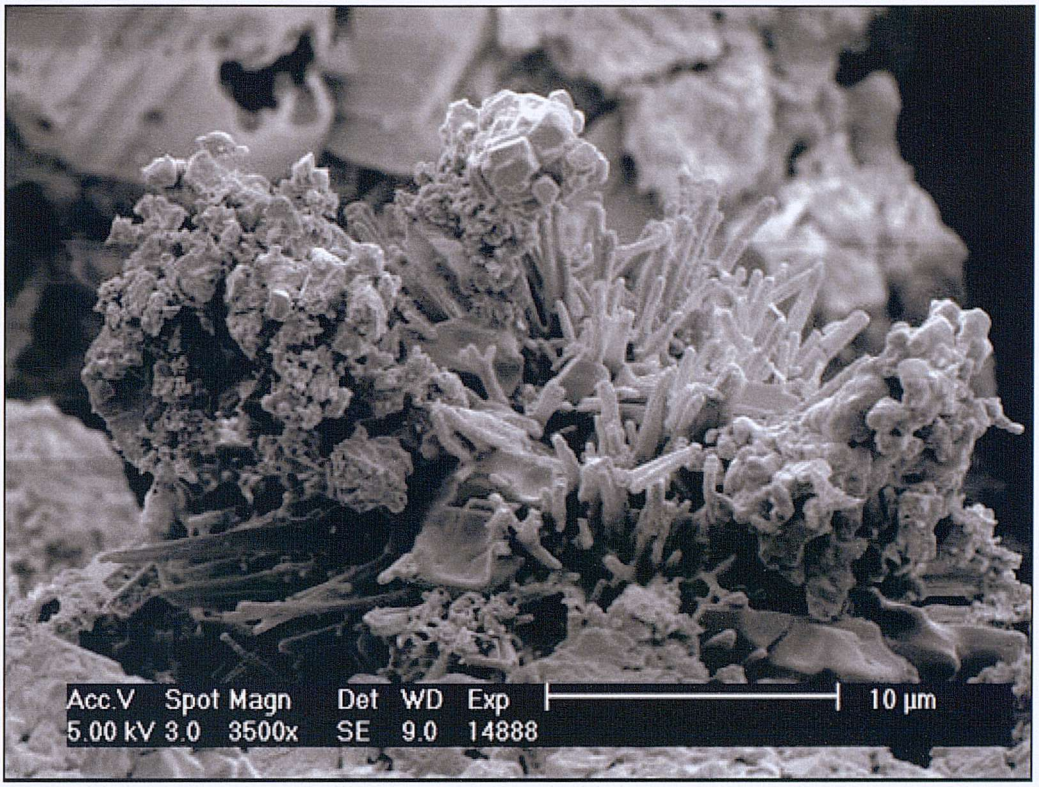

Figure 5.20a – An aggregation of small (<1µm) filaments located between two tube interlayers. These filaments can be seen to be intimately associated with a poorly crystalline mineral aggregation.

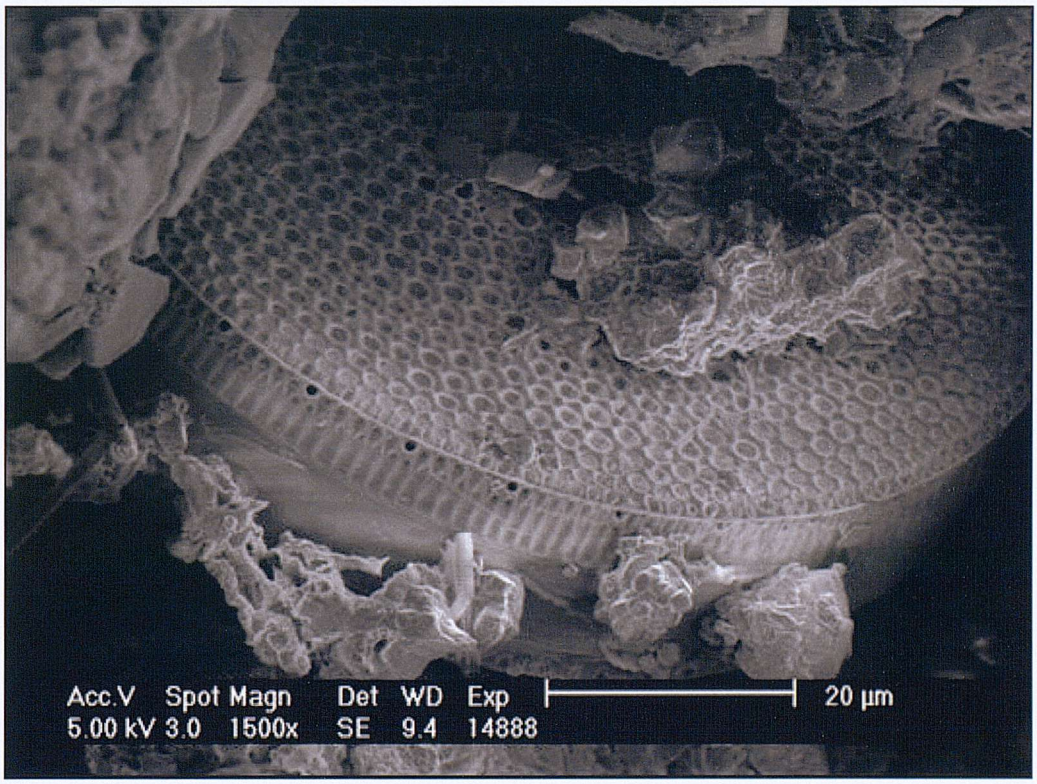

Figure 5.20b – An individual diatom can be seen lodged at the juncture between two individual tube layers.

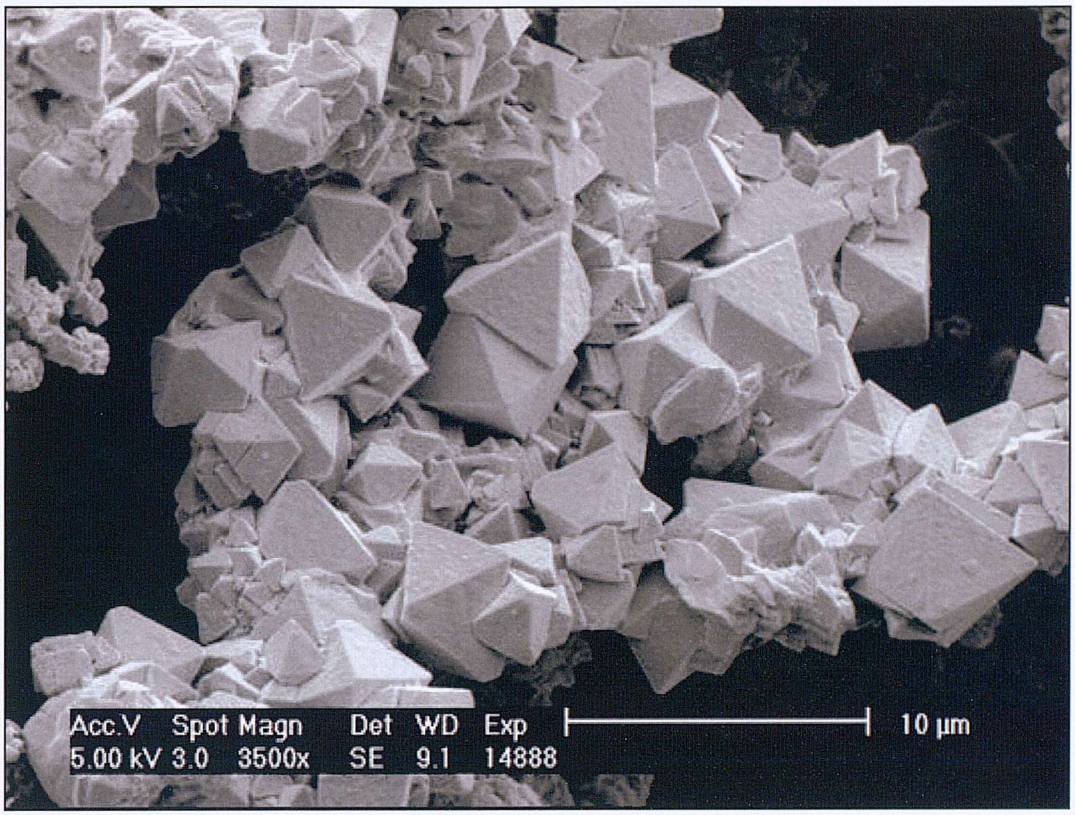

Figure 5.21a – Euhedral pyrite crystals within the tube layers.

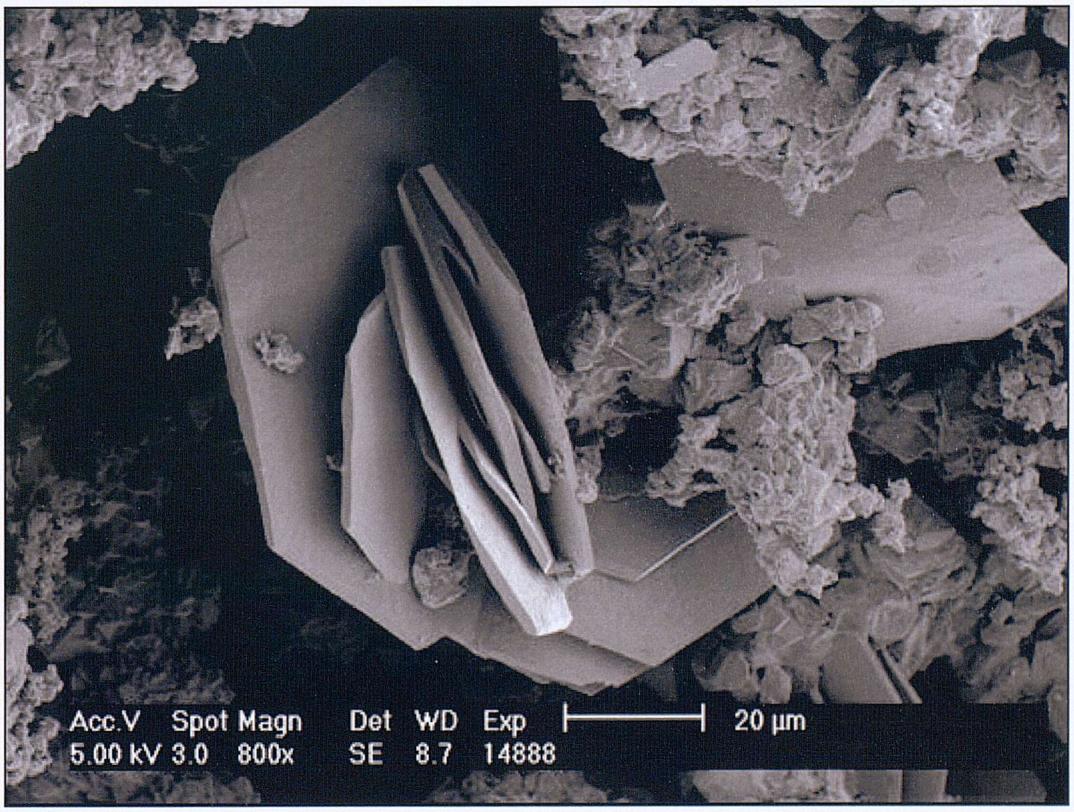

Figure 5.21b –Bladed barite crystals within the stockwork zone.

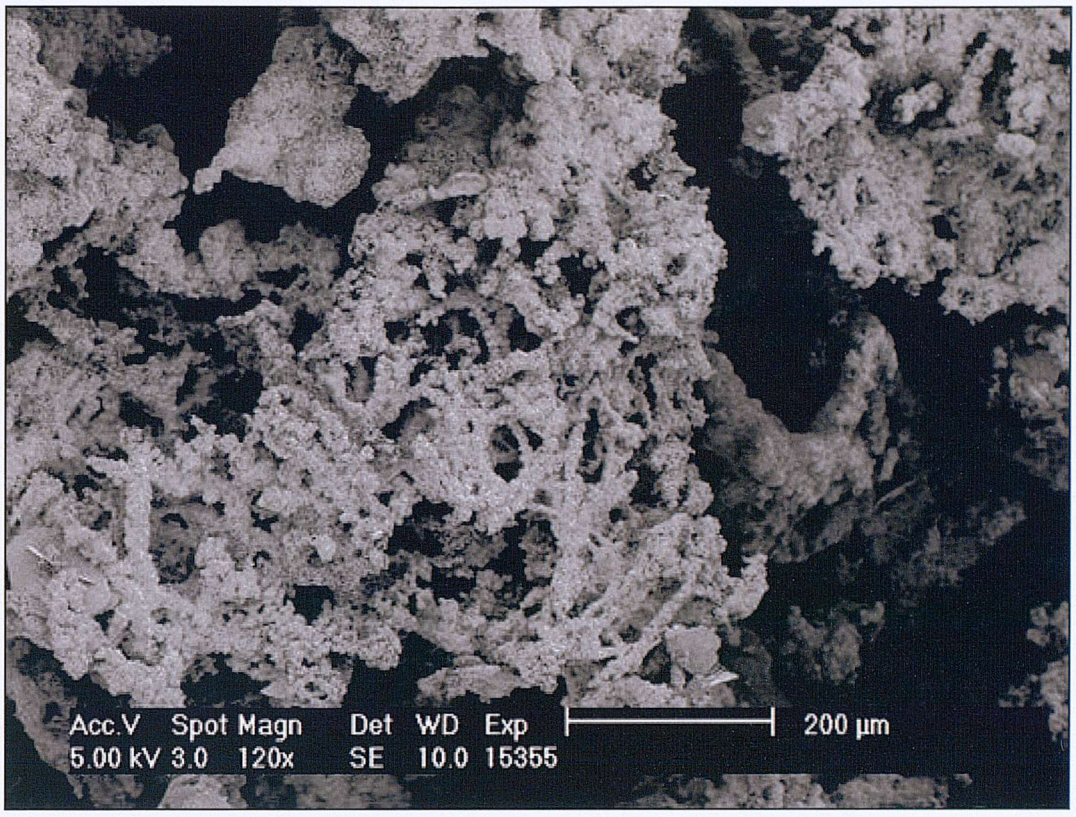

Figure 5.22a – Branching networks of sulphidised filaments within the stockwork zone.

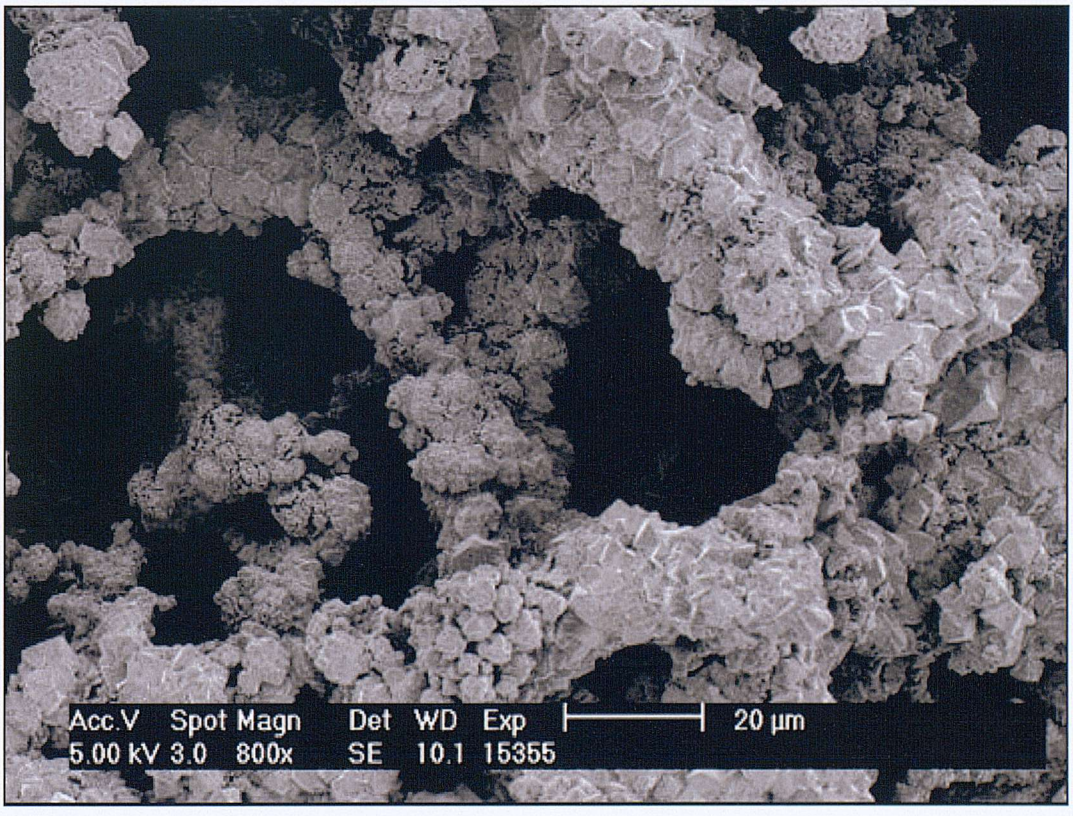

Figure 5.22b – Higher magnification view of branching networks show the individual filaments to be composed of euhedral sulphide crystals.

5.3.4 - Sulphur isotopes

$\delta^{34}S$ of 16 sulphide phases analysed within the tube wall sulphides (n=9), and the stockwork sulphides (n=7) is in the range +3.8 – +10.7‰ (Δ = 6.9‰), with a mean value of +7.3‰: Table 5.5). No other published isotope study of mid-ocean ridge sulphides have yielded isotopic values as heavy as those from this study (Figure 5.23), indeed some of these data are the heaviest of any East Pacific Rise vent areas, and amongst the heaviest from any deep ocean vent site. Mean $\delta^{34}S$ values for the dominantly pyrite-rich sulphides within the tube wall are +8.5‰, and for the dominantly chalcopyrite-rich stockwork sulphides are +5.8‰, a difference of 3.0‰. The average values generated for the two different tubes studied (EPR 99 01A, mean $\delta^{34}S$ = +8.75‰; EPR 99 02A, mean $\delta^{34}S$ = +7.08‰) also show a significant difference between the values (1.67‰).

The range of $\delta^{34}S$ data from this study (Δ=6.9‰), is similar to sulphur isotope data generated independently, by Marchig *et al.* (1997: Δ=6.1‰) for the same sample location (Table 5.6). However, it is apparent that the mean values from this study are substantially heavier than those in the earlier study ($\delta^{34}S$ = +7.5‰ and +4.3‰ respectively). This is further exemplified by considering the mean value for tube wall pyrite of +8.8‰, which compares to +4.0‰ for pyrite in the Marchig *et al* (1997) study. Figures 5.24a – c show histograms for the frequency distribution of $\delta^{34}S$ data for sulphides measured in this study and the sulphides from Marchig *et al.* (1997).

Chimney	Sample	Tube wall (Py) $\delta^{34}S$	Stockwork (Cpy) $\delta^{34}S$
402 G	EPR 99 02A	8.1	
402 G	EPR 99 02A	9.4	
402 G	EPR 99 02A		5.8
402 G	EPR 99 02A	6.9	
402 G	EPR 99 02A	8.3	
402 G	EPR 99 02A	8.8	
402 G	EPR 99 02A	8.2	
402 G	EPR 99 02A	8.2	
402 G	EPR 99 02A		7.8
402 G	EPR 99 02A		3.9
402 G	EPR 99 02A		5.8
402 G	EPR 99 02A		3.8
402 G	EPR 99 01A	10.6	
402 G	EPR 99 01A	10.7	
402 G	EPR 99 01A		7
402 G	EPR 99 01A		6.7

Pyrite Summary Stats		*Chalcopyrite Summary Stats*	
Mean	8.8	Mean	5.8
Standard Deviation	1.2	Standard Deviation	1.5
Range	3.8	Range	4
Minimum	6.9	Minimum	3.8
Maximum	10.7	Maximum	7.8
Count	9	Count	7

Table 5.5.- $\delta^{34}S$ values for spot analyses of tube wall and stockwork sulphides, and data summary table.

Chimney	Position	Bulk sulphide $\delta^{34}S$	Py $\delta^{34}S$	Sph $\delta^{34}S$	CPY $\delta^{34}S$	CPY & Sph $\delta^{34}S$
402 G	2d/1		+3.05	+3.38		
402 G	2d/2		+1.36			
402 G	2d/A	+2.82		+2.74		
402 G	2d/C	+2.89	+3.12			
402 G	2d/E	+2.84	+3.95			+2.58
402 G	2d/F		+3.4	+3.01		
402 G	3a/1		+4.07		+4.24	
402 G	3a/2		+2.93	+4.76		
402 G	3a/3		+3.49		+3.57	
402 G	3a/4			+3.84		
402 G	3a/A	+3.68	+4.14	+3.39		
402 G	3a/B	+5.15	+4.87	+3.32		
402 G	3a/C	+3.80	+4.22			+3.14
402 G	3a/D	+8.94	+4.84			+3.62

Table 5.6.- $\delta^{34}S$ for bulk sulphides and mineral separates (data from Marchig *et al.*, 1997).

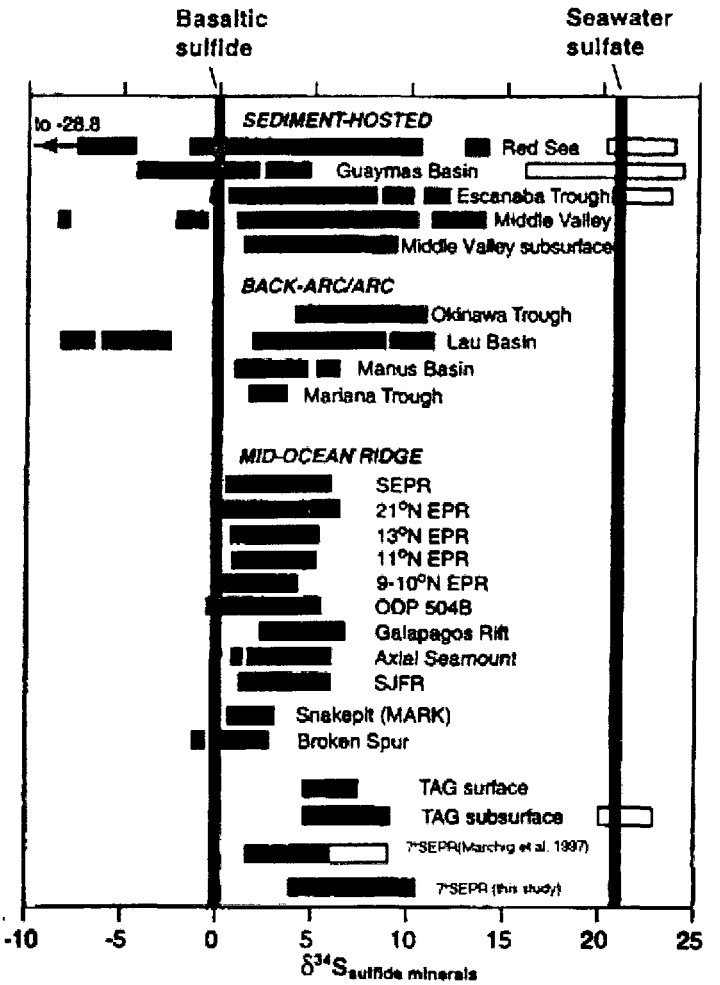

Figure 5.23 – Sulphur isotope values of sulphide minerals from various seafloor hydrothermal deposits. Modified from Herzig *et al.* 1988 and Shanks (2001) with additional data from this study and Marchig *et al* (1997).

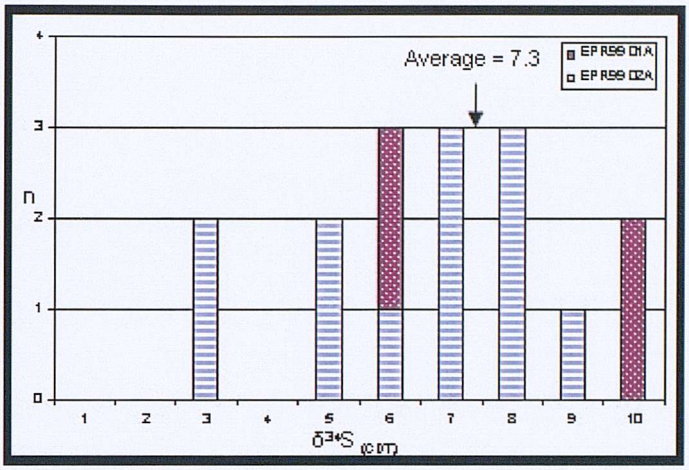

Figure 5.24a – Histogram representing the distribution of $\delta^{34}S$ values from samples EPR9901A and EPR9902A.

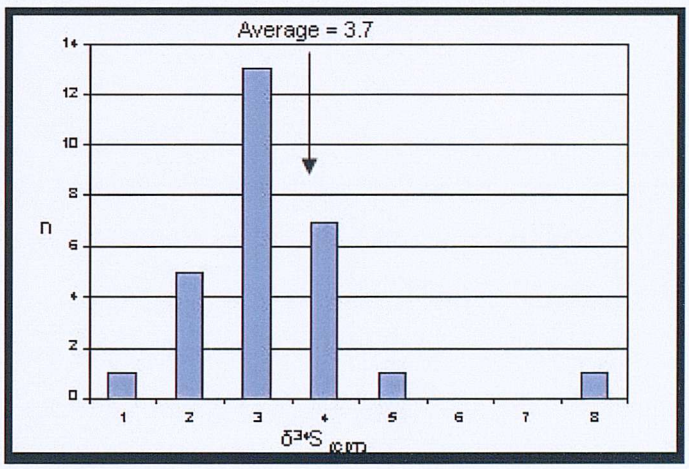

Figure 5.24b – Histogram representing the distribution of $\delta^{34}S$ values determined by Marchig *et al.*,1997 for sulphides recovered from inactive chimneys at 7°S EPR.

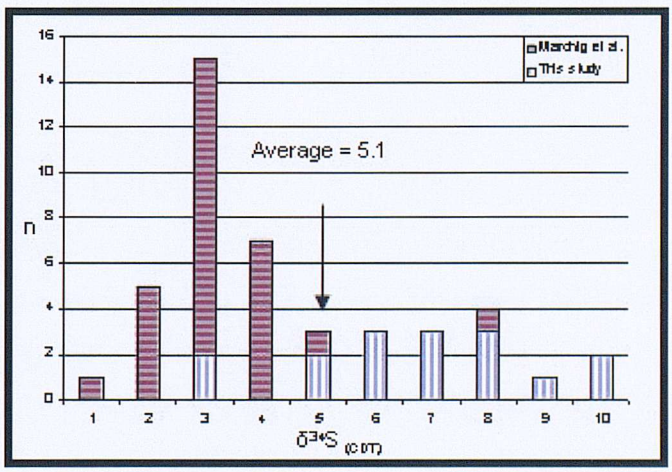

Figure 5.24c – Histogram displaying the combined $\delta^{34}S$ values of sulphides from 7°S EPR (this study and Marchig *et al.*, 1997).

5.4- Discussion.

5.4.1 - Tube identification

Biogenic tube structures have been observed associated with various chimneys located at vent sites on the East Pacific Rise (Desbruyères, *et al.*, 1985; Tunnicliffe & Juniper, 1990; Juniper *et al.*, 1992a; Chevaldonné & Jollivet, 1993; Juniper & Martineu, 1995), and fossil tube structures described from a number of locations (see Chapter 2). However, because of the dynamic paragenesis associated with hydrothermally active locations, the seemingly simple identification of organic tube structures can be rendered extremely difficult, and the taxonomic identification of specimens often impossible. As such, it is possible to envisage how the identification of mineralised biogenic structures, within walls of hydrothermal chimneys can be overlooked or misidentified.

The tube structures identified here, show remarkable similarities to the *Alvinella pompejana* dwelling tubes described in Chapter 4. They are roughly circular, with a concentric layered structure, and have dimensions comparable to those described by other authors (e.g. Desbruyères *et al.*, 1983; 1985; 1997; Gaill & Hunt, 1987; 1994; Zbinden *et al.*, 2001, 2003). SEM observations reveal textural features along individual laminae, which form branching, dendritic structures, growing towards the inner-surface of the tube (e.g. Figure 511b). These branching structures are inferred to be the annealed remnants of the microbial moulds seen in the interlayered marcasite horizons described from alvinellid tubes in Chapter 4 (e.g. Figure 4.9).

Using HFSEM to attain even higher magnification, a sinusoidal fabric can be seen (Figure 5.19) preserved within the pyrite crystals, which is attributed to mineralisation of the original organic tube wall material. Figure 5.19b shows a diatom preserved within the layered remains of the tube wall. Although planktonic in life, diatoms can often end up at the seafloor due to fall out from the photic zone as 'marine snow', and in this case the diatom would appear to have adhered to the sticky integument of a Pompeii worm, during an excursion from the dwelling tube, and then later become incorporated into the tube wall, during an episode of tube building.

Possibly the most convincing argument for tube structures being of biological origin is the presence of interlayered pyrite and marcasite structures (Figure 5.12b). Again, these structures are analogous to the interlayered structures observed in Chapter 4, and although much remineralisation, and re-equilibration appears to have taken place throughout the tube structure (Figure 5.12b – f), primary textural features are still distinguishable.

Although no specific taxonomy can be ascribed to the tubes here, it is speculated that they are most likely *Alvinella* sp. dwelling tubes, based on morphological characteristics, locality and chimney proximity.

5.4.2 - Mineralisation and paragenesis

Unlike the proposed models for black smoker chimney growth (Haymon, 1983 etc.), where evolution of the chimney wall progresses in controlled stages, many of the mineralisation processes occurring within the walls of the tube structure appear to have proceeded within similar time scales which is evident from the intermixed mineral phases, and thus makes the paragenetic sequence difficult to resolve.

Petrographic investigations show at least three stages of sulphide mineralisation occurring within a single tube structure. It is clear from the mineralogical textures observed within the tube wall (Figure 5.12 a – f) that a considerable amount of recrystallisation and re-equilibration has taken place, which is likely to be due to dynamic variations in temperature and fluid flow.

Gross mineralogy within the tube wall structure is depicted by XRD (Figure 5.13) which indicates the dominant presence of pyrite, lesser chalcopyrite, and minor marcasite. XRD data are also consistent with petrological estimates of tube wall mineralogy (Table 5.1). The marcasite / pyrite phase (PY-1) is inferred to be the same mineral phase observed to develop along the microbial horizons, which formed the boundaries between successive organic layers of *Alvinella pompejana* dwelling tubes (described in Chapter 4). Here it can be seen that the microcrystalline, colloform py/ma phase (PY-1) has undergone authigenic growth to idiomorphic pyrite (PY-2: Figure 5.12b).

Recrystallisation of PY-1 to PY-2 often occurs on the outer edges of the mineralised horizons (Figure 5.12e), to form a zonal, or progressive replacement front, which is likely due to re-equilibration and modification of the metastable primary py / ma mineral phase. However, subsequent overgrowth of PY-2 forms a significant multi-layered mineral structure throughout the tube wall replacing the original organic layers, through growth over a biogenic mineral template (PY-1).

Mechanisms for the formation of pyrite have been discussed previously (Chapter 4). Pyrite can precipitate from hydrothermal fluids over a wide temperature range (~25 – 250°C), which has been calculated from previous studies based on direct vent measurements and fluid inclusions of vent sulphides (Murrowchick & Barnes, 1986; Koski *et al.*, 1984; Hannington & Scott, 1988; Paradis *et al.*, 1988; Koski *et al.*, 1994).

One mechanism for pyrite (PY-2) precipitation is the interaction of (Fe-rich) hydrothermal fluids, which percolate through the tube wall and react with sulphur compounds, and polysulphides generated from decaying tube wall material (Equation 5g; Paradis *et al.*, 1988). Alternative sources of polysulphide compounds arise from mixing of reduced and oxidised sulphur compounds:

$$7H_2S + H^+ + HSO_4^- \rightarrow 4H_2S_2 + 4H_2O \qquad (5g)$$

Textural evidence for diagenetic alteration of minerals within the tube wall can be seen in Figure 5.12f, where 'bird's eye' textures have formed. Bird's eye replacement textures are associated with the alteration of pyrrhotite minerals to a fine-grained mixture of pyrite and marcasite, which in this case, has remineralised further to form fine-grained chalcopyrite (CPY-1), which in-turn has recrystallised to CPY-2. Precipitation and diagenetic alteration of metastable sulphide complexes is a good indication that the sulphide minerals precipitated are not in equilibrium with the mineralising fluids.

Chalcopyrite (either as CPY-2 or CPY-3) is present throughout the tube wall, where it has replaced existing Fe- and Zn-sulphide minerals (Figure 5.12d-e), forming initial 'caries', and later, more extensive 'atoll' corrosion textures. EMP mapping, and EMP scan line traverses indicate that chalcopyrite forms most extensively on the outer

layers of the tube, by replacing the existing pyrite horizons. Figures 5.15 demonstrates that at the inner boundary, a high proportion of chalcopyrite can be seen in the stockwork mineralisation, which is beginning to form over the inner pyrite layers. Whereas, at the outer tube boundary (Fig. 5.16), Cu-rich sulphides have almost completely replaced the pyrite layers. The EMP scan line traverses (Figures 5.17a-e) also indicate that the outer pyrite layers are preferentially replacing the layers within the middle of the tube structure. This is probably due to the infiltration of Cu-rich fluids being restricted by low permeability caused by the precipitation, and consequent annealing of pyrite in the tube wall. The older, outer layers of Alvinellid tubes are known to be more porous, despoiled, and blistered (Gaill & Hunt 1987; 1991), and therefore are likely to exhibit porous behaviour, even after primary mineralisation has taken place, whereas the inner, and relatively younger layers of the tube have a more consolidated organic structure, are therefore more likely to only allow limited fluid movement after pyritisation.

Although direct nucleation of chalcopyrite has been identified in hydrothermal systems (Morimoto & Ohmoto, 1991), the precipitation of chalcopyrite commonly occurs *via* replacement of a pre-existing sulphide mineral such as pyrite. The favoured mechanism of replacement over direct nucleation is principally due to the difference in valency between Cu^+ and (for example) Fe^{2+}. Copper in hydrothermal solution is typically transported as copper (I) chloride which has a valence of +1, whereas the copper in chalcopyrite has a valence of +2. Therefore a mechanism of oxidation is required to form chalcopyrite from Cu^+, Fe^{2+}, and H_2S in solution. Examples of some typical replacement reactions are as follows (Equations 51 – n):

$$Cu^+ + FeS_2 + {}^1/_2\ H_2 \rightarrow CuFeS_2 + H^+ \quad (51)$$

$$2Cu^+ + Fe^{2+} + FeS_2 + 2\ ZnS \rightarrow CuFeS_2 + 2\ Zn^{2+} \quad (5m)$$

$$Cu^+ + FeS + H_2S \rightarrow CuFeS_2 + H^+ + {}^1/_2\ H_2 \quad (5n)$$

Chalcopyrite makes up around 85-90% of the stockwork mineral suite, with minor contributions from pyrite, sphalerite, barite and silica (Table 5.2). Chalcopyrite is either formed as medium- coarse grained (up to 150μm), well crystallised, euhedral idiomorphic

crystals, or fine-grained (<25μm) anhedral aggregates, which may also form dendritic networks (Oleander texture described by Marchig *et al.* 1997: Figures 5.22a & b). Idiomorphic pyrite is present within the suite of stockwork minerals, and is estimated to form no more than 10% of the total assemblage. Generally, good euhedral crystals characterise the stockwork pyrite, which appears to infill the gaps and pore-spaces within the chalcopyrite mass, or can occasionally be observed as discrete aggregates of crystals, or single crystals adhering to proximal areas of the outer tube boundary. There appears to be only a minor degree of replacement of the stockwork chalcopyrite by pyrite. Replacement of this type is likely to be indicative of precipitation during the waning stages of hydrothermal activity, after the higher temperature precipitation of chalcopyrite from hydrothermal solution.

Hannington & Scott (1988) tabulated data estimating the conditions of pyrite deposition, at various hydrothermal locations (Table 5.7), which suggested that pyrite could be precipitated over a wide range of temperatures (100 – 405°C: with all 5 sites falling with the range 224 – 355°C). From previous work (Chapter 4) it is acknowledged that py/ma can form within the tube lamina at temperatures of between 20 – 81°C (Cary *et al.*, 1998: mean temp = 50.5°C). Chalcopyrite mineralisation is recognised to have a lower limit of approximately 270°C for precipitation at vent sites (Hannington *et al.*, 1995: Table 5.8). Therefore it can be envisaged that the paragenetic sequence of events responsible for these sulphidised tube structures occurred over a broard temperature range, with the mineral suite evolving as the local temperature increased from 50°C to in excess of 270°C.

	Axial Seamount (1)	21°N EPR (2)	Explorer Ridge (3)	Southern Juan de Fuca Ridge (4)	Endeavour Ridge (5)
pH	5.0	3.6	4.6 – 5.0	3,2	-
T°C	235 – 250	355	276 – 306	224 – 284	100 - 405
Log aO_2	-36	-31	-34	-38	<-31
Mineral	Py	Py +/- Po	Py	Py +/- Po	Py +/- Po

Table 5.7 – Estimated conditions for pyrite precipitation at selected polymictic sulphide deposits. (adapted from Hannington & Scott, 1998).

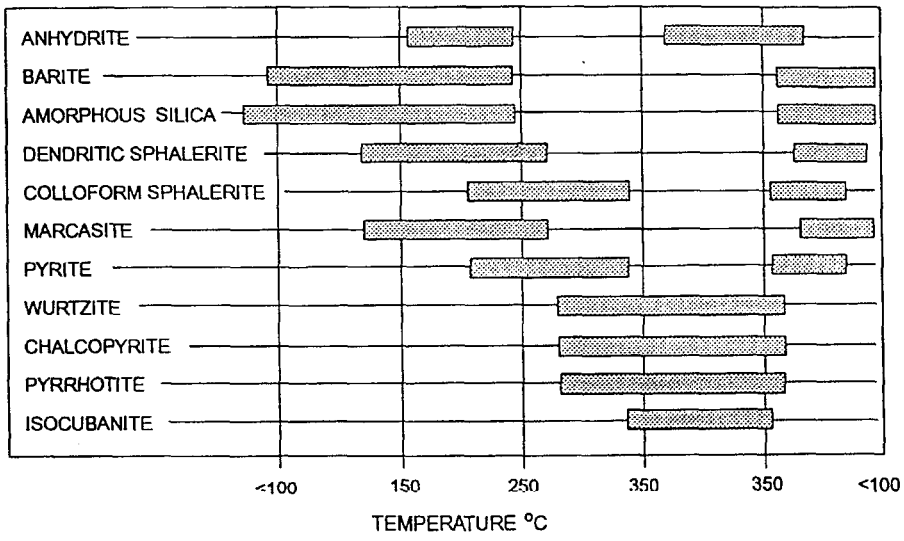

Table 5.8 - Hypothetical mineral paragenesis for a sulphide-sulphate-silica chimney. (after Hannington 1995).

From the textural and geochemical observations discussed above, a paragenetic sequence can be formulated:

1. Initial interlayered pyrite and marcasite horizons (PY-1) began formation during the lifetime of the host alvinellid worm, as mineralised moulds around trapped microbial laminae (*cf.* Chapter 4). Trapped inorganic sulphide particles, also formed discrete precipitates due to nucleation of percolating fluids (e.g. SPH-1) and the paramorphic degradation of metastable components such as pyrrhotite, to micro-grained pyrite and marcasite.

2. Replacement, and overgrowth of PY-1 by euhedral pyrite (PY-2) proceeded, probably due to increasing temperature and fluid flow rates, to form overgrowth and consolidation of the thin mineralised inter-layers to form thick Fe-sulphide bands throughout the tube (Figure 5.12a), causing reduced permeability, and consequently inhibiting fluid flow through the tube structure.

3. Chalcopyrite precipitation ensued by replacement of the Fe- and Zn-sulphides within the tube, as local temperatures increased significantly, probably due to the progressive growth of the sulphide chimney, or modification of the fluid flow channels within the hydrothermal mound. The production of atoll textures within the tube have occurred where replacement by CPY-2 was incomplete. Permeability within the tube structure is believed to have been inhibited by the precipitation and growth of PY-2, as the bulk of CPY replacement only occurs near the outer margins of the tube, and only extensively in the older layers. Fine-grained chalcopyrite (CPY-1) is also replaced by CPY-2. The bulk chalcopyrite (CPY-2 and CPY-3)in the stockwork zone has presumably proceeded by replacement of earlier Fe- and Zn- sulphides and direct nucleation.

4. High temperature precipitation of CPY-2 and CPY-3 would have continued to form the stockwork zone, whilst thermodynamic conditions, and fluid flow continued at sufficient rates, but as temperatures began to fall during the waning stages of hydrothermal venting, idiomorphic pyrite has precipitated in the network

of pore-spaces and cavities left within the stockwork chalcopyrite. Little or no replacement is observed in this late pyrite mineralisation.

5. Finally, where temperatures were sufficiently low, and seawater entrainment sufficiently high, the precipitation of minor barite and silica has begun in the stockwork zone.

5.4.3 - Geochemistry

When comparing bulk geochemical and microprobe spot analyses for highly spatially variable systems such as hydrothermal chimneys there are often significant differences for analyses made on the same samples. Although Marchig *et al.* (1997) describe their samples as relatively Si-rich, in the material studied here the mean wt% Si (n =400 is 0.288%: range of values = 0.00 - 16.009 wt% / only 4.25% of points are above 1.00wt % Si: 16.75% are above 0.1wt%) for the microprobe analyses on the tube material. Although spot analysis show Si to be relatively low, elemental maps for Si (not shown) show that discrete aggregates (5 – 15μm) of silica are occasionally observed in the stockwork zone and are therefore inferred to be associated with the later stage mineralisation

Nanocrystalline zinc-iron sulphide $(Zn_{0.88}Fe_{0.12})S$ minerals have been found within tubes of *Alvinella pompejana*, collected at 9°N on the East Pacific Rise. The zinc-iron sulphide nanocrystals were grouped in submicrometer-sized clusters which form layers, concentrically to the proteinaceous tube axis. Such layers of nanocrystalline zinc-iron sulphide minerals are valuable markers of annelid tubes (Zbinden *et al.*, 2001). Marchig *et al.* (1997) measured bulk Zn contents of x-y % within their chimney samples but most of the microprobe measurements demonstrate that sphalerite is a minor phase within the tube walls of the samples analysed in this study.

5.4.4 - Sulphur isotopes

Sulphide minerals and their parent hydrothermal fluids rarely attain equilibrium in active hydrothermal systems (Bluth & Ohmoto, 1988; Shanks, 2001). If the Fe- and Cu-sulphides within the tube structures were in equilibrium, it would be possible to determine the temperature of mineral precipitation. By plotting the equilibrium fractionation of chalcopyrite and pyrite in aqueous ore forming systems (Figure 5.25), a value can be calculated. Using the mean $\delta^{34}S$ value (+8.8‰) of pyrite in the tube, and the mean $\delta^{34}S$ value (+5.8‰) of chalcopyrite in the stockwork zone, a formation temperature of 135°C is calculated. Because chalcopyrite is known to precipitate from solution at temperatures above ~270°C (Hannington *et al.*, 1995), the calculated formation temperature appears unfeasible, and that the system is therefore in disequilibrium. If pyrite and chalcopyrite were precipitated in equilibrium at temperature of 270°C, then it would be expected that $\delta^{34}S$ values for pyrite should be +1.58‰ heavier than chalcopyrite precipitated from the same fluid, due to the equilibrium isotopic fractionation factors (Figure 5.26). However, the calculated difference between mean values for chalcopyrite (5.8‰), and pyrite (8.8‰) is 3.0‰) strongly suggests that there is disequilibrium within the system.

Speciation of cations in fluid/sulphide systems is very complex, and highly dependant on oxygen fugacity and pH (Faure, 1987). The extent of sulphur isotopic fractionation is controlled largely by this speciation, more especially oxygen fugacity, with the most extreme fractionations resulting when oxidised species become significant (Ohmoto, & Rye, 1979. For instance, in magmatic systems the $\delta^{34}S$ value of pyrite precipitating from a vent fluid where $\delta^{34}S = 0$ ‰, can vary between +5 ‰ and -27‰ due to variable oxygen fugacity and pH conditions. Hannington *et al.*, (1995) have demonstrated that oxygen fugacity is relatively low in typical hydrothermal vent systems, and Murrowchick & Barnes (1986) reported that marcasite is likely to be precipitated in more acidic solutions (pH = <5) than pyrite (pH = >5). Since (at least initially) both pyrite and marcasite are precipitated within the tube structure, it can be assumed that the pH of the local tube environment would be around 5. These described conditions would not cause a great deal of fractionation from the end-member vent fluid, and therefore would not be conducive to producing the range in $\delta^{34}S$ values observed here.

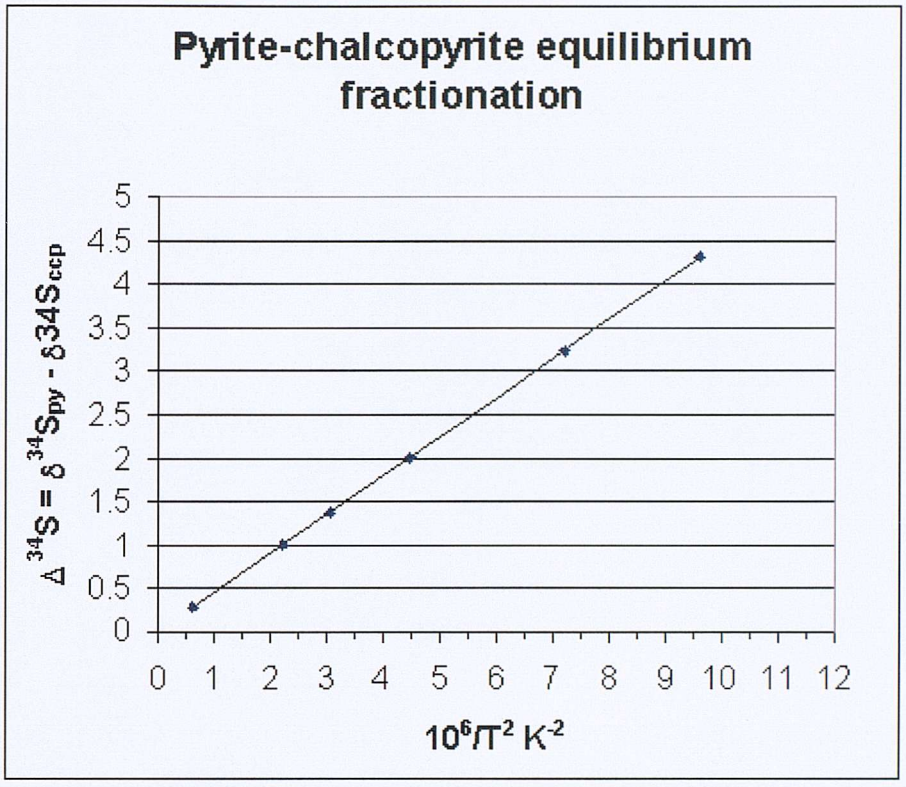

Figure 5.25 – Pyrite – chalcopyrite equilibrium fractionation fraction

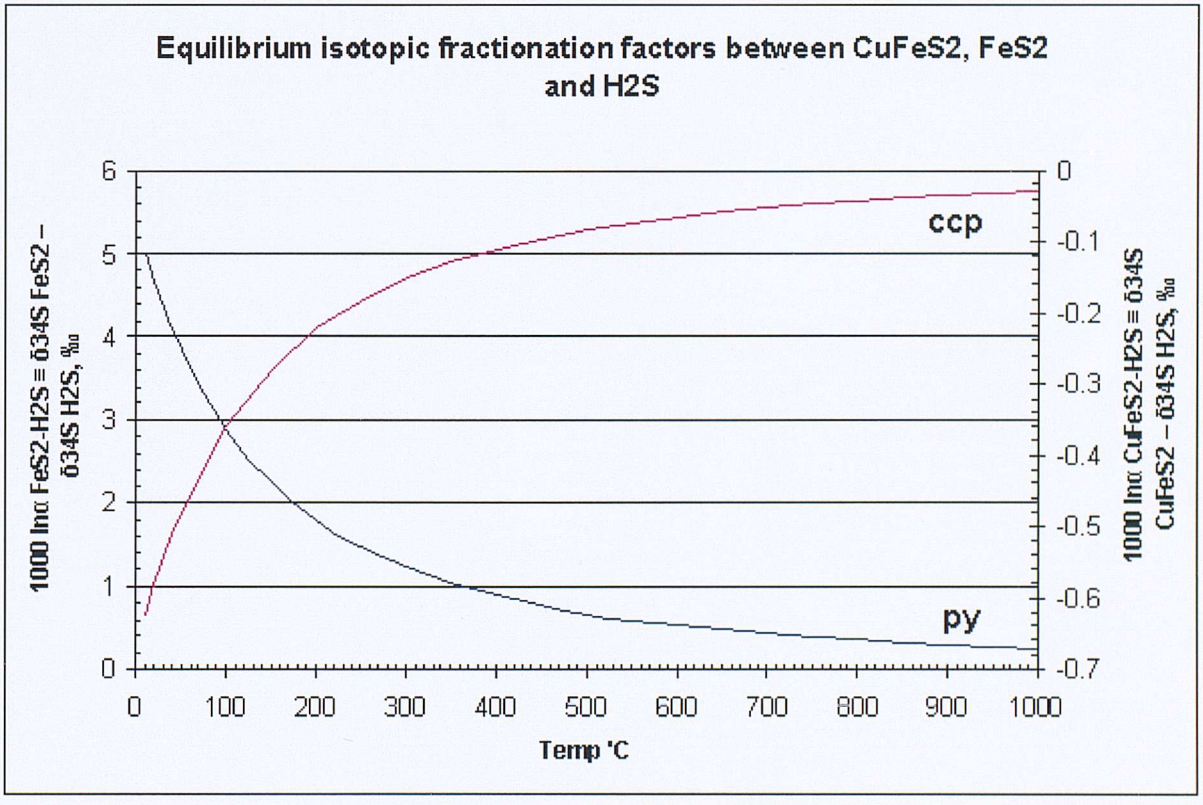

Figure 5.26 – Equilibrium fractionation factors between chalcopyrite, pyrite and hydrogen sulphide

The relatively heavy $\delta^{34}S$ values observed in this study could be attributed to a number of scenarios that will be discussed in turn:

1. Physical mixing of sulphide and sulphate phases within the tube wall. Inclusion of minor amounts of sulphates (e.g. barite) in the sulphide.
2. Entrainment of seawater locally into the hot hydrothermal structure, reduction of sulphate and mixing with the hydrothermal fluid.
3. Microbial processes in micro-reducing environments associated with the worm tube.
4. Production of isotopically heavy polysulphide species locally enhancing pyrite nucleation.

1. Physical admixtures of barite (and/or anhydrite) and pyrite (during the entrainment of seawater into hydrothermal fluid) can be ruled out as a process for producing heavy $\delta^{34}S$ in the tube wall sulphides, simply by using an isotope mass balance equation for the mixing of barite and pyrite (Results: Figure 5.26). It should be noted here that the ratio of sulphur in pyrite (FeS_2) to barite ($BaSO_4$), is 2 : 1 per mole, and therefore not a simple linear mix. Using the mean $\delta^{34}S$ value (4.3‰) for all of the sulphides measured by Marchig *et al.* (1997), and the mean $\delta^{34}S$ value for tube sulphides measured in this study (8.8‰), and assuming the $\delta^{34}S$ value of barite in seawater is 21‰, the ratio of mixing can be calculated to be 55 : 45 (Figure 5.27). Therefore, from this calculation, 55% barite would have to be present in the sampled sulphide to produce isotopic fractionation values of +8.8‰. However, petrographic investigations indicate that sulphate species are very much a minor component of the tube wall structure, ruling out this scenario as a realistic cause of the observed isotopic variations.

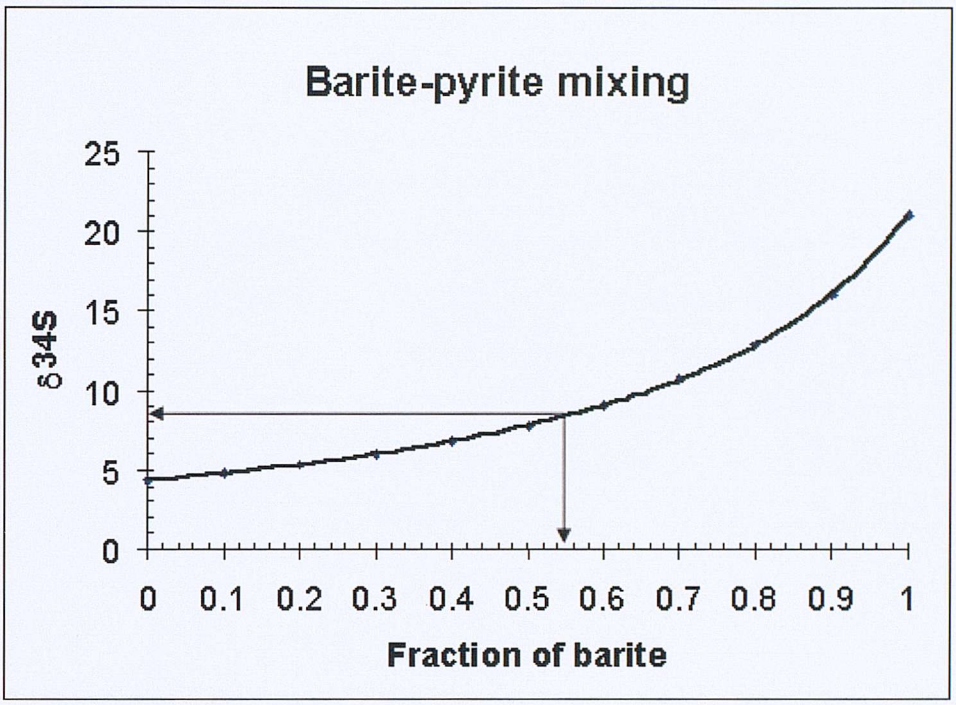

Figure 5.27 – Isotopic shift due to the physical mixing of pyrite (vent derived) and barite (seawater derived)

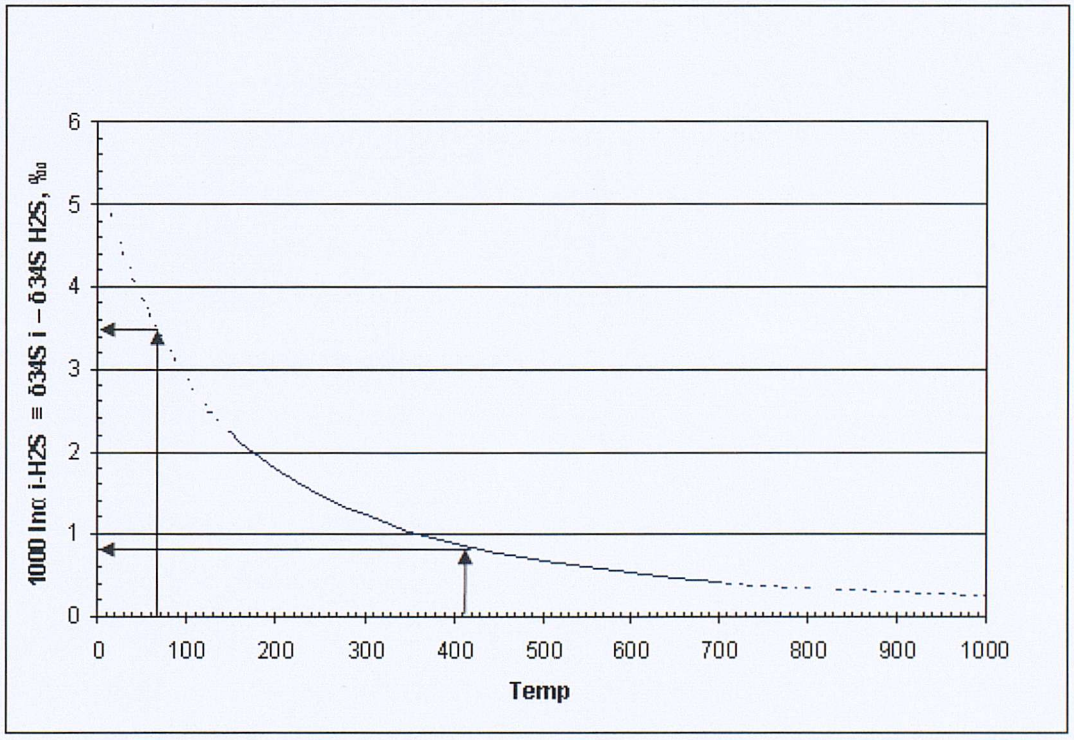

Figure 5.28 – Equilibrium isotopic fractionation factors between FeS_2 and H_2S

2. The obvious source of isotopically heavy sulphur is seawater, which is locally entrained into basement, chimneys and mound structures and reduced at temperatures ~250°C. The annelid *Alvinella pompejana* is probably the most heat-tolerant metazoan organism known. Previous results have shown that the level of thermal stability of its interstitial collagen is significantly greater than that of coastal annelids and of vent organisms, such as the vestimentiferan *Riftia pachyptila*, living in colder parts of the deep-sea hydrothermal environment. However the upper limits that these organisms can tolerate is approximately 105°C. The high thermal gradients associated with hydrothermal chimneys suggest that *Alvinella* spp. have developed behavioural responses to avoid heat (Shillito *et al.*, 2001). Therefore any inorganic SO_4 reduction must occur away from the dwelling tube. The sharp thermal gradients along chimney walls mean that the locale of any reduction could be 10's of cm from the dwelling tube.

Seawater entrainment and SO_4 reduction is observed to some degree at all sites of hydrothermal venting (i.e. $\delta^{34}S_{H2S}>\delta^{34}S_{MORB}$) but this cannot directly explain the extremely high values observed here, particularly in the biogenic pyrite phase associated with the tube wall. A mixture of vent fluid: seawater of 63:37 is required to generate the heavier $\delta^{34}S$ values observed (+10). This amount of seawater entrainment would cause a significant temperature drop (~220°C) and extensive sulphate precipitation. That the normal upper limit of hydrothermal sulphide $\delta^{34}S$ values is ~4-5‰, unless remobilisation of subsurface anhydrite is invoked, suggests that simple mixing cannot both reduce the seawater sulphate and still maintain conditions required for precipitation of the observed mineral assemblages (low $f(O_2)$, low SO_4, pH ~5).

3. Molecular characterizations of microbial communities from hydrothermal sites indicate the predominance of bacteria belonging to the epsilon subdivision of the Proteobacteria which can use sulphur lithoautotropically, either by means of oxidation or reduction reactions. These organisms have been observed in vent fluids and associated with alvinellid species. Optimal growth temperatures of the bacteria range from 41 to 45°C (Campbell *et al.*, 2001). Thiotrophic bacteria thrive only in aerobic conditions, and oxidise vent H_2S to liberate metabolic energy, whereas sulphate reducers are facultative anaerobes. Micro-reducing environments exist within the dwelling tube structure that allow these organisms to carry out chemolithoautotrophy.

The tube wall environment would be open with respect to SO_4, though locally there might be some closed behaviour (and therefore Rayleigh-type fractionation). Of the metabolic processes that utilise sulphur compounds, only the reduction of sulphate to sulphide can generate significantly remodelled $\delta^{34}S$ values (Kenniticutt *et al.*, 1992). Sulphur isotope data from vent animals (bivalves and vestimentifera) from 21°N EPR have shown that the thiotrophic oxidation of H_2S, within the tissues of vent fauna, and subsequent utilisation by the animals themselves, does not show any significant isotopic shift (Fry, 1983), and would therefore be produce isotopically similar $\delta^{34}S$ values to the parent sulphur compound. In contrast, if microbial sulphate reduction were an important process we would expect to see a wide range of $\delta^{34}S$ values which would be isotopically lighter than seawater. With open system kinetic fractionation during sulphate reduction the $\delta^{34}S_{py}$ would be –10 ‰ to –50 ‰ depending on temperature (Ohmoto and Goldhaber, 1997). If the system were closed on the microscale then locally much more positive values could be obtained. While it is possible for an open system to generate heavy values, such as those seen here, for such a system to keep generating similar values time and time again is unrealistic.

4. Two mechanisms of polysulphide generation have been discussed: breakdown of organic precursors (*cf.* Chapter 4) and mixing of oxidised and reduced species (Equation 5e). Both of these processes will produce sulphide species with $\delta^{34}S$ values that are intermediate between seawater SO_4 values and reduced sulphide values. The $\delta^{34}S$ value of the polysulphide species will depend on the $\delta^{34}S$ of the organic sulphur compounds, the fractionation factor associated with breakdown, the pH of the fluid and $f(O_2)$. None of these variables are well constrained but this proposed mechanism is thermodynamically feasible and consistent with observed measurements.

Assuming organic generation of polysulphides within the tube wall are responsible of pyritisation of the tube wall layers, then the $\delta^{34}S_{py}$ values could be highly variable. Organic sulphur identified within the tube layers of 'live' dwelling tubes (*cf.* Chapter 4) is likely a product of detoxification of the host worm's metabolic system, which has shifted excess sulphur compounds into the tube by producing mucus as a by-

product. Because the biological pathways that necessitate the detoxification of sulphur from the worm are likely to be complexed by associated microbial as well as metabolic routes, $\delta^{34}S$ values could be highly variable, but are likely to lie somewhere between seawater sulphate and vent fluid. Chapter 4 describes how decomposing microbial cells could produce polysulphides, and consequent marcasite precipitation, due to local manipulation of the geochemicstry. Here it is suggested that further decomposition of the organic tube material, and increased temperatures could also generate polysulphides suitable for pyrite precipitation, and consequent preservation of the tube wall layers.

If inorganic generation of polysulphides due to local reduction of seawater sulphate is to be assumed, then a $\delta^{34}S$ value for the generated polysulphide species can be calculated. As the $\delta^{34}S$ value of polysulphide species generated from reaction (6e) is dependant on the $\delta^{34}S$ value of the parent H_2S in the fluid, a suitable $\delta^{34}S$ value must be estimated. Ohmoto & Goldhaber (1997) have plausibly demonstrated that $\delta^{34}S$ of H_2S in vent fluids can be considerably higher (+ ~1.5 – 4.7‰, 9°N EPR: mean value = +3.1‰) than co-existing chimney sulphide precipitated from the same fluid. Therefore, using the mean $\delta^{34}S$ value for bulk sulphide at 7°N EPR (+4.3‰: Marchig *et al.*, 1997) an estimated minimum $\delta^{34}S$ value for vent fluid can be inferred as +5.8‰. This inferred minimum value seems reasonable, when compared to vent fluid $\delta^{34}S$ values from other vent sites (Figure 5.23) Using the equation (5i) the fraction of vent fluid needed to form polysulphides (and consequent pyrite/chalcopyrite at 270°C) can be found for the range of $\delta^{34}S$ values measured in the tube layers (Table 5.9).

$$R_{(meas)} = (R_{(vent)} * F_{(vent)}) + R_{(S.W.)} * (1 - F_{(vent)}) \quad (5i)$$

Where:

F = Fraction of fluid for a specific component

R = relative isotopic composition of a specific component

$R_{(meas)}$ [pyrite] (‰)	equl. Frac py (@270°C)	$R_{(calc)}$ (‰)	$R_{(vent)}$ (‰)	$R_{(S.W.)}$ (‰)	$F_{(vent)}$ (%)
6.10	**1.4**	7.5	*5.8*	*20.9*	88.74
7.50	**1.4**	8.9	*5.8*	*20.9*	79.47
7.50	**1.4**	8.9	*5.8*	*20.9*	79.47
8.00	**1.4**	9.4	*5.8*	*20.9*	76.16
8.10	**1.4**	9.5	*5.8*	*20.9*	75.50
8.20	**1.4**	9.6	*5.8*	*20.9*	74.83
9.40	**1.4**	10.8	*5.8*	*20.9*	66.89
10.56	**1.4**	11.96	*5.8*	*20.9*	59.21
10.73	**1.4**	12.13	*5.8*	*20.9*	58.08
				mean	**73.15**

Table 5.9 – The calculated fraction of vent fluid ($F_{(vent)}$) needed to generate the measured $\delta^{34}S$ values ($R_{(meas)[pyrite]}$) , at 270°C, observed in the samples EPR 99 01A & EPR 99 02A. (The value in column two is measured from Figure 5.27)

Stoicimetrically, for the inorganic generation of polysulphides (equation 5e), a minimum $F_{(vent)}$ of 87.5% would be needed for the reaction to proceed completely. However, from the range of values calculated for $F_{(vent)}$ (58.08 – 88.74%), this is not seen to be the case. Therefore it is suggested that a combination of organic and inorganic polysulphide generation is responsible for the relatively heavy $\delta^{34}S$ values observed within the pyritised dwelling tube layers. The evidence for which is summarised as follows:

1. Because the metabolic processes of the host Alvinellid worm are dominated by seawater rather than vent fluid (ie. the worm lives in an environment dominated by a large fraction of seawater over vent fluid), and thiotrophic metabolisation processes are known not to greatly influence $\delta^{34}S$ values, if organic polysulphide generation within the tube wall acted exclusively, then this would generate heavier isotopic values than those seen in the pyrite tube layers.

2. Although inorganic generation of polysulphides by reduction of seawater sulphate is perfectly feasible, some of the heavier $\delta^{34}S$ values observed in the pyritic tube layers would require seawater fractions of over 12.5%, which is stoicimetrically inhibited.

3. A marked difference of 2.82‰ between the mean $\delta^{34}S$ values for the tube wall sulphides in the two tube samples (EPR 99 01A: 10.65‰, and EPR 99 02A: 7.82‰), and a difference of 1.40‰ between the mean $\delta^{34}S$ values for stockwork sulphides in the two samples (EPR 99 01A: 6.82‰, and EPR 99 02A: 5.42‰), indicates that the local internal fluid flow (and therefore mixing processes) can cause significantly different $\delta^{34}S$ values in the precipitated sulphides.

The pyrite laminae preserved within the tube structures is an example of an organicly produced material become fossilised. Pyrite (PY-2) is formed over a biological template (tube wall organic layers), and by replacement of biologically facilitated py/ma precipitates (PY-1). Usually (as is demonstrated here in the stockwork zone), chalcopyrite replaces pyrite preferentially where thermodynamic conditions allow. However, the preservation of the tube layers by pyrite, with distinctively heavier isotopic values, have inhibited the total replacement of pyrite by, in turn, inhibiting fluid flow and porosity, after pyrite (PY-2) precipitation.

The fact that the $\delta^{34}S$ values for the chalcopyrite phases measured are different from the biogenic pyrite suggest that the chalcopyrite could, at least in part, form from a vent fluid H_2S precursor (Equation 5j):

$$Cu^{+} + Fe^{2+} + 2H_2S \rightarrow CuFeS_2 + 3H^{+} + \tfrac{1}{2}H_2 \qquad (5j)$$

or via a non-biogenic FeS precursor (Equation 5k):

$$Cu^{+} + FeS + H_2S \rightarrow CuFeS_2 + H^{+} + \tfrac{1}{2}H_2 \qquad (5k)$$

The $\delta^{34}S$ values measured in this study encompass the heaviest values sampled from any mid-ocean ridge environment to date (Figure 5.23). In fact, most of the individual $\delta^{34}S$ values measured from the stockwork matrix are heavier than those measured from other EPR vent sites. When the isotope data is compared to the values generated by Marchig *et al.* (1997) from the same sample site, it appears curious that the two data sets are so different (mean Δ= 3.2‰). However, close inspection of the data generated by Marchig *et al.* (1997) shows that one of their data points does show a heavy

$\delta^{34}S$ value (8.94‰), comparable to the values in this study. Marchig *et al.* (1990 & 1997) describe 'gel-like interlayerd pyrite and marcasite' in both their studies, however, the images they associate with this description in the earlier study (Marchig *et al.*, 1990: Figure 3a) show what appears to be a mineralised alvinellid tube (reminiscent of Figure 5.12a). This suggests that Marchig *et al.* (1997) may have inadvertently sampled a biogenic tube structure, which was misinterpreted as a chimney structure. If so, this indicates that biogenic structures, when heavily sulphidised, preserve an isotopic signature which could be used to identify them as fossils.

5.5 - Model for tube formation & conclusions

By combining mineralogical and sulphur isotope data, a model for the formation of fossilised biogenic tube structures can be produced:

1. New chimneys are rapidly colonised by Alvinellid polycheate worms, which build dwelling tubes which adhere to the outer walls of black smoker chimneys. During the life time of the worm, interlayered marcasite and pyrite horizons are formed, due to geochemically favourable conditions induced by Fe-rich vent fluid percolating through the tube walls, and the decomposition of microbial lamina trapped between the tube layers (*c.f.* Chapter 4).

2. Initially, replacement of the primary, biogenic pyrite/marcasite would progress as Fe-rich fluid, reacts with both polysulphides species generated from within the chimney walls, due to seawater mixing (Figure 5.28), and due to decomposition of the organinc tube wall layers.

3. As hydrothermal venting persists, the chimney structure builds upwards and outwards (e.g. Haymon, 1983; Tivey, 1995). Hydrothermal fluids migrate outwards, through the chimney walls, forming a sulphide replacement front which enables the local replacement of the anhydrite framework, with Zn- (and in this instance), Fe-sulphides. As mineralisation progresses, at any given point within the chimney wall, the temperature of the migrating fluids would increase, due to conduction though the tube wall, and improved thermal isolation from

seawater. Metastable compounds such as pyrrhotite degenerate into fine-grained pyrite and marcasite. As local temperatures within the tube wall reach 150 – 250°C pyrite (py-2) replacement of the PY-1 horizons, and of organinc tube layers would be nearing completion, and inadvertently restricting the porosity of the tube structure. Such elevated thermal conditions would also allow for the precipitation of a pyrite (Fe-sulphide) dominated outer stockwork zone.

4. Further increase of local temperatures (+270°C), heralds the onset of pyrite replacement by chalcopyrite. In the stockwork zone where porosity, and conduits allow effectively unrestricted fluid flow, chalcopyrite precipitation continues unchallenged. However, within the tube structure, pyritisation has reduced porosity sufficiently, to inhibit the total replacement of previously formed Fe- and Zn-sulphides by chalcopyrite. Thus, restricting chalcopyrite precipitation to only the older, outer portion of the tube, and a relatively small portion of the inner layers .

5. As hydrothermal fluid flow from the chimney edifice begins to decline, and local temperatures fall below ~270°C, conditions allow for pyrite precipitation within the pore spaces of the chalcopyrite stockwork zone. As temperatures decrease further, due to seawater penetration of the chimney, a suite of low-temperature, oxidised precipitates (e.g. silica and barite), can be expected.

Mineralisation associated with dissimilatory sulphate reduction in sedimentary environments includes pyrite (Bubela and McDonald, 1969; Trudinger et al., 1985), mackinawite (Benning et al., 2000) and greigite (Mann et al., 1990). Microbial communities from hydrothermal sites comprise both heterotrophs and lithoautotrophs which can use sulphur species (Campbell et al., 2001). Sulphate reducers are facultative anaerobes and the optimum temperature range is as wide as 38-68°C for heterotrophic S-reducers (Miroshnichenko et al., 2002) which encompasses a range that includes the periphery of active chimney structures. Dissimilatory sulphate reduction in hydrothermal environments is largely performed by heterotrophic organisms, particularly *Desulfovibrio desulfuricans* (Jøgensen et al., 1992; Trudinger et al., 1985).

Dissimilatory sulphate reducers exhibit a wide range in fractionation factors in experimental studies (Detmers et al., 2001) and large values (α=0.982) have been observed for cultured thermophiles (Bottcher, 2001). Micro-reducing environments exist within the Alvinellid dwelling tube structure that allow facultative sulphate reducers to metabolise sulphate (Desbruyeres et al., 1998). Figure 5.3 shows how the $\delta^{34}S$ composition of the sulphate and precipitated pyrite vary in a closed system as pyrite precipitation progresses. The range in $\delta^{34}S$ values observed in the tube samples (+6.1 to +10.7‰) is consistent with sulphide precipitation when 64-82% of the sulphate present has been removed. Rayleigh type fractionation of $\delta^{34}S$ is the only way to generate the observed values. The limited range in reaction progression (f=0.63-0.82) is partly an artefact of choosing a single fractionation factor for the reaction pathway and the homogenization of the micro-scale variability that occurs during analysis (~100 μm).

The pyrite laminae preserved within tube structures from the SEPR are examples of biomineralisation preserved in the fossil record. Pyrite is formed over a biological template (tube wall organic layers), and by replacement of biologically facilitated pyrite/marcasite precipitates. Dissimilatory sulphate reduction catalyses FeS_2 mineralisation and the heavy $\delta^{34}S$ signature of the remnant tube structures can be explained by Rayleigh type fractionation of S. Preservation of the tube layers by pyrite inhibits complete replacement with later stage chalcopyrite by restricting fluid exchange.

Chapter 6

Mineralisation in *Ridgea piscesae* tubes from two actively venting sulphide edifices, high rise vent field, Juan de Fuca Ridge.

Ridgea piscesae *Jones, 1985 is an ecosystem structuring organism, and amongst the most numerous (in terms of biomass and individuals) of vestimentiferan tube worm species present at North Eastern Pacific hydrothermal vent sites.* R. piscesae *build their tubes from a chitinous matrix, which provides adequate protection from predators, and allows the worm to maintain a close proximity to the venting fluid that it relies on for nutrition via its symbiotic bacteria within its troposomic tissue. Previous studies of* R. piscesae *tube growth has demonstrated that exceptionally high tube production rates and that these tubes are well preserved on relict hydrothermal structures and even preserved at fossil vent sites. New observations from samples studied here include micro-tubes (~50 μm length) associated with adult R. piscesae and a silicified mucus lining to inhabited worm tubes. The function of this mucus lining is discussed in relation to the mineralisation observed. Associated with the mucus lining is a ligament which runs along the inside of the tube, and is tentatively inferred to be a form of anchor, allowing the worm to rapidly retract into the tube when threatened.*

Optical microscopy, SEM, FT-IR and EMP analyses have been used to demonstrate that R. piscesae *can become fossilised during the life of the worm, in that their tubes are mineralised whilst still inhabited by the worm. The organic component of the worm tube is rapidly replaced by amorphous silica which undergoes dewatering to form opal-A. This mineralisation is then overgrown by barite laths, and microbially templated amorphous silica. The timing of mineralisation is well constrained from* in situ *observations of tube growth rates and leads to extensive silicification within the worm's life cycle. Silicate and sulphate minerals precipitate in the inter-tube spaces, to form a consolidated, yet porous mineralised matrix. With time, prograde mineralisation causes the further precipitation and consequent over printing of the primary mineral suite with iron- and zinc-sulphides. This process of sulphide mineralisation and replacement masks the original textural and geochemical components of the tube and allows the tube structure to be preserved in the sulphide mound talus associated with active vent fields.*

6.1 - Introduction.

6.1.1 – Physiology and ecology of *Ridgea piscesae.*

Vestimentiferan tubeworms, such as *Ridgea piscesae* Jones (1985) and *Riftia pachyptila* Jones (1981), are characteristic organisms associated with deep-sea hydrothermal vents. *R. piscesae* is one of the most abundant macrofauna observed at actively venting sites on the Juan de Fuca Ridge, Explorer Ridge, and Gorda Ridge (Urcuyo *et al.*, 1998; Holmes & Zierenberg, 1990). Clusters of *R. piscesae* may be seen growing gregariously at sites of diffuse fluid flow, at temperatures ranging between 2 – 35°C. This species can be characterised as a primary producer, due to its symbiotic association with internal, chemoautotrophic, sulphide oxidising bacteria (Urcuyo *et al.*, 1998). The trophosomal tissue of the *R. piscesae* worm is densely saturated with intracellular bacteria. These bacteria are intimately associated with the vestimentiferan blood vessel network, and are themselves surrounded by mitochondria (Tunnicliffe, 1985), allowing for the ultimate mediation and transport of nutrients and metabolites from the vent fluid to the *R. piscesae* tissue.

Many vestimentiferan worm species show a remarkable degree of phenotypic plasticity (Tunnicliffe, 1988). *R. piscesae* exhibits a range of variation in tube shape, size and colour, and also 'soft part' morphology (Figure 6.1: Tunnicliffe 1988; Southward *et al.*, 1995; Desbruyères & Laubier, 1997; van Dover 2000). This morphological variation would appear to link directly to environmental habitat, specifically vent-fluid conditions, such as sulphide concentration, flow rate and temperature etc.. Originally, *R. piscesae* was described as 7 distinct morphospecies (Tunnicliffe, 1988), later refuted by Southward *et al.* (1995) and Black *et al.* (1997), who used molecular techniques to illustrate that they were genetically indistinct. This level of morphologic variation is not necessarily mirrored in other vent genera, for example, many vesicomyid clam species are morphologically identical (Kojima, 1995).

A significant part of the vestimentiferan growth is accounted for by tube production (Ravaux, 1998). The tube structures of *R. piscesae* are highly variable in terms of size (max length: 1900mm; anterior diameter 2 – 13mm: Southward, 1997) and morphology (straight or sinuous; soft or stiff), which is suggested to be a function of

distinct environmental regimes (Urcuyo *et al.*, 1998). The roughly conical tubes have a branchial funnel at the open end, tapering down to approximately 1mm diameter at the posterior end (Southward, 1997), and have saucer-shaped, external flanges along their lengths, which mark the end of previous episodic 'growth spurts' (Urcuyo *et al.*, 1998) Production of the organic tube wall in many vestimentiferan species is achieved through the secretion of a complex chitinous matrix, with associated embedded proteins (Gaill & Hunt, 1986) from specialised chitin secreting glands, located in areas of 'secreting tissue' (Ravaux, 1998).

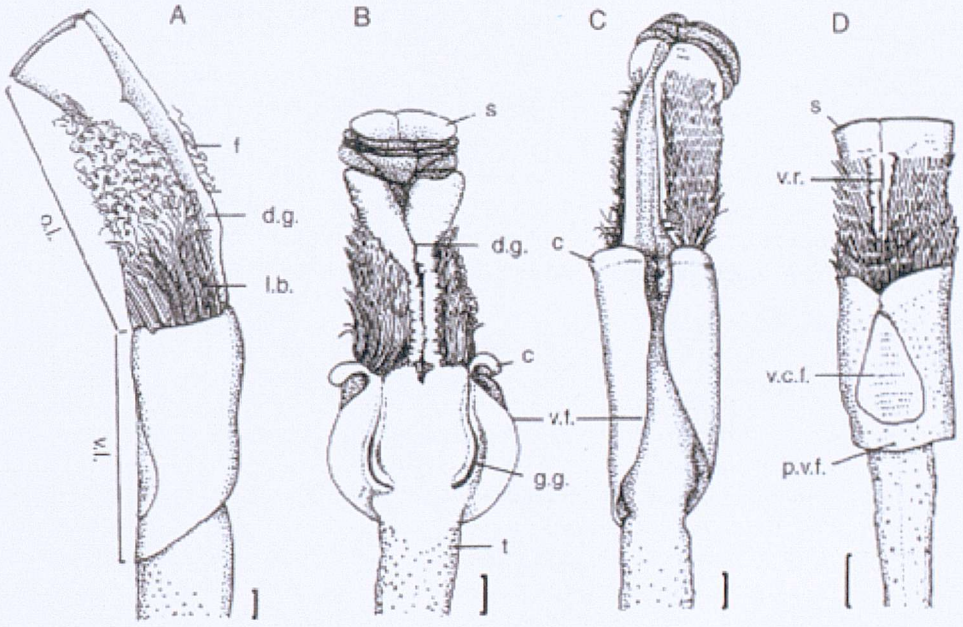

Figure 6.1 – An example of phenotypic plasticity in the morphology of the anterior of four individual *Ridgea piscesae* tubeworms recovered from the northeast pacific (from Southward, 1995).

The tube takes on the role of the invertebrate worm's protective shell and external skeleton, allowing the anterior region to open out close to venting (Ravaux, 1998). *R. piscesae* appear to be more tolerant of environmental variation than many other vestimentiferan species such as *R. pachyptila* which is only found in areas of relatively strong, and steady hydrothermal fluid flow, coupled with high sulphide availability (Urcuyo *et al.*, 1998). In contrast, *R. piscesae* is able to inhabit areas of low, diffuse fluid flow, with low sulphide levels and temperatures marginally above that of ambient seawater, to areas of highly sulphurous, high temperature, diffuse fluid flow (Urcuyo *et al,*, 1998). The growth rates of *R. piscesae* are controlled by its habitat, and can be

generally assumed to increase with environmental temperature, and dissolved sulphide concentration, and consistency of the hydrothermal fluid flow to the upper limits of their environmental tolerances (Urcuyo *et al.*, 1998). In addition to this, it has been demonstrated that there may be variable growth rates exhibited by individuals from the same habitat, and even from individual tubeworms from the same clustered niche (Urcuyo *et al.*, 1998). Growth rates measured by Tunnicliffe *et al.* (1997) are reported to be as fast as 95cm y^{-1}, considerably higher than the growth rates reported by Lutz *et al.* (1994) for other tube worm species (*Riftia pachyptila*: 85cm y^{-1}; *Tevina jerichonana*: 30cm y^{-1}). However, growth rates of only 6.1cm y^{-1} reported by Urcuyo *et al.* (1998), clearly demonstrate the variable nature of *R. piscesae* worms.

The exterior of the tubes provide a surface for microbial colonisation and mineral precipitation, whereas the dense tubeworm aggregations provide a protective habitat for vent-endemic micro- and macrofauna such as colonial Loricate ciliates (e.g. *Folliculina* sp.), ampharetids (e.g. *Amphisamytha galapagensis*); limpets (e.g. *Lepetodrilus fucensis* and *Lepetodrilus corrugatus*); and gastropods (e.g. *Depressigyra globulus*). Around actively venting fissures, vestimentiferans form densely packed clusters or 'bush-like' clumps. Individual tube components may be bound together by glutinous mucus strands, possibly formed by non-tubiculous alvinellid worms; and roaming polynoid polychaetes (Tunnicliffe, 1985), as well as free-living microbes; and bacterial biofilms. Where tubeworm aggregations are significantly large (approximately 2 – 4m^2) the fluid flow through the clump can be sufficiently modified so as to cause ecological zonation of the associated, endemic biology, forming central and outer niches, likely caused by graduated temperature variation (Tunnicliffe, 1985).

6.1.2 - Structural elements & mineralisation associated with vestimentiferan tubes

6.1.2.1 - Chitin.

Chitin is a fibrous, crystalline polymer (*N*-acetylgluosamine), consisting of linear, unbranched chains of β1 – 4 linked 2-acetamido-2-deoxy-D-glucose residues (Kent, 1960). Chitin and cellulose are reminiscent of one another in terms of chemical composition and physical properties. Chitin is absent from higher plants and the tissue of vertebrate animals, but present in the cell walls of fungi, several algal species and

crystoflagellates. It is also found in the cuticle of insects and arthropods: contributing to the structure of the exoskeleton; the gut lining; tendons; wing coverings; and the internal skeleton, in the chaetea of polychaetes, and in bacterial cell walls (Richards, 1951; Rudall, 1965; Kent, 1960). The primary role of chitin in the animal kingdom is support and defence. The effectiveness of chitin in nature is often enhanced by the association with protein, as well as with other substances such as inorganic calcium salts; lipids and other organic materials. In fact it has been argued that chitin in its purest form does not exist in nature, and the 'chitin' described in the majority of biological and chemical literature is, in fact, more accurately described by Hunt (1970) as a 'chitin-protein-complex'.

6.1.2.2 – Silica

Abiotic silica precipitation is common in hydrothermal environments ranging from the siliceous thermal springs of Yellowstone National Park, USA (Cady & Farmer, 1996) to the TAG hydrothermal mound of the 26°N Mid-Atlantic Ridge (Hopkinson *et al.*, 1999). The deposition of silicate minerals during high temperature venting of hydrothermal fluids is well documented (e.g. Karl, 1995; Tivey *et al.*, 1995; Cady & Farmer, 1996; Jones & Renaut, 1996; Hesse, 1998; Hopkinson *et al.*, 1999). However, it is the rapid decrease in temperature that is the cause of supersaturation in silica solutions in these environments, and the consequent polymerisation of these solutions into silica-rich gels (Iler, 1979). The crystallisation of silica at temperatures below 100°C is principally due to two methods of formation: Flocculation of colloidal silica (Iler, 1979) and progressive diagenesis of biogenic amorphous silica (Hein *et al.*, 1978).

Flocculation of colloidal silica can be instigated by a number of different environmental factors such as: a decrease in temperature, a change in pH, or the addition of metal hydroxides. Conditional changes such as these result in the formatio of silica sols produced from monosilicic acids contained in silica gels. In an environment such as a hydrothermal vent field, gelation may be catalysed by the presence of Cl^- ions in seawater (Iler, 1979). Minerals formed under these conditions of extreme disequilibrium are typically characterised by a branching or radiating non-crystallographic morphology, and have a non-constant density morphology. Mineral morphology is controlled by the growth processes involved, and not dictated by growth on an external template (Fowler,

1989). An example of an entirely abiotic silica-depositing system is the production of agates from silica rich gels (e.g. Ortoleva *et al.*, 1995), or partially polymerised siliceous fluids (Heaney, 1993). Agates are siliceous minerals that are composed of concentric bands of quartz, chalcedony and opaline silica. Fine concentric banding, or irregular variegated patterns are thought to be caused by chemical admixtures and microinclusions of haematite, limonite and other minerals. 'Moss agates' contain dendritic forms of iron and manganese oxides, or chlorite minerals, which may be falsely identified as being of biotic/microbial origin, but are in fact, wholly abiotic, and involve geochemical self-organisation (Ortoleva *et.al.*, 1987; Fowler, 1990; Hopkinson *et.al.,1999*).

Ortoleva *et al.* (1987) describes self-organisation as the autonomous passage from an unpatterned state (i.e. fluid) to a patterned state (i.e. solid) without the intervention of an external template. There are two necessary conditions for self-organisation in minerals, feedback, and a geochemical environment in disequilibrium. Self-organisation has been described in rocks and minerals from various geochemical systems and environments.

These abiotic mineralisation mechanisms are important on a wide variety of scales in hydrothermal systems; from sub-micron to macroscale. Superimposed on the abiotic mineralisation is microbially mediated silica precipitation.

The progressive diagenesis of biogenic silica from opal-A to quartz, takes place after deposition at low temperatures and pressures (Mizutani, 1977; Pisciotto, 1981; Isaacs, 1982). Diagenesis of Opal-A (biogenic silica) proceeds through a number of stages (reaction 6a).

SiO_2	$\Rightarrow$	SiO_2	$\Rightarrow$	SiO_2	$\Rightarrow$	SiO_2	6a
Opal-A		opal-A'		opal-CT		quartz	

Acurately prediciting the geological times scale for the reaction of opal-A to quartz is difficult due to the large time-scales involved. However geological and experimental data can give some indication of the reaction rates. For instance: opal-A is found in deep sea sediments up to 60Ma, and also in surface rocks up to 85Ma; the cristobalite and tridymite peaks with denote the presence of opal-CT can be identified in rocks as young as 5 -

10Ma, but are not observed in rocks over 140Ma; and quartz can be identified in rocks over 40Ma Moxon, 1996). However, these diagenetic timescales can be radically altered in laboratory experiment, where different redox and chemical environments can be simulated. For example and experiment with a silica gel containing a Mg^{2+} solution at room temperature and pH of 8.2, showed evidence of converting to opal-CT after 14 years (Moxon, 1996). Which is a strong indication that chemically active, redox sensitive environments (such as deep sea hydrothermal vents) could greatly effect the behaviour of silica reaction rates.

6.1.2.3 - Barite.

Barite is saturated in seawater throughout most of the world's oceans (Monnin *et al.,* 1999). Thermodynamic consideration of the Ba and SO_4 contents of seawater suggest that equilibrium is reached between the dissolved and solid phase at depths of 2000-3500 m in the Pacific Ocean. While barite saturation is common in seawater, precipitation from solution is associated with biological productivity in the euphotic zone with release of barite particles in the upper water column as the organic substrate is remineralised by microbial activity. Biogenic barite accumulation has been used widely as a proxy for primary productivity through time (Jeandel *et al.*, 2000). There is a convincing correlation between barite accumulation in deep sea sediments and other proxies associated with particle scavenging (Thomas *et al.,* 2000).

Barium is enriched in hydrothermal fluids yet barite usually only forms a minor component of sediment-free hydrothermal deposits. This is due to the relatively low Ba content of MORB, the low SO_4 content of vent fluids and the preferential precipitation of anhydrite during mixing of vent fluids with SO_4 rich seawater. Barite is, however, a major component in back-arc and sediment-covered hydrothermal settings, chiefly due to the increased Ba content in tholeiitic rocks, and terrigenous sediments (Hanor, 2000). The abundance of barite at any given hydrothermal location primarily depends on the quantity of Ba leached from the source rocks by hydrothermal fluids circulating through the reactions zone (Seyfried & Bischoff, 1981; Seyfried & Mottl, 1982). Therefore the deposition of barite at sediment starved ridge crests, is controlled by the composition of the underlying lithospheric rocks.

Most of the barite in the Earth's crust has been formed through the mixing of fluids which contain Ba leached from silicate minerals, and oxidised shallow fluids which contain dissolved sulphate, such as seawater (Hanor, 2000) . Barite is a common mineral in Volcanic-Hosted Massive Sulphide (VMS) deposits from the Early Archean (<3.4 Ga) (Barley, 1992: Cameron & Hattori, 1985), though to modern active spreading centres, and currently forming sedimentary exhalative (SEDEX) deposits (Franklin *et al.*, 1985; Franklin 1991). Commonly, VMS-barite deposits are associated with a suite of exhalative hydrothermal sulphide minerals, which may form 50 – 80% of the total deposit. Venting hydrothermal fluids, precipitate Cu, Fe and Zn sulphides, whilst producing a fluid enriched in Ba, Pb and Au, which in turn reacts with seawater to form sulphates. Barite is a common mineral in Juan de Fuca hydrothermal deposits, where it is precipitated due to the mixing of hydrothermal fluids and seawater (Hannington & Scott, 1988). At the Southern Juan de Fuca Ridge and Axial Seamount, the underlying basalts are substantially enriched in Ba, when compared to equivalent sites on the EPR, which may exhibit an order of magnitude lower Ba contents (Hannington & Scott, 1988). Barite formation is associated with chimney growth and fluid-seawater mixing (Haymon and Kastner, 1981). Most barite mineralisation has been attributed to mixing of high temperature fluids with seawater during early stages of fluid-seawater interaction within hydrothermal chimneys. There has been very little study of low-temperature barite mineralisation in hydrothermal systems.

6.1.3 – Chapter outline.

In this Chapter, a variety of analytical and observational techniques are used to explore, in detail, the functionality of the *R. piscesae* tube, the nature and timing of tube mineralisation, and the possible interactions between microbes and the mineralised vestimentiferan tubes.

6.2 – Sampling and Methods.

6.2.1 – Sampled material.

During the 'High Rise Expedition' cruise, Legs 1 and 2, in August and September 1995, 20 discrete samples of hydrothermal vent organisms were collected from one low-temperature hydrothermal field (located at Clam Bed, Endeavour Field, Juan de Fuca Ridge), and four from sulphide edifices (High Rise Field, Juan de Fuca Ridge), on board the *DSVSS Laney Chouest*. The cruise was devoted to the sampling of hydrothermal vent organisms, and sampled biota were sorted onboard and preserved for histological sectioning on shore (van Dover, 1995).

The samples used in this study comprise a small $12cm^2$ clump (at time of sampling) of living and dead vestimentiferan worms and associated fauna, collectively embedded in life position in a hydrothermal matrix of silica and barite minerals. The major faunal components in the sample are *Ridgea piscesae*, which form the bulk of the biota (in terms of individuals and biomass). Associated fauna within the sample include: *Nicomache venticola, Lepetodrilus fucensis, Depressigyra globules, Paralvinella palmiformis, Paralvinella pandore* and *Amphisamytha galapagensis*. The sample was recovered from the Ventnor Field, located at 47°58.0750N / 129°05.3330W at 2225m depth (Figure 3.3). Although the *Ridgea* sp. sample was recovered from an actively venting field (temperature 285 – 330°C), the temperature of the immediate environment around the sample can be estimated from the faunal assemblage. The temperature proximal to the worm tubes is thought to be between 2 - 35°C based on previous observations of *R. piscease* habitats (Urcuyo *et al.*, 1998).

The second sample studied here is a sulphidised block, containing silicified vestimentiferan dwelling tubes, presumed to be *R. piscesae* or similar species, based on size and general morphology (see later section for details and reasoning). This fossiliferous sulphide talus section was presented to the author as a 10 x 6 x 2 cm machine cut slab, which had randomly sectioned the embedded tubes obliquely, cross-sectionally and longitudinally. The sample was recovered from an area of sulphide talus, at the base of an active chimney at the Fairy Castle Field, located at 47°58.0233N / 129°05.5673W at approximately 2200m depth (Figure 3.3).

Sample macro-analysis, using a hand lens and low-magnification binocular light microscopy, allowed for a general appreciation of the samples to be attained, and areas of interest to be identified. Individual sub-samples were isolated and prepared using light microscopy. Some were left as three-dimensional samples, mounted on metal stubs, and sputter coated in gold (Au thickness = ~ 2-3 Å) for use with SEM and HFSEM. Sub-samples were resin impregnated using AY105 epoxy resin under vacuum, thin-sectioned, polished and carbon coated, to be used in conjunction with SEM / EDS, or EMP analysis. Samples for FT-IR analysis were prepared by a similar method, with the exception that the sections were in the form of double polished wafers (i.e. were not glass mounted).

A full description of the investigational and analytical techniques used in this Chapter can be found in Chapter 3.4.

6.3 – Results.

The sampled material from the two locations will be systematically described here in two sections. The first will concern the Ventnor Field samples, and the second, the Fairy Castle Field samples.

6.3.1 - Ventnor sample.

6.3.1.1 – Tube description and mineralogy.

The tubes of *Ridgea piscesae* form a sinuous, twisting mass (Figures 6.2 a & b), rooted in a mineralised matrix, dominantly composed of silica and barite (Figure 6.3a - c). The number of individual worm tubes contained within the Ventnor sample is estimated to be around 300 – 400. The tubes are densely packed together (Figures 6.3b & c), and are generally aligned upwards, radiating upwards and outwards from the base of the mineralised mound (Figure 6.3b), but may also seen to twist and wrap around other tubes. Individual tubes measure between <1cm and 15cm in length, and between <1mm and ~5mm maximum diameter (Figure 6.4a). Textural features common to all *R. piscesae* tubes include terminal flanges (Figure 6.4b), concentric growth lines, and longitudinal wavy ridges (Figure 6.4c).

Mineralisation of the tube structures is extensive, among both inhabited (live), and uninhabited (dead) tubes. Figure 6.4a demonstrates that mineralisation of an inhabited tube structure occurs during the live cycle of the tubeworm. Silicification of the tube material is prominent throughout the sample. The silicified tube wall is commonly overgrown by barite, and mantled by further silica precipitates (Figure 6.5a). Often the concentrically layered nature of the tube is preserved within the tube wall (Figure 6.5b), and can be observed under high magnification where the tube wall is sectioned (Figure 6.5c). The silica within the mineralised tube wall has an amorphous (or occasionally colloform) habit, which is invariably overgrown by radiating acicular barite crystals (Figure 6.6a). Individual barite crystals habitually form small, euhedral crystals which are tabular, with blade- or wedge-like terminations. Inclusions of anhydrite, or other commonly associated sulphates, within the barite crystals, were not observed. Further, later amorphous silica precipitates can be seen to mantle the fibrous barite crystals. In

cross-section, mineralised tubes show that the distribution of both, the silica and barite mineralisation phases, are not uniform around the circumference of the tube (Figure 6.6b), and instances where one tube abuts against another, may be seen to either inhibit, or promote mineralisation patterns. In cross section, tubes which are less extensively mineralised tend to show a common phenomenon: a thin inner halo, which appears to represent a desiccated organic inner layer, which may be either circular and uninterrupted, or broken, and randomly orientated within the inside of the tube (Figure 6.6c).

A flaky, desiccated coating is often observed to form on the inner surfaces of many of the mineralised tubes (Figure 6.7a). Inhabited tubes contain an organic, clear to pearlescent, layer which adheres to the inner surface of the tube (Figure 6.7b), and may represent a desiccated mucus layer. Within the organic layer, a dark coloured strand can commonly be observed, running along the length of the tube (Figure 6.7c). The base of the strand appears to be 'anchored' onto the tube wall by a network of dark organic filaments, which are embedded in the organic mucus layer (Figure 6.7d). Rarely however, radially cockade crystalline silica growth can be observed to infill the tube (Figure 6.7e), which masks the presence of any original organic features that may have been present.

Microbial silicified networks, and mineralised biofilms are extensively developed throughout the Ventor sample. Loosely interwoven silicified filaments form within the voids between individual tubes, and show varying degrees of silicification (Figures 6.8 a & b). A number of bacterial morphotypes have been identified within the sample, often adhering to the outer surfaces of tubes, and entangled within bladed barite precipitates. Coccoidal and rod-shaped bacilliform microbes can be observed sparsely covering relatively young and unmineralised tubes (Figures 6.9 a – c). As mineralisation (particularly silicification) of the tube wall becomes more prevalent, the number of preserved microbes consequently increase, allowing for the preservation of a larger number of both taxa and individuals (Figures 6.10a - c). Where silicification potential is sufficiently high, the sticky mucus which forms over and between individual microbial cells may be preserved (Figure 6.10a). Many of the filamentous microbes present here are formed of solid, amorphous silica, and show no evidence of a sheath, cell wall, or central void that would have once house the bacterial trichome. Occasionally however, broken or severed filaments do show evidence of a mineralised sheath-like covering

(Figure 6.10a), or of a central opening (e.g. Figure 6.10b), which may have accommodated the internal cellular components. Many sulphur oxidising bacteria incorporate sulphur globules within the cell wall, as by-products of metabolic processes, and may form vesicles or voids, due to remineralisation of the sulphur compounds. Vesicles within the filamentous cells have not been observed here, but filamentous bacteria have been identified in close proximity to sulphur grains and granules. Whilst most of the filaments are formed from amorphous silica, and show few external features, in rare incidences individual microbial filaments show some evidence of external ornamentation (Figure 6.10c), which may represent very early nucleation or encrustation of the filament. In the more heavily mineralised areas of the sample, complex, interwoven microbial biofilms can be observed, preserved in silica (Figures 6.11a – c). Commonly, interlayered networks can be observed to form concentric coatings radiating out around the tubes (Figure 6.12a), and draped over the barite crystal overgrowths (6.12b & c), as either thin, wispy, branching strands, where mineralisation is in its initial stages, or as thick, substantial botryoidal filaments, where mineralisation is more advanced.

Microbial filaments often accumulate within the sheltered terminal flanges of the tube, where they become silicified. The progressive silicification and further growth of new filaments over the top of the old, can eventually lead to a 'microstromatolite-like' layered structure (e.g. Figure 6.18a). As well as microbes, small tube structures are also observed, nestled in the tube flanges (Figure 6.13a – c). The tube structures appear to be composed of organic material (i.e. chitin or a similar organic tube building material, and are similar in morphology to the adult *R. piscesae* tubes. Concentric growth lines are present (Figure 6.13b) together with longitudinal wavy lines, and terminal growth flanges (Figure 6.13c). The tubes are in the order of 20 – 30μm in diameter, and between 50 – 70μm in length.

In older, uninhabited tubes, mineralisation of the inner tube surface is evident. Figures 6.14a – c show silica precipitates forming on the inner surface of a tube. The tube wall is silicified, and overgrown with barite and encrusted siliceous filaments, and the inner surface hosts straight, unbranching, 'finger-like' filaments which grow out towards the centre of the tube, into open space. The size and shape of the filaments differ from the microbial filaments described above. Where the described microbial filaments tend to

form branching, meandering networks, the 'finger-like filaments, are straight, unbranching, individual precipitates of amorphous silica. No visual or textural evidence of a mineralised organic coating (e.g. Figure 5.6) can be distinguished. Where mineralisation of the inner surface is more extensive, barite rosettes can be observed to form as isolated crystal groups, and then later, as dense aggregations of crystals (Figure 6.15a). Rarely, Fe- and Zn-sulphide mineral precipitates can be seen to form as isolated assemblages (Figure 6.15b), crudely replacing the outer barite and silica precipitates, and adhering to the siliceous tube wall structure.

6.3.1.2 – Micro FT-IR analysis

Figures 6.16 and 6.20 show the areas of the tube investigated using FT-IR and geochemical analysis. Figure 6.16 is located about the middle section of an inhabited tube, and Figure 6.20 is located towards the uppermost (and therefore younger) section of the same tube. Previous studies of *R. piscesae* tube construction (summarised earlier in this Chapter), have shown that each tube section from one terminal flange, sequentially to the next flange, is formed during episodic growth periods which may last up to 18 days of tube building and a further 18 days resting period and tube for reinforcement. These studies infer an age difference of around 36 days between each terminal flange and the adjacent material of the same tube (Urcuyo *et al.*, 1998). Therefore, the areas around the tube flanges were specifically targeted for FT-IR and geochemical analysis in an effort to compare the nature, and timing, of mineralisation, as they are sections of the same piece of tube, but with a measurable difference in the age of their formation.

Micro FT-IR analysis in reflectance and absorbance modes have been used to assess the degree of crystallinity in the silicified tube wall structure, and in the microbially templated silica precipitates. Initially, specific areas rich in silica, barite and chitin were analysed using EDS and then analysed using FT-IR to produce the end-member reference spectra. Spectral traverses were collected from two areas of the silicified tube wall where terminal flanges are present, and one traverse through a single cross-section of tube wall. The analysed areas and corresponding FT-IR spectra are shown in figures 6.17 and 6.20.

6.3.1.3 - Geochemistry.

Figure 6.19a – c shows EDS spot analyses for specific areas of the mineralised tube wall. Figure 6.19a is centred about the end-most section of a terminal flange, overgrown by acicular, bladed barite. Spot analyses (Figures 6.19a & a) indicate the presence of barite, which appears to have replaced the peripheral part of the tube flange. Sub-micrometer circular vesicles are present in the barite laths, and are inferred to be microbial moulds. Quantitative microprobe analysis of barite shows that Sr and Ca are ubiquitous in minor amounts, having a mean value of 0.45 wt% Sr (3.96% of total Ba wt%); and a mean value of 0.136 wt% of Ca (1.25% of total Ba wt%).

Analysis of the tube wall in Figure 6.19b(1.3 – 1.5) indicate almost identical EDS traces for Si, with the exception that a minor S peak can be observed at point 6.19b(1.4), in a darker layer which runs parallel with the tube wall. This S-rich horizon, also appears to host micro-crystalline barite laths, which are orientated along the length of the tube. Texturally, the areas forming the inner edge (6.19b(1.3)), the S-rich horizon (6.19b(1.4)), and the inner tube area (6.19b(1.5)) appear different. A more porous texture is observed in the horizon about the point 6.19b(1.5), possibly indicating incomplete silicification, or remnant organic material. A S-rich horizon is also present along the inner layer (point 6.19c(1.8)) of the area analysed in Figure 6.19c.

EDS elemental maps are presented for two different tube/flange intersecting areas for four elements (Si, Ba, S, P: Figures 6.20a & 6.21). The elements Si, Ba and S are all component parts of the mineralised tube wall, whereas P is present at levels only marginally above the detection limit (0.01%), and is included to show that there is no phosphorus biomarker mineral present in any remnant organic layers (Chapter 4).

Figure 6.22 shows a quantitative elemental traverse through a cross-sectional area of mineralised tube wall from an inhabited tube structure. The tube itself displays a discreetly layered structure, with areas (generally towards the centre of the section) which appear less consolidated and porous. A lighter coloured, unstructured layer is present as part of the inner surface of the tube The major and minor chemical elements present are plotted as distance vs. weight % of each individual element (Figures 6.22b & c, respectively). Of the major elements (>1.0 wt%), Si (and corresponding O), S and Ba are

the most abundant. Si can be seen to be concentrated in particular regions of the tube cross-section, Ba is concentrated in the areas of barite crystal growth which tend to overgrow the tube outer surfaces and S is concentrated along the inner portion of the tube (from 20 – 80μm), and in the area of barite crystal growth. The minor elements (<1wt%) are also concentrated along the same inner portion of the tube as S. Ca and P show similar distribution patterns, and are likely representative of the mineral apatite ($CaPO_4$), which is often associated with the excretion products of marine organisms. Similarly, Mg is also associated with the excretion products of marine organisms (seawater has a relatively high Mg content of 53 mM (Elderfield & Schultz, 1996). Fe, Cu and Zn however, are present in trace amounts in seawater (Fe: <0.01 μM; Zn: 0.01 μM; Cu: 0.007 μM (Elderfield & Schultz, 1996)), but are present in hydrothermal fluid (Fe: 750 – 6500 μM; Zn: 40 – 100 μM; Cu: 10 – 40 μM; Elderfield & Schultz, 1996), and are present in significantly elevated quantities along the inner (20 – 80μm) portion of the tube. It can be demonstrated from analysis of the stoichiometry of the geochemical analyses that there is excess S remaining if Fe, Zn, and Cu were all present as sulphide minerals. This excess S is inferred to be present as elemental S.

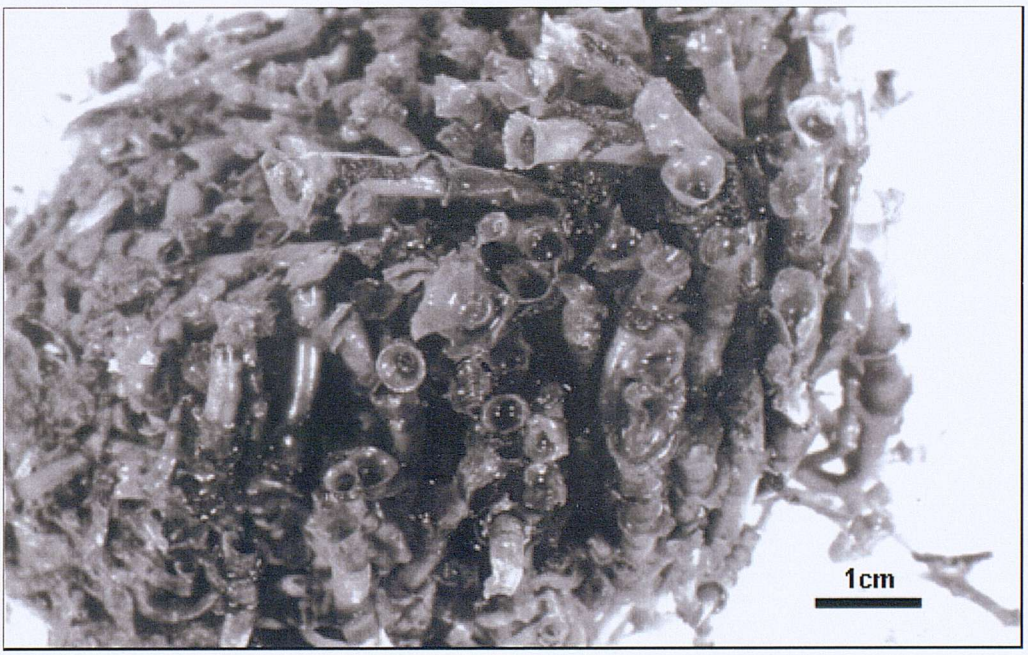

Figure 6.2a (top) – A view of the aggregation of *R. piscesae* tube worms used in this study.
Figure 6.2b (bottom) – A view from above of the *R. piscesae* tube worms used in this study, emphasising the densely packed nature of the worms.

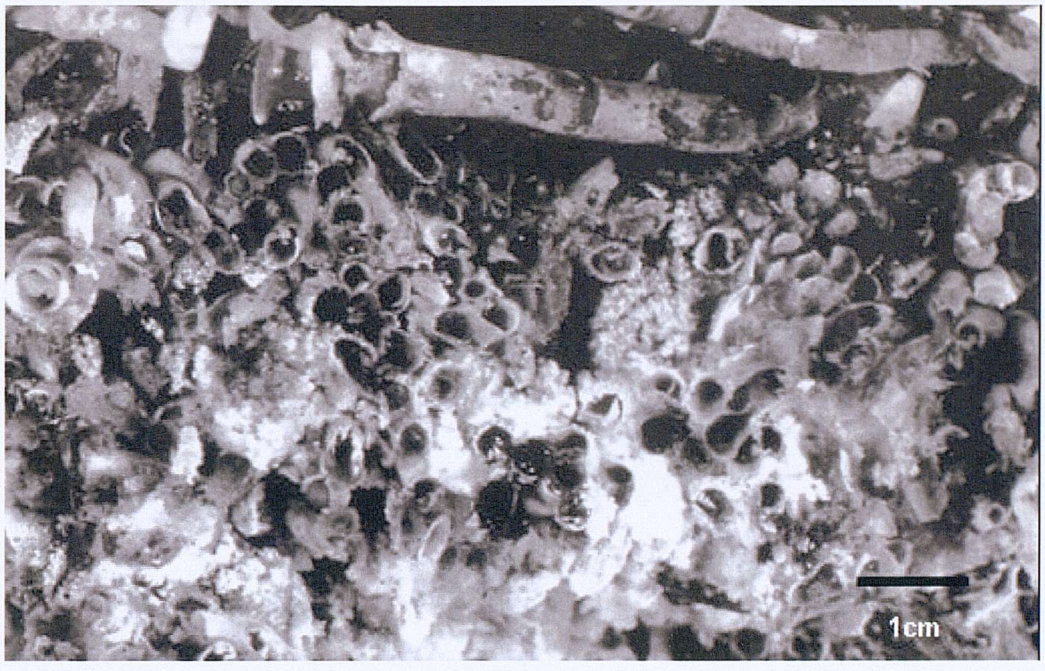

Figure 6.3a (top) – A broken cross-section through the mineralised matrix, into which the tube worms are embedded.

Figure 6.3b(left) – Sinuous worm tubes can be observed preserved in 'life' position by silica and barite mineralisation.

Figure 6.3c (right) – An aggregation of densely packed worm tubes preserved by silica and barite forms the basis of a porous, mineralised matrix.

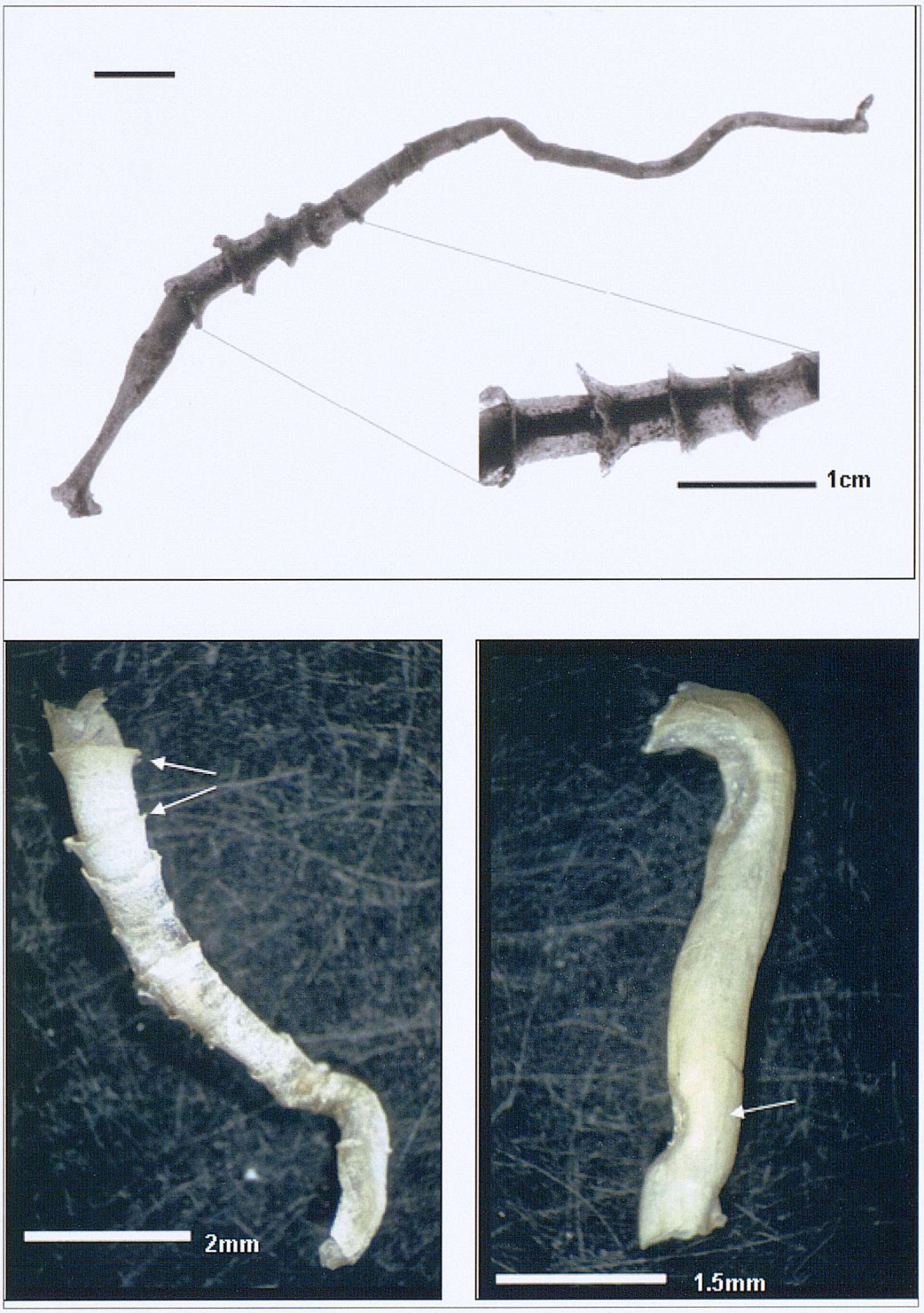

Figure 6.4a (above) – A back-lit image of a single worm tube, containing the desiccated remains of a worm. The tube is encrusted with silica and barite mineralisation at the posterior end, which grades to unmineralised chitin at its anterior end. The insert shows a magnified view of the middle section where the mineralised area is opaque, and the chitinous section is translucent.

Figure 6.4b (left) – A section of partially mineralised tube clearly showing the terminal growth flanges (arrows).

Figure 6.4c (right) – A section of tube exhibiting longitudinal wavy ridges (arrow).

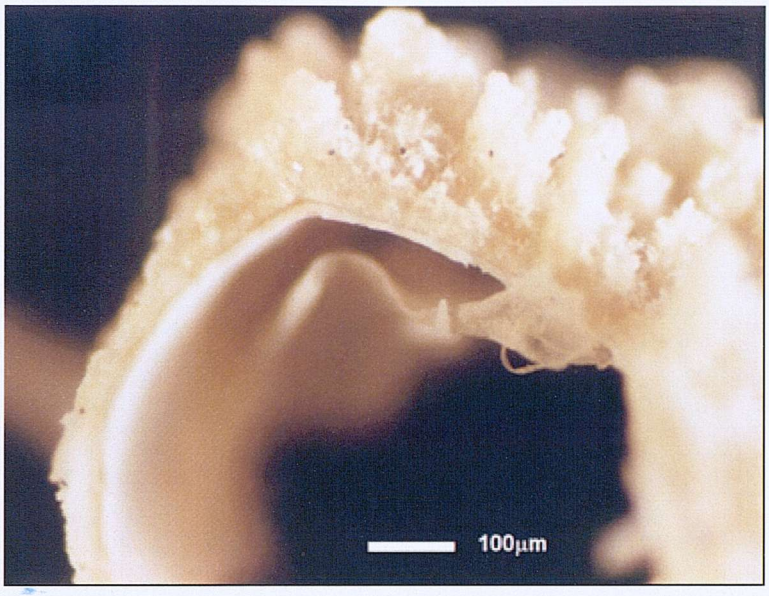

Figure 6.5a (left) – A silicified tube viewed in cross-section showing a thick mantle of barite and filamentous silica encrustations. A peeling, flakey inner layer is also visible.

Figure 6.5b (right) – A cross-section of a silicified worm tube , with concentric layers visible within the tube structure. A thin encrustation of barite and silica is present on tne inner suface.

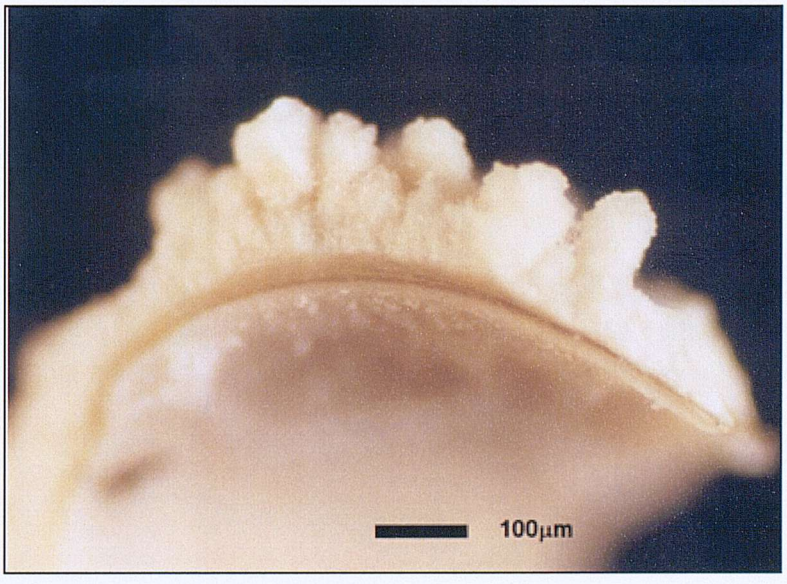

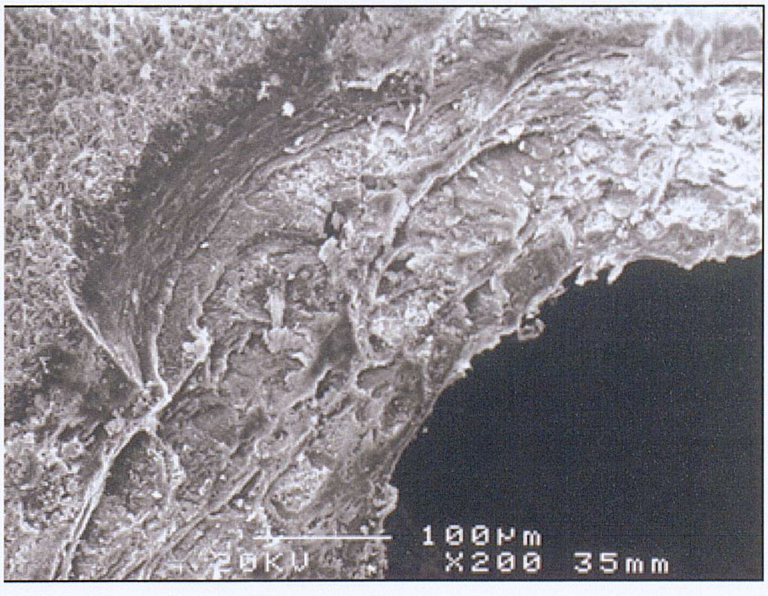

Figure 6.5c (left) – An obliquely cut tube section viewed under SEM depicts the concentrically layered nature of the tube.

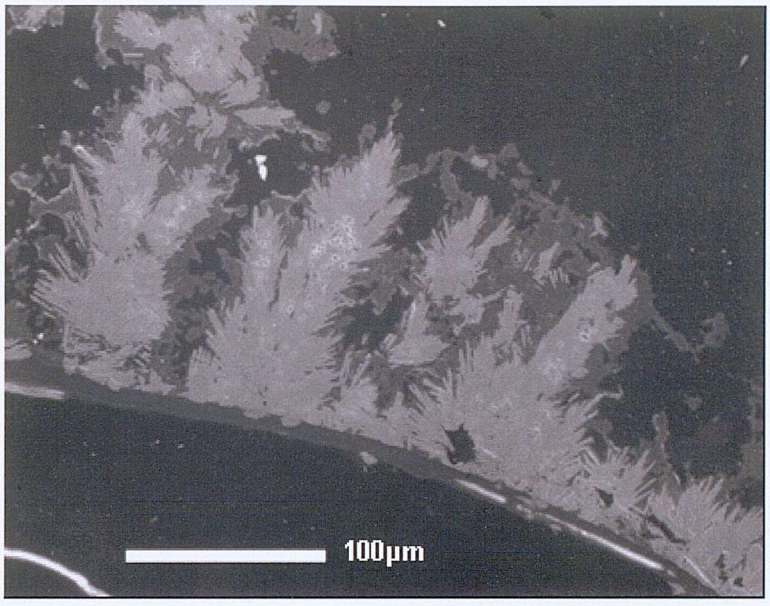

Figure 6.6a (left) – A BSEI micrograph which clearly shows the thin silicified tube wall (dark grey) overgrown by acicular bladed barite crystals (light grey), and filamentous silica (medium grey).

Figure 6.6b (right) – Mineralisation of individual tubes is generally inconsistent, and patchy around the circumference of the tube.

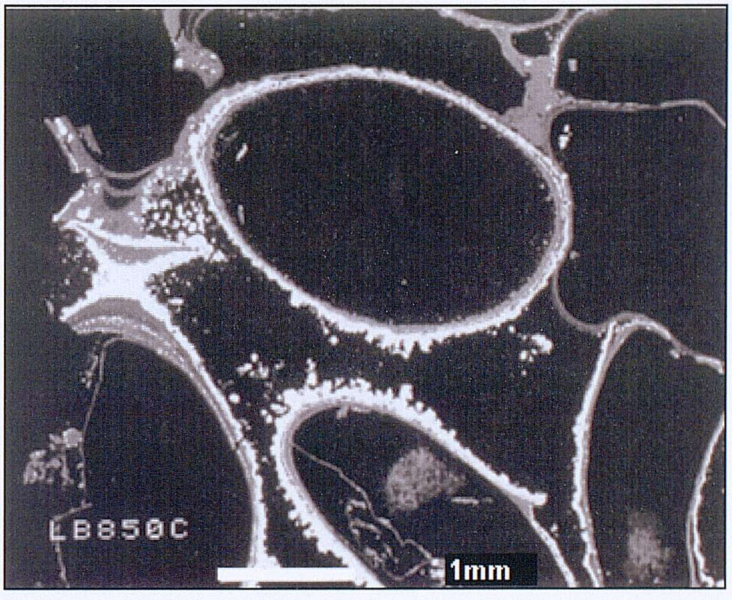

Figure 6.6c (left) – The densly packed nature of the worm tubes often causes individual tubes to be squeezed out of shape. Once the tube becomes mineralised the new shape is permanent, and in extream cases may prevent the worm from using the full length of the tube. Note the dessicated inner halo of organic material present within many of the tubes.

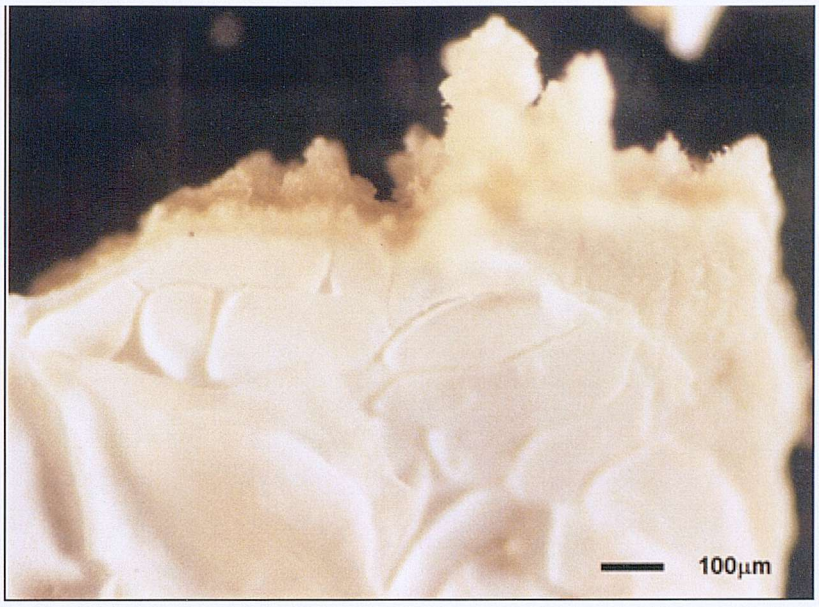

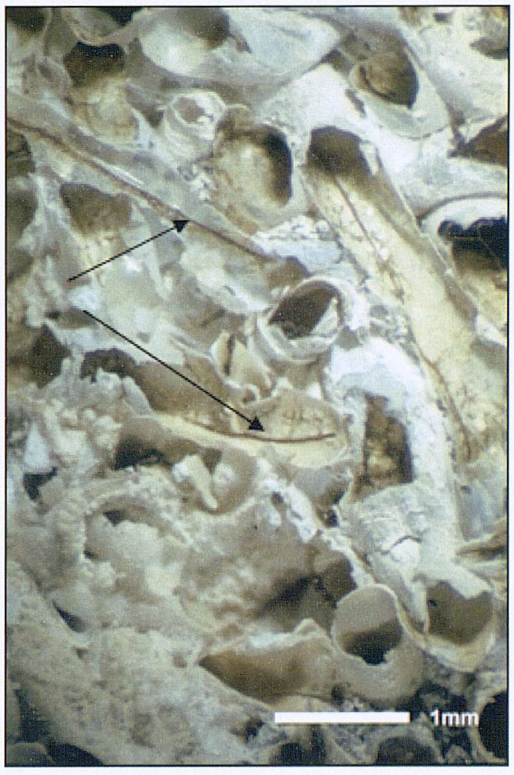

Figure 6.7a (above) – A flaky, desiccated coating on the inner surface of a tube wall.

Figure 6.7b (left) – A pearlescent layer on the inner surface of an inhabited tube (arrow).

Figure 6.7c (right) – Dark coloured strands observed to adhere to the inner surface of some inhabited tubes, often associated with a network of dark filaments which spread out across the inner tube surface (arrows).

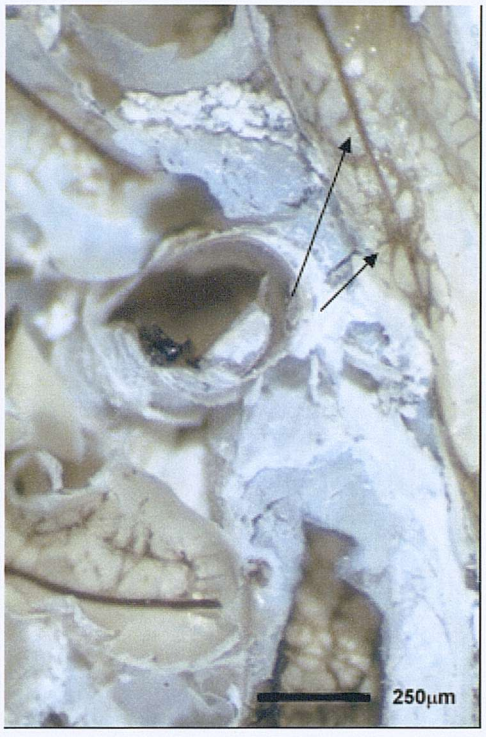

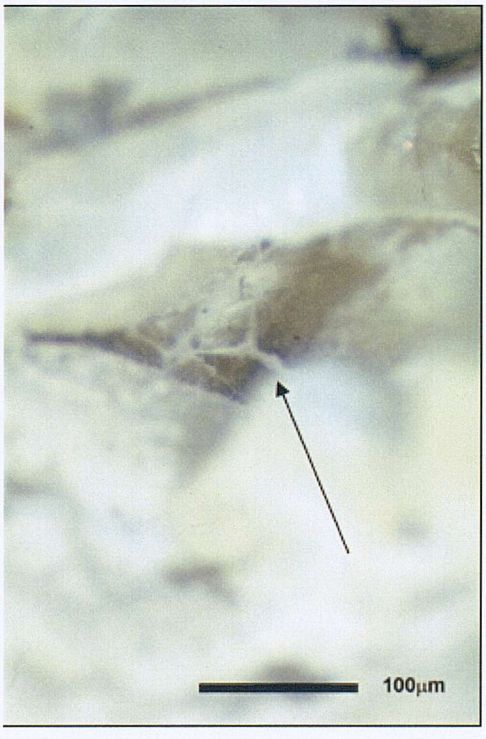

Figure 6.7d (top left) – A network of filaments anchoring the main ligand to the inner tube surface (arrows).

Figure 6.7e (top right) – Silica infilling a mineralised tube (arrow).

Figure 6.8a (bottom left) – Silicified microbial network stretching between tubes (arrow).

Figure 6.8b (bottom right) – A number of silicified microbial networks filling the inter tube spaces (arrows).

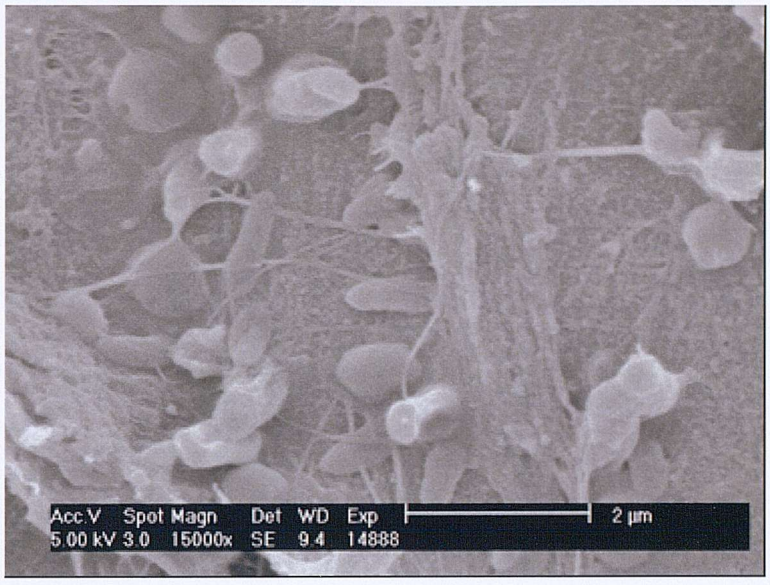

Figure 6.9a (left) – A BSEI image of bacterial cells and associated mucus adhering to the outer surface of a tube.

Figure 6.9b (right) – microbial cell structures associated with a ridge structure formed on the outer wall of a tube.

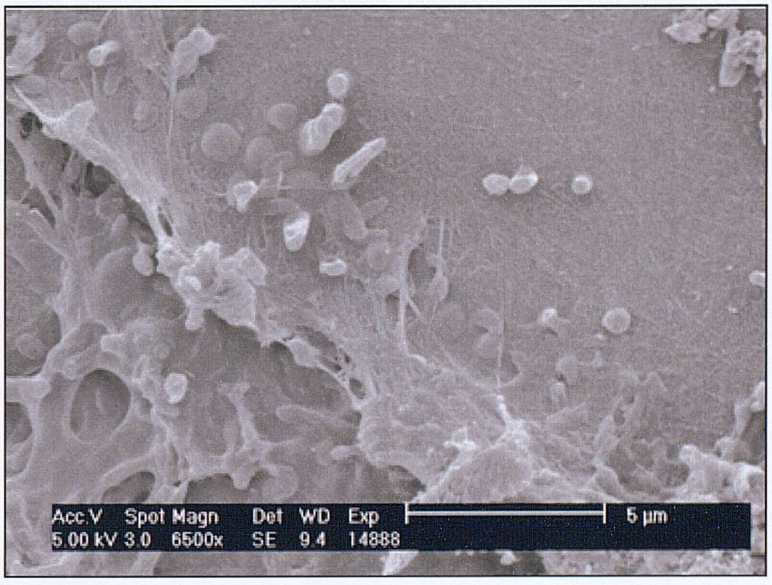

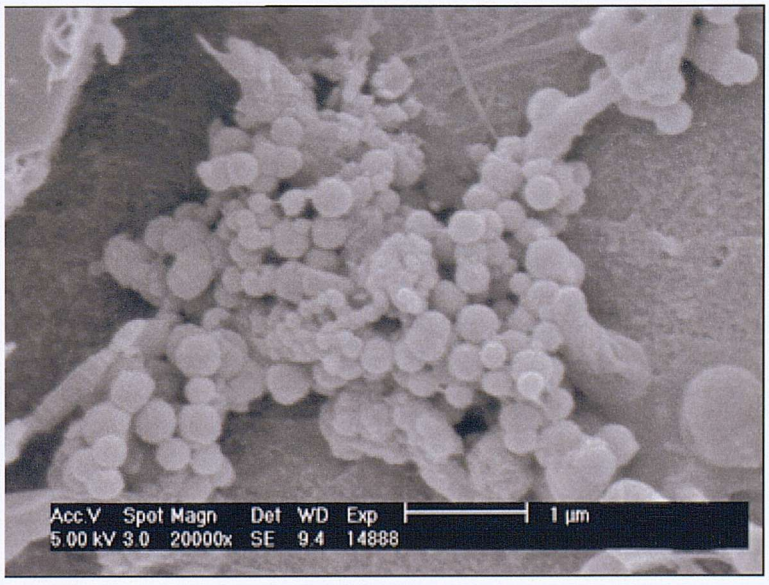

Figure 6.9c (left) – A cluster of globular, coccoidal spheres, of presumed microbial origin, affixed to the outer surface of a tube.

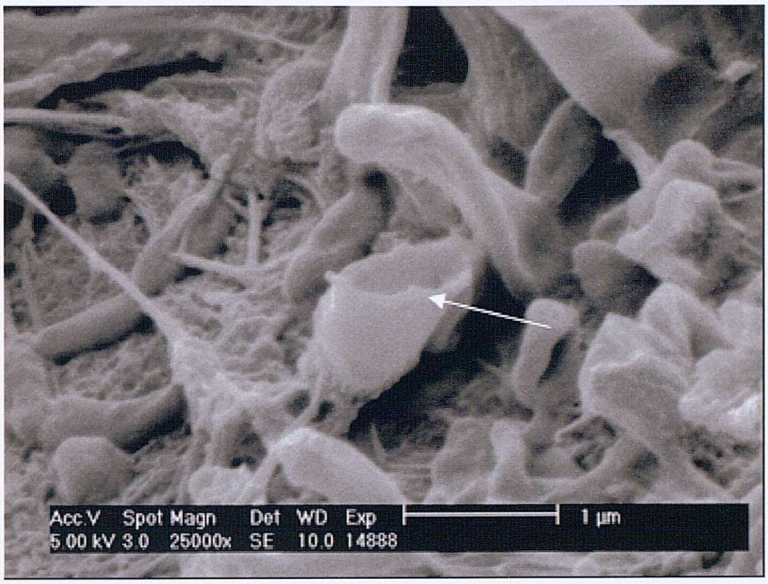

Figure 6.10a (left) – . This image shows preservation of the outer cell wall of a microbe by silica. Where the cell is broken a central void can be observed which would have contained the cellular components (arrow). Individual sheath-like filaments are rarely preserved in such detail

Figure 6.10b (right) – Filiamentous microbes are preserved by silica. The inter-cellular mucus is also preserved (arrow a). The filaments display central openings which may have previously contained the internal cell components (arrows b).

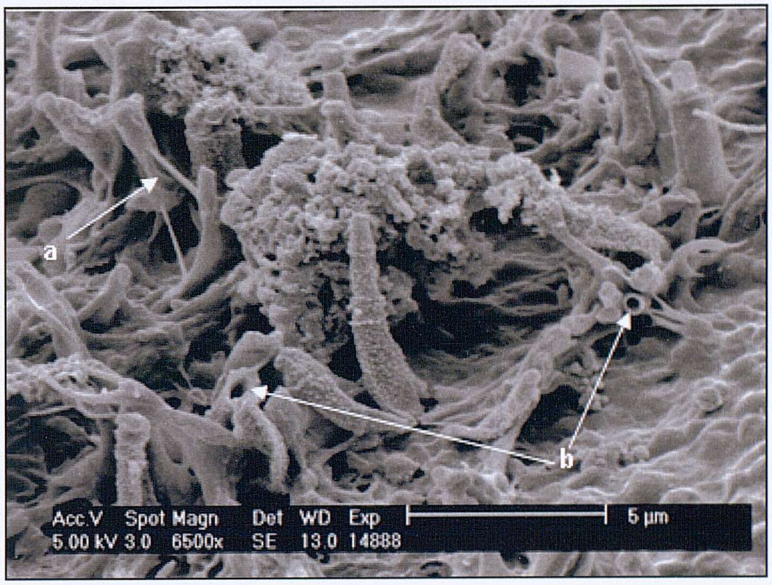

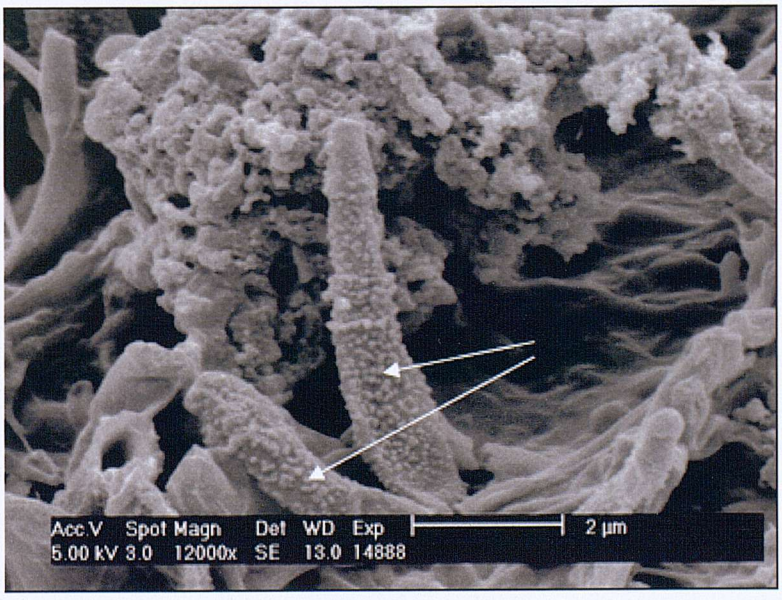

Figure 6.10c (left) – Ornamentation of the outer surface of microbial filaments can be observed here in the form of nannoscopic spherules silica, which may represent an early nucleation phase.

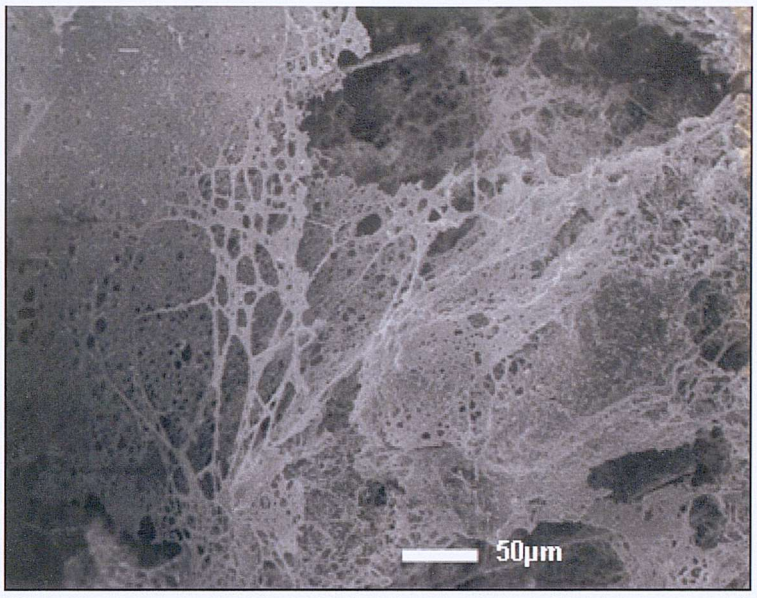

Figure 6.11a (left) – Multilayered mineralised biofilms can be observed to pervade the inter-tube spaces, and often form layered, concentric coverings around individual tubes.

Figure 6.11b (right) – At high magnification, the biofilms within the inter tube pore spaces can be seen to extend predominantly in two dimensions only, forming 'web-like' layers which are the thickness of one cell only.

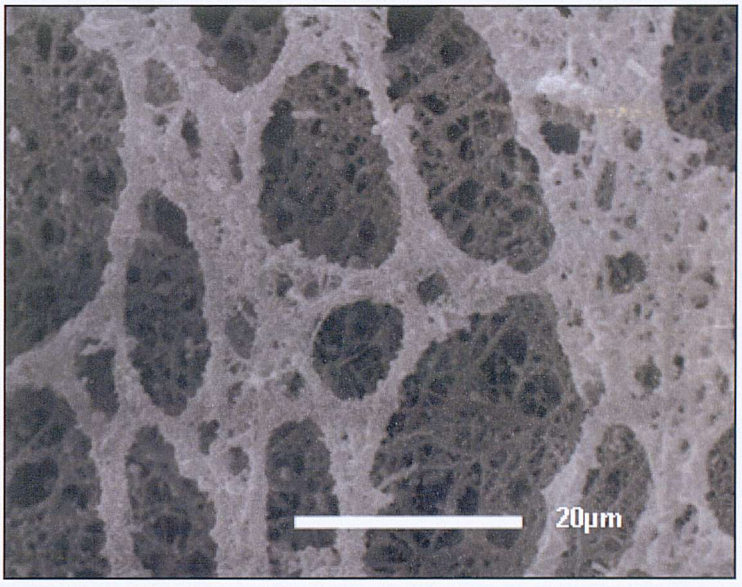

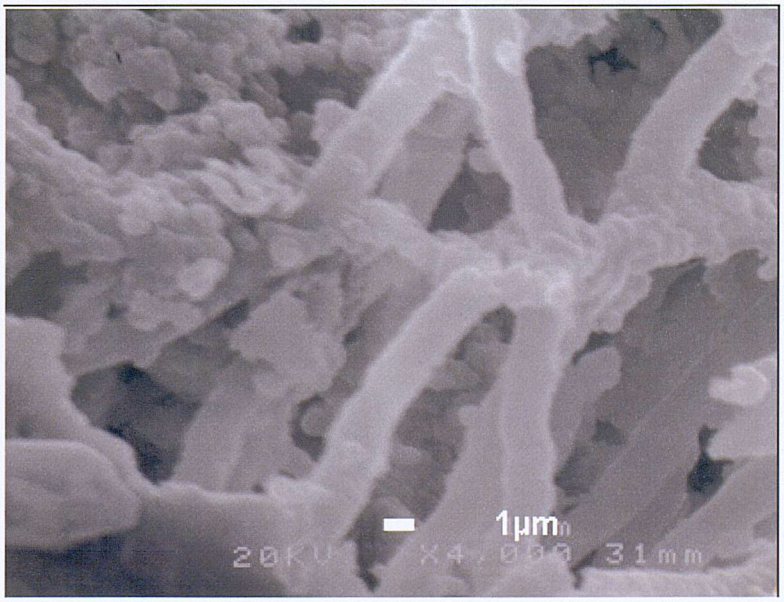

Figure 6.11c (left) - Where filaments form on the tube wall or associated barite precipitates, the filament networks extend out in three dimensions.

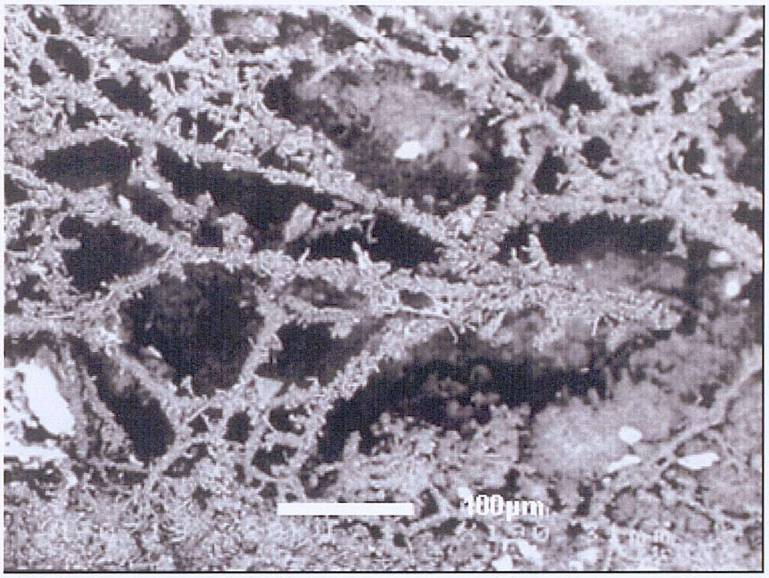

Figure 6.12a (left) – Mineralised microbial networks, encrusted with silica and barite laths

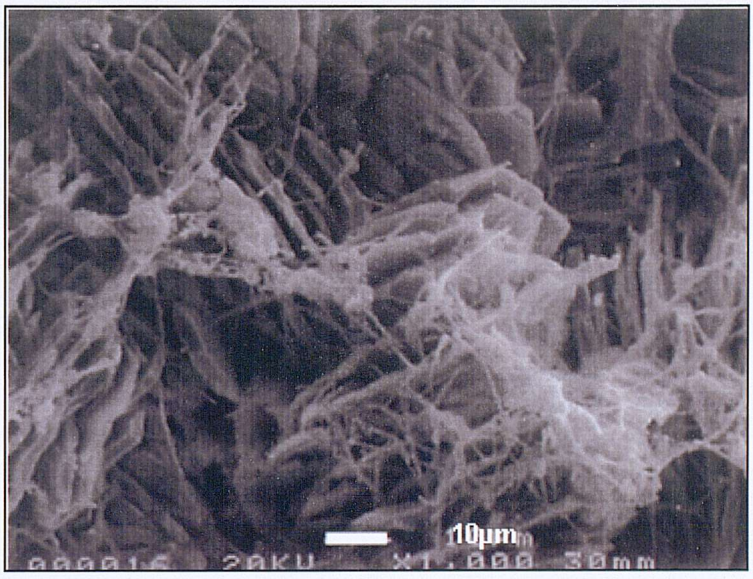

Figure 6.12b (right) - Thin stand-like microbial mucus filaments covering barite rosettes, which cover the outer surface of a tube structure.

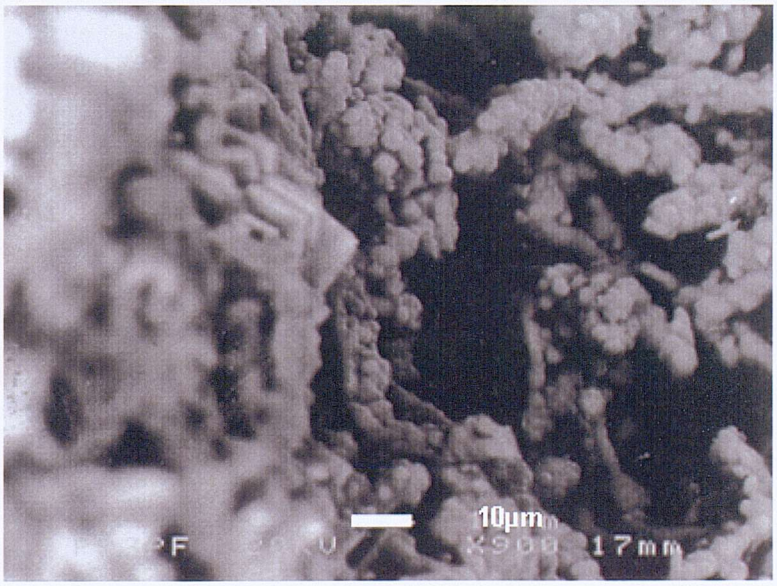

Figure 6.12c (left) – Botryoidal silica filiaments preserved on the outer tube surface, associated with barite mineral overgrowths.

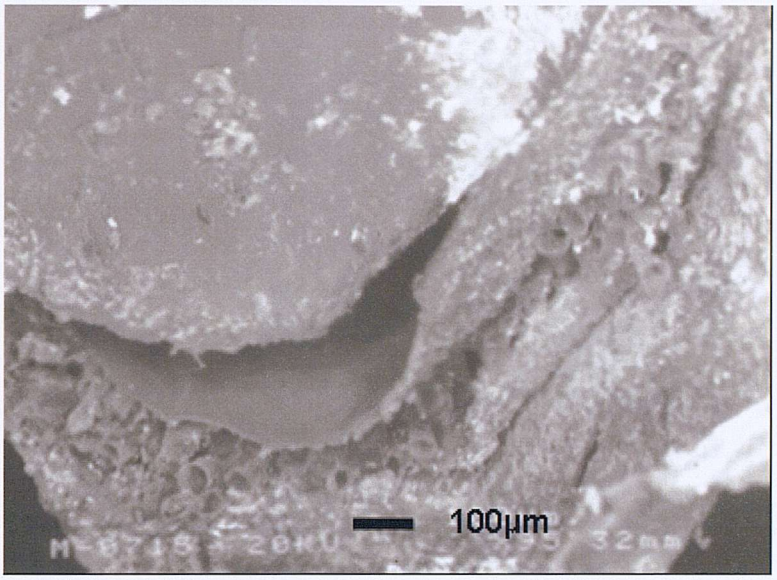

Figure 6.13a (left) – A terminal tube flange containing a number of (presumed) juvenile *R. piscesae* tubes.

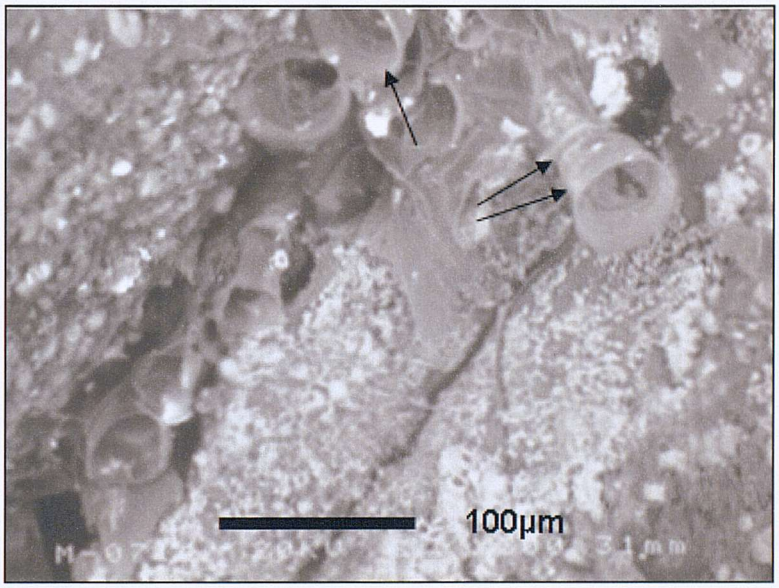

Figure 6.13b (right) - Juvenile tubes are morphologically similar to the adult *R. piscesae* tubes. Concentric growth lines (arrows) and longtitudinal wavey lines are often present.

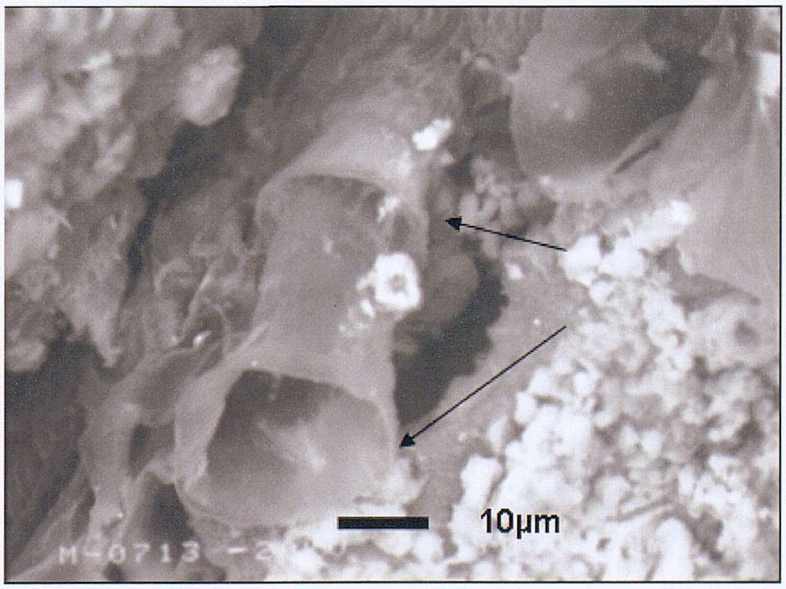

Figure 6.13c (left) – In this image a juvenile tube can be seen to exhibit terminal growth flanges (arrows). Terminal growth flanges are characteristic features observed in many hydrothermal tube worm species.

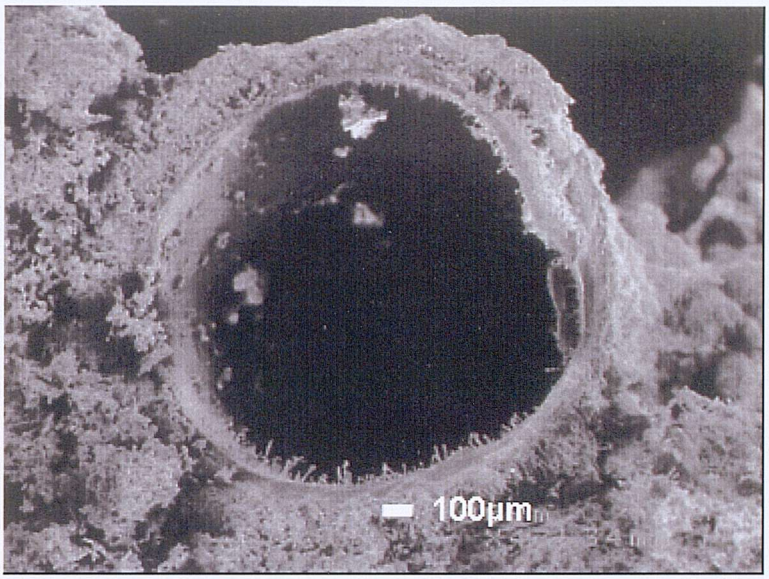

Figure 6.14a (left) – An uninhabited tube cut in cross-section displays mineralisation on the inner and outer surfaces.

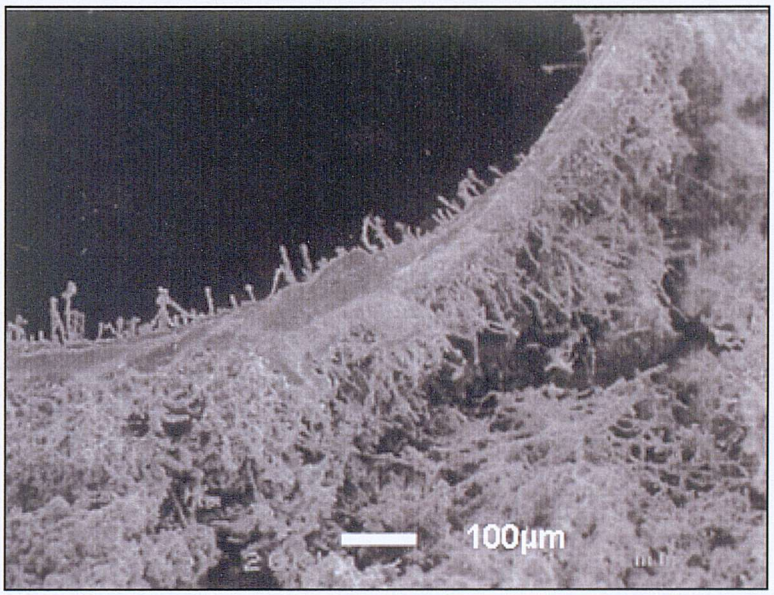

Figure 6.14b (right) – A magnified view of the tube wall shows that the filaments on the outer surface are dominantly formed of branching, dendritic filamentous networks.

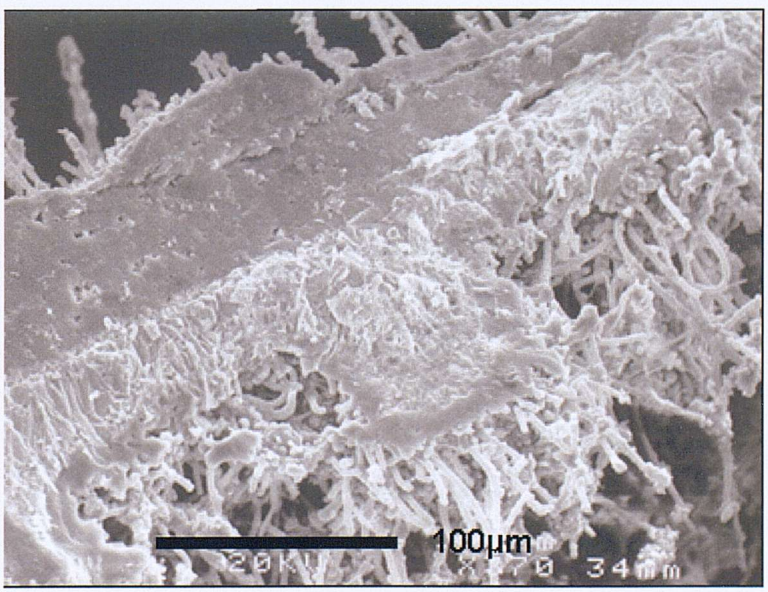

Figure 6.14c (left) – The filaments on the inner wall surface are single 'finger-like' filaments that grow outwards, towards the centre of the tube, into open space.

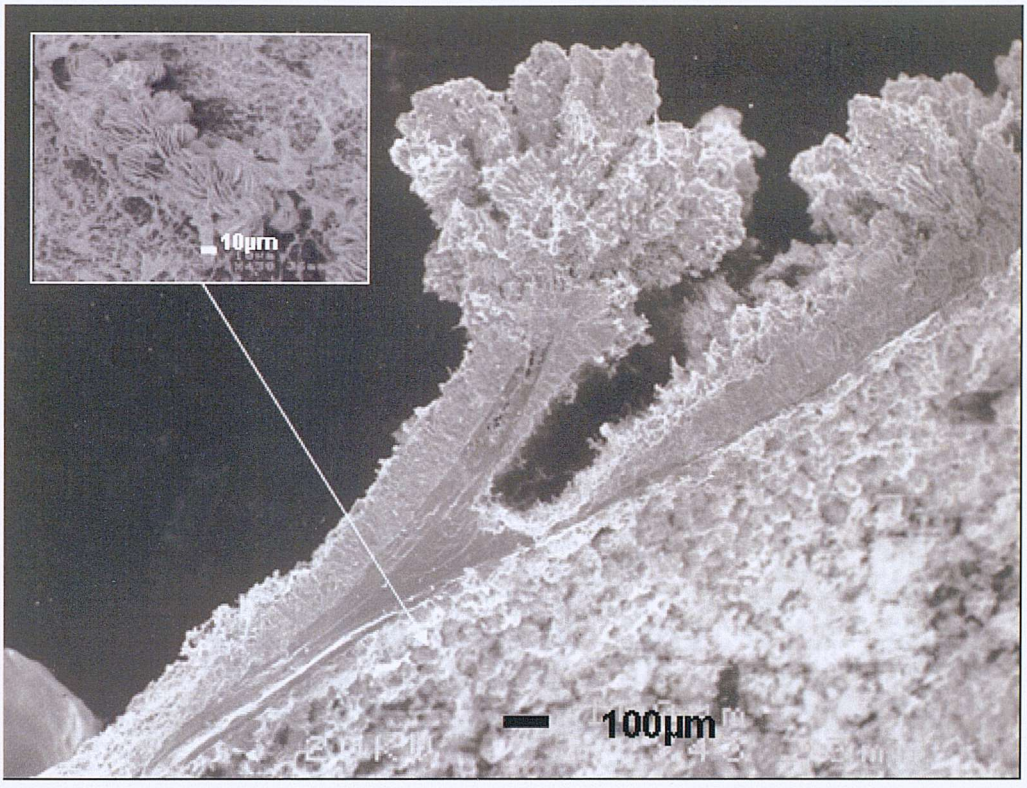

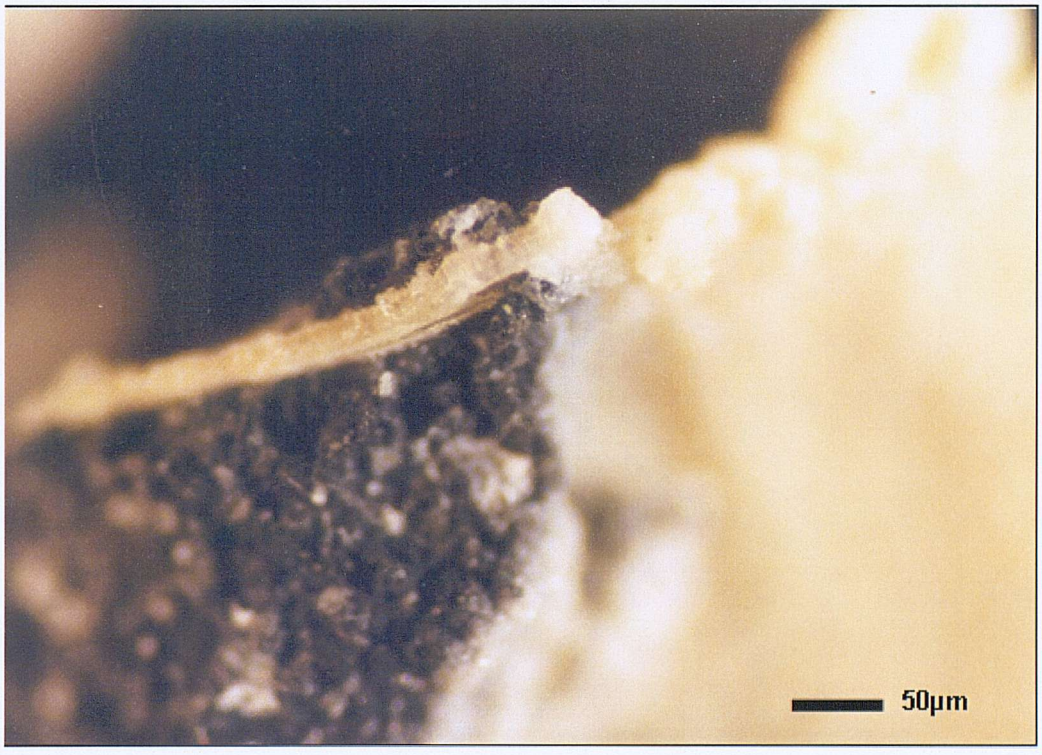

Figure 6.15a (top) – A cross-section of a mineralised tube centred on the a terminal flange section. The outer surface (especially the flange) is heavily mineralised. The inner surface is also mineralised by barite and siliceous filamentous structures (**insert**).

Figure 6.15b (bottom) – An isolated assemblage of metal-rich sulphide minerals precipitated on the inner and outer surfaces of a tube structure.

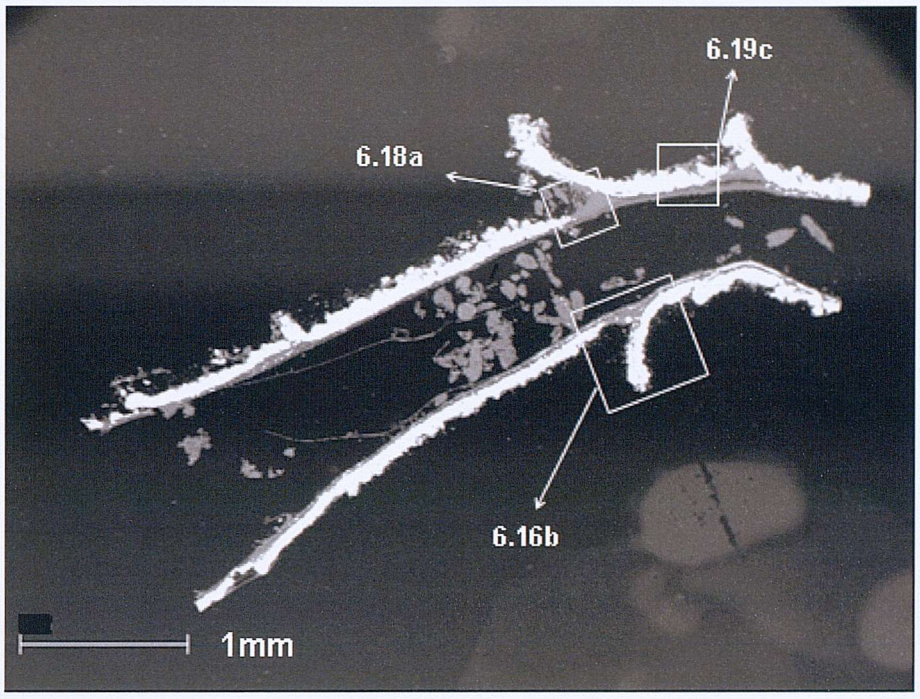

Figure 6.16a (top) - BSEI image of a cross- section of a tube structure showing multiple growth stages (as indicated by the numerous terminal flanges). The tube shows moderately extensive silica and barite mineralisation (silica-rich mieralisation = light grey: barit-rich mineralisation = white). The white boxes indicate magnified areas shown in other corresponding figures or used for geochemical analyses.

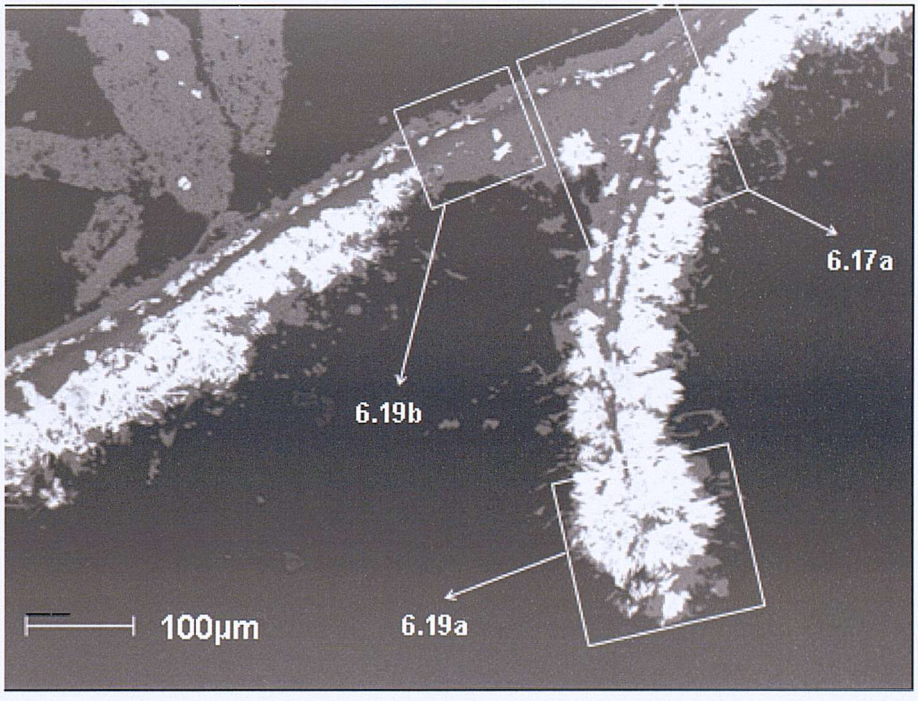

Figure 6.16b (bottom) – BSEI image of a magnified cross-section of a tube structure centred about a terminal flange, showing mineralisation of the tube wall (silica-rich mieralisation = light grey: barit-rich mineralisation = white). The white boxes indicate magnified areas shown in other corresponding figures or used for geochemical analyses.

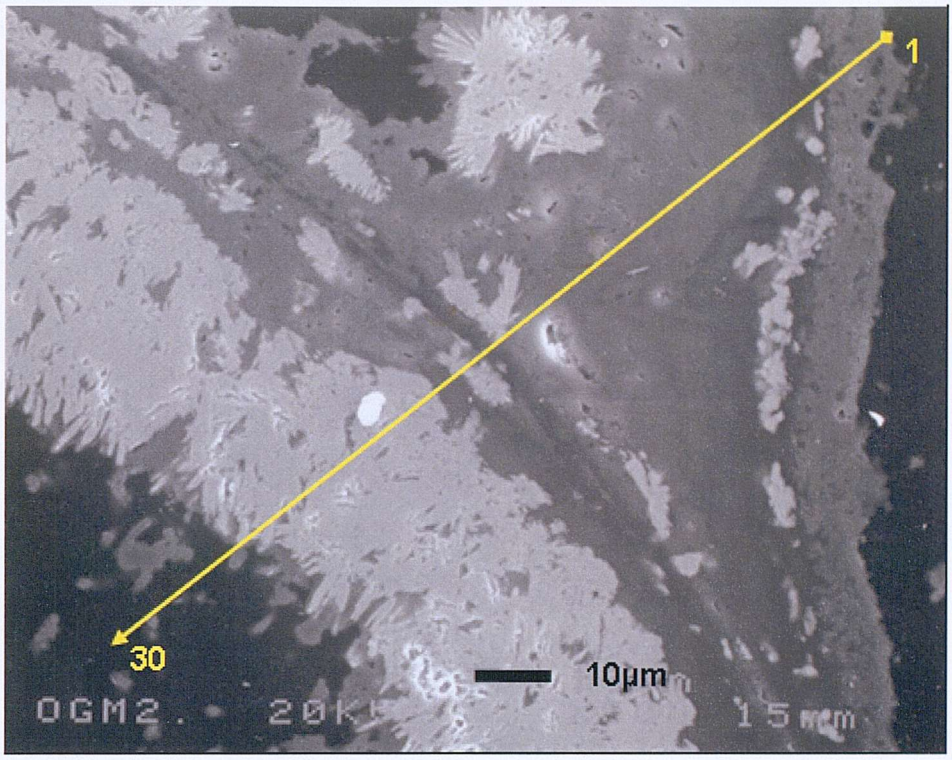

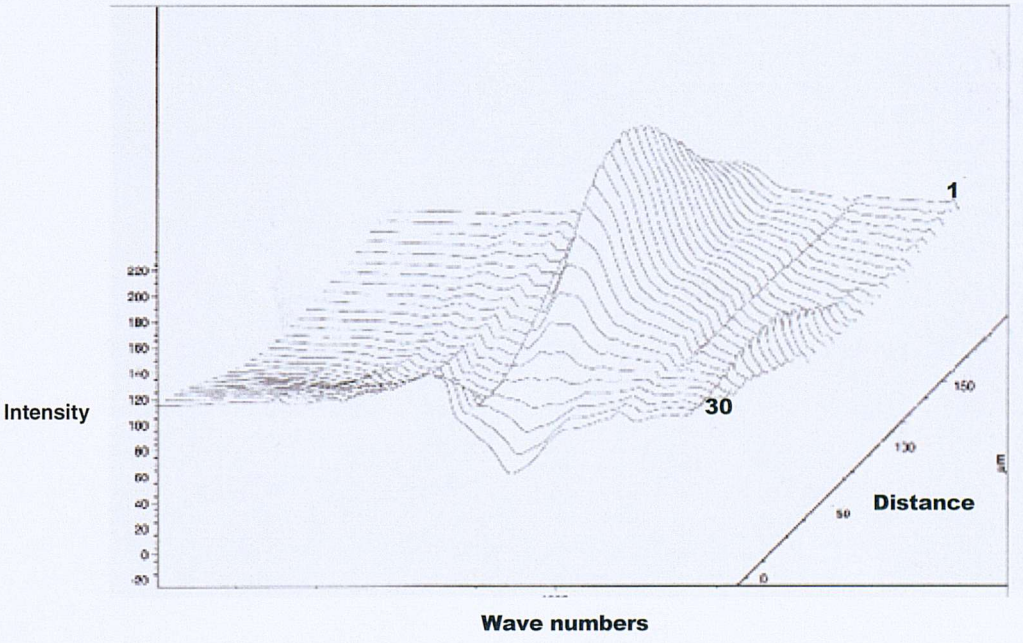

Figure 6.17a (top) – A cross-section of a terminal flange structure used to produce a 30 point FT-IR traverse through the relatively older tube wall, and into the relatively younger tube wall. Yellow arrow denotes traverse line, and corresponding first and last analysis points.

Figure 6.17b (bottom) – A spectral plot showing a 30 point FT-IR traverse with peaks at approximately 1650 cm^{-1} (OH bonds), 1100cm^{-1} (Si – O bonds), 800cm^{-1} (O-Si-O bonds) and 600cm^{-1} (s – O) bonds.

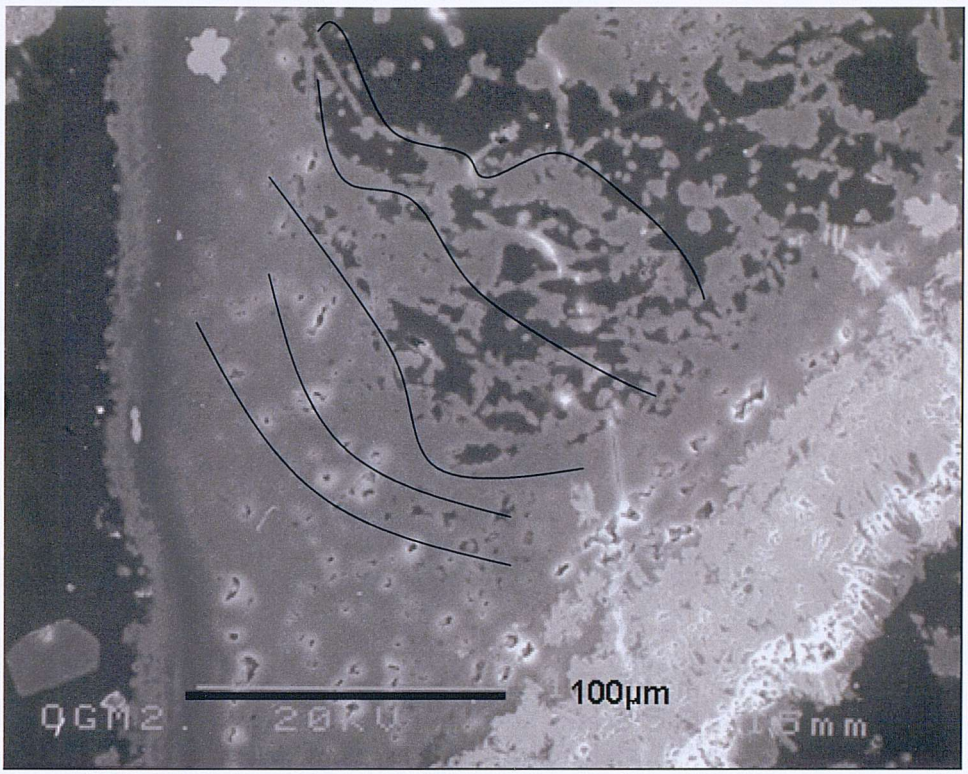

Figure 6.18a – Image to show the accumulation of progressive layers of silicified microbial filaments (indicated by black lines) in the juncture between a terminal flange and the outer tube surface.

Figure 6.19a (left) – Image located around the end of a terminal flange shows extensive barite mineralisation. 'Arrow a' shows the tip of the flange structure, which has been replaced by barite. Arrows b indicate inferred microbial cell ghosts within the barite precipitates encrusting the flange tip. Point analyses shown in later figures.

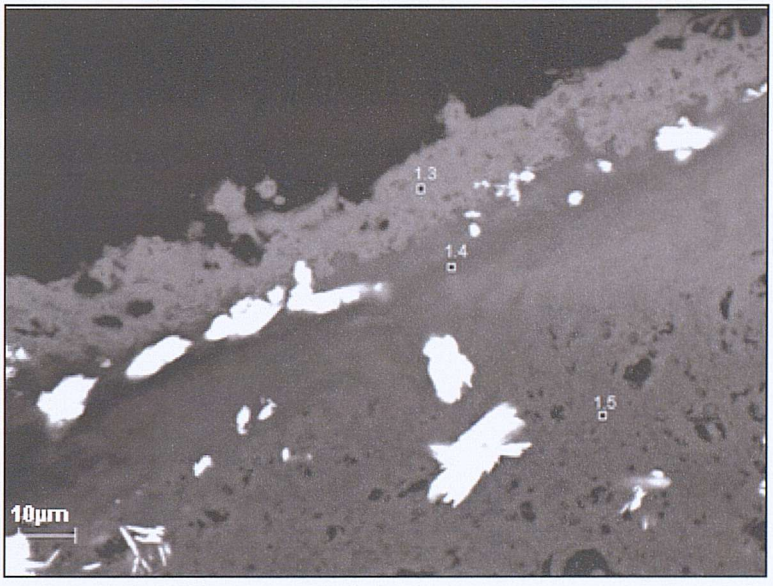

Figure 6.19b (right) – An area of tube wall used for EDS spot analysis (1.3 – 1.5). Inner tube surface located towards the top the frame.

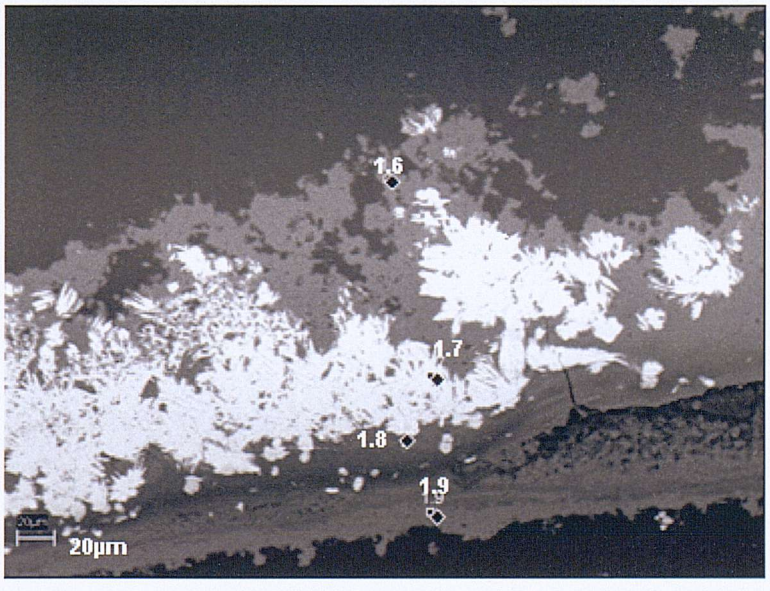

Figure 6.19c (left) - An area of tube wall used for EDS spot analysis (1.6 – 1.9). Inner surface is located towards the bottom of the frame.

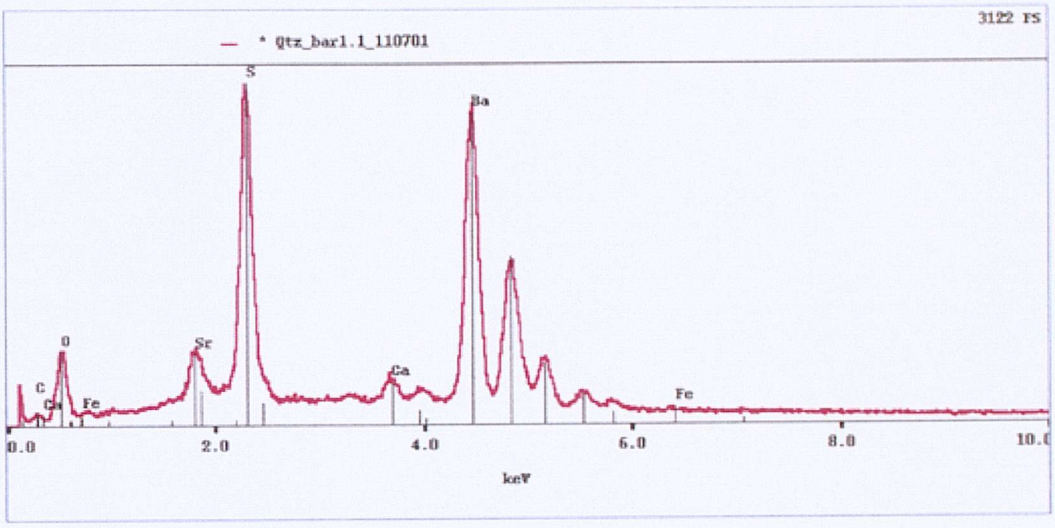

Figure 6.19a – EDS analysis of point 1.1

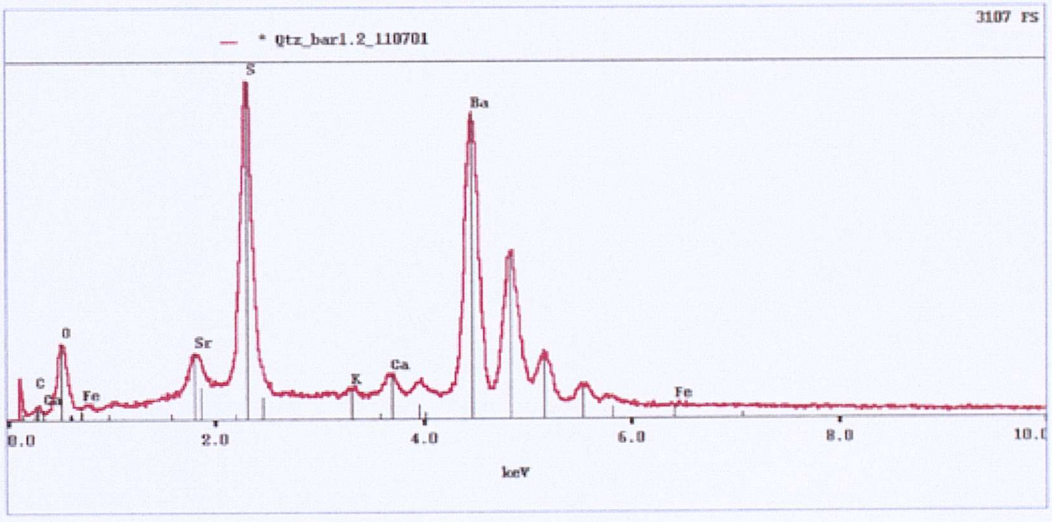

Figure 6.19a - EDS analysis of point 1.2

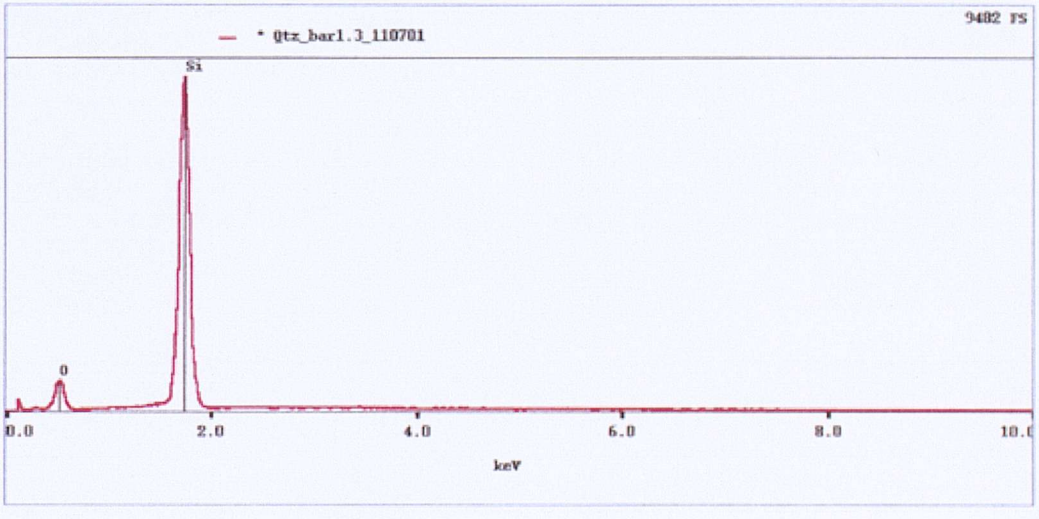

Figure 6.19b - EDS analysis of point 1.3

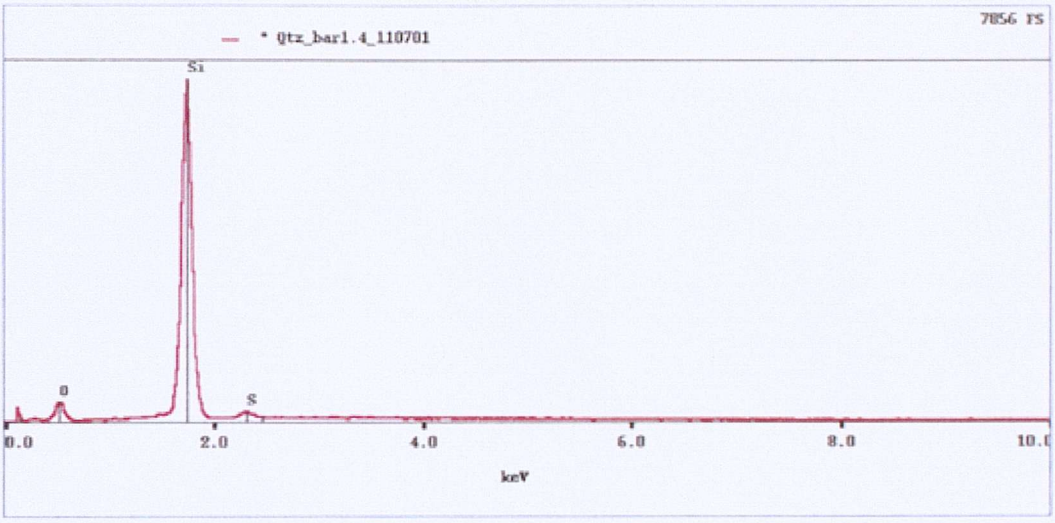

Figure 6.19b - EDS analysis of point 1.4

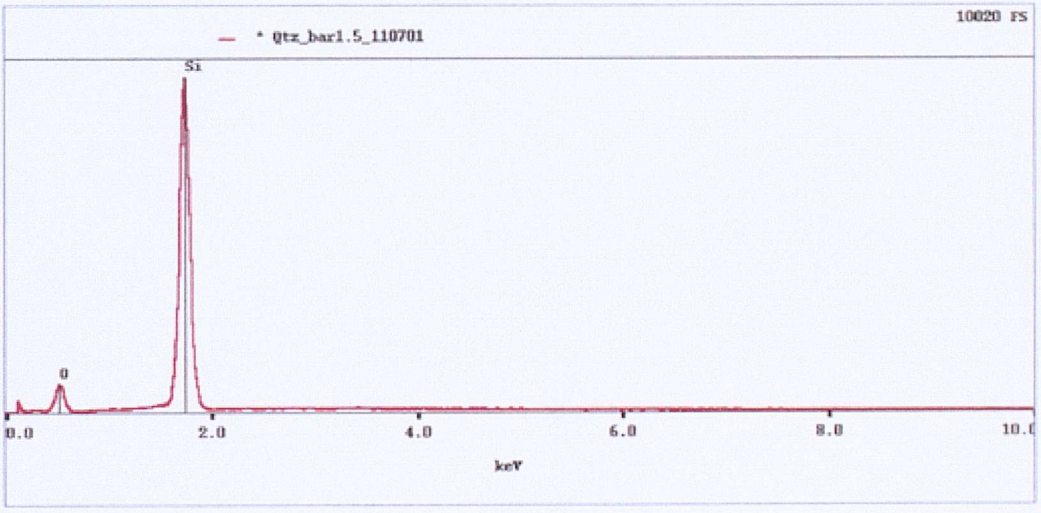

Figure 6.19b - EDS analysis of point 1.5

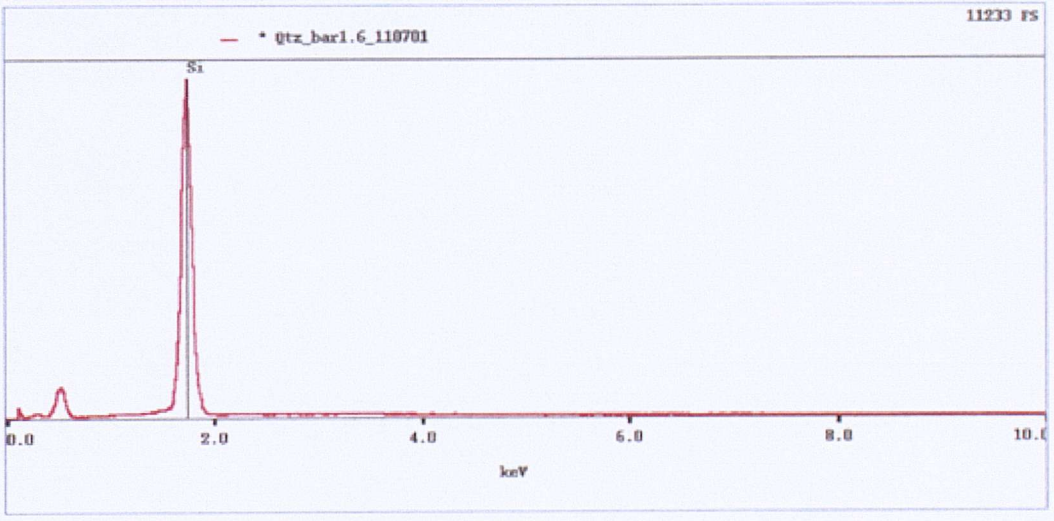

Figure 6.19c - EDS analysis of point 1.6

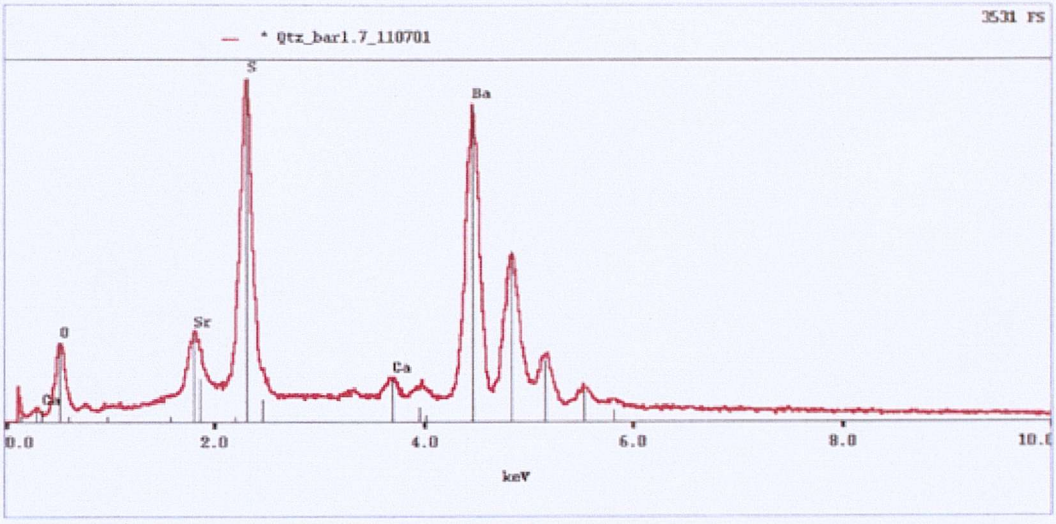

Figure 6.19c - EDS analysis of point 1.7

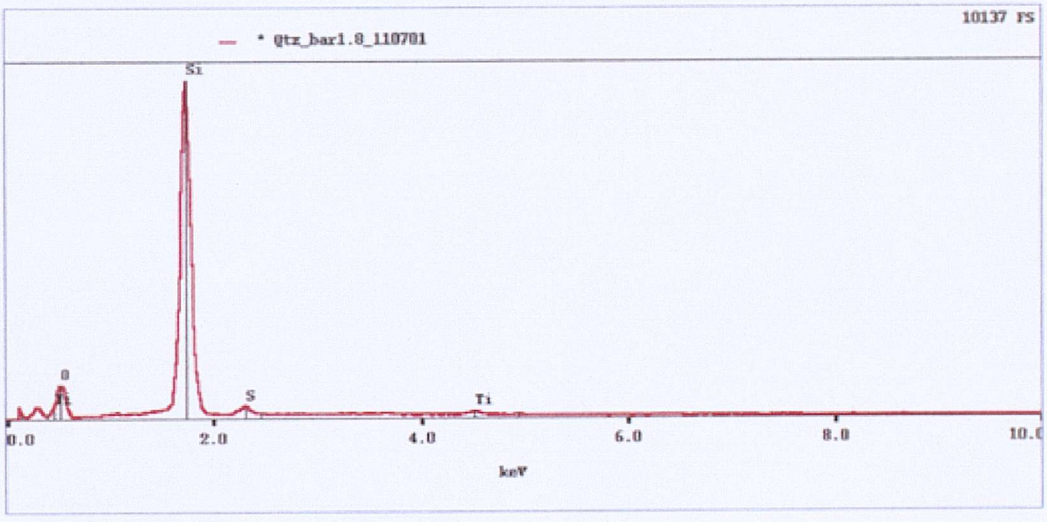

Figure 6.19c- EDS analysis of point 1.8

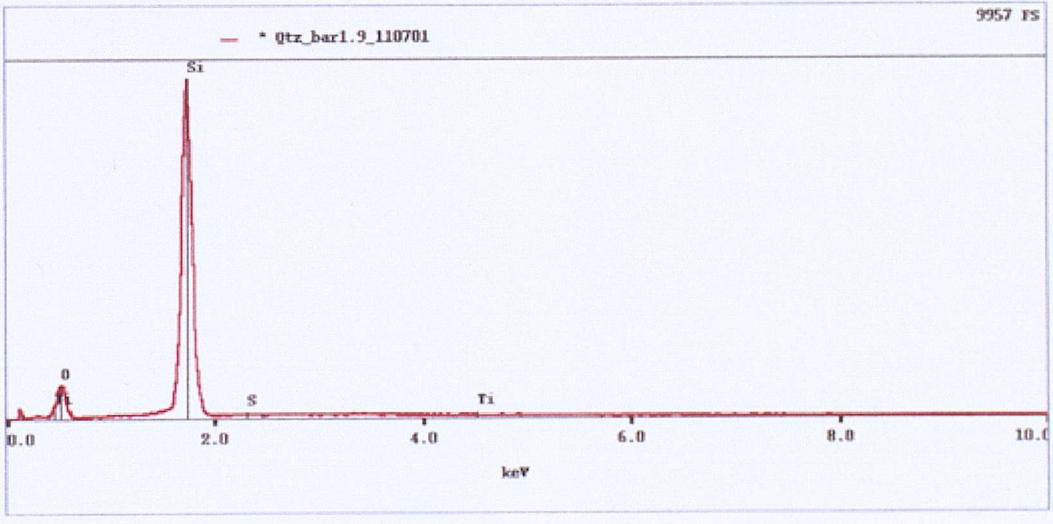

Figure 6.19c- EDS analysis of point 1.9

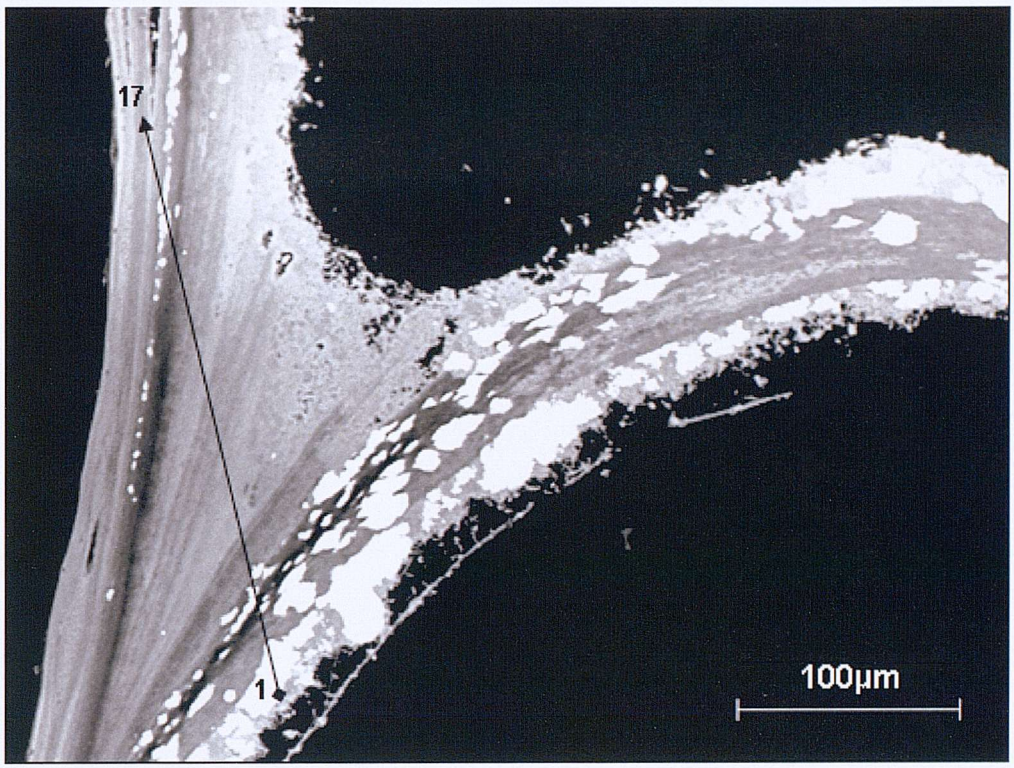

Figure 6.20a – An area of tube wall sectioned through a terminal growth flange, showing some internal structure due to overcontrasting of the image. Black arrow denotes traverse line, and corresponding first and last analysis points for data plotted in Figure 6.20b.

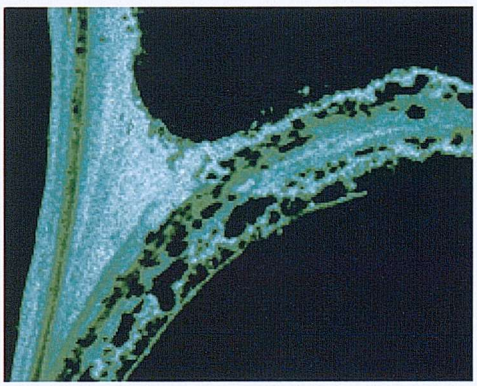

Figure 6.20 – Elemental map for silica.

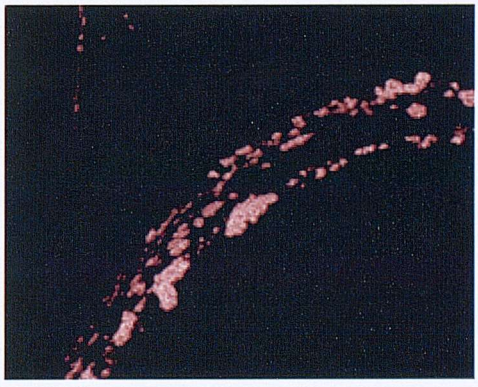

Figure 6.20 - Elemental map for barite.

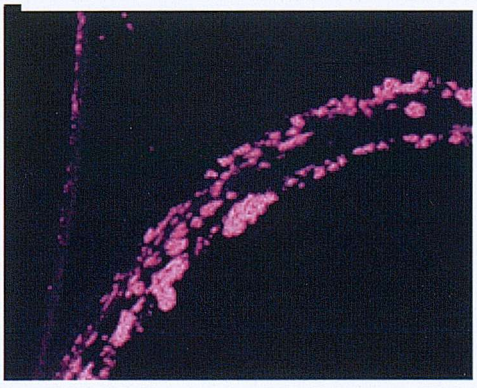

Figure 6.20 - Elemental map for sulphur.

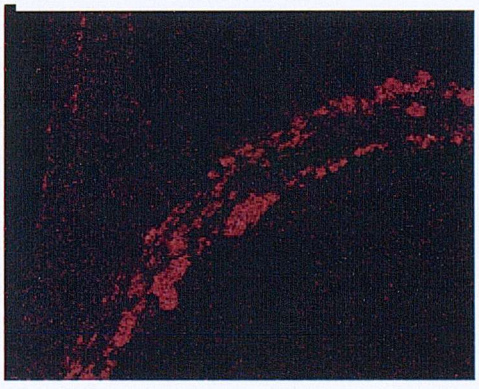

Figure 6.20 - Elemental map for phosporous

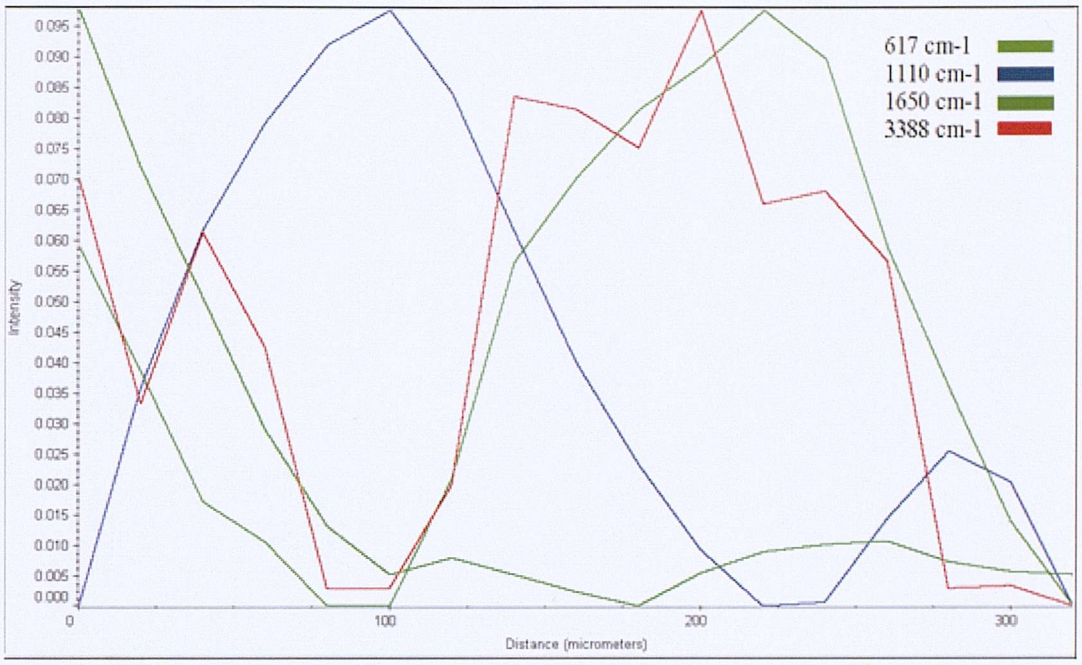

Figure 6.20(b) – Plot showing the maximum peak height for different spectral wavelengths for FT-IR traverse in Figure 6.20a.

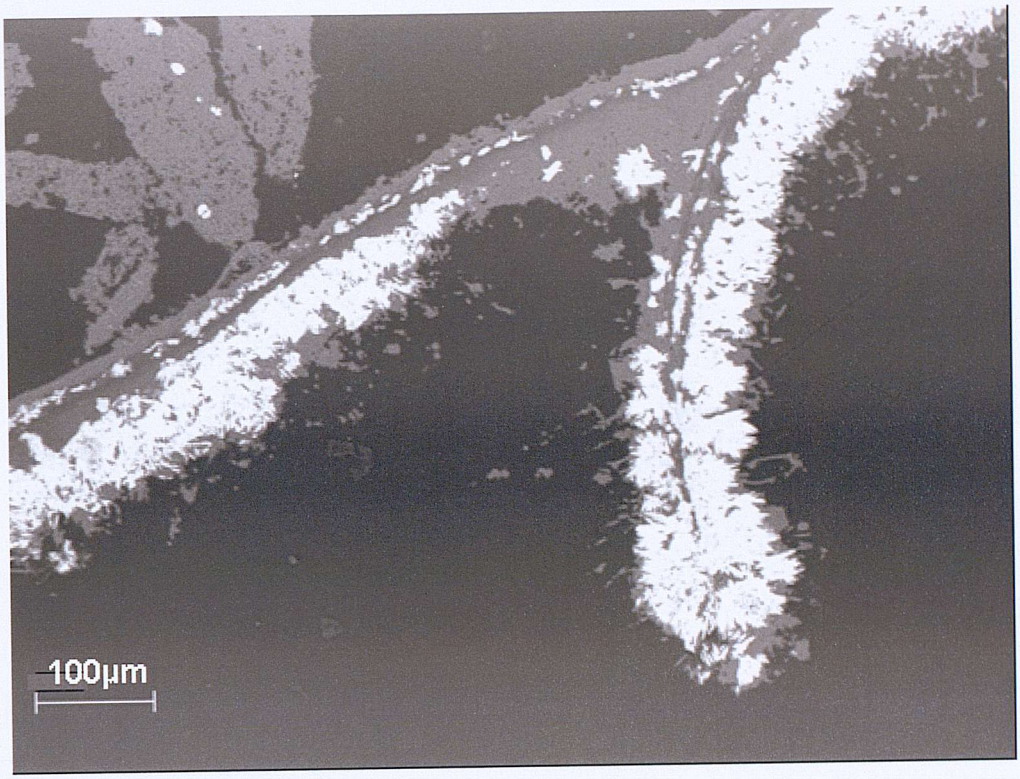

Figure 6.21 - An area of tube wall sectioned through a terminal growth flange. Inner surface located towards top left of frame.

Figure 6.21 - Elemental map for silica.

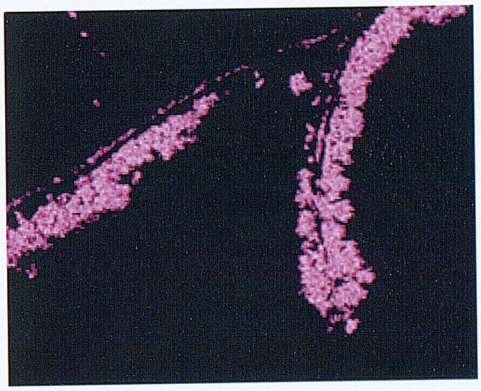

Figure 6.21 - Elemental map for barite.

Figure 6.21 - Elemental map for sulphur.

Figure 6.21 - Elemental map for phosporous.

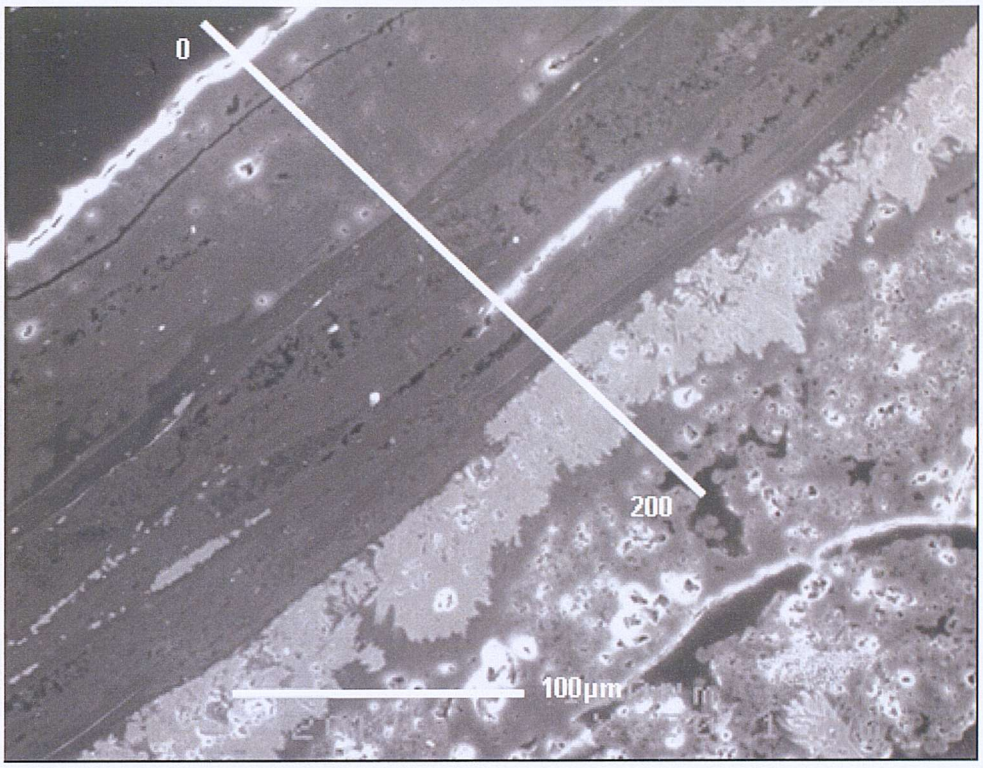

Figure 6.22a – An area of silicified tube wall mantled by barite and filamentous silica. White line marks the trace of a quantitative EMP traverse which runs from 0 – 200µm distance (Figures 6.22 b & c). The inner surface of the tube is located towards the top left of the frame.

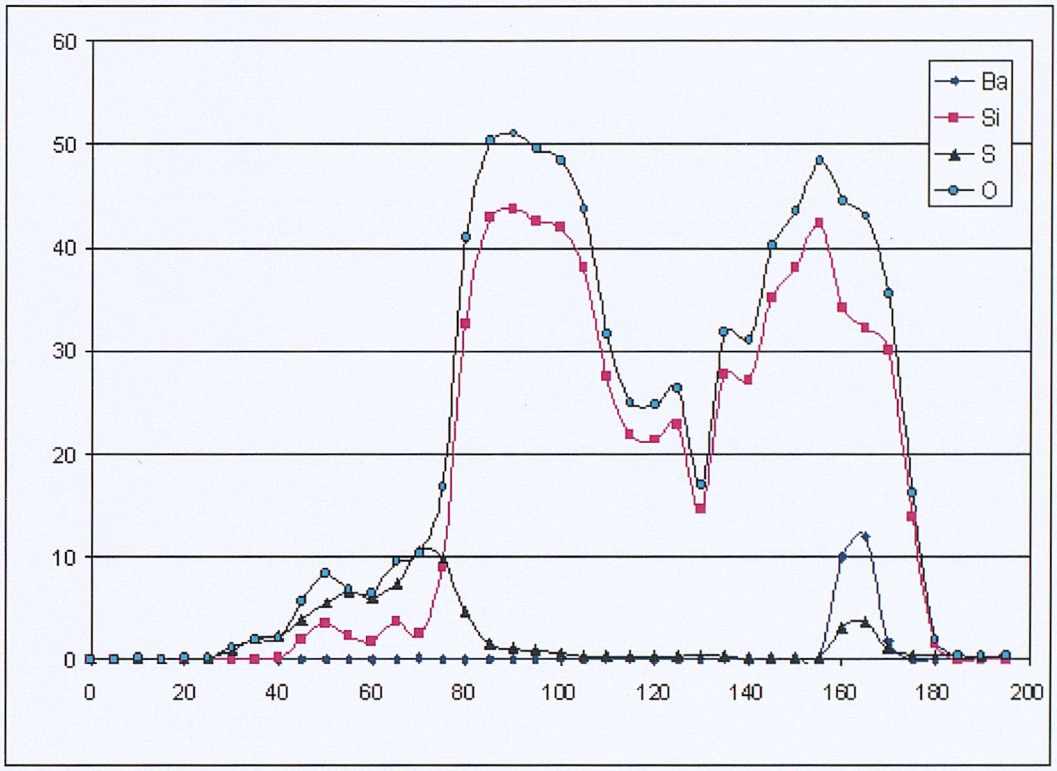

Figure 6.22b – Major elements measured using EMP from the scan-line 0 – 200 shown in Figure 6.22a.

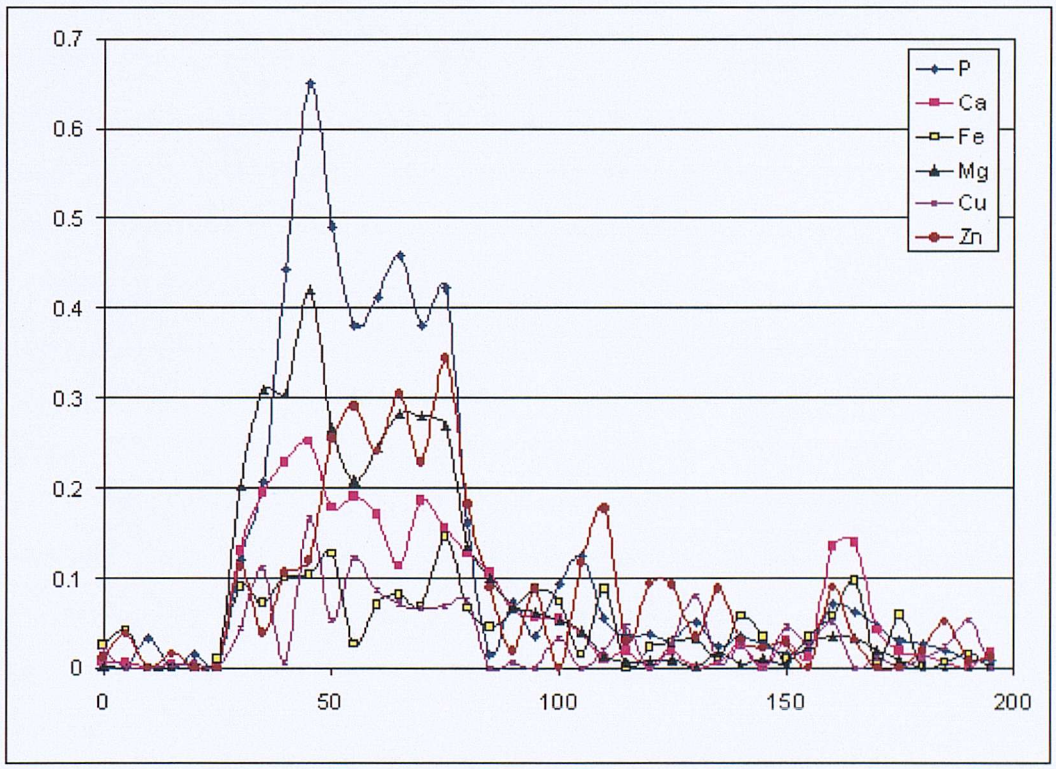

Figure 6.22c – Minor elements measured using EMP from the scan-line 0 – 200 shown in Figure 6.22a.

6.3.2 – Fairy Castle sample.

Preliminary light microscopic investigations of the Fairy Castle sample indicate that 150 – 200 individual worm tubes are contained within the 10 x 6 x 2 cm sulphidised block. Measurements of the tubes indicate that no single tube diameter exceeds 5mm, and generally diameter size ranges between 2 – 5mm. Tube wall thickness is estimated to be less than 0.5mm in all cases, however, the mineralised nature of some of the tubes makes this difficult to gauge accurately. The bulk mineralogical components of the sample are pyrite, sphalerite, silica, barite, and minor galena (PbS) and iron oxide minerals. Bulk geochemical analysis also identify Fe, Zn, S, Ba and Si as the major elements present.

6.3.1.1 – Textural observations and mineralogy.

The majority of the tube structures in the Fairy Castle sulphide, as bisected in cross section and therefore give a sense of orientation to the sample, (assuming that, like other samples, the worms tend to grow upwards and outwards: Figure 6.23a). The matrix is moderately well consolidated and exhibits a porous vuggy nature, with a mesh-like fabric throughout (Figure 6.23b). The lattice texture is manifest as an interworked concentric network of filaments at closer proximity to the tube structures (Figures 6.23c & d) The sample shows some areas of erosion, particularly on one side, and pitting (Figure 6.24a) and an associated coating of iron oxide over the matrix minerals and tubes (Figure 6.24b). Varying degrees and styles of mineralised infill of the tube structures is commonly observed. Of all the tubes structures present, approximately 50% exhibit a high degree of mineral infill (> 50%: e.g. Figure 6.24c); 30% exhibit a moderate degree of mineral infill (10 – 50%: e.g. Figure 6.24d); and < 20% have only a minor degree of infill (<10%: e.g. Figure 6.25a). The infill minerals are generally either oxidised minerals such as silica or barite, or reduced sulphide minerals. Figure 6.25b shows a tube partially infilled with silica spheroids, and another tube partially infilled with an aggregation of dendritic silica and barite. A close-up view of the same dendritic infill (Figure 6.25c) suggests that one side of the tube structure may have been replaced or over grown by the dendritic precipitate. Figure 6.25d is a silicified tube in transverse-section, that has been almost completely infilled with metal sulphide minerals. Within the inter-tube spaces, silicified filaments can be observed. Figure 6.26a shows a network of silicified mucus-

like filaments which may represent a mineralised biofilm. Closer inspection of the same area (Figure 6.26b) reveals a collection of mineralised globules which measure between 10 - 50μm, and may represent heavily mineralised individual microbial cells, or silicifed spherules. Figure 6.26c, shows the dendritic growth of epitaxial galena in an inter-tube pore space. It is likely that the galena has precipitated over the top of an acicular barite lath, such as that shown in Figure 6.26d, which are commonly found in the inter-tube voids, possibly indicating cooling of the local environmental fluids or a local change in fluid chemistry.

6.3.2.2 – Geochemistry

Figure 6.27 shows the thin section sample in detail, and the mapped tube areas used for geochemical analysis in this part of the study. Elemental maping and corresponding scan-line traverses were undertaken for five areas of the sample. Figures 6.28, 6.29, & 6.30 show maps and traverses for three different areas of the same tube. Whereas the two other areas analysed (Figures 6.31 & 6.32) are both from separate tubes.

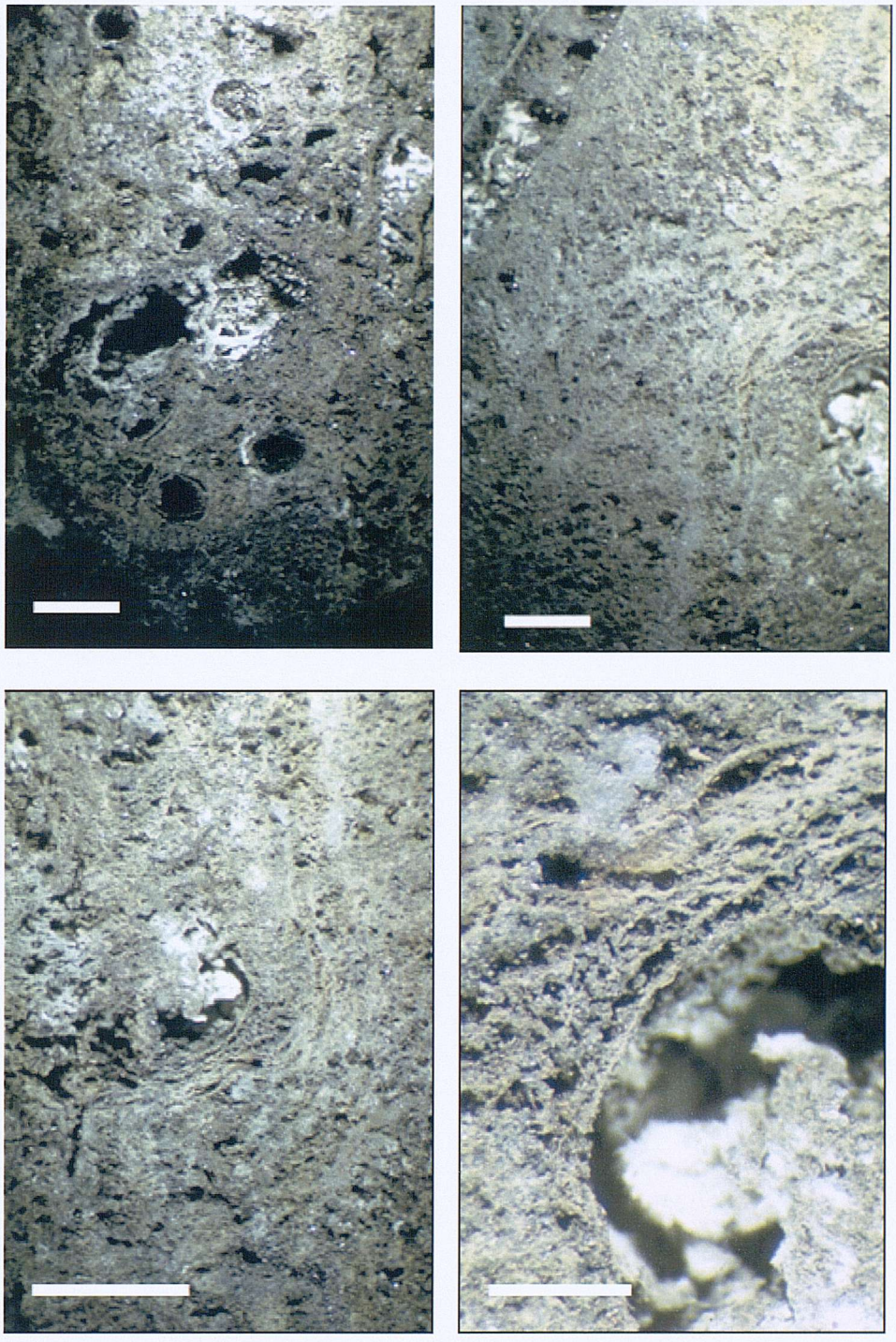

Figure 6.23a (top left) – A randomly distributed scattering of tubes can be seen in cross-section. Scale bar = 3mm

Figure 6.23b (top right) – A porous, mesh-like matrix is present, formed from sulphide minerals. Scale bar = 3mm

Figure 6.23c (bottom left) – A concentric fabric can be seen to envelope many of the mineralised tube structures. Scale bar = 2mm

Figure 6.23d (bottom right) – At higher magnifications the filamentous nature of the matrix is revealed. Scale bar = 500μm

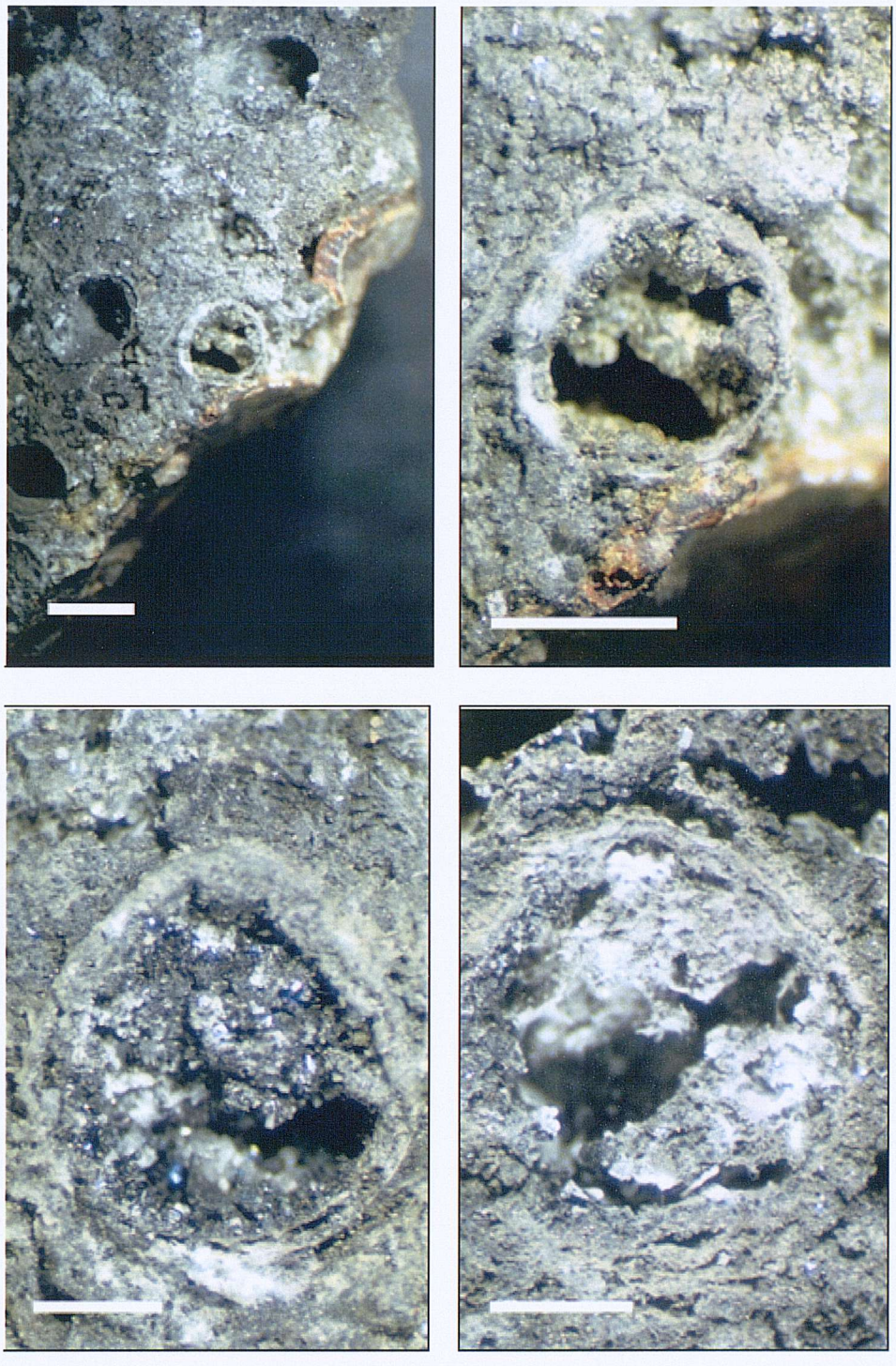

Figure 6.24a (top left) – Weathered surfaces of the sample are pitted and eroded, and are coated in a thin oxide veneer likely formed after the sample had broken or fallen away from the main chimney structure that produced the sample. Scale bar = 3mm

Figure 6.24b (top right) – The porous nature of the matrix, allows for a shallow penetration of oxide minerals into the specimen. Scale bar = 3mm

Figure 6.24c (bottom left) – A tube structure displaying a high degree of mineral infill. Scale bar = 2mm

Figure 6.24d (bottom right) – A tube structure displaying a moderate degree of mineral infill. Scale bar = 1.5mm

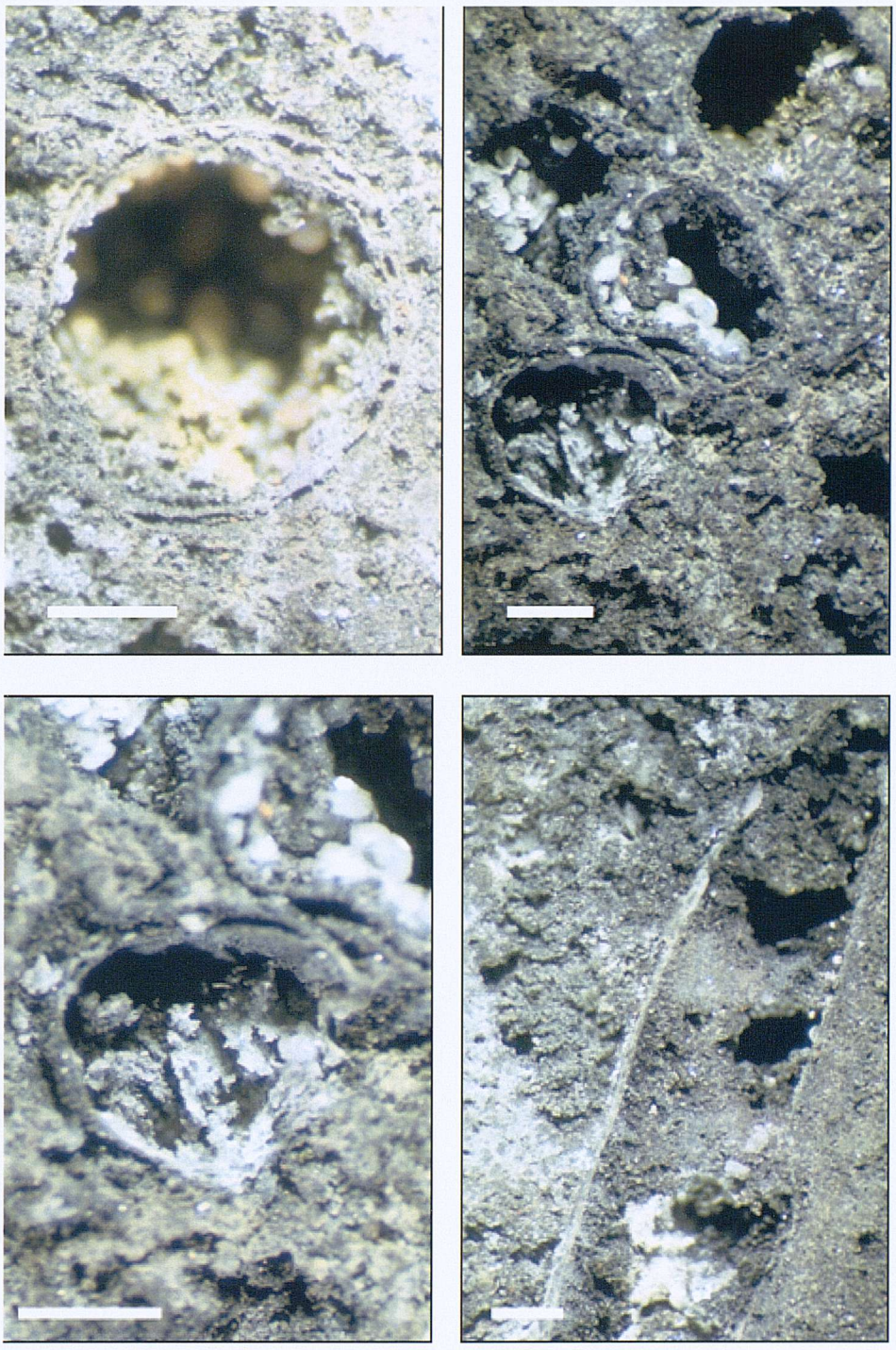

Figure 6.25a (top left) – A tube structure displaying a small degree of mineral infill. Scale bar = 1mm.

Figure 6.25b (top right) – Adjacent tube structures may exhibit different styles of infill mineralisation. The tube in the centre of the frame contains spheroids of silica, whereas the tube adjacent to it (below) contains radiating dendritic silica precipitates. Scale bar = 1mm.

Figure 6.25c (bottom left) – At high magnification the lower tube structure appears to have been partially infilled by dendritic silica. Scale bar = 1mm.

Figure 6.25d (bottom right) – In trans-section this tube structure can be seen to be clogged by sulphide minerals. Scale bar = 500μm.

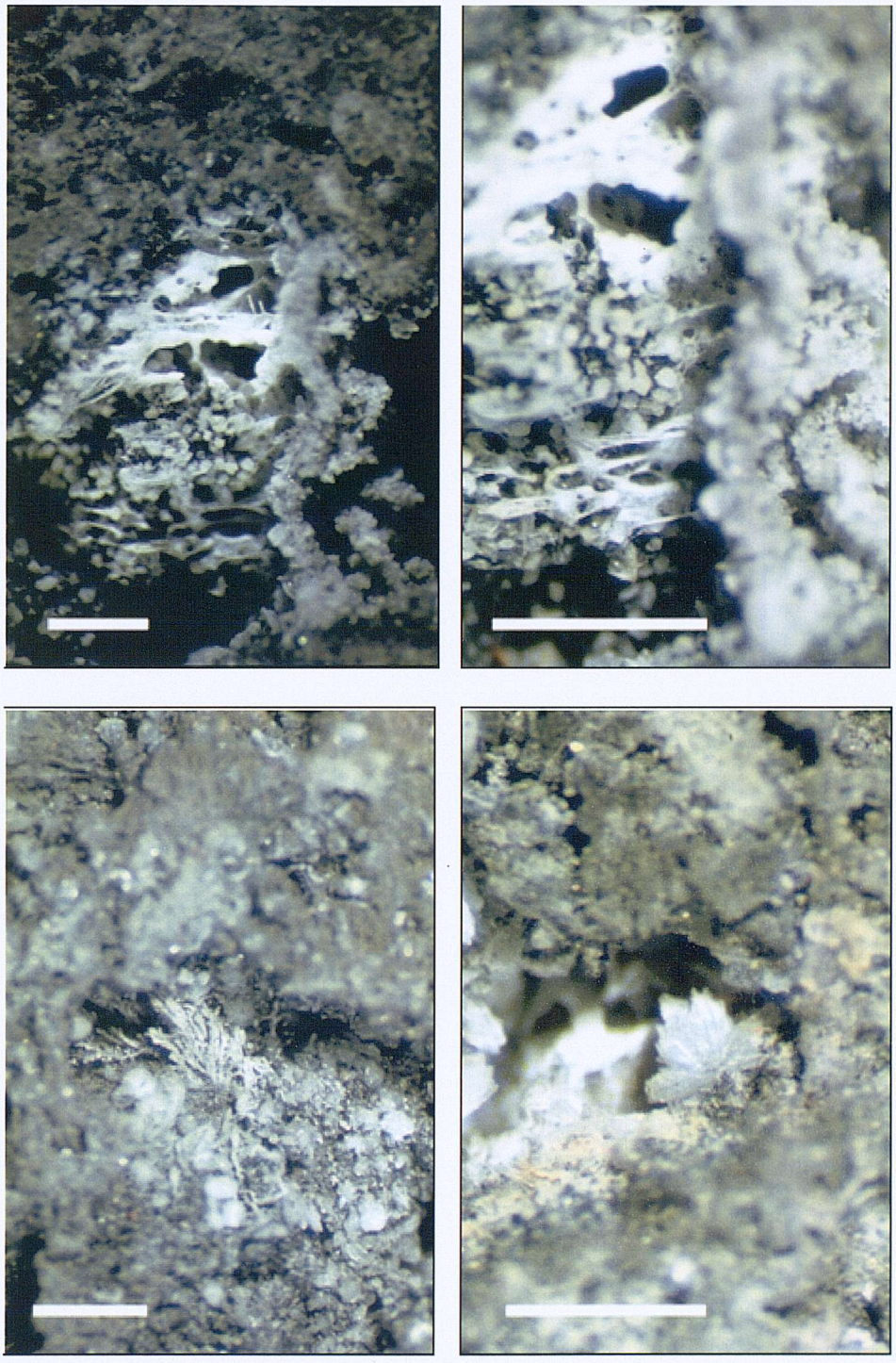

Figure 6.26a (top left) – An inter-tube pore space containing a silicified biofilm. Scale bar = 45μm.

Figure 6.26b (top right) – At higher magnification strands of mucus can be seen to be preserved by silica mineralisation. Scale bar = 50μm.

Figure 6.26c (bottom left) – Epitaxial galena forms a dendritic precipitate in a pore space. Scale bar = 200μm.

Figure 6.26d (bottom right) – A rosette of barite forms a characteristic 'cocks-comb' structure in an inter-tube pore space Scale bar = 200μm.

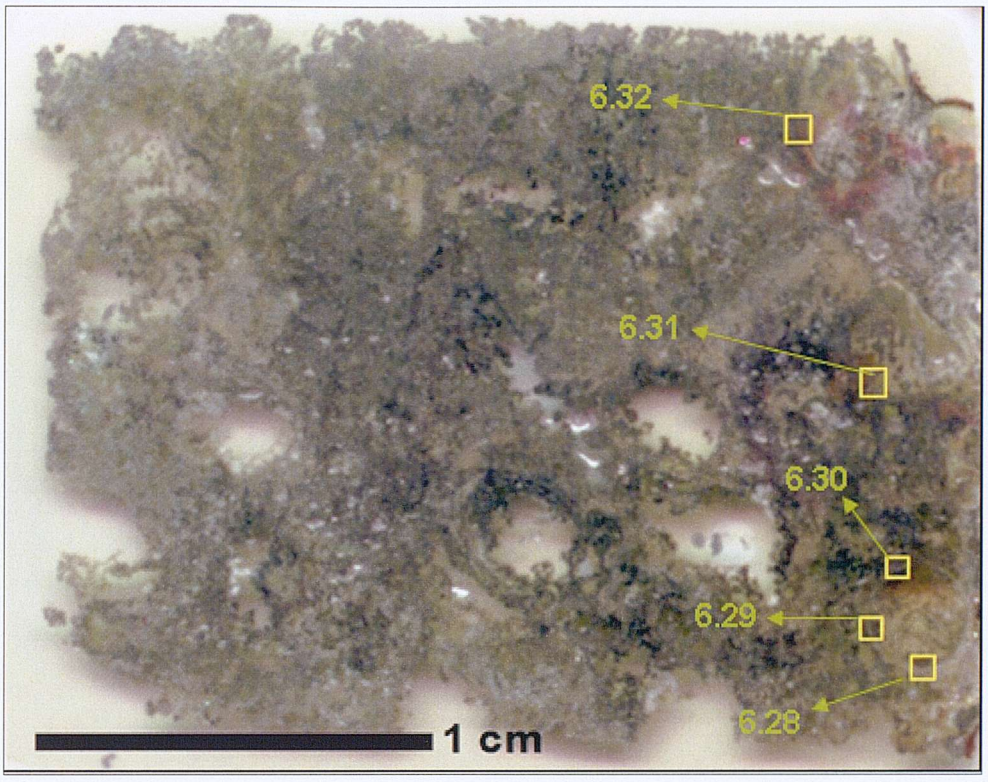

Figure 6.27 – Sample HRF3A showing the spatial relationship between the areas analysed by qualitative and quantitative elemental mapping techniques.

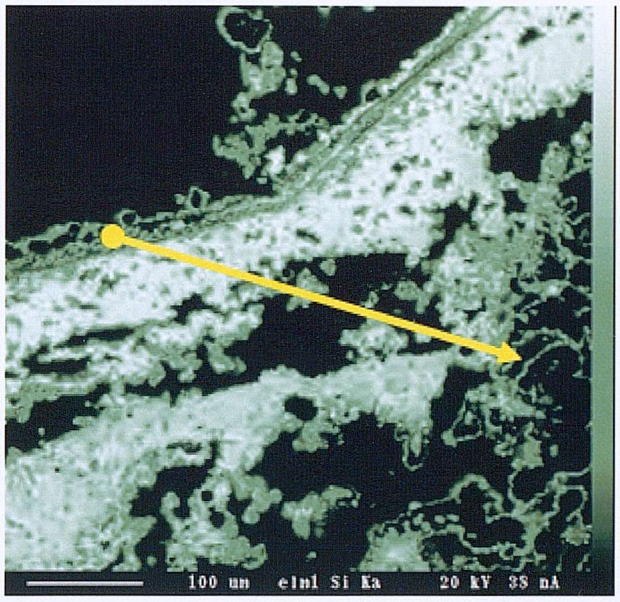

Figure 6.28a (left) – Qualitative EDS elemental map for silica centered about an area of mineralised tube wall. Yellow arrow represents the quantitative elemental traverse trace. Note Figures 6.28 a-e are elemental distribution patterns from the same area.

Figure 6.28b (right) – Qualitative EDS elemental map for barite centered about an area of mineralised tube wall

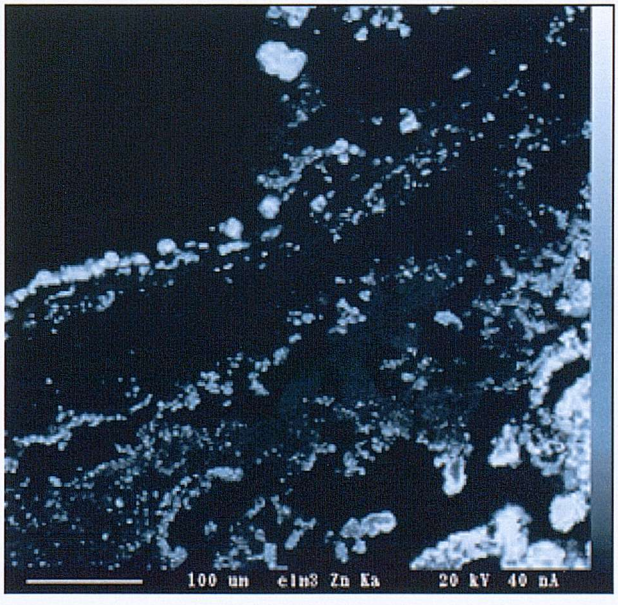

Figure 6.28c (left) - Qualitative EDS elemental map for zinc centered about an area of mineralised tube wall.

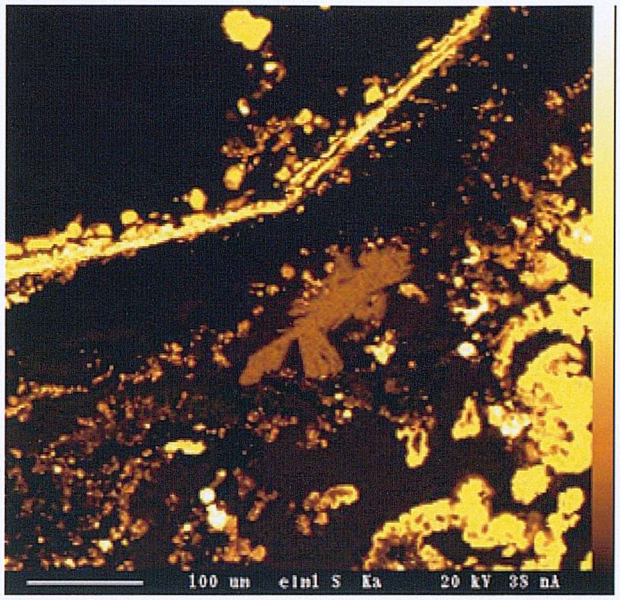

Figure 6.28d (left) - Qualitative EDS elemental map for sulphur centered about an area of mineralised tube wall.

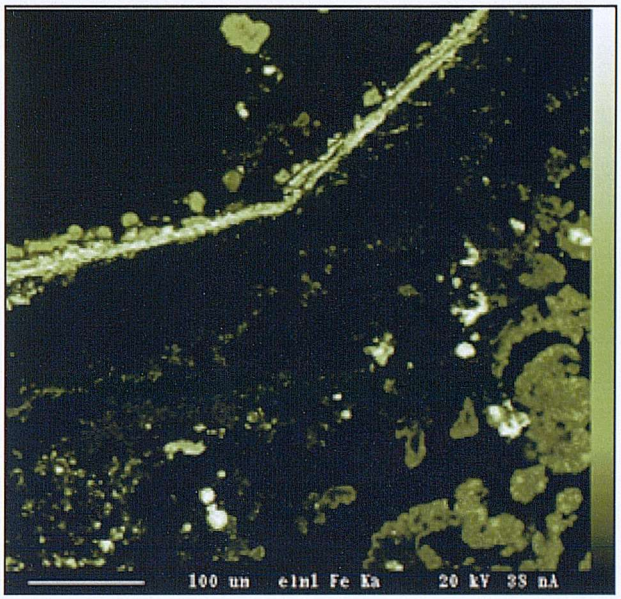

Figure 6.28e (left) - Qualitative EDS elemental map for iron centered about an area of mineralised tube wall.

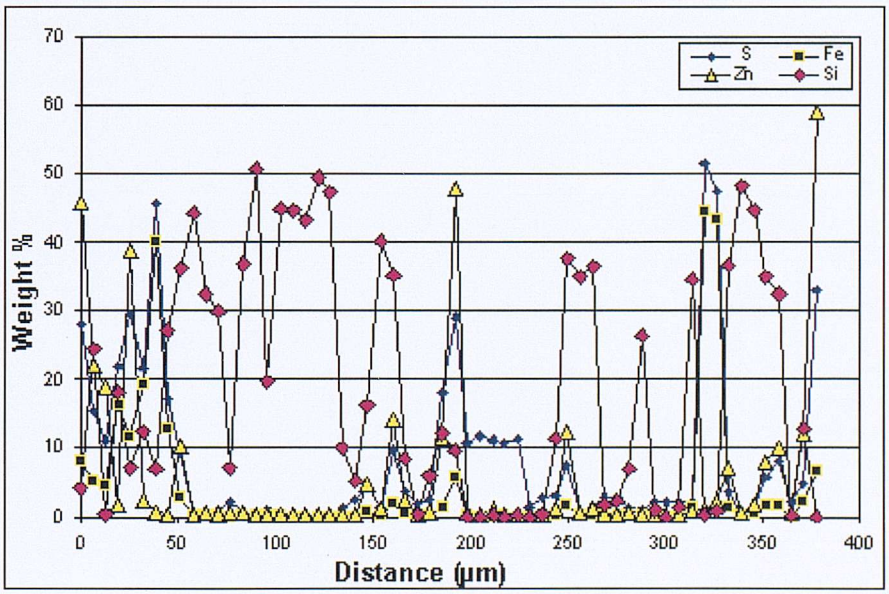

Figure 6.28f (left) – Quantitive EDS scan-line traverse measuring the major mineralogical components (S, Fe, Zn, Si), weight % vs

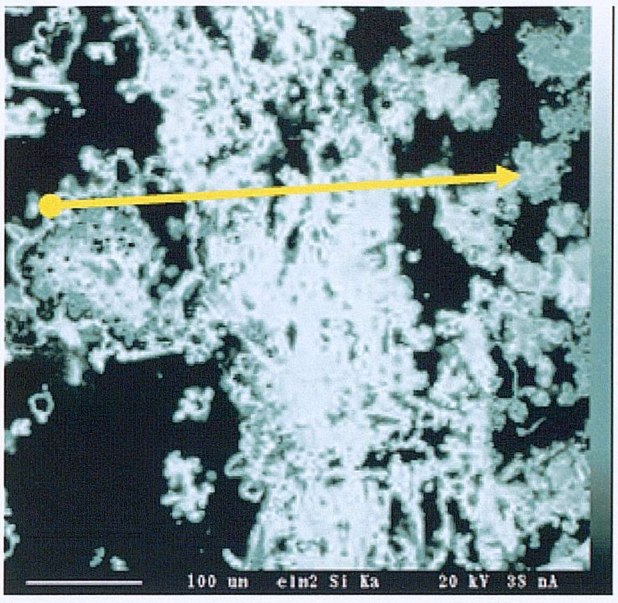

Figure 6.29a (left) - Qualitative EDS elemental map for silica centered about an area of mineralised tube wall. Yellow arrow represents the quantitative elemental traverse trace. Note Figures 6.29 a-e are elemental distribution patterns from the same area.

Figure 6.29b (right) - Qualitative EDS elemental map for barite centered about an area of mineralised tube wall.

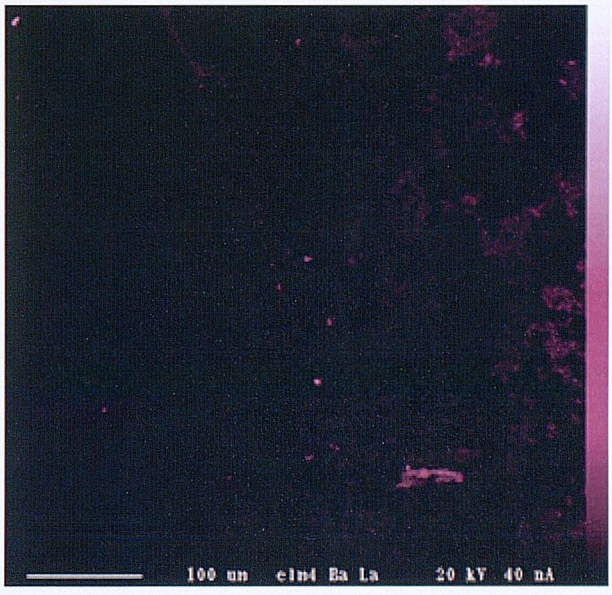

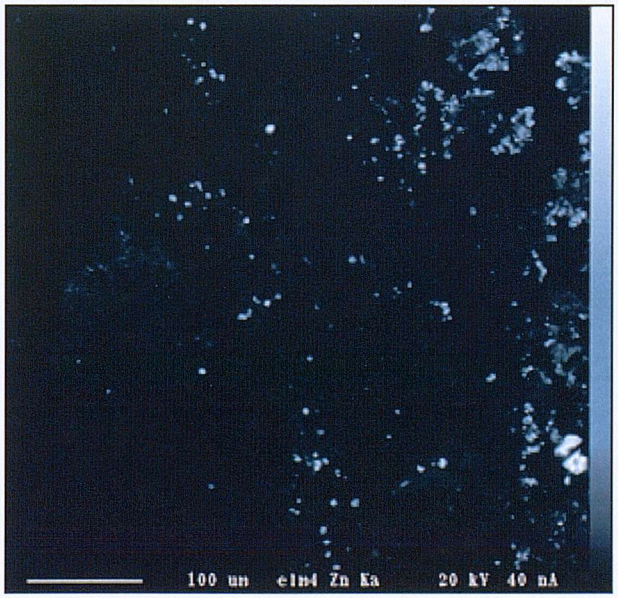

Figure 6.29c (left) - Qualitative EDS elemental map for zinc centered about an area of mineralised tube wall.

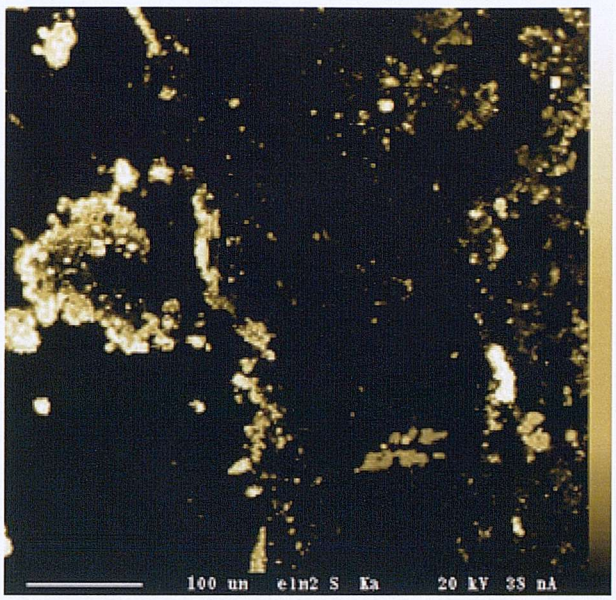

Figure 6.29d (left) – Qualitative EDS elemental map for sulphur centered about an area of mineralised tube wall.

Figure 6.29e (left) – Qualitative EDS elemental map for iron centered about an area of mineralised tube wall.

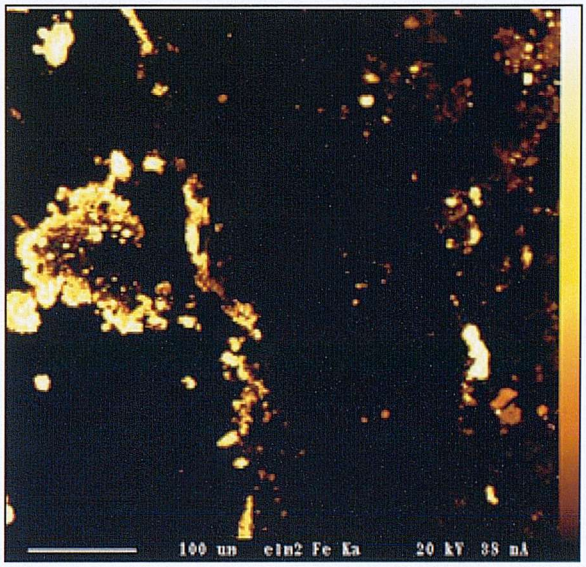

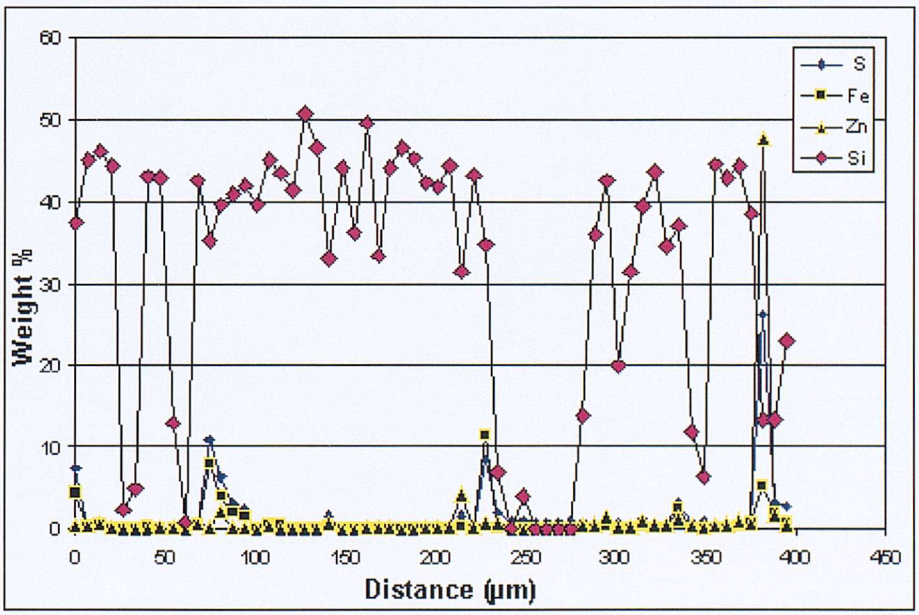

Figure 6.29f (left) – Quantitive EDS scan-line traverse measuring the major mineralogical components (S, Fe, Zn, Si), weight % vs distance.

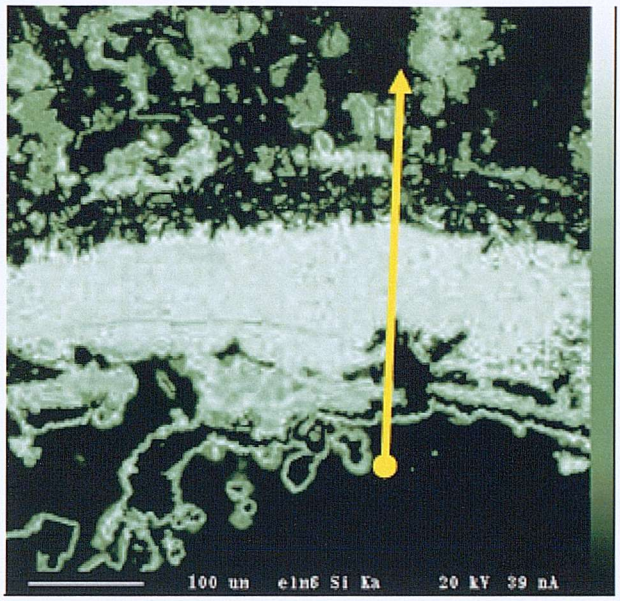

Figure 6.30a (left) - Qualitative EDS elemental map for silica centered about an area of mineralised tube wall. Yellow arrow represents the quantitative elemental traverse trace. Note Figures 6.30 a-e are elemental distribution patterns from the same area.

Figure 6.30b (right) - Qualitative EDS elemental map for barite centered about an area of mineralised tube wall

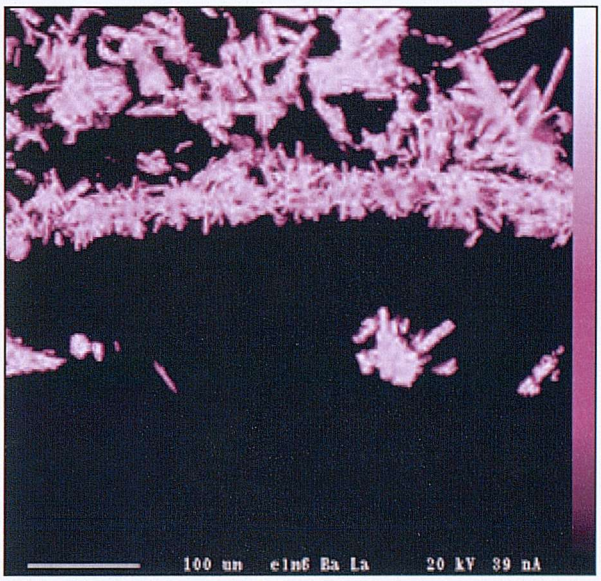

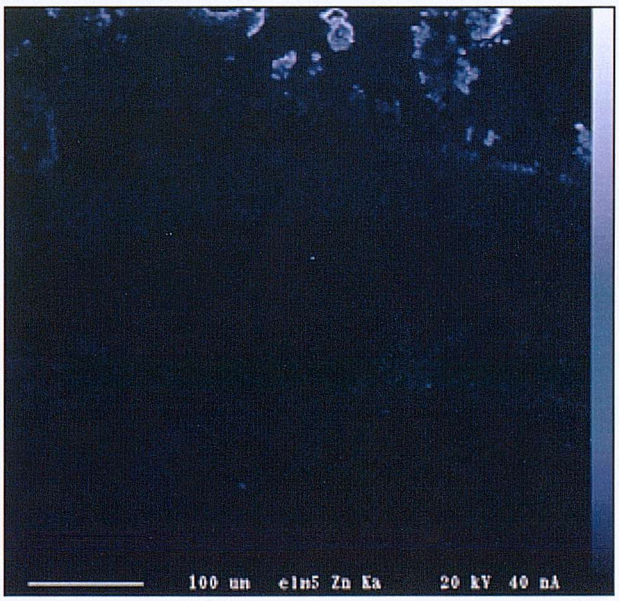

Figure 6.30c (left) - Qualitative EDS elemental map for zinc centered about an area of mineralised tube wall.

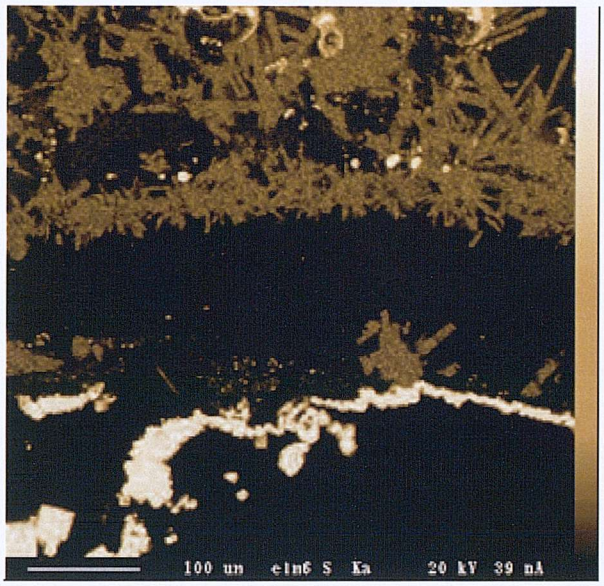

Figure 6.30d (left) - Qualitative EDS elemental map for sulphur centered about an area of mineralised tube wall.

Figure 6.30e (left) – Qualitative EDS elemental map for Iron centered about an area of mineralised tube wall.

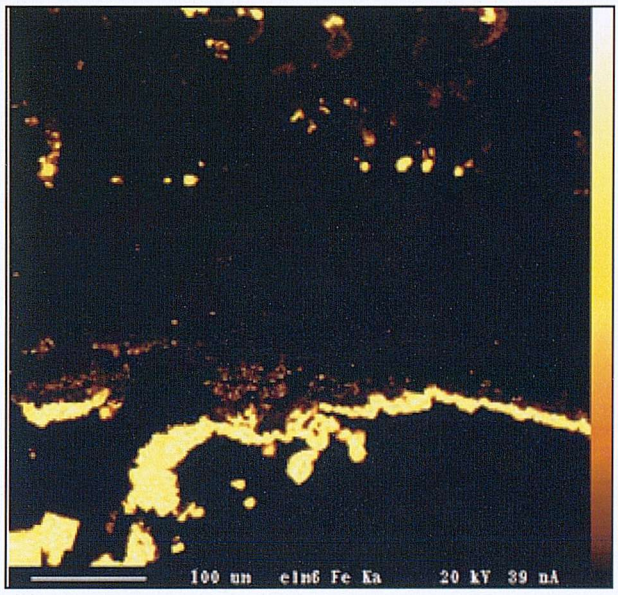

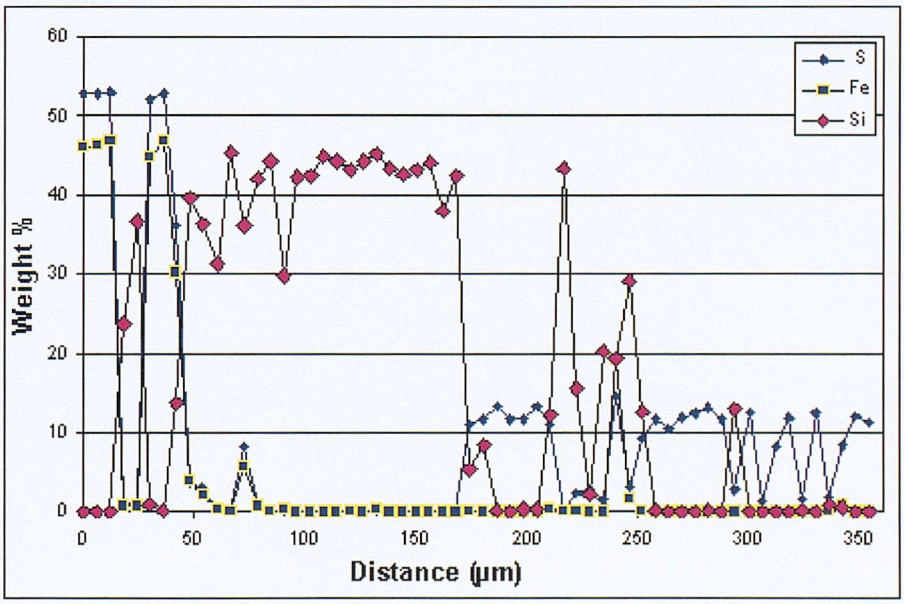

Figure 6.30f (left) – Quantitive EDS scan-line traverse measuring the major mineralogical components (S, Fe, Si), weight % vs distance.

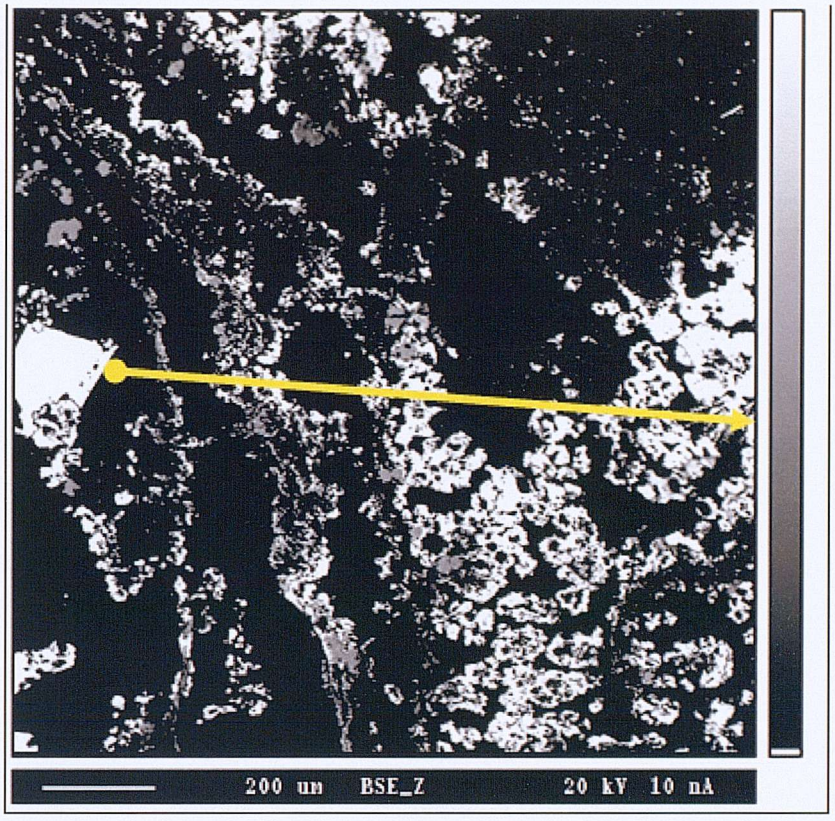

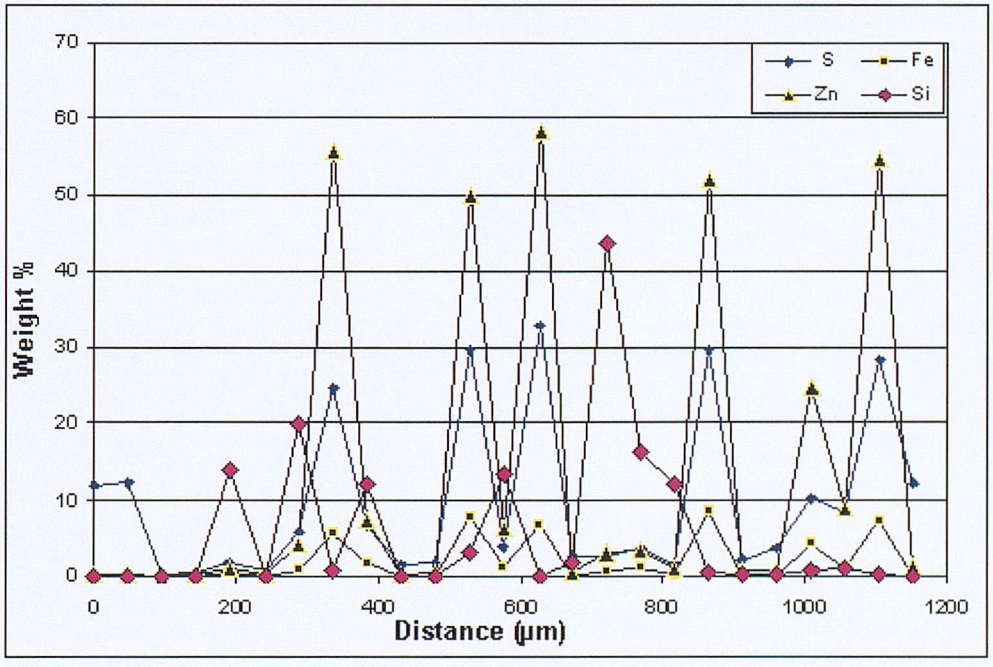

Figure 6.31a (top) – BSEI image of a mineralised filamentous texture which concentrically surrounds a mineralised tube structure. Yellow arrow denotes quantitative elemental traverse trace.

Figure 6.31b (bottom) – Quantitive EDS scan-line traverse measuring the major mineralogical components (S, Fe, Si, Zn), weight % vs distance.

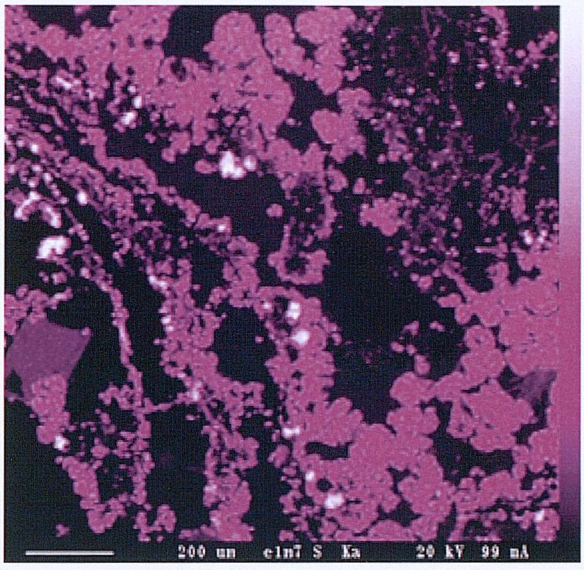

Figure 6.31c (right) – Qualitative EDS elemental map for sulphur centered about an area of mineralised tube wall shown in Figure 6.31a.

Figure 6.31d (right) – Qualitative EDSelemental map for iron centered about an area of mineralised tube wall. shown in Figure 6.31a.

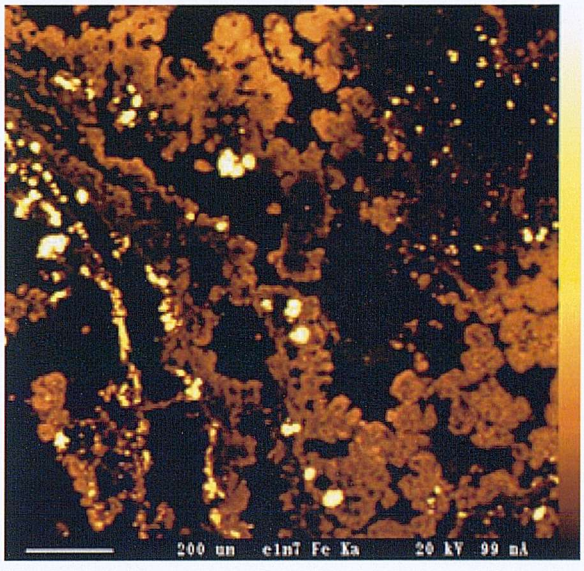

Figure 6.31e (right) - Qualitative EDSelemental map for barite centered about an area of mineralised tube wall shown in Figure 6.31a.

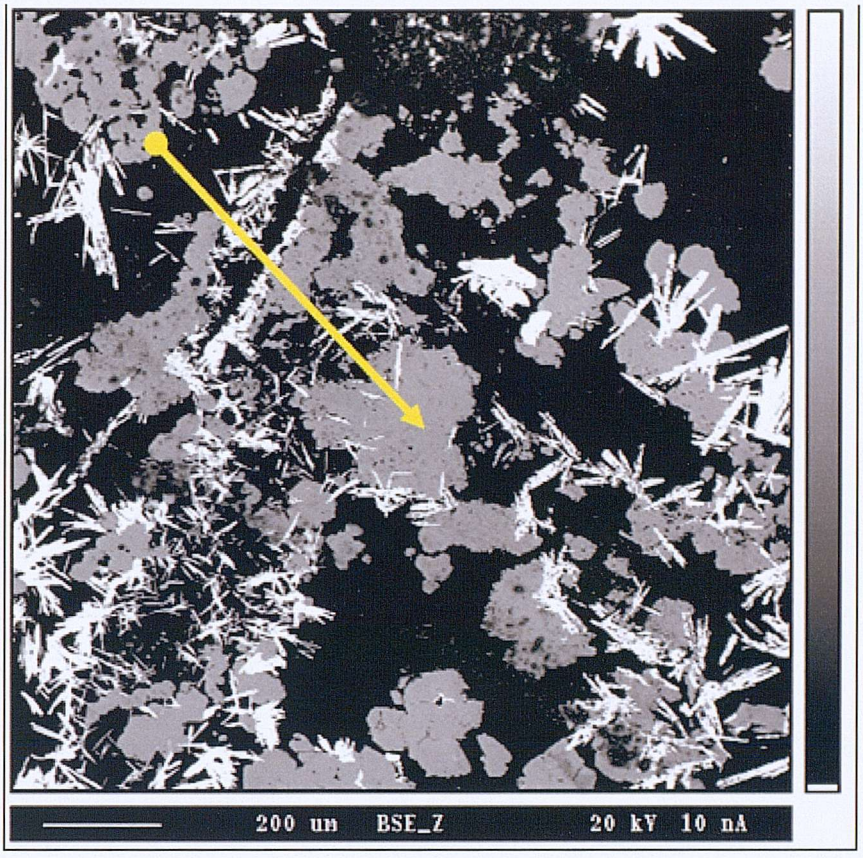

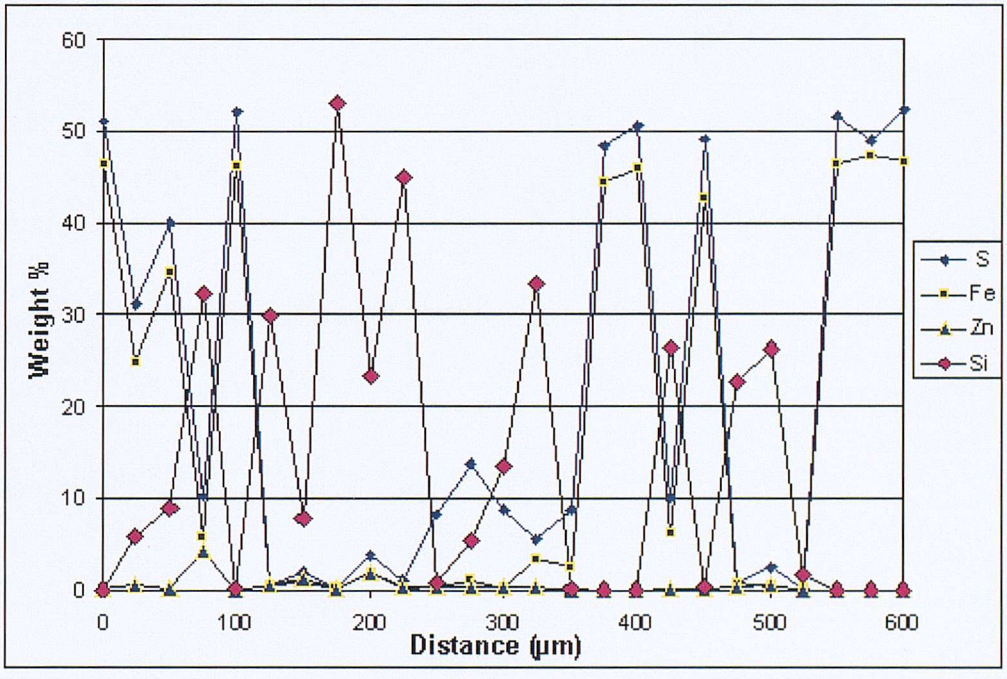

Figure 6.32a (top) – BSEI image of a mineralised tube wall structure. Yellow arrow denotes quantitative elemental traverse trace.

Figure 6.32b (bottom) – Quantitive EDS scan-line traverse measuring the major mineralogical components (S, Fe, Si, Zn), weight % vs distance.

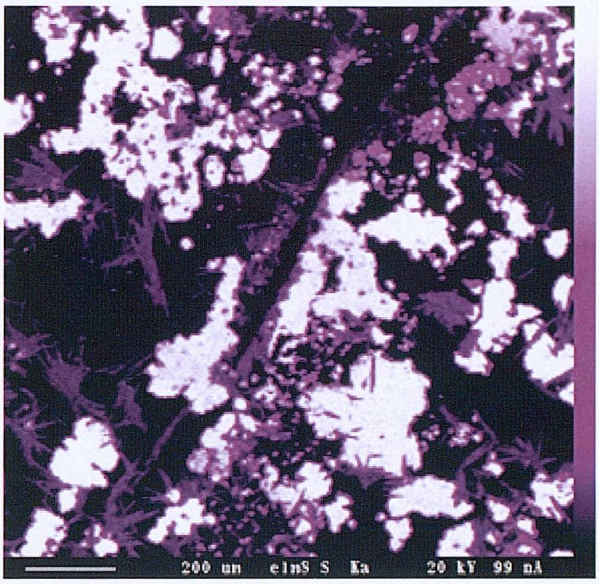

Figure 6.32c (right) - Qualitative EDS elemental map for sulphur centered about an area of mineralised tube wall shown in Figure 6.32a.

Figure 6.32d (right) - Qualitative EDS elemental map for iron centered about an area of mineralised tube wall shown in Figure 6.32a.

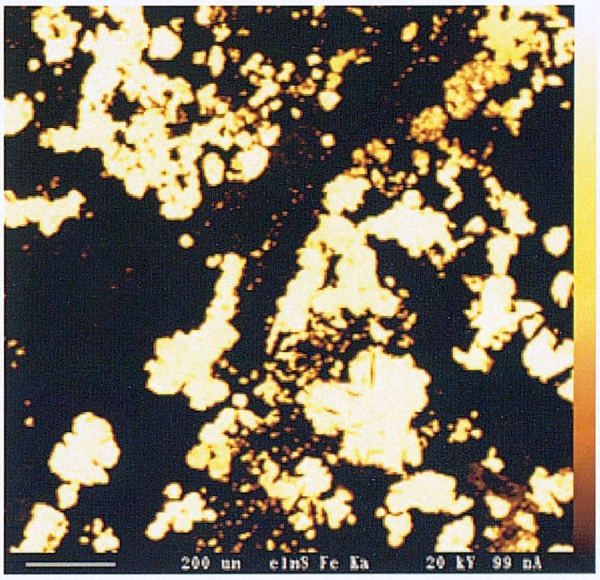

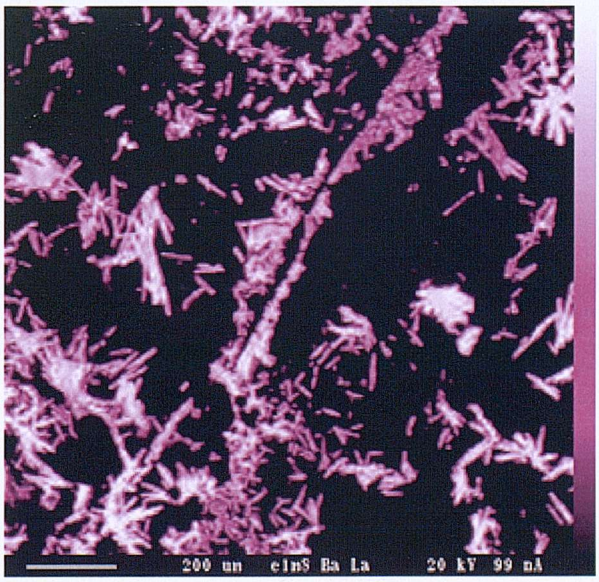

Figure 6.32e (right) - Qualitative EDS elemental map for barite centered about an area of mineralised tube wall shown in Figure 6.32a.

6.4 – Discussion.

Individual animal species found at hydrothermal vents have not been particularly well studied mainly due to the difficulties, and expense associated with sampling them, and their limited (if any) life-span when brought to the surface for study. Therefore, geological studies of such creatures, can also yield biological information which has been previously unreported in the scientific literature. The results of this Chapter will be discussed here with respect to biology, geochemistry and mineralogy.

6.4.1 - ?Juvenile? worm tubes.

The larval stages of vestimentiferans had not been identified until the trochophore stages of *Ridgea piscesae* were recovered from clumps of adult worms by Jones and Gardiner in 1989. The juvenile stages of *Ridgea piscesae* development, and early tube production were investigated by Southward (1988) using light and electron microscopy. Southward showed that the smallest tubes (around 2mm in length) were flask shaped, with a bulbous anterior end which is affixed to the substrate. Further to this Southward (1988) also suggested that juvenile *R. piscesae* tube did not produce their characteristic flanges until the tube was at least 10mm in length. Here, however, tubes similar morphologically to those produced by adult *R. piscesae* have been observed to nestle within the flanges of larger tubes (Figures 6.13a & b) which measure as little as 50μm in length (Figures 6.13c), have multiple flanges, and are around an order of magnitude smaller than the larval stages of newly settled *Ridgea* sp. described by Southward (1988). The smallest tube building organisms known from hydrothermal vent sites are protistan ciliates (Small and Gross, 1985: e.g. ciliophorans such as *Thuricola* sp., *Corthunia* sp. and *Metafolliclinid* sp.) which, at their smallest, are around twice the size of the tubes observed here (Figure 6.33). Further investigation of these tubes is warranted, but these preliminary observations suggest that the tubes are smaller than the tubes of any other tube building organism reported in the scientific literature to date (Southward, E.C., *pers comm.*; Tyler, P.A., *pers. comm.*; Copley, J.T., *pers. comm.*).

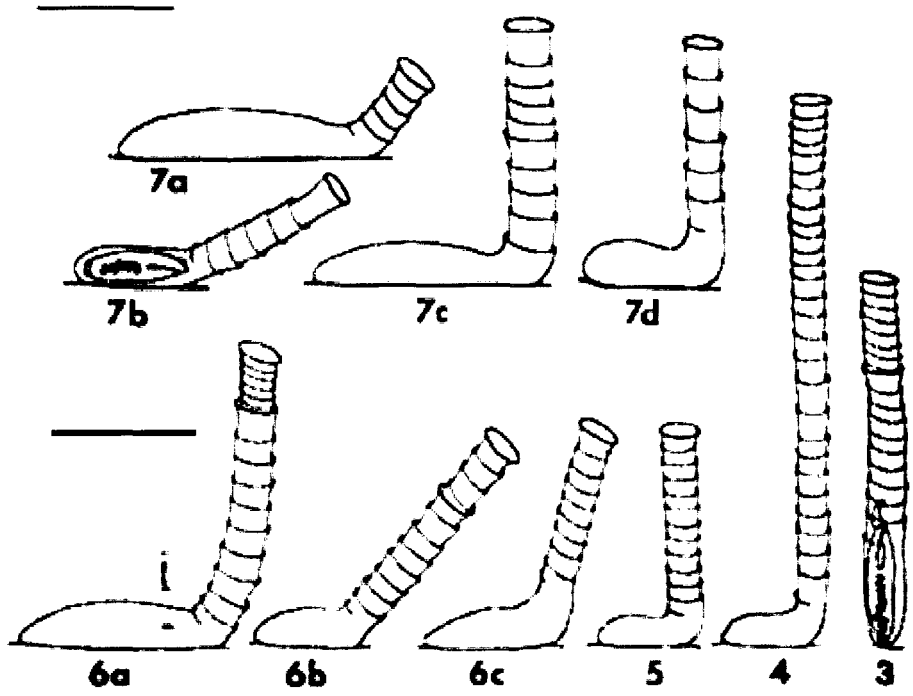

Figure 6.33 – *Metafolliculina* species: comparative morphology (adapted from Small & Gross, 1985). Scale bar = 300μm. *M. norgardi,* Dons (3); *M. elongatum,* Das (4); *M. producta,* (Wright) Dons (5); *M. andrewsi,* Uhlig (6a-c); a variety of *Metafolliculina* sp. exhibiting variable lorica (7a – d).

6.4.2 - Mucus production on the inner tube surface

The thin, papery layer observed on the inner surface of occupied *R. piscesae* tubes (e.g. Figure 6.7 a – d) has also, not yet been described in the scientific literature associated with this species of vestimentiferan. It is presumed that *Ridgea* spp., like other vestimentiferan and polychaete species may produce organic mucus rich in inorganic components, for the purpose of metabolic detoxification (as discussed in previous Chapters). The mucus produced is thought to be secreted onto the inner surface of the tube, as the thin inner coating seen on many of the inhabited tubes (e.g. Figure 6.7b). A mucosic lining such as this, may have several applications: it may be used in order to lower frictional forces, and prevent injury to the worm's soft body when it retracts into the tube; it may be used to strengthen the wall of the tube, or possibly repair damaged areas of the tube structure; or it may prevent mineralisation of the inner surface of the tube. The

Is possibly mucosic lining of inhabited tubes, has a shiny, iridescent appearance, and a smooth texture (e.g. Figure 6.7b), which peels away from the tube surface with

ease. In cross section under SEM, many tubes contain a thin (<20μm) inner ring within the actual tube structure, that is often broken or discontinuous (e.g. Figure 6.6c). This inner ring is inferred to be the desiccated remains of the mucus lining, which has dried out during sample preparation.

In other tubes the mucus lining appears to have been silicified, and is often white, smooth and flaky (e.g. Figure 6.7a). Geochemical analysis of the tube in Figure 6.7a indicates that the inner (~60μm) portion is incompletely silicified, and contains a significant number of chemical elements not contained in the silicified portion of the tube wall (Figures 6.22 b & c). Here it is inferred that the mucus lining, containing a mixture of vent-derived metal cations (Fe, Zn and Cu) and S, and seawater derived elements (Mg, Ca and P) adhered to the inner surface of the tube and was subsequently partially silicified.

6.4.3 – Abiotic silica precipitation.

In uninhabited tubes, where the organic mucus layer is absent, mineral precipitates form on the inner tube surface (e.g. Figure 6.14 & 6.15). Figure 6.14a shows a silicified tube structure embedded within a matrix of barite and filamentous silica. Figure 6.14b & c clearly show that the filaments covering the outer surface of the tube form a number of branching networks, whereas the filaments on the inner surface are single fingers growing out into open space. These 'viscous finger' structures are inferred to have been formed by diffusion limited aggregation (DLA). The gelation of silica into DLA clusters is well documented (e.g. Viczek, 1989; 1990; Mandelbrot, 1990; Hasmy *et al.*, 1997; Chin, 1998). DLA-clusters are aggregates, where the shape of the cluster is to a greater or lesser extent controlled by the possibility of particles to reach the cluster, which is driven by Brownian motion within the fluid. From the starting point of a saturated fluid with a uniform distribution, particles collide and if a favourable electrostatic attraction is present, they will aggregate. The aggregates may grow so long as there are particles in motion. During growth it may happen that "fingers" of the cluster "catch" particles so that they are less likely to reach inner parts of the cluster. Older (inner) parts of the cluster tend not to catch new particles as the younger, outer parts of the cluster intercept them first. During the diffusion of a particle

through the solution it is more likely that it attaches to the outer regions, thus forming finger-like outgrowths.

It is thought that the mucus layer, secreted on the inner wall of inhabited tubes, may form an unfavourable substrate for the nucleation of significantly sized abiotic precipitates.

6.4.4 - Mineralisation of the tube wall

6.4.4.1 – Silica crystallinity

The results of the FT-IR analysis show a varying degree of crystallinity with the silicified tube wall structure. From the spectral map (Figure 6.17b) generated from the traverse in Figure 6.17a, a clear gradation of spectral peaks can be observed. The first of the points in the traverse shows a great deal of 'noise' which is thought to be due to a combination of the remnant organic mucus layer on the inner surface and the organic component in the resin which holds the sample. However, a broad peak about the 1650 cm^{-1} wavelength (corresponding to the vibration of the H-O-H bonds in molecular water) can be seen. As the traverse progresses, peaks with wavelengths of 1650 cm^{-1}, 1110 cm^{-1}, 1040cm^{-1}, and 479 cm^{-1} (attributed to H-O-H, Si-O-Si, Si-O, and O-Si-O vibrations respectively) begin to develop, indicating the presence of amorphous hydrous silica in the younger section of the tube. A clear focusing of the peaks about the 1080 – 1110 cm^{-1} wavelengths (which are attributed to the stretching of Si-O, and Si-O-Si bonds respectively), and a diminishing of the 479 cm^{-1}, and 1650 cm^{-1} wavelengths is seen as the traverse moves into the older section of tube wall. These spectra are interpreted as indicating the dewatering of the amorphous silica gel, and evolution into a more crystalline phase such as opal-A. As the traverse moves into the barite zone along the outer edge of the tube, the spectral peaks diminish.

The traverse across the tube wall section in Figure 6.20a is presented as a plot of comparative maximum peak heights for particular wavelengths along the length of the traverse in order to show the areas with relatively high inter- (-OH) and intra- (H-O-H) molecular water content (wavelengths 1650 cm^{-1}, and 3388 cm^{-1}respectively) with respect to silica (1110 cm^{-1}). The 617 cm^{-1} wavelength is thought to be attributed to a vibrational

energy generated by a particular bond within barite. The traverse progresses from older tube material, through a mineralised juncture area, to younger tube material on the interior of the structure. The older tube wall material shows a variable pattern of crystallinity, with the more silicified tube layers (shown by Figure 5.20(Si)) being more crystalline. A marked increase can be seen in the spectral peaks associated with –OH, and H-O-H bonds as the tube rapidly grades into the middle area. This indicates the presence of a gel-like silica polymorph in the area between the two growth stages, which is possibly attributed to the presence of silicified microbes, within juncture of the tube flange (e.g. Figure 6.18). Towards the end of the traverse, the youngest tube section is only partially silicified, and poorly crystalline, as it maintains a relatively high 1650 cm^{-1} peak. The unsilicified area which runs along the core of the tube wall is relatively S-rich, and is likely representative of the original organic tube wall material.

6.4.4.2 –Organically templated petrification

Silica mineralisation of the tube structures is high prevalent in the Ventor sample, in fact, it is difficult to identify tubes which have not undergone some degree of silicification. The rates of amorphous silica precipitation have been determined experimentally, and through field observations in a number of previous studies (Rimstidt & Barnes, 1980; Bohlmann *et al.*,1980; Fleming, 1986; Carroll *et al* ., 1998). Both Fleming (1986) and Carroll *et al.* (1998) have demonstrated that aqueous silica polymerisation will occur in a matter of hours (at pH ~3), to minutes (at pH ~7), at a range of temperatures from 25 – 100°C. Increasing temperature is also shown to increase the rate of amorphous silica precipitation (Carroll *et al.*, 1998). It is inferred that the nucleation of amorphous silica (Equation 6a) is not due homogeneous nucleation, but instead, controlled by reactions at the solid-solution interface. This inference is verified by the fact that silica precipitation in the study conducted by Carroll, *et al.* (1998) seeded experiments proceeded fast and produced a higher yield of silica, than purely homogenous nucleation experiments.

$$H_4SiO_2 \rightarrow 2H_2O + SiO_{2(Am.Si)} \qquad (6a)$$

Figure 6.22a shows a section of silicified tube wall with minor barite precipitation, and a mantle of microbially templated silica and barite intergrowths on the outer surface of the tube. Quantitative geochemical analysis of the tube wall in Figure 6.22a displays peaks in the distribution of Si (and corresponding O) at the inner and outer parts of the tube wall (Figure 6.22b). This is attributed to the increased precipitation of silica along the inner and outer margins of the chitinous tube wall (Figure 6.34). It is inferred that the silicification of the tube wall is induced by silica nuclei, pre-seeded in the organic chitin matrix, and derived from the ambient diffuse venting fluid, which is utilised by the worm for metabolic processes. Simply explained, Si and other chemical components, present in the mixed fluid, are unselectively taken up, by the worm from their immediate aqueous environment, and also unselectively removed in any secretion which requires the presence of water (e.g. tube building processes, mucus production, sperm production, etc.). Transport of Si into the tube wall through the inner and outer surfaces *via* diffusive processes will then cause the further nucleation of silica. Silica penetrates further into the centre of the tube structure with time, and eventually results in the silicification of the entire tube wall. The density of the nucleation sites and saturation level of the diffuse fluid influences the final mineralogical texture. If nuclei were relatively few, then fine-grained aggregates could be expected to form from a solution saturated with silica. However, where nuclei are numerous and evenly distributed, as is inferred here, an amorphous, gel-like precipitate, or colloidal/botryoidal texture will result. Colloidal textures, unlike amorphous gels, are metastable, but are susceptible to recrystallisation due to loss of water (Ineson, 1989).

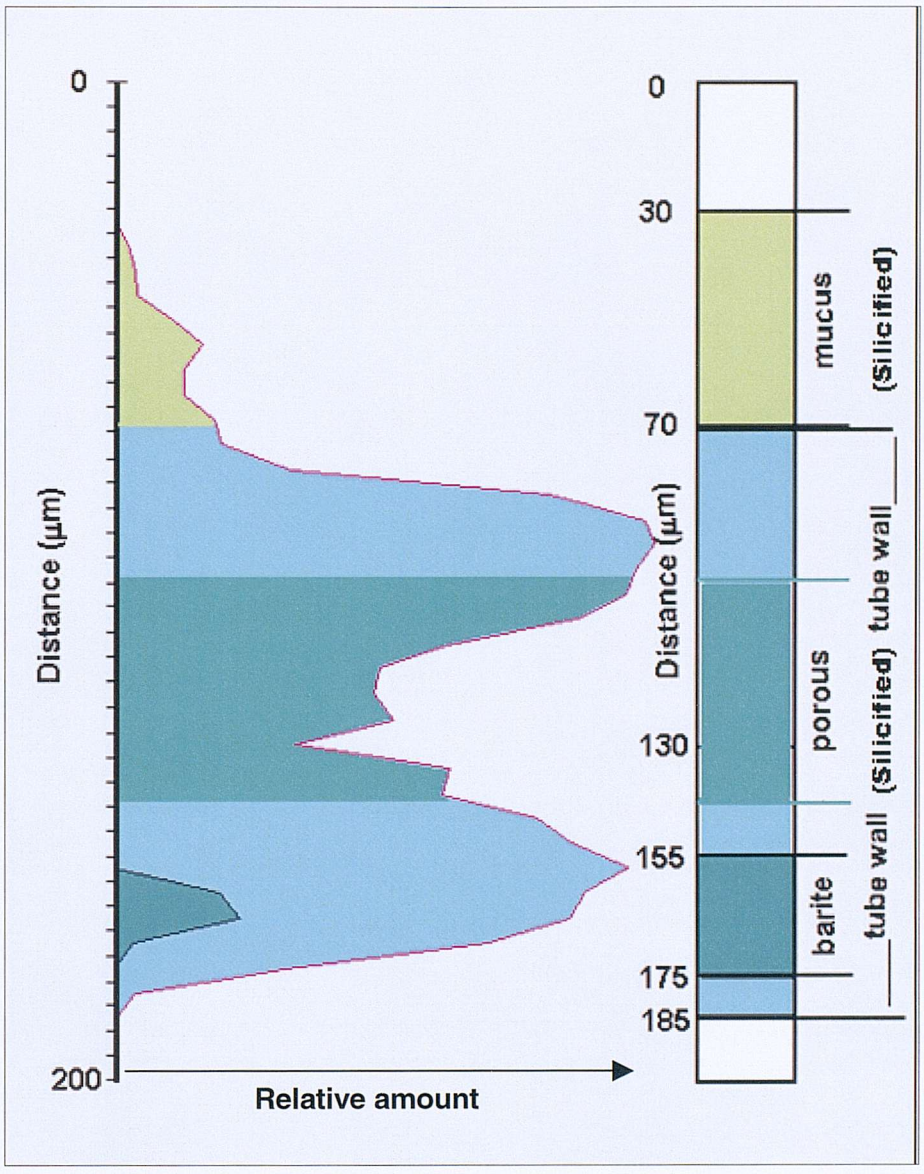

Figure 6.34 – Model to show the mineralised areas of the wall of a *R. piscesae* tube.

6.4.4.3 – Barite mineralisation

Barite mineralisation is a major component in the Ventnor sample. Figure 6.19a show extensive barite mineralisation along the tip of a flange structure. EDS point analysis (Figure 6.19a) show that the mineralised tube section is composed of the same elements as the surrounding barite overgrowth. Spherical – sub-spherical voids in the barite laths may be representative of microbial cell moulds formed as barite has precipitated outwards and overgrown silicified microbes. An area of relatively new tube was examined using qualitative EDS point analysis in Figure 6.19b. The back-scattered image of the tube highlights textural differences within the tube layers. EDS profiles show

little variation with respect to silica, but do show a minor S peak along a dark horizon, which is seen to contain newly forming barite crystals, close to the inner surface of the tube wall. A similar situation is observed in Figure 6.19c; 6.20 & 6.21. In Figure 6.21 the S-rich horizon coincides with a Si-deficient horizon along the middle of the silicified tube, which likely represents an area of remnant organic tube wall. The S-rich horizon is possibly an artefact produced by the concentration of sulphur by the progressing silica mineralisation front. Small (<10μm) barite laths can be seen forming along the S-rich horizon. Barite crystal growth is predominant within the flange of the older (adjacent) tube wall section. Unusually for barite crystal growth, the axes of the crystals can be seen to align parallel to the tube layers. Where the individual clusters of barite are larger (>10μm) they begin to assume a more radiating, acicular quality. The main area of barite growth occurs on the outer surface of the tube wall, (although it is noted that seeding of barite may occur within the tube) where presumably its growth uninhibited by external forces (such as the tube layers), and more able to nucleate by diffusion of passing ions. Figure 6.21shows a relatively older section of tube wall (than Figure 6.20). Barite is seen to partially replace the silicified tube structure, and precipitate out into open space. In particular, the tips of the flanges are often lavishly encrusted with barite (e.g. Figure 6.15a), whereas the area inside the flanges is usually totally devoid of barite precipitates (e.g. Figure 6.18), or else contains very few (Figures 6.15a; 6.16a & b; 6.17a). This mineralisation pattern is indicative diffusion limited aggregation, whereby the ions diffusing towards the tube wall are captured by the protruding flanges, and therefore removed from solution before reaching the inner flange area. Assuming that the insides of the tubes are essentially a closed system with respect to diffuse fluid flow, this mechanism would also partially explain the limited barite precipitates observed along the inner tube wall surfaces, when compared to the substantial barite encrustations present on the outer tube surface.

6.4.4.4 – Timing of mineralisation

The timing of mineralisation can be considered with respect to the time taken for the worm to build tube sections. As previously described in this Chapter, the growth rates of *R. piscesae* tubes can be highly variable. However, Urcuyo *et al.*, (1998) have suggested that the tube building activities for individual *R. piscesae* worms from the Juan

de Fuca Ridge exhibited a 36 day tube-section building cycle. Which would imply that the increased level of mineralisation between each successive tube section, could take as little as 36 days to develop. Such fast rates of mineralisation allow substantial mineralisation to develop during the worm's life-cycle.

6.4.5 – Microbial templating of silica.

The silicification of microbes in hydrothermally active areas has been relatively well studied in recent years (e.g. Cady & Farmer, 1996; Jannasch, 1983; 1984; 1993; 1996; Juniper & Sarrazin, 1995; Karl, 1980; 1995; Karl *et al.*, 1988; Pentecost, 1996; Tunnicliffe, 1992; Tunnicliffe & Fountain, 1987; Stetter, 1996; Westall *et al.*, 1995). There has been much interest in this field since Davis *et al.* (1997) demonstrated the potential application of microbial templating of biogenic silica in the production of nanoscale silica polymers.

There have been various mechanisms proposed to describe processes involved in micro organism silicification (Oehler, 1976; Francis *et al.*, 1978a; 1978b; Ferris *et al.*, 1988; Westall *et al.*, 1995; Cady & Farmer, 1996; Jones & Renaut, 1996; Jones *et al.*, 1996; Pracejus & Halbach, 1996). Westall *et al.*(1995) suggest that the preservation of the dead cell for a period of time long enough to allow its mineralisation is an important factor in the process of micro-organism fossilisation. Most bacteria do not actively precipitate silica, but have been observed to accelerate the rate of precipitation in hydrothermal systems, by providing suitable bonding or sorption surfaces, which in turn affect the equilibrium reactions of their aqueous environment (Fortin & Beveridge, 1997b; Fortin *et al.* 1997). Trace amounts of Fe in solution within hydrothermal systems may be significant for microbial silicification and in particular, the preservation of bacterial cell structures. Ferris *et al* (1988) suggested that the binding of metals prior to silicification, may facilitate the preservation of the original cell morphology, by inhibiting the action of lytic enzymes which destroy the cell wall on death. Metals may also serve to nullify repulsion due to the electronegative charges of the anionic cellular boundary, and silicate anions in solution (Fortin *et al.*, 1997), such as in the binding of silicates to the cell surfaces of *Thiobacillus* in hydrothermal conditions (Fortin & Beveridge, 1997b).

Commonly vent bacteria are enveloped within sheaths of secreted organic material, and may also secrete extra-cellular mucosic material (extracellular polymeric substances EPS: Westall *et al.*, 1995) that contains trapped mineral particulates or minerals derived from metabolic activities (Tunnicliffe & Fountaine, 1987). Secretions between bacterial cells can form filaments which are particularly sticky (Stetter, 1996), and enable the organism to trap further particulate matter. The continued growth of bacteria can result in the formation of biofilms that may be responsible for the successive precipitation and continued growth of silica, although at present there are no known studies that have demonstrated that silica precipitation can be produced by the metabolic activity of bacteria.

Mineral replacement, encrustation and petrification may be the methods by which the fossilisation of microbial material occurs in hydrothermal samples. Knoll (1985) suggested that the model proposed by Leo & Barghoorn (1976), for the silicification of wood is applicable to microbial fossilisation. Leo & Barghoorn (1976) explained that the vascular tissues of plants, as well as their degradation products, provide a template for silica deposition *via* hydrogen bonding with carboxyl and hydroxyl molecular groups. This type of attachment can take place with the addition of a silica molecule to organic functional groups, enabling the organic matter to act as a template for the nucleation of silica (Westall *et al.*, 1995). Once this initial nucleation has taken place, further silica precipitation may be achieved by the silicic acid polymerisation of mono- and poly-silicic acids. However, Westall (1994) and Westall *et al.*(1995) suggest that bacterial mineralisation processes could be species specific, with the rate and mechanism of petrification being influenced by the character of the cell wall, degree of cellular degradation, and external organic layers, as well as temperature, pressure and silica availability.

The timescales of silicification of micro-organisms at deep-sea pressures and temperatures (500 atm, and 4°C respectively) have been investigated experimentally by Westall *et al.* (1995). These authors demonstrated that the rate of silicification of the organic structures within the microbial mats was increased by a factor of 4 when compared to similar microbial compounds silicified at 1 atm. Many of the bacteria in this

earlier study exhibited textures which consisted of small (sub-micron) silica spherules over a smooth encrusted cell wall surface. The cellular surfaces were often translucent enough to allow the internal organelles within the cell to be viewed. Si infiltration of the cell wall, cytoplasm, and internal organelles of the micro-organisms leads to good preservation of the cell structure (Westall *et al.,* 1995). Rapid silicification of the cellular degradation products was also observed. After a few weeks the disseminated and loosely aggregated spherules within the EPS had consolidated to from mammiliated surfaces and larger spheres. By the end of the incubation (4 weeks), all of the bacteria had been covered with botryoidal silica deposits, rendering the once individual silicified bacterial filaments indistinguishable from the botryoidal mass. Longer incubations led to advanced silicification such that micro organism remains were no longer visible in the granular mass and only minerals such as clays could be distinguished.

While the rates of mineralisation observed in subaerial hydrothermal systems are much lower than those inferred for deep sea environments, the processes are probably very similar. Cady & Farmer (1996) suggest that precipitation of silica in subaerial thermal springs may have two phases. The first phase is the deposition of opaline silica which preferentially adheres to the sticky extracellular mucus, enclosing the cell contents in a sheath of opal, probably resulting in the death of the enclosed cell. The second phase involves the nucleation of silica to the opaline template, by a process of silicic acid polymerisation (Leo & Barghoorn, 1976).

Microbes are commonly identified either by their genetic characteristics or by characteristics determined by their cellular morphology (Phillips *et al.*, 1989; Golubic & Knoll, 1993). Indicative characteristics include: habitat and environmental conditions; DNA / RNA composition; cell morphology (e.g. shape, size and planes of fission); cell wall ultrastructure; colony morphology; and trichome morphology (Castenholz & Waterbury, 1989; Jones *et al.*, 1999). However, in most geological settings, diagenetic processes acting on the cell destroys most of the crucial biological information, even if the microbes are apparently well preserved (Phillips *et al.*, 1989; Jones 1988; 1989; Schultze-Lam, 1995; Jones *et al.*, 1999). Silicification in particular, can warp the size characteristics of preserved microbes out of all proportions, as progressive layers of amorphous silica are precipitated, and often, as the degree of silicification increases

cellular components become completely engulfed. Accurate taxonomic identification of microbes from any environment can be a difficult task, but identifying fossilised microbial remains, taxonomically or otherwise, can be exceptionally challenging, and often prove inconclusive, and is therefore considered outside the scope of this study.

Bacterial surfaces are highly interactive with their environment, as they depend on diffusion for both their nourishment and excretion (Beveridge, 1988). Bacteria are contained within an organic cellular membrane, which is generally tough and chemically resilient (Beveridge, 1981, 1989a), but their exceptionally high surface area to volume ratio, and macromolecular chemistry make them susceptible to the precipitation of metal ions and fine-grained mineral precipitates over the surface membrane (Beveridge, 1989a; Ferris *et al.*, 1988; Fortin & Beveridge, 1997a). During respiration, waste products such as H_2S can affect the adjacent micro-habitat sufficiently enough to force the precipitation of minerals within close proximity of the cell, or induce the precipitation of specific mineral assemblages (Schultze-Lam *et al.*, 1992; Urrutia *et al.*, 1992; Fortin & Beveridge, 1997a; Thompson *et al.*, 1997). Mucus and biofilm production can dramatically increase the mineralisation potential of a microbial colony, as the biofilms are highly interactive with metallic ions within the adjacent environment, and over time can become completely mineralised (Beveridge & Doyle, 1989; Fortin *et al.*, 1997).

Microbial filaments of many different sizes and shapes are present throughout the sample, and represent different taxa, and/or varying degrees of mineralisation. Commonly, filaments that have been (fortuitously) sectioned, show no evidence of internal features, or voids. However, those rare filaments that do preserve evidence of outer sheaths, or contain voids or central openings (e.g. Figures 6.10a – c) lend strong evidence to a biogenic origin (Cady & Farmer, 1996; Jones *et al.* 1999), as opposed to self-organised filamentous textures formed from silica gels (Hopkinson *et al.*, 1998). Sub-micron spherules, presumably formed from silica can be observed on the outer surface of the filaments in the centre of Figure 6.10c, an observation which is analogous to that of Westall (1994). The metals present in solution derived from the local vent fluids may act to catalyse nucleation of silica species. The inference is that silicification of individual microbes, microbial networks and biofilms progress by a process of microbial templating. This, over time can form significant precipitates (10s – 100s of micrometer thick) which

mantle both the silicified tube and the associated barite overgrowth, and form an inter tube framework for further barite, silica, and eventually sulphide mineralisation.

6.5.6 – Sulphide mineralisation.

The regions sampled for geochemical mapping (Figure 6.27) are from an area covering approximately 1.5 x 0.5cm^2, and are therefore only a relatively small distance from one another. The first three of the mapped areas (Figures 6.28, 6.29 & 6.30) are all from different areas of the same tube. The tube wall varies in thickness slightly and ranges from ~150μm to ~250μm. The tube wall is uniformly composed of silica (Figures 6.28a, 6.29a & 6.30a). Barite is only present in one of the mapped areas (Figure 6.30b), where it can be seen to encrust the outer surface of the tube, and replace parts of the outer mantle of microbially templated silica. Fe-sulphide minerals form a thin crust on the inner surface of the tube, but do not appear replacive (Figures 6.28d,e, 6.29d,e & 6.30d,e). Zn/Fe sulphides have developed in the outer matrix, replacing the silicified microbial structures (Figures 6.28c – e). These features may be indicative of a developing chemically reducing environment.

The area mapped in Figure 6.31 is adjacent to the outer wall of a tube, where a concentrically layered filamentous texture is observed (e.g. Figure 6.23d). Si and Ba are almost entirely absent in this area, and the scan-line traverse (Figure 6.31b) indicates quantitatively that Zn, and lesser Fe sulphides are present. These traverses are representative of sphalerite mineralisation (empirical formula: $Zn_{0.95}Fe_{0.05}S$), which is believed to have replaced and coarsely overprinted, the layers of siliceous microbial biofilms which originally enveloped the adjacent tube, and now forms the template of the mineralised matrix (e.g. Figures 6.11 & 6.12). This style of mineralisation is inferred form the larger-scale textures observed in Figures 6.23c, d & 6.25b.

The area mapped in Figure 6.32 is centred around the outer edge of another discrete tube structure. Silicified elements of the tube still remain intact, but much has been replaced by needle-like crystals of barite. (Figure 6.32e). From the scan-line traverse (Figure 6.32b), and the elemental maps for S & Fe (Figures 6.32d & e) it can be seen that

both poorly crystalline and more crystalline forms of Fe-sulphides are replacing the barite precipitates. Atomic ratios calculated for the S and Fe elements, are consistently around 2:1 (only points over 10 wt% are considered), indicating the presence of pyrite (FeS_2). A likely mechanism for precipitation here is the dissolution of barite due to a shift in redox conditions, and the subsequent utilisation of liberated sulphur ions by percolating Fe ions at the barite solid/solution boundary. Zinc is not present in any significant quantity in this area..

Despite being consolidated as a hand specimen, the sample is obviously porous on the microscale, but may not be totally permeable to percolating fluids. The analysed areas around the three different tubes mapped (Figures 6.28/6.29/6.30, Figure 6.31, & Figure 6.32) show significantly different degrees of sulphide mineralisation. There are two possible explanations for the spatial discontinuity in mineralisation:

1) There is a simple, gradational variability within the sample from pyritisation of the tube wall and barite overgrowths(Figure 6.32); through sphalerite mineralisation of the microbially templated silica networks (Figure 6.31); to minor Fe/Zn-sulphide precipitation and replacement over a predominantly oxidised mineral assemblage (Figures 6.28/6.29/6.30). Which is indicative of a prograde mineralisation front, advancing through the sample.

2) Micro-scale geochemical/redox environments set up within the sample, due to local areas of restricted permeability and/or thermal conduction. Assuming that sulphide replacement and mineral growth could only serve to restrict permeability further still, isolated areas could develop that are geochemically insulated from the caustic, overprinting effects of sulphide replacement on the tube structures.

Although both explanations are based on the same idea of prograde mineralisation, the second point could explain how single, isolated fossil tubes are occasionally preserved in large sulphide deposits (e.g. Little *et al.*, 1997; Little *et al.*, 1998; Boyce *et al.* 2002).

6.4.7 – Late stage silica and barite precipitation

Located about the weathered, and iron oxide-encrusted zone (Figures 6.24 a & b), and within the inter-tube pore spaces, well-preserved silicified microbial filaments and their mineralised intercellular mucus are observed (Figure 6.26a & b). Barite rosettes are also observed adhering to the sulphidised substrate. These mineralogical features are inferred to be a paragenetically later stage of silica and barite precipitates, formed after the sample had fallen as a talus block, to the base of the chimney, where it was recovered by submersible

6.5 - Conclusions

From the observations made in this Chapter, it can be seen that the tube of *Ridgea piscesae* are effectively becoming 'living' fossils. Silicification of the dwelling tubes can proceed at a rate that almost equals the rapid growth of the tubes themselves. Further encrustation by barite and silicified microbes form a metastable matrix which fixes the tubes firmly into the geological record, until prograde sulphide mineralisation removes the biological textures and associated geochemical features though over-printing of the paragenetically earlier silica and barite minerals. In this instance however, further late stage silica and barite precipitation could have proceeded in the Fairy Castle sample, because it fell to the base of the chimney as a block of sulphide talus.

An organic mucus layer has been identified which coats the inner surface of inhabited worm tubes. Elemental analysis has shown the mucus to contain inorganic metabolic by-products, in the form of Ca, P, S, Cu, Zn, Fe. The mucus coating is thought to be used to a) reduce friction between the inner surface of the tube and the soft body of the worm during movement and b) inhibit mineral precipitation on the inner surface of the tube, probably because it is a poor substrate for nucleating crystals. Where no mucus lining is evident, such as in uninhabited worm tubes, silica precipitation by means of diffusion limited aggregation forms 'viscous finger' structures which protrude from the inner surface at a tangential angle to the tube wall.

Associated with the mucus lining is a ligament which runs along the inside of the tube, and is tentatively inferred to be a form of anchor, allowing the worm to rapidly retract into the tube when threatened.

Small (<100μm) tube structures, morphologically similar to adult *R. piscesae* tubes have been identified, located within the flanges of adult worm tubes. These tubes may represent very small, juvenile *R. piscesae* worms, or a different and as yet unreported species of tube-building organism. These preliminary observations show that the tubes are smaller than any other tube structures currently reported from hydrothermal vent sites.

A model for the mineralisation of *R. piscesae* tubes has been hypothesized here, which suggests exceptionally rapid replacement of the organic tube structures by passive silica biomineralisation of an organic template. Over a relatively short period of time (in the order of tens of days) the silica gel-like polymorphs replacing the tube, modified to allow the dewatering and subsequent crystallisation to amorphous opal A. Despite recrystallisation, the mineralised tube structure retains elements of the original organic tube inter-layers. Barite intergrowths often occur within the tube, along S-rich horizons of the tube wall. Initially the crystallographic axes of newly forming barite, orientate themselves along the planes of the tube layers, these crystals may then form the seeds for later, more extensive barite precipitates. Barite also precipitates from solution via diffusion limited aggregation processes to form encrustations on the outer tube surfaces, which over time, with continued precipitation, can form relatively extensive accumulations. Barite is also seen to overgrow and incorporate the silicified microbial networks that blanket the outer surface of the tubes.

Increasing ambient hydrothermal temperatures cause prograde zinc- and iron-sulphide mineralisation to replace the silica and barite mineral assemblage, and consequently overprint the organic tube textures preserved by silica. Micro-reducing environments are setup within the mineralised tube cluster, which allow different replacive processes to occur within close proximity.

Paragenetically later silica and barite precipitation within pore spaces, and mineralisation of microbial biofilms, occur when ambient conditions allow.

Chapter 7

Summary, conclusions and further work

7.1 – Summary models

This study has proposed two separate models for the complete mineralisation of two phylogenetically different hydrothermal vent tubeworm species. The first model demonstrates that sulphidisation occurs rapidly, beginning during the worm's lifecycle and does not require precursor mineralisation. The second demonstrates that rapid silicification occurs during vestimentiferan life cycles which is key to the preservation of this species in the surrounding sulphide talus.

7.1.1 - Model A

The sulphidisation of Alvinella sp. polychaete worms tubes is a multi-stage mineralisation process which is sumariesed below . This model is developed from the observations described in detail in Chapters 4 and 5 of this dissertation.

i. Mats of microorganisms growing on the inner surface of the *A. pompejana* tube wall trap iron and zinc sulphides, elemental sulphur and other metal rich particles both between cells and on cellular surfaces.
ii. Subsequent tube wall growth entombs the microorganisms and trapped particulate sulphide particles within the laminated structure of the tube wall. The larger filaments become cropped, probably by the worm feeding on them.
iii. The microorganism cellular components begin to decompose after entombment and the degradation products are released through the cell walls, to combine with trapped Fe ions, leading to the formation of a precursor iron mono-sulphide mineral, which envelopes the cell wall. Microorganism decay provides a reducing microenvironment, which allows for the precipitation of mackinawite, then greigite, followed by pyrite along the internal microbial lamina. This leads to the formation of significant iron sulphide mineralisation on a biological

template with the sulphide texture replacing original organic layer. Passive biomineralisation continues until the degradation of the microorganism cells is complete. The pyrite phase observed is the recrystallisation product of an earlier, iron monosulphide precursor mineralisation stage. Complete degradation of the microorganism cells results in spherical and elongate pores within the pyrite/biomineralised layer.

iv. A later phase of marcasite-rich mineralisation envelops many of the pyrite-rich mineral horizons. In places the marcasite phase also replaces the organic tube wall material but preserves the gross laminated morphology of the tube. This mineral growth is assumed to be abiogenic and diffusion limited, which is indicated by the distinct fine-scale differential growth bands, picked out by differential tarnish of the layers. Most of the marcasite growth occurs in horizons nearer to the outer edge of the tube wall, either because the tube material is older, and mineralisation is more progressive; or because the tube layers are older and more fractured and therefore allow greater ease of vent fluid penetration.

v. As local temperatures within the tube wall reach 150 – 250°C pyrite replacement of the laminated horizons, and of organic tube layers would be nearing completion, and inadvertently restricting the porosity of the tube structure. Such elevated thermal conditions would also allow for the precipitation of a pyrite dominated outer stockwork zone around the tube structure. Marcasite recrystallises due to high temperature (+150°C) instability.

vi. Further intensification of local temperatures (+270°C), leads to the onset of pyrite replacement by chalcopyrite. In the tube stockwork zone where porosity, and conduits allow effectively unrestricted fluid flow, chalcopyrite precipitation continues unchallenged. However, within the tube structure, pyritisation has reduced porosity sufficiently enough, to inhibit the total replacement of previously formed Fe- and Zn-sulphides by chalcopyrite. Thus, restricting chalcopyrite precipitation to only the older, outer portion of the tube, and a relatively small portion of the inner layers.

vii. As hydrothermal fluid flow from the chimney edifice begins to decline, and local temperatures fall below ~270°C, conditions allow for pyrite precipitation within the pore spaces of the chalcopyrite stockwork zone. As temperatures

decrease further, due to seawater penetration of the chimney, a suite of low-temperature, oxidised precipitates (e.g. silica and barite) are observed.

7.1.2 - Model B

The silicification of Ridgea piscesae worm tubes, is also a multi-stage process which is sumaried below. This model is developed from detailed observations of the two samples described in Chapter 6.

i. Over a relatively short period of time (of the order of tens of days) the silica gel-like polymorphs which replace the tube are remodified to allow the dewatering and subsequent crystallisation to amorphous opal A. Despite recrystallisation, the mineralised tube structure retains elements of the original organic tube inter-layers. Barite intergrowths often occur within the tube, along S-rich horizons of the tube wall. Initially the crystallographic axes of newly forming barite, orientate themselves along the planes of the tube layers, these crystals may then form the seeds for later, more extensive barite precipitates. Barite also precipitates from solution via diffusion limited aggregation processes to form significant encrustations on the outer tube surfaces, which over time can form relatively extensive accumulations. Barite is also inferred to overgrow and incorporate the silicified microbial networks that blanket the outer surface of the tubes.

ii. Increasing ambient hydrothermal temperatures cause prograde zinc- and iron-sulphide mineralisation to replace the silica and barite mineral assemblage, and consequently overprint the organic tube textures preserved by silica. Micro-reducing environments are set up within the mineralised tube cluster, which allow different replacive processes to occur within close proximity.

iii. Silica and barite precipitation occurs later within pore spaces, and mineralisation of microbial biofilms occurs when ambient conditions allow.

Both of these models result in preservation of the worm tube structure and replacement of organic components. Whilst P is sometimes an effective biomarker within the laminated sulphide horizons, there is little other evidence for the original biological components of the tube wall. What is preserved is the tube morphology and some of the original mineral textures associated with the tube formation. Identification of these textures and mineral assemblages in the fossil record will help in the search for fossil vent species in the geological record.

7.2 - Conclusions

The mineral assemblages observed within the fossil samples studied here record the local chemical environment at the time of mineralisation. Recent *in situ* studies from the East Pacific Rise have demonstrated that chemical speciation controls the vent ecology and the sharp gradients in pH, H_2S and metal ion concentrations lead to ecological gradients across the vent site (Luther *et al.*, 2001). The alvinellid worm tubes and fossilised tube structures studied here record the time intergrated history of fluid evolution. The marcasite/pyrite assemblage that dominates the living alvinellid tube mineralisation implies low local pH values of 5 or below (Murrowchick & Barnes, 1986), which is comfirmed independently by research carried out by Zbinden *et al.* (2003). The low pH values require conductive cooling of mixed vent and/or transport, mixing and reaction (Tivey, 1995). These processes lower the pH and remobilise elements such as Zn leading to elevated values in the fluids (Tivey, 1995). Marcasite precipitation by alvinellid colonies is described to significantly alter the local geochemistry, fluid flow, and mineralisation patterns of hydrothermal vents (Juniper & Tebo, 1995). The dominance of marcasite over pyrite is promoted by the presence of the tube (Zbinden *et al.*, 2003), and more specifically by the presence of microbes within the tube inter-layers. The ZnS content of the living alvinellids studied here is relatively low compared with studies of the same species from the 9°N EPR colonisation site (Zbinden *et al.*, 2003). The difference in ZnS content must reflect the varied Zn content of the fluid bathing each tube worm colony. However, no geochemical data exist at present to confirm this hypothesis.

On death of the tube worm, during subsequent fossilisation processes at higher temperatures, marcasite is remineralised and only the pyrite laminae remain as remnants

of the microbial process inferred to enhance the formation of marcasite/pyrite *via* the monosulphide precursor. At further elevated temperatures still, pyrite is either replaced or overgrown by chalcopyrite which is inferred to form due to changes in the local geochemistry of the host chimney brought about by growth as per standard models of chinmney growth (e.g. Haymon, 1983; Janecky & Seyfried, 1984). However, the preservation of the pyrite layering within the fossil tube structures is achieved by encapsulation and effective isolation of pyrite from percolating hydrothermal fluids by chalcopyrite, which due to its crystalline nature prevents/inhibits fluid exchange within the tube structure as local temperatures increase.

Silica however, does not require a precursor mineral (such as the iron monosulphide/disulphide system does) and as such can precipitate when hydrothermally derived, Si saturated solutions cool during the mixing with seawater. However, the presence of seed crystals of silica, or minerals, such as iron, which catalyse the preciptation of silica can make the precipitation much more kinetically favourable Konhauser, 1996). The presence of microorganisms, and biological tube structures which contain elevated concentrations of Si and Fe can act as a biological template for silica precipitation, and subsequent barite precipitation if conditions allow.

By formulating a hypothesis which explains how biomineralisation pathways can produce sulphide minerals with isotopically distinct signatures relative to the host sulphides, it is hoped that further studies of hydrothermal chimney material, and in particular fluid conduits, may be examined with the idea of this type of geochemical finger print in mind. Allowing for the distinction between 'true' fluid formed mineral conduits, and biomineralised tube structures.

7.3 – Further work

This investigation into the fossilisation process of hydrothermal vent tubeworm species has given an insight in to the geochemical and early mineralogical processes associated with living and dead vent faunal species. In order to more fully understand the micro-scale sulphide mineralisation processes within the tube structures, a more extensive, higher resolution stable sulphur isotope study has been proposed (with Dr. A. Boyce, S.U.R.R.C, Glasgow), to enhance the spatial resolution of the study already

conducted (Chapter 5), and to provide complementary sulphur isotope data for the micro-sulphide layers observed within the tube layers of *Alvinella pompejana* tubes (Chapter 4). The hypothesis arising from the current work is that the pyrite/marcasite laminations will have relatively heavy $\delta^{34}S$ signatures (+8-+10 ‰) reflecting the seawater contribution to the biomineralisation process.

Many of the conclusions drawn in Chapter 6, rely on assumptions made concerning the nature of mixing within the diffuse hydrothermal fluid, and the sulphur isotope values that would be present. This is because there has been no sampling of diffuse fluids, with respect to $\delta^{34}S$ values reported in the scientific literature to date, only end-member fluids, and chimney sulphides have been measured. Therefore many of the alternative hypotheses discussed in Chapters 4 and 5 would be resolved, if sulphur isotope data for diffuse venting fluids were available for a range of hydrothermal vent sites.

To further constrain the timing of the silica and barite mineralisation discussed in Chapter 6, a more thorough investigation into the *in situ* growth rates of vestimentiferan tube worms would prove useful. Although preliminary studies (e.g. Tunnicliffe et al., 1997 and Urcuyo et al., 1998) have revealed much about the growth rates of Ridgea piscesae tubes, more detail on how morphology changes with time would allow constraints to be placed on the replacement of silica with barite and the onset of sulphide mineralisation.

Vibrational spectroscopy methods such as micro-FT-IR and micro-laser Raman are still relatively new analytical methods with respect to geological applications. The Micro-FT-IR analysis undertaken in this study, have acted as a preliminary investigation for a more in-depth study (proposed with Dr. K. Grant, GREMAQ, University of Toulouse) of the crystallinity and mineral characteristics of silica replaced hydrothermal vent worm tubes from the Juan de Fuca Ridge.

Appendix A

Locations of known hydrothermal venting -

Active Spreading Ridges:

Explorer Ridge, Northeast Pacific (McConachy and Scott. 1987)

Juan de Fuca Ridge

Middle Valley near 48.5°N (Davis *et al.,* 1987)

Endeavour segment near 48°N (Tivey and Delaney. 1986; Delaney *et al.*, 1992)

Axial Seamount near 46°N (CASM, 1985; Baker *et al.,* 1990)

CoAxial segment near 46°N (Baker *et al.,* 1993)

Cleft segment near 45°N (Nommark *et al.,* 1983, 1987)

Gorda Ridge (Baker *et al.*, 1987; Morton *et al.,* 1987)

East Pacific Rise

Guaymas Basin, Gulf of California (Lonsdale and Becker. 1985)

21°N (RISE, 1980 Ballard *et al.,* 1981; Von Damm *et al.*, 1985)

13°N (Hekinian *et al.*, 1983a, b)

11 °N (McConachy *et al.,* 1986)

9-10°N (Haymon *et al.*, 1991, 1993)

15°S (Lupton and Craig, 1981)

18 – 21°S (Marchig *et al*, 1990)

Galapagos Rift near 86°W (Corliss *et al.,* 1979: Crane and Ballard, 1980)

Mid-Atlantic Ridge

~39°N: Menez Gwen (Fouquet *et. al.,* 1994)

36 - 39°N: Rainbow (German *et. al.,* 1996)

37°N: Lucky Strike (Langmuir *et al.*, 1993)

29°N: Broken Spur (Murton *et al.*, 1993)

26°N: TAG (Rona *et al.,* 1986; Thompson et al., 1988: Rona and Thompson, 1993)

23°N: Snake Pit (Detnck *et al.*, 1986: Campbell *et al.*, 1988b)

15°N (Rona *et al.*, 1987, 1992)

Red Sea (Degens and Ross, 1969; Shanks and Bischoff, 1980)

'Hornsunds Fault', Barents Sea *(un-nammed team of US – USSR – Norwiegen scientists)*

Back-arc basins and marginal seas:

Okinawa Trough (Halbach *et al.*, 1989)

Maniana Trough (Honhe *et al.,* 1986)

Manus Basin (Both *et al.,* 1986)

Woodlark Basin

North Fiji Basin Ridge (Auzende *et al.*, 1991)

Lau Basin (Fouquet *et al.,* 1991a, b)

Hot-spot and arc volcanoes:

Loihi Seamount. Hawaii (Malahoff *et al.*, 1982; Karl *et al.*, 1988; Sedwick *et al.,* 1992)

MacDonald and Teahitia Seamounts (McMurtry *et al.,* 1989; Stuben *et al.*, 1989; Michard *et al.*, 1993)

Kasuga seamounts (McMurtry, *et al.*, 1993)

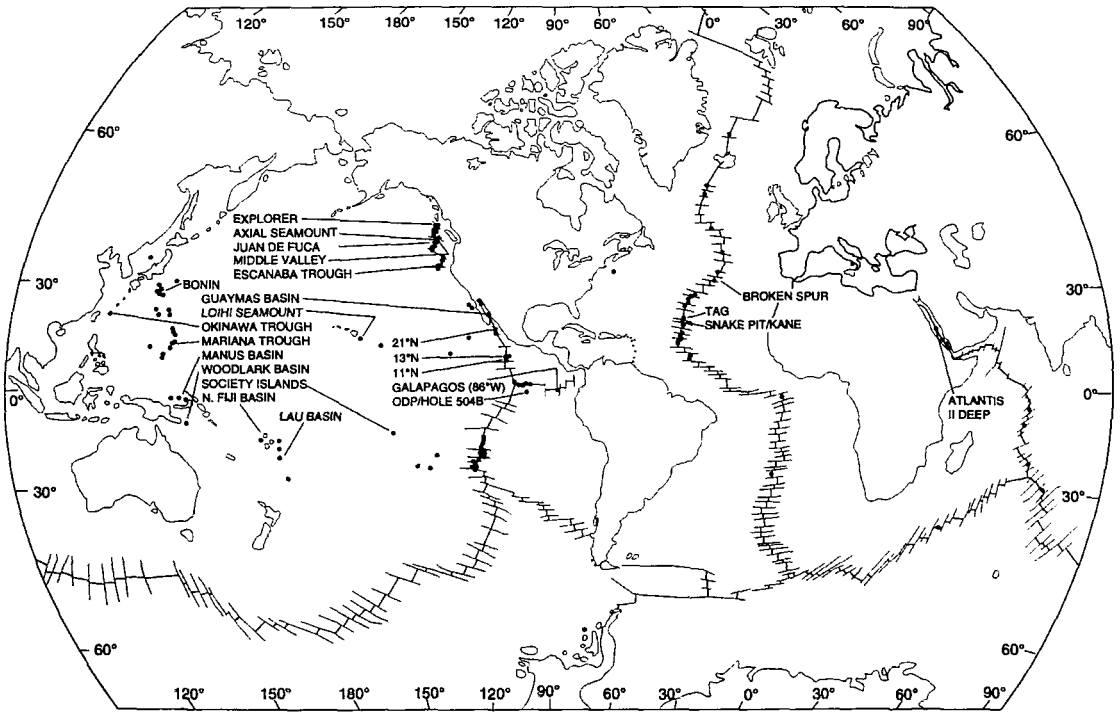

Figure A.1 – Locations of known hydrothermal vent sites, polymetalic sulphides & Fe-Mn oxide deposits in the oceans. After Barns

Appendix B

Data & Images -

All raw data and images can be found on the enclosed CD-ROM:

\Appendix B\Data\

\Appendix\Images\

References

ALAYSE-DANET, A.M., DESBRUYÈRES, D., GAILL. F., 1987. The possible nutritional or detoxification role of the epibiotic bacteria of Alvinellid polychaetes: review of current data. *Symbiosis.* **4,** 51-62.

ALLEN, E.T., CRENSHAW, J.L., JOHNSON, J., LARSEN, E.S., 1912. The mineral sulphides of iron with crystallographic study. *Amer. J. Sci.*. **23**, 169-236.

ALT, J.C. 1995. Subseafloor processes in Mid-Ocean Ridge hydrothermal systems. *In: (Humphries, Zierenberg, Mullineaux & Thompson (Eds) "Seafloor Hydrothermal Systems".* American Geophysical Union, 85 – 114.

ALT, J.C. 1994. A sulphur isotopic profile through the Troodos Ophiolite, Cyprus. *Geochem. Cosmochem. Acta.,* **58**, 1825 – 1840.

ALT, J.C., HONNOREZ, J., LAVERNE, C. & EMMERMANN, R. 1986. Hydrothermal alteration of a 1-Km section through the upper oceanic-crust, Deep-sea Drilling Project Hole 504B. *Geophys. Res-solid. Earth Pl.,* **91**, 309 – 335.

ARNOLD, M., & SHEPPARD, S. M. F., 1981. East Pacific Rise at latitude 21°N: Isotopic composition and origin of the hydrothermal sulphur. *Earth and Planetary Science Letters,* **56,** 148 - 156.

ARP, A.J. & CHILDRESS, J.J. 1981. Blood function in the hydrothermal vent vestimentiferan tube worm. *Science,* **213**, 342 – 344.

ARP, A.J. & CHILDRESS, J.J. 1983. Sulphide binding by the blood of the hydrothermal vent tube worm *Riftia pachyptila. Science,* **219**, 295-297.

BAKER, E.T., GERMAN, C.R. & ELDERFIELD, H. 1995. Hydrothermal plumes over spreading center axes: global distribution and geological inferences. *In:*

Humphris, S.E. (ed.) *Seafloor Hydrothermal Systems: Physical, Chemical, Biological and Geological Interactions.* American Geophysical Union, Washington DC. 47 – 71.

BALLARD, R.C. HEKINIAN, R. & FRANCHETEAU, J. 1984. Geological setting of hydrothermal activityat 12°50'N on the East Pacific Rise: a submersible study. *Earth Planet. Sci. Letts.*, **69**, 176 – 186.

BANKS, D.A. 1985. A fossil hydrothermal worm assemblage from the Tynagh lead-zinc deposit in Ireland. *Nature*, **313**, 128-131.

BARNS, H.L. 1997. Geochemistry of hydrothermal ore deposits. *John Wiley & Sons, Chichester.* pp 972.

BARNS, S.M., DELWICHE, C.F., PALMER, DAWSON, S.C., HERSHBERGER, K.L. & PACE, N.R., 1996. Phylogenetic perspectives on microbial life in hydrothermal ecosystems, past and present. *In:* Bock, G.R. & Goode, J.A. (eds.) *Evolution of Hydrothermal Ecosystems on Earth (and Mars?)* - Ciba Foundation Symposium; 202. John Wiley & Sons, London. 24 - 31.

BAROSS, J.A. & DEMMING, J.W. 1983. Growth of 'black smoker' bacteria at temperatures of at least 250°C. *Nature,* **303**, 423 – 426.

BAZYLINSKI, D.A., WIRSEN, C.O. & JANNASCH, H.W. 1989. Microbial utilisation of naturally-occuring hydrocarbons at the Guaymas Basin hydrothermal vent site. *Appl. Environ. Microbiol.,* **55**, 2832 – 2836.

BECHTEL, A., PERVAZ, M. & PUTTMANN, W. 1998. Role of organic matter and sulphate-reducing bacteria for metal sulphide precipitation in the Bahloul Formation at the Bou Grine Zn/Pb deposit (Tunisia). *Chem. Geol.*, **144**, 1 – 21.

BENNING, L.G., WILKIN, R.T., BARNES, H.L., 2000. Reaction pathways in the Fe-S system below 100°C. *Chem. Geol.* **167**, 25-51.

BECKER, K., SAKAI, H., ADAMSON, A., ALEXANDROVICH, J., ALT, J.C. and 20 others. 1989. Drilliing deep into young oceanic crust, Hole 504B, Costa Rica Rift. *Rev. Geophys.*, **27**, 79 – 102.

BERNDT, M.E., SEYFRIED, W.E. & BECK, J.W. 1988. Hydrothermal alteration process at Mid-ocean Ridges – experimental and theoretical constraints from Ca and Sr exchange-reactions and Sr isotopic-ratios. *Geophys. Res-solid. Earth Pl.*, **93**, 4573 – 4583.

BERNDT, M.E., SEYFRIED, W.E. & JANECKY, D.R. 1989. Plagioclaise and epidote buffing of cation ratios in Mid-Ocean Ridge hydrothermal fluids: experimental results in and near the supercritical region. *Geochem. Cosmochem. Acta.*, **53**, 2283 - 2300.

BERNER, R. A., 1964, Distribution and diagenesis of sulfur in some sediments from the
Gulf of California. *Marine Geology,* **1**, 117 - 140.

BERNER, R.A., 1980. *Early Digenesis: a Theoretical Approach.* Princeton University Press, Princeton, N.J., 241pp.

BERNER, R. A., 1984, Sedimentary pyrite formation: An update. *Geochimica et Cosmochimica Acta,* 48, 605 - 615.

BEVERIDGE, T.J. & MURRAY, R.G.E.1976. Uptake and retention of metals by the cell walls of *Bacillus subtilis. J. Bacteriology,* **127**, 1502 – 1518.

BEVERIDGE, T.J., MURRAY, R.G.E., 1980. Sites of metal deposition in the cell wall of Bacillus subtilis. *J. Bacteriol.* **141,** 876-887.

BEVERIDGE, T.J., FYFE, W.S., 1985. Metal fixation by bacterial cell walls. *Canadian J. Earth Sci.* **22**, 1892-1898.

BEVERIDGE, T.J. 1989b. Role of cellular design in bacterial metal accumulation and mineralisation. *Annul. Rev Microbiology*, **43**, 147 – 171.

BIRNBAUM, S.J. & WIREMAN, J.W. 1984. Sulphate reducing bacteria and silica solubility: a possible method for evaporite digenesis and silica precipitation in banded iron formations. *Canadian Journal of Earth Sciences*, **22**, 1904 – 1909.

BISCHOFF, J.L. & SEYFREID, W.E. 1978. Hydrothermal chemistry of seawater from 25°C to 350°C. *Am. J. Sci.*, **278**, 838 – 860.

BOHLMANN, E.G., MESMER, R.E. & BERLINSKI, P. 1980. Kinetics of silica deposition from simulated geothermal brines. *Society of Petrological Engineering Journal.* 239 – 248.

BOSCHKER, H.T.S., NOLD, S.C., WELLSBURY, S.C., BOS, D., DE GRAAF, W., PEL, R., PARKES, R.J., CAPPENBERG, T.E. 1998. Direct linking of microbial populations to specific biogeochemical processes by ^{13}C – labelling of biomarkers. *Nature*, **392**, 801 – 804.

BOTTCHER, M.E., 2001, Sulphur isotope fractionation in the biogeochemical sulphur cycle of marine sediments. *Isotopes in Environmental and Health Studies*, **37,** 97-99.

BOTTCHER, M.E., THAMDRUP, B., AND VENNEMANN, T.W. 2001. Oxygen and sulphur isotope fractionation during anaerobic bacterial disproportionation of elemental sulphur. *Geochimica Et Cosmochimica Acta*, **65**, 1601-1609.

BRIGGS, D E.G. 1991. Extraordinary Fossils. *American Scientist*, **79(2),** 130 – 132.

BRIGGS, D.E.G., BOTTRELL, S.H., RAISWELL, R., 1991. Pyritisation of soft-bodied fossils: Beecher's Trilobite bed, Upper Ordovician, New York State. *Geology.* **19**, 1221-1224.

BRUNE, H., GIOVANNINI, M., BROMANN, K. & KERN, K. 1998. Self-organised growth of nanostructure arrays on strain-relief patterns. *Nature*, **394**, 451 – 453.

BUBELA, B., AND MCDONALD, J.A., 1969, Formation of banded sulphides: Metal ion separation and precipitation by inorganic and microbial sulphide sources.: *Nature,* **221**, 465-466.

BUTTERFIELD, D.A., JONASSON, I.R., MASSOTH, G.J., FEELY R.A., ROE, K.K., EMBERLY, R.E., HOLDEN, J.F., McDUFF, R.E., LILLEY, M.D. & DELANEY, J.R. 1999. Seafloor eruptions and evolution of hydrothermal fluid chemistry. *In:* Cann, J.R., Elderfield, H, & Laughton, A (eds.) *Mid-Ocean Ridges: Dynamics of Processes Associated with Creation of New Ocean Crust.* Cambridge University Press, Cambridge, UK., pp355.

CADY, S.L. & FARMER, J.D. 1996. Fossilisation processes in siliceous thermal springs: Trends in preservation along the thermal gradient. *In:* Bock, G.R. & Goode, J.A. (eds.) *Evolution of Hydrothermal Ecosystems on Earth (and Mars?).* Ciba Foundation Symposium**; 202**. John Wiley & Sons, London. 150 - 169.

CAMPBELL, B.J., JEANTHON, C., KOSTKA, J.E., LUTHER, G.W., AND CARY, S.C. 2001. Growth and phylogenetic properties of novel bacteria belonging to the epsilon subdivision of the Proteobacteria enriched from Alvinella pompejana and deep-sea hydrothermal vents. *Applied and Environmental Microbiology*, **67,** 4566 - 4572.

CANFIELD, D.E., AND THAMDRUP, B., 1994. The production of ^{34}S-depleted sulfide during bacterial disproportionation of elemental sulfur: *Science*, **266**, 1973-1975.

CANN, J.R., STRENS, M.R. & RICE, M.R. 1985. A simple magma-driven thermal balance model for the formation of volcanogenic massive sulphides. *Earth and Planetary Science Letters*, **76**, 123.

CARROL, S., MROCZEK, E., ALAI., M. & EBERT, M. 1998. Amorphous silica precipitation (60 - 120°C): Comparison of laboratory and field rates. *Geochemica et Cosochimica Acta*, **62**, 1379 – 1392.

CARY, S.C., COTTRELL, M.T., STEIN, J.L., CAMACHO, F. & DESBRUYERES, D. 1997. Molecular identification and localisation of filamentous symbiotic bacteria associated with the hydrothermal vent annelid *Alvinella pompejana*. *Applied and Environmental Microbiology.* **63 (3)**, 1124 – 1130.

CARY, S.C., SHANK, T. & STEIN, J. 1998. Worms bask in extreme temperatures. *Nature,* **391**, 545 – 546.

CHASSARD-BOUCHARD, C.M., FIALA-MEDIONI, A., BOUMATI, P., ESCAIG, F., KLEINBAUER, F., BRISSARD, J. & GALLE, P. 1988. *Calyptogena phaseoliformis* (Mollusque bivalve) indicateur biologique des phenomenes geochimiques associes aux zones de subductionsituees au large du Japon. *C. R. Acad. Sci. Paris, Ser. III.*, **306**, 237 – 244.

CHASSARD-BOUCHARD, C.M., FIALA-MEDIONI, A. & GALLE, P. 1986. Microanalytical study of the hydrothermal vent Mytilidae *Bathymodiolus sp.* from the East Pacific Rise: preliminary data. *C. R. Acad. Sci. Paris, Ser. III.,* **302,** 117 – 124.

CHATELLIER, X., FORTIN, D., WEST, M.M., LEPPARD, G.G., & FERRIS, F.G. 2001. Effect of the presence of bacterial surfaces during the synthesis of Fe oxides by oxidation of ferrous ions. *European Journal of Mineralogy*,**13,** 705-714.

CHEN, C.T.A. & MARSHALL, W.L. 1982. Amorphous silica solubilities. 4. Behavious in pure water and aqueous sodium chloride, sodium sulphate, magnesium chloride and magnesium sulphate solutions up to 350°C. *Geochim. Cosmochim. Acta.*, **46**, 279 – 287.

CHEVALDONNE, P., DESBRUYÈRES, D., CHILDRESS, J.J., 1992. Some like it hot – and some even hotter. *Nature*. **359**, 593-594.

CHILDRESS, J.J, FISHER, C.R., BROOKS, J.M., KENNITICUT, M.C.I., BRDIGARE, R. & ANDERSON, A.E. 1986. A methanotrophic marine molluscan (Bivalvia, Mytilidae) symbiosis: mussels fuelled by gas. *Science*, **223**, 1306-1308.

CHILDRESS, J.J., H. FELBECK AND G.N. SOMERO. 1987. Symbiosis in hydrothermal vent animals. *Scientific American.* **255**,114-120.

CHILDRESS, J.J., FISHER, C.R. FAVUZZI, J.A., KOCHEVAR, R, SANDERS, N.K. & ALAYSE, A.M. 1991a. Sulphide-driven autotrophic balance in the bacterial symbiont-containing hydrothermal vent tubeworm, *Riftia pachyptila* Jones. *Biol. Bull.,* **180**, 135 – 153.

CHILDRESS, J.J. & FISHER, C.R. 1992. The biology of hydrothermal vent animals: physiology, biochemistry and autotrophic symbiosis. *Oceanogr. Mar. Biol. Annu. Rev.,* **30**, 337 – 441.

CHIN, W-C., ORELLANA, M.V. & VERDUGO, P. 1998. Spontaneous assembly of marine dissolved organic matter into polymer gels. *Nature*, **391**, 568 – 572.

CLARKE, W.A., KONHAUSER, K.O., THOMAS, J.C. & BOTTRELL, S.H. 1997. Ferric hydroxide and ferric hydroxysulphate precipitation by bacteria in an acid mine drainage environment. *FEMS Microbiology Reviews,* **20**, 315 – 326.

COMTET, T & DESBRUYERES, D. 1998. Population structure and recruitment in mytilid bivalves from the Lucky Strike and Menez Gwen hydrothermal vent fields (37°17'N and 37°50'N on the Mid-Atlantic Ridge). *Marine Ecology Progress Series,* **163**, 165 – 177.

CONVERSE, D.R., HOLLAND, H.D. & EDMOND, J.M. 1984. Flow rates in the hot axial springs of the East Pacific Rise (21°N): implications for the heat budget and the formation of massive sulphide deposits. *Earth Planet Sci. Lett.,* **69**, 159 – 175.

COOK, T.L., STAKES D.S., 1995. Biogeologicalmineralisationin deep-sea hydrothermal deposits. *Science* **267,** 1975-1979.

COPLEY, J.T.P., TYLER, P.A., MURTON, B.J. & VAN DOVER, C.L. 1997. Spatial and interannual variation in the faunal distribution at broken spur vent field (29°N, Mid-Atlantic Ridge). *Marine Biology*, **129**, 723 – 733.

CORLISS, J.B., DYMOND, J., GORDON, L., EDMOND, J.M., VON HERZEN, R.P., BALLARD, R.D., GREEN, K., WILLIWMS, D., BAINBRIDGE, A. CRANE, K. & VAN ANDLE, T.H. 1979. Submarine thermal springs on the Galapagos Rift. *Science*, **203**, 1073 – 1083.

CORLISS, J.B., BAROSS, J.A. & HOFFMAN, S.E. 1981. An hypothesis concerning the relationship between submarine hotsprings and the origin of life on Earth. *Oceanol. Acta.,* **39**, 59 - 69

CORLISS, J.B., DYMOND, J., GORDON, L.I., EDMOND, J.M., VON HERZEN, R.P., BALLARD, R.D., GREEN, K., WILLIAMS, D., BAINBRIDGE, A., CRANE, K. & VAN ANDEL, T.H. 1979. Submarine thermal springs on the Galapagos Rift. *Science*, **203**, 1073 - 1983.

COSSON-MANNEVY, M.A., R. COSSON & F. GAILL 1986. Mise en évidence de protéines de type métallothionéine chez deux invertebrés de sources hydrothermales, le pogonophore vestimentifère *Riftia pachyptila* et l'annélide polychète *Alvinella pompejana. Compte r. Acad. Sci. Paris* Ser. III, **302**, 347-352.

COSSON-MANNEVY, M.A., COSSON, R.P., GAILL, F. & LAUBIER, L. 1988. Transfert, Accumulation et regulation des elements mineraux chez les organismes des sources hydrothermales. *Oceanol. Acta. Special volume,* **8**, 219 – 226.

DAVIES, P.C.W. 1996. The transfer of viable micro-organisms between planets *In:* Bock, G.R. & Goode, J.A. (eds.) *Evolution of Hydrothermal Ecosystems on Earth*

(and Mars?) - Ciba Foundation Symposium; **202**. John Wiley & Sons, London. 304 - 317.

DAVIS, S.A., BURKETT, S.L., MENDELSON, N.H. & MANN S. 1997. Bacterial templating of ordered macrostructures in silica and silica-surfactant mesophases. *Nature,* **385**, 420 - 423.

DELANEY, J.R., KELLEY, D.S., LILLEY, M.D., BUTTERFIELD, D.A., BAROSS, J.A., WILCOCK, W.S.D., EMBLEY, R.W. & SUMMIT, M. 1998. The quantum event of oceanic crustal accretion: impacts of diking at Mid-Ocean Ridges. *Science*, **281**, 222 – 230.

DELANEY, J.R., ROBIGOU, V., MCDUFF, R.E. & TIVEY, M.K. 1992. Geology of a vigorous hydrothermal sysyem on the Endeavour Segment, Juan de Fuca Ridge. *Journal of Geophysical Research*, **97**, 19663 – 19682.

DEER, W.A., HOWIE, R.A. & ZUSSMAN, J. 1966. "An Introduction to the Rock Forming Minerals". *Longmans, London.* pp 528.

DESBRUYERES, D. 1995. Temporal variations of deep-sea hydrothermal communities at 13°N/EPR. *InterRidge News*, **4** (2), 6-10.

DESBRUYÈRES, D., GAILL, F., LAUBIER, L., PRIEUR, D. RAU, G.H., 1983. Unusual nutrition of the 'Pompeii worm' *Alvinella pompejana* (polychaetous annelid) from the hydrothermal vent environment: SEM, TEM, ^{13}C and ^{15}N evidence. *Mar. Biol.* **75**, 201-205.

DESBRUYÈRES, D., LAUBIER, L., 1980. *Alvinella pompejana*, Ampharetidae aberrant des sources hydrothermals de la ride Est Pacifique. *Oceanol. Acta.* **3**, 267-274.

DESBRUYERES, D. & SEGONZAC, M. 1997. *"Handbook of Deep-sea Hydrothermal Vent Fauna"*. IFREMER, Brest, France. pp 279.

DESBRUYERES, D., CHEVALDONNE, P., ALAYSE, A.M., JOLLIVET, D., LALLIER, F.H., JOUIN-TOULMOND, C., ZAL, F., SARRADIN, P.M., COSSON, R., CAPRAIS, J.C., ARNDT, C., O'BRIEN, J., GUEZENNEC, J., HOURDEZ, S., RISO, R., GAILL, F., LAUBIER, L., AND TOULMOND, A. 1998. Biology and ecology of the "Pompeii worm" (*Alvinella pompejana* Desbruyeres and Laubier), a normal dweller of an extreme deep- sea environment: A synthesis of current knowledge and recent developments. *Deep-Sea Research Part I - Topical Studies in Oceanography*, **45,** 383-+.

DETMERS, J., BRUCHERT, V., HABICHT, K.S., & KUEVER, J. 2001. Diversity of sulfur isotope fractionations by sulfate-reducing prokaryotes. *Applied and Environmental Microbiology*, **67,** 888-894.

DICKSON, D. 1998. Science summit sets ambitious agenda. *Nature,* **396**, p299.

DUNN, K.A., MCLEAN, R.J.C., UPCHURCH Jr., G.R., & FOLK, R.L. 1997. Enhancement of leaf fossilisation potential by bacterial biofilms. *Geology*, **25**, 1119 – 1122.

ELDERFIELD, H. & SCHULTZ, A. 1996. Mid-ocean ridge hydrothermal fluxes and the chemical composition of the ocean. *Annu. Rev. Earth. Planet. Sci.,* **24**, p191.

EMBLEY, R.W., MURPHY, K.M. & FOX, C.G. 1990. High-resolution studies of the summit of Axial Volcano. *J. Geophys. Res-Solid.,* **95**, 12785 – 12812.

FALLICK AE, MCCONVILLE P, BOYCE AJ, BURGESS R, KELLEY SP. 1992. Laser microprobe stable isotope measurements on geological-materials - some experimental considerations (with special reference to $\delta^{34}S$ in sulfides). *Chem. Geol.*, **101**, 53-61.

FELBECK, H., SOMERO, G.N. & CHILDRESS, J.J. 1981. Calvin-Benson cycle sulphide oxidation enzymes in animals from sulphide rich habitats. *Nature*, **293**, 291 – 293.

FERRIS, F.G. & BEVERIDGE, T.J. 1986. Phisiochemical roles of soluble metal cations in the outer membrane of *Escherichia coli* K-12. *Can. J. Microbiology*, **32**, 594 – 601.

FERRIS, F.G., FYFE, W.S. & BEVERIDGE, T.J. 1986. Iron-silica crystallite nucleation by bacteria in a geothermal sediment. *Nature,* **320**, 609 – 611.

FERRIS, F.G., FYFE, W.S. & BEVERIDGE, T.J. 1987. Bacteria as nucleation sites for authigenic minerals in a metal contaminated lake sediment. *Chem. Geol.,* **63**, 225 – 232.

FERRIS, F.G., FYFE, W.S. & BEVERIDGE, T.J. 1988. Metallic ion binding by bacillus subtilis: implications for the fossilisation of microorganisms. *Geology*, **16**, 149 – 152.

FERRIS, F.G., KONHAUSER, K.O., LYVEN, B., & PEDERSEN, K. 1999. Accumulation of metals by bacteriogenic iron oxides in a subterranean environment. *Geomicrobiology Journal*, **16,** 181-192.

FISCHER, F., ZILLIG, W., STETTER, K.O. & SCHREIBER, G. 1983. Chemolithoautotrophic metabolism of anaerobic extremely thermophilic archaebacteria. *Nature*, **301**, 511 – 513.

FISHER, A.T., BECKER, K. & NARASIMHAN, T.N. 1994. Off-axis hydrothermal circulation – parametric tests of a refined model of process at Deep-sea Drilling Project Ocean Drilling Program Site 504. *J. Geophys. Res. Solid Earth.,* **99**, 3097 3121.

FISHER, A.T. & BECKER, K. 1991. Heat flow, hydrothermal circulation and basalt intrusions in the Guaymas Basin, Gulf of California. *Earth Planet. Sci. Lett.* **103**, 84 – 99.

FISHER, C.R., J.J. CHILDRESS AND E. MINNICH., 1989. Autotrophic carbon assimilation by the chemoautotrophic symbionts of *Riftia pachyptila. Bio. Bull.*, **177,** 372-385.

FISHER, C.R., CHILDRESS, J.J., ARP, A.J., BROOKS, J.M., DISTEL, D., FAVUZZI, J.A., FELBECK, RH., HESSLER, HR., JOHNSON, K.S., KENNICUTT, M.C., MACKO, S.A., NEWTON, A., POWELL, M.A., SOMERO, G.N. & SOTO, T. 1988B. Microhabitat variation in the hydrothermal vent mussel *Bathymodiolus thermophillus*, at Rose Garden vent on the Galapagos Rift. *Deep-Sea Res.*, **35**, 1769 – 1792.

FISHER, CR. 1995. Toward an Appreciation of Hydrothermal-Vent Animals: Their Environment, Physiological Ecology, and Tissue Stable Isotope Values. *In: (Humphries, Zierenberg, Mullineaux & Thompson (Eds) "Seafloor Hydrothermal Systems"*. American Geophysical Union, 279 - 316

FISK, M.R., JOHNSON, K.T.M., AND ALT, J.C., 1994 The effect of assimilation of altered oceanic crust on magma chemistry: An experimental study. *Proceedings of the Ocean Drilling Program, Scientific Results,* **140**, 43-51.

FLEMING, B. A. 1986. Kinetics of reaction between silicic acid and amorphous silica surfaces in NaCl solutions. *Journal of Colloid interface Science*, **110**, 40 -64.

FORNARI, D.J. & EMBLEY, R.W. 1995. Tectonic and volcanic controls on hydrothermal processes at the Mid-Ocean Ridge: An overview based on near-bottom and submersible studies. *In: Humphris (Ed.) Seafloor Hydrothermal Systems: Physical, Chemical, Biological, and Geological Interactions*. American Geophysical Union. Washington D.C. 1 - 46.

FOUQUET, Y., VON STACKELBERG, U., CHARLAU, J.L., DONVAL, J.P., FOUCHER, J.P., ERZINGER, J., HERZIG, P., MUHE, R., WIEDICKE, M., SOAKAI, S. & WHITECHURCH, H. 1991. Hydrothermal activity in the Lau Back-Arc Basin: Sulphides and water chemistry. *Geology*, **19**, 303 - 306.

FOUQUET, Y., KNOTT, R., CAMBON, P., FALLICK, A., RICKARD, D. & DESBRUYERES, D. 1996. Formation of large sulphide mineral deposits along fast spreading ridges. Examples from off-axial deposits at 12°43'N on the East Pacific Rise. *Earth Planet. Sci. Letts.*, **144**, 147 – 162.

FOURNIER, D., LAFITTE, M. & MAURY, R. 1983. Analytical study of Cu-Zn and Cu-Ni sulphides from Labrador. *C. R. Acad. Sci. Ser. II.*, **297**, 137 – 140.

FORTIN, D., FERRIS, F.G., & SCOTT, S.D. 1998. Formation of Fe-silicates and Fe-oxides on bacterial surfaces in samples collected near hydrothermal vents on the Southern Explorer Ridge in the northeast Pacific Ocean. *American Mineralogist*, **83**, 1399-1408.

FOWLER, A.D. 1990. Self-organised mineral textures of igneous rocks: the fractal approach. *Earth Sciences Reviews,* **29**, 47 – 55.

FRANCIS, S., MARGULIS, L & BARGHOORN, E.S. 1987a On the experimental silicification of microorganisms. II. On the time appearance of eukaryotic organisms in the fossil record. Precambrian Research, 6, 65 – 100.

FUSTEC, A., DESBRUYERES, D. & JUNIPER, S.K. (Author). 1987. Deep-sea hydrothermal vent communities at 13N on the East Pacific Rise: micro-distribution and temporal variations. *Biological Oceanography*, **4(2),** 121-164.

GAGE, J.D. & TYLER, P.A. 1991. *Deep-sea Biology.* Cambridge University Press, Cambridge. pp504

GAILL, F & HUNT, S. 1986. Tubes of deep sea hydrothermal vent worms *Riftia pachyptila* (Vestimentifera) and *Alvinella pompejana* (Annelida). *Marine Ecology Progress Series,* **34**, 267 – 274.

GAILL, F & HUNT, S. 1991. The biology of annelid worms from high temperature hydrothermal vent regions. *Reviews in Aquatic,* **4(2-3)**, 107 – 137.

GAILL, F., SHILLITO, B., MENARD, F., GOFFINET, G. & CHILDRESS, J.J. 1997. Rate and process of tube production by the deep-sea hydrothermal vent tubeworm *Riftia pachyptila. Marine Ecology Progress Series*, **148**, 135 – 143.

GAILL, F., VOSS-FOUCART, M.F., GERDAY, C., COMPERE, P. & GOFFINET, G. 1992b. Chitin and protein content in the tubes of vestimentiferan worms from hydrothermal vents. *In:* Brine, C.J., Standford, P.A. & Zizakis, J.P. (eds) *Advances in Chitin and Chitosan.* Elsevier Applied Science, Barking, 232-236.

GERMAN, C.R., PARSON, L.M. & *HEAT* SCIENTIFIC TEAM. 1996. Hydrothermal exploration near the Azores Triple Junction: tectonic control at slow spreading ridges. *Earth and Planetary Science Letters,* **138**, 93 – 104.

GHIORSE, W.C. 1984. Biology of iron and manganese-depositing bacteria. *Annual Review of Microbiology*, **38**, 515 – 550.

GILLIAN, D.C. & DE RIDDER, C. 1997. Morphology of a ferric iron-encrusting biofilm forming on the shell of a burrowing bivalve (Mollusca). *Aquatic Microbial Ecology,* **12**, 1 - 10.

GILLIS, K.M. & ROBINSON, P.T. 1990. Patterns and processes of alteration in the lavas and dikes of the Troodos Ophiolite, Cyprus. *J. Geophys. Res.*, **95**, 21523 – 12548.

GILLIS, K.M., THOMPSON, G. & KELLEY, D.S. 1993. A view of the lower crustal component of hydrothermal systems at the Mid-Atlantic Ridge. *J. Geophys Res-solid. Earth.*, **98,** 19597 – 19619.

GITTENS, D. 1995. Digital X-ray mapping: A guide to obtaining better data. *Rev 2.1. PGT, UK.*

GINSTER, U., MOTTL, M.J. & VON HERZEN, R.P. 1994. Heat flux from black smokers on the Endeavour and Cleft segments, Juan de Fuca Ridge. *Journal of Geophysical Research,* **99,** 4937 – 4950.

GLEESON, J.T. 1997. Dendritic growth of electro-hydrodynamic convection in a nematic liquid crystal. *Nature,* **385**, 511 - 513.

GOLDHABER, M. B., AND KAPLAN, I. R., 1974, The sulfur cycle *in:* Goldberg, E. D. (ed.), *The Sea.* New York, John Wiley and Sons, 569-655.

GOTZINGER, J.P. & ROTHMAN, D.H. 1996. An abiotic model for stromatolite morphogenesis. *Nature,* **383**, 423 - 425.

GRAHAM, U.H. & OHMOTO, H. 1993. Experimental study of formation mechanisms of hydrothermal pyrite. *Geochemica et Cosmochimica Acta,* **58**, 2187 – 2202.

GRASTY, R.L. SMITH, FRANKLIN, J.M., AND JONASSON, I.R., 1988, Radioactive orphans in barite-rich chimneys, Axial Caldera: *Canadian Mineralogist,* **26(3),** 627-636.

GREGG, M. 1973. Microstructure of the Ocean. *Scientific American.* **228 (2).** 64 - 77

HADDAD, A., CAMACHO, F., DURAND, P. & CARY, S.C. 1995. Phylogenetic

characterisation of the epibiotic bacteria associated with the hydrothermal vent polychaete *Alvinella pompejana. Applied and Environmental Microbiology.* **61**, 1679 – 1687.

HAMMOND, S.R. 1990. Relationships between lava types, seafloor morphology, and the occurrence of hydrothermal venting in the ASHES vent field of Axial Volcano. *J. Geophys. Res.*, **98**, 12875 – 12893.

HANNINGTON, M.D. & SCOTT, S.D. 1988. Mineralogy and geochemistry of a hydrothermal silica-sulphide-sulphate spire in the Caldera of Axial Seamount, Juan de Fuca Ridge. *Canadian Mineralogy,* **26**, 603 –625.

HANNINGTON, M.D. AND SCOTT, S.D., 1989. Sulphidation equilibria as guides to gold mineralisation involcanogenic massive sulphides: evidence from sulphide mineralogy and the composition of sphalerite. *Econ. Geol.*, **84**, 1978 – 1995.

HARDING, I.C. 1996. An investigation of the Miocene fossil cold Seep deposits of Barbados. *Final Report on the NERC Small Grant GR9/00966'A'.* (unpublished).

HART, S.R., BLUSZTAJN, J., DICK H.J.B. & LAWRENCE, J.R. 1994. Fluid circulation in the oceanic crust: contrast between volcanic and plutonic regimes. *J. Geophys. Res.*, **99**, 3163 – 3174.

HASMY, A., ANGLARET, E., THOUY, R. AND JULLIEN, R. 1997. Fluctuating Bond Aggregation: a Numerical Simulation of Neutrally-Reacted Silica Gels. *J. Phys.*, **7**, 521-542

HAYMON, R.M. 1983. Growth history of black smoker hydrothermal chimneys. *Nature*, **301**, 695 – 698.

HAYMON, R. M., D. J. FORNARI, K. L. VON DAMM, M. D. LILLEY, M. R. PERFIT, J. M. EDMOND, W. C. SHANKS, III, R. A. LUTZ, J. M. GREBMEIER, S.

CARBOTTE, D. WRIGHT, E. MCLAUGLIN, M. SMITH, N. BEEDLE, AND E. OLSON. 1993.Volcanic eruption of the mid-ocean ridge along the East Pacific Rise crest at 9°45'N: Direct submersible observations of seafloor phenomena associated with an eruption event in April 1991, *Earth Planet. Sci. Lett.*, **119**, 85-101.

HAYMON, R.M., D.J. FORNARI, M.H. EDWARDS, S. CARBOTTE, D. WRIGHT and K.C. MACDONALD. 1991. Hydrothermal vent distribution along the East Pacific Risecrest (09'-54' N) and its relationship to magmatic and tectonic processes on fast-spreading mid-ocean ridges. *Earth Plan. Sci. Letts.* **104.** 513-534

HAYMON, R.M. & KOSKI. R.A. 1985. Evidence of an ancient hydrothermal vent community: fossil worm tubes in Cretaceous sulfide deposits of the Samail ophiolite, Oman. *Bull. Biol. Soc. Wash.* **6**, 57-65.

HAYMON, R.M., KASTNER, M., 1981. Hot spring deposits on the East Pacific Rise at 21°N: preliminary description of mineralogy and genesis. *Earth Planet. Sci. Lett.* **53,** 363-381.

HAYMON, R.M., KOSK, R.A. & SINCLAIR, C. 1984. Fossils of hydrothermal vent worms from Cretaceous sulphide ores of the Samail ophiolite, Oman. *Science*, **223**, 1407-1409.

HEIN, J.R., SCHOLL, D.W., BARRON, J.A., JONES, M.G. & MILLER, J. 1978. *Diagenesis of of late Cenozoic diatomaceous deposits and formation.* 155 – 181.

HEKINIAN, R., FEVRIER, M., BISCHOFF, J.L., PICOT, P & SHANKS, W.C. 1980. Sulphide deposits from the East Pacific Rise near 21°N. *Science*, **207**, 1433 – 1444.

HEKINIAN, R., FRANCHETEAU, J., RENARD, V., BALLARD, R.D, CHOUKROUNE, P., CHEMINEE, J.L., ALBAREDE, F., MINSTER, J.F., CHARLOU, J.L., MARTY, J.C. & BOULEGUE, J. 1983. Intense hydrothermal

activity at the axis of the East Pacific Rise near 13°N: submersible witnesses the growth of a sulphide chimney. *Marine Geophys. Res.*, **6**, 1 – 14.

HENLEY, R.W. 1996. Chemical and physical context for life in terrestrial hydrothermal systems: Chemical reactors for the early development of life and hydrothermal ecosystems. *In:* Bock, G.R. & Goode, J.A. (eds.) *Evolution of Hydrothermal Ecosystems on Earth (and Mars?)* - Ciba Foundation Symposium; 202. John Wiley & Sons, London. 61 - 75.

HERBERT Jr, R.B., BENNER, S.W., PRATT, A.R. & BLOWES, D.W., 1998. Surface chemistry and morphology of poorly crystalline iron sulphides precipitated in media containing sulphate-reducing bacteria. *Chemical Geology,* **14**, 87 – 97.

HERZIG, P.M., HANNINGTON, M.D. & ARRIBAS, A. 1998. Sulfur isotopic composition of hydrothermal precipitates from the Lau back-arc: implications for magmatic contributions to seafloor hydrothermal systems. *Am. J. Sci.,* **291**, 541 – 648.

HERZIG, P.M. & HANNINGTON, M.D. 2000. Third dimension of a presently forming VMS deposit: TAG hydrothermal mound, Mid-Atlantic Ridge, 26 degrees. *Miner. Deposita.,* **35**, 223 – 259.

HESSE, R. 1988. Origin of chert, I: diagenesis of biologic siliceous sediments. *Geosci. Can.,* **15 (3).** 171 – 192.

HESSLER, R.P. & LONSDALE, P. 1991. Biogeography of the Mariana Trough hydrothermal vent communities. *Deep-Sea Research,* **38A.** 185-199.

HESSLER, R.R., SMITHEY, Jr., W.M. & KELLER, C.H. 1985. Spatial and temporal variation of giant clams, tubeworms and mussels at deep-sea hydrothermal vents. *Biological Society of Washington.* **6**, 411 – 428.

HOEFS, J., 1987, *Stable Isotope Geochemistry.* Berlin, Springer-Verlag, 241 p.

HOLDEN JF, SUMMIT M, BAROSS JA. 1998. Thermophilic and hyperthermophilic microorganisms in 3-30 degrees C hydrothermal fluids following a deep-sea volcanic eruption. *Fems Microbiol. Ecol.*, ***25,*** 33-41.

HOLMES, M.L. & ZIERENBERG, R.A. 1990. Submersible observations in Escanaba Trough, Southern Gorda Ridge. *In: McMurray (Ed.) "Gorda Ridge: a seafloor spreading center in the United States' Exclusive Ecconomic Zone. Proceedings of the Gorda Ridge Symposium, 11-13 May 1987". `p 93 - 116*

HONJO, S. 1976. Coccoliths: Production, transportation and sedimentation. *Marine Micropalaeontology,* **1**. 65 - 79.

HOPKINSON, L., ROBERTS, S., WILKINSON, J. & HERRINGTON, R. 1998. Self-organisation of submarine hydrothermal siliceous deposits: Evidence from the TAG hydrothermal mound, 26°N Mid Atlantic Ridge. *Geology,* **26**, 347 – 350.

HUMPHRIES, S.E. & THOMPSON, G. 1978b. Trace element mobility during hydrothermal of oceanic basalts. *Geochim. Cosmochim. Acta.*, **42**, 127 – 136.

HUMPHRIS, S.E., HERZIG, P.M., MILLER, D.J. 1995. The internal structure of an active sea-floor massive sulphide deposit. *Nature.* **377**, 713-716.

HUNT, S. 1970. *Polysaccharide-protein complexes in invertebrates.* Academic Press, London, New York. pp329.

HUNT, S. 1992. Crystalline Sulphur Deposits on the Tube of the Hydrothermal Vent Worm *Alvinella-Pompejana. Comparative Biochemistry and Physiology a-Physiology,* **102,** 71-77.

ILER, R.K. 1979. *Chemitry of silica.* Wiley Interscience, New York.

INESON, P.R. 1989. "Introduction to Practical Ore Microscopy" *In: Zussman & Mackenzie (eds.), Longman Earth Science Series., Longman, London.* pp181.

ISAACS, C.M. 1982. Influence of rock composition on kinetics of silica phase changes in the Monteray Formations, Santa Barbara area, California. *Geology,* **10,** 304 – 308.

JANECKY, D.R., & SEYFRIED, W.E. 1984 Formation of Massive Sulphide Deposits on Oceanic Ridge Crests - Incremental Reaction Models for Mixing between Hydrothermal Solutions and Seawater. *Geochimica Et Cosmochimica Acta*, **48,** 2723-2738.

JANNASCH, H.W. 1983. Microbial processes at deep sea hydrothermal vents. *In*: Rona, P.A. (ed.) *Hydrothermal Processes at Seafloor Spreading Centers*. Plenum, New York. 677 - 709.

JANNASCH, H.W. 1984. Chemosynthesis: The nutritional basis for life at deep-sea vents. *Oceanus,* **27**, 73-79.

JANNASCH, H.W. & MOTTL, M.J. 1985. Geomicrobiology of deep-sea hydrothermal vents. *Science,* **229,** 717 - 725.

JANNASCH, H.W. 1993. Two new findings in hydrothermal vent microbiology. *RIDGE Events*, **7**, 10 - 11.

JANNASCH, H. W. 1995. Microbial interaction with hydrothermal fluids. *In: Humphris (Ed.) Seafloor Hydrothermal Systems: Physical, Chemical, Biological, and Geological Interactions*. American Geophysical Union. Washington D.C. 273-296.

JANNASCH, H.W. 1995 Anaerobic oil degradation by a new sulphate-reducing bacterium isolated from Guaymas Basin geothermal sediments. *RIDGE Events,* **June 1995**, 7 - 8.

JANNASCH, H.W. 1996. Microbial interactions with hydrothermal fluids. *In:* Humphris, S.E. (ed.) *Seafloor Hydrothermal Systems: Physical, Chemical, Biological and Geological Interactions.* American Geophysical Union, Washington DC. 273 - 297.

JANNASCH, H. W. 1997. Biocatalytic transformations of hydrothermal fluid. *Proc. Royal Soc.* (London), **A355**, 475-486

JANNASCH, H.W. & WIRSEN, C.O. 1979. Chemosynthetic primary production at East Pacific sea floor spreading centers. *Bioscience*, **29**, 592 - 598.

JANNASCH, H.W., WIRSEN, C.O., 1981. Morphological survey of microbial mats near deep-sea thermal vents. *Appl. Env. Microbiol.*, **41,** 28-538.

JEANDEL C, TACHIKAWA K, BORY A, DEHAIRS F. 2000. Biogenic barium in suspended and trapped material as a tracer of export production in the tropical NE Atlantic (EUMELI sites). *Marine Chemistry*, **71 (1-2),** 125 - 142.

JEANTHON, C., PRIEUR, D., 1990. Susceptibility to heavy metals and characterisation of heterotrophic bacteria isolated from two hydrothermal vent polychaete annelids, *Alvinella pompejana* and *Alvinella caudata. Appl. Env. Microbiol.* **56**, 3308-3314.

JENSEN, M. L., & NAKAI, N., 1962. Sulphur isotope meteorite standards--Results and recommendations. *In: Biogeochemistry of sulfur isotopes Symposium*, Yale University, 30-35.

JOHNSON, H.P. & EMBLEY, R.W., 1990.Axial seamount - an active ridge axis volcano on the central Juan de Fuca Ridge. *J. Geophys. Res-Solid.*, **95**, 12689-12696.

JOHNSON, J.W. & NORTON, D. 1991. Critical phenomena in hydrothermal systems – state, thermodynamic, electrostatic, and transport properties of H_2O in the critical region. *Am. J. Sci.,* **291**, 541 – 648.

JONES, B. & RENAUT, R.W. 1996. Influence of thermophilic bacteria on calcite and silica precipitation in hot springs with water temperature above 90°C: evidence from Kenya and New Zealand. *Canadian Journal of Earth Sciences,* **33**, 72 – 83.

JONES, B., RENAUT, R.W. & ROSEN, M.R. 1996. High-temperature (>90°C) calcite precipitation at Waikite Hot Springs, North Island, New Zealand. *Journal of the Geological Society, London,* **153,** 481 – 496.

JORGENSEN, B.B., ISAKSEN, M.F. & JANNASCH, H.W. 1992. Bacterial sulphate reduction above 100°C in deep-sea hydrothermal vent sediments. *Science*, **258**, 1756-1757.

JUNIPER, S.K. & FORQUET. Y. 1988. Filamentous iron-silica deposits from modern and ancient hydrothermal sites. *Can. Mineral.,* **26**, 859 – 869.

JUNIPER, S.K. & SARRAZIN, J. 1996. Interaction of vent biota and hydrothermal deposits: Present evidence and future experimentation. *In:* Humphris, S.E. (ed.) *Seafloor Hydrothermal Systems: Physical, Chemical, Biological and Geological Interactions.* American Geophysical Union, Washington DC. 178 - 193.

JUNIPER, S.K. JONASSAN, I.V., TUNNICLIFFE, V., SOUTHWARD, A., 1992. Influence of a tube-building polycheate on hydrothermal chimney mineralisation. *Geology,* **20**, 895-898.

JUNIPER, S.K., SARRAZIN, J., 1995. Interaction of vent biota and hydrothermal deposits: Present evidence and future experimentation. In: Humphris, S.E., Zierenberg, R.A., Mullineaux L.S., Thomson, R.E., (Eds.), *Seafloor Hydrothermal Systems: Physical, Chemical, Biological, and Geological Interactions*. Amer. Geophys. U. Mono., **91**, 178-193.

JUNIPER, S.K., TEBO, B.M., 1995. Microbe - metal interactions and mineral deposition at hydrothermal vents. In: Karl, D.M. (Ed.) *The Microbiology of Deep-Sea Hydrothermal Vents.* CRC Press, Boca Raton. pp. 219-253.

JUNIPER, S.K., THOMSON, J.A.J. & CALVERT, S.E. 1986. Accumulation of trace elements in biogenic mucus at hydrothermal vents. *Deep-sea Research,* **33(3)**, 339 - 347.

KADKO, D. & BUTTERFIELD, D.A. 1998. The realtionship of hydrothermal fluid composition and crustal residence time to maturity of vent fields on the Juan de Fuca Ridge. *Geochemica et Cosochimica Acta.*, **62**, 1521 – 1533.

KADKO, D. AND MOORE, W. 1988. *Geochim. Cosmochim. Acta.,* **52**, 659 - 668.

KAPLAN, I. R., 1983, Stable isotopes of sulfur, nitrogen and deuterium in Recent marine environments. *In:* Arthur, M. A., Anderson, T. F., Kaplan, I. R., Veizer, J., and Land, L. S., (Eds.) *Stable Isotopes in Sedimentary Geology* Columbia, SEMP Short course, 2-1 - 2-108.

KAPLAN, I. R., EMERY, K. O., & RITTENBERG, S. C., 1963, The distribution and isotopic abundance of sulphur in recent marine sediments off southern California.*Geochimica et Cosmochimica Acta*, **27**, 297 - 331.

KAPLAN, I. R., & HULSTON, J. R., 1966, The isotopic abundance and content of sulfur in meteorites. *Geochimica et Cosmochimica Acta*, **30**, 479 - 496.

KARL, D.M. 1995. Ecology of free living, hydrothermal vent microbial communities. *In:* Karl, D.M. (ed.) *The Microbiology of Deep-Sea Hydrothermal Vents.* CRC Press, Boca Raton. 35 - 124.

KARL, D.M., TAYLOR, G.T., NOVITSKY, J.A., JANNASCH, H.W., WIRSEN, C.A., PACE, N.R., LANE, D.J., OLSEN, G.J. & GIOVANNONI, S.J. 1988. A

microbiological study of Guaymas Basin high temperature hydrothermal vents. *Deep-sea Research.* **35(5)**, 777 – 791.

KARL, D.M., WIRSEN, C.O. & JANNASCH, H.W. 1980. Deep-sea primary productivity at the Galapagos hydrothermal vents. *Science*, **207**, 1345-1347.

KELLEY, S.P. & FALLICK, A.E. 1990. High precision spatially resolved analysis of $\delta^{34}S$ in sulphides using a laser extraction technique. *Geochimica Cosmochimica Acta,* **54**, 883-888.

KELLEY, D.S., GILLIS, K.M. & THOMPSON, G. 1993. Fluid evolution in submarine magma-hydrothermal systems at the Mid-Atlantic Ridge. *J. Geophys. Res.,* **98**, 19579 – 19596.

KENNICUTT, M.C., BURKE, R.A., MACDONALD, I.R., BROOKS, J.M., DENOUX, G.J., & MACKO, S.A. 1992. Stable Isotope Partitioning in Seep and Vent Organisms - Chemical and Ecological Significance. *Chemical Geology*, **101,** 293-310.

KENT, P.W. 1960. *Biochemical Society Symposium.* **20.** Cambridge University Press, Cambridge. pp90.

KENT, V.C. & WILSON, B.R. 1985. A new mussel (Bivalvia, Mytilidae) from hydrothermal vents in the Galapagos Rift Zone. *Malacologia*, **26**, 253 – 271.

KNOLL, A.H. & WALTER, M.R. 1996 The limits of palaeontological information: finding the gold among the dross. *In:* Bock, G.R. & Goode, J.A. (eds.) *Evolution of Hydrothermal Ecosystems on Earth (and Mars?)* - Ciba Foundation Symposium; 202. John Wiley & Sons, London. 198 - 209.

KNOWLTON, A. & VAN DOVER, C.L. 1995. *High Rise Expedition Cruise Report.* (unpublished).

KONHAUSER, K.O., 1998. Diversity of bacterial iron mineralisation. *Earth Sci. Rev.* 43, 91-121.

KONHAUSER, K.O., 1997. Bacterial iron biomineralisation in nature. *Fems Microbiology Reviews*, **20**, 315-326.

KONHAUSER, K.O. 1996. Diversity of iron and silica precipitation by microbial mats in hydrothermal waters, Iceland: Implications for Precambrian iron formations. *Geology*. **24(4).** 323 – 326.

KONHAUSER, K.O., FISHER, Q.J., FYFE, W.S. & LONGSTAFF, F.J. 1998. Authigenic mineralisation and detrital clay binding in freshwater biofilms: The Brahmani River, India. *Geomicrobiology Journal,* **15**, 53 – 66.

KOSKI, R.A., CLAUGE, D.A. & OUDIN, E. 1983. Mineralogy and chemistry of massive sulphide deposits from the Juan de Fuca Ridge. *Geol. Soc. Am. Bull.* **95**, 930 – 945.

KOSKI, R.A., LONSDALE, P.F., SHANKS, W.C., BERNDT, M.E. & HOWE, S.S. 1985. Mineralogy and geochemistry of a sediment-hosted hydrothermal sulphide deposit from the Southern Trough of Guaymas Basin, Gulf of California. *Journal of Geophysical Research,* **90**, 6695 – 6707.

KUENEN, J.G., BEUDEKER, R.F., SHIVELY, J.M. & CODD, G.A. 1982. Microbiology of thiobacilli and other sulphur-oxidising autotrophs, mixertrophs and heterotrophs. *Philos. Trans. Roy. Soc. London B.,* **298**, 473 – 497.

LALLIER, F.H., GAILL, F., DESBRUYERES, D. & 33 OTHERS. 1999. The HOPE cruise: back to 13°N EPR. *International Ridge-Crest Research*, **8**, 19 – 22.

LALOU, C. 1992. Radiochemical dating of massive sulphide chimney sulphides from the cruise SO62-GEOMETEP 5. *In:* "SO62 (GEOMETEP 5) scientific report".

Federal Institute for Geosciences and Natural Resources, BMFT Project Nr: 03R393. pp 399.

LALOU, C., REYSS, J.-L., BRICHET, E., ARNOLD, M., THOMPSON, G., FOUQUET, G.Y. & RONA, P.A. 1993. New age data for Mid-Atlantic Ridge hydrothermal sites: TAG and Snakepit chronology revisited. *Journal of Geophysical Research*, **98.** 9705.

LAUBIER, L. & DESBRUYERES, D. 1985. Oases at the bottom of the ocean. *Endeavour, New Series,* **9(2)**, 67 - 77.

LAVOIE, D. 1997. Hydrothermal vent bacterial community in Ordovician ophicalcite, Southern Quebec Appalachians. *Journal of Sedimentary Research*, **67**, 47 – 53.

LEE, K. & SACKETT, W.M. 1998. The high temperature titration of biogenic silica. *Deep-Sea Research I,* **45**, 1015 – 1028.

LEO, R.F. & BARGHOORN, E.S. 1976. The silicification of wood. *Botanical Museum Leaflets,* **25 – 1**, *Botanical Museum, Harvard University, Cambridge, MA.*

LILLEY, M.D., BUTTERFILED, D.A., LUPTON, O.E.J.J.E., MACKO, S.A. & McDUFF, R.E. 1993. Anamolous CH_4 and NH_4^+ concentrations at an unsedimented Mid-Ocean Ridge hydrothermal system. *Nature*, **364**, 45 – 47.

LISTER, C.R.B. 1996 On the thermal balance of a subduction zone. *Tectonophysics,* **257(1),** 25-38.

LITTLE, C.T.S., CANN, J.R., HERRINGTON, R.J., MORISSEAU, M., 1999b. Late Cretaceous hydrothermal vent communities from the Troodos Ophiolite, Cyprus. *Geology*. 27, 1027-1030.

LITTLE, C.T.S., HERRINGTON, R.J., HAYMON, R.M., DANELIAN, T., 1999c. Early Jurassic hydrothermal vent community from the Franciscan Complex, San Rafael Mountains, California. *Geology*. 27, 167-170.

LITTLE, C.T.S., HERRINGTON, R.J., MASLENNIKOV, V.V., MORRIS, N.J. & ZAYKOV, V.V. 1997. Silurian hydrothermal vent community from the Southern Urals of Russia. *Nature,* **385**, 146 - 148.

LITTLE, C.T.S., HERRINGTON, R.J., MASLENNIKOV, V.V., MORRIS, N.J., ZAYKOV, V.V., 1997. Silurian hydrothermal vent community from the Southern Urals of Russia. *Nature.* 385, 146-148.

LITTLE, C.T.S., HERRINGTON, R.J., MASLENNIKOV, V.V., ZAYKOV, V.V., 1998. The fossil record of hydrothermal vent communities. In: Mills, R.A., Harrison, K., (Eds.), Modern Ocean Floor Processes and the Geological Record. *Geol. Soc. Lond. Spec. Publ.* **148,** 259-270.

LITTLE, C.T.S., MASLENNIKOV, V.V., MORRIS, N.J., GUBANOV, A.P., 1999a. Two Palaeozoic hydrothermal vent communities from the southern Ural mountains, Russia. *Palaeontology*. **42**, 1043 – 1078.

LONSDALE, P. 1977. Clustering of suspension-feeding macrobenthos near abyssal hydrothermal vents at oceanic spreading centers. *Deep-sea Research*, **24**, 857 - 863.

LONDALE, P. 1989. Segmentation of the Pacific-Nazca spreading center, 1°N – 20°S. *Journal of Geophysical Research*, **94**, 12197.

LOVLEY, D. R. 1990. Magnetite formation during microbial dissimilatory Fe(III) reduction. *In* R. B. Frankel and R. P. Blakemore (eds.), *Iron Biominerals.* Plenum Press, New York, N.Y. 151-166.

LOWELL, R.P. & GERMANOVICH, L.N. 1994. On the temporal evolution of high-temperature hydrothermal systems at ocean ridge crests. *Journal of geophysical research. Solid earth,* **99**, pp 565.

LOWELL, R.P., RONA, P.A. & VON HERZEN, R.P. 1995. Seafloor hydrothermal systems. *Journal of Geophysical Research,* **100B,** 327 - 352.

LOWENSTAM, H.A., 1981. Minerals formed by organisms. *Science.* **211,** 1126 - 1131.

LOWENSTAM, H.A., AND S. WEINER. 1989.*On Biomineralization*, Oxford University Press, New York.

LUPTON, J.E. & CRAIG, H. 1981. A major helium-3 source at 15°S on the East Pacific Rise. *Science*, **214**, 13 – 18.

LUPTON, J.E., BAKER, E.T., MOTTL, M.J., SANSONE, F.J., WHEAT, C.G., RESING, J.A., MASSOTH, G.L., MEASURES, C.L. & FEELY, R.A. 1995. Chemical and physical diversity of hydrothermal plumes along the East Pacific Rise, 8°45'N to 11°50'N. *Geophys. Res. Letts.,* **22**, 155 – 158.

LUTHER, G.W. 1991 Pyrite synsthesis via polysulphide compounds. *Geochim. Cosmochim. Acta.,* **55**, 2839 – 2849.

LUTHER, G.W., ROZAN, T.F., TAILLEFERT, M., NUZZIO, D.B., DI MEO, C., SHANK, T.M., LUTZ, R.A. & CARY, S.C. 2001. Chemical speciation drives hydrothermal vent ecology. *Nature,* **410**, 813 - 816.

MAGINN, E.J., LITTLE, C.T.S., HERRINGTON, R.J. & MILLS, R.A. 2002. Sulphide mineralisation in the deep sea polychaete, *Alvinella pompejana*: implications for fossil preservation. *Marine Geology*, **181**, 337 – 356.

MALAKHOV, V.V., POPELYAEV, I.S. & GALKIN, S.V. 1996. Microscopic anatomy of *Ridgeia phaleophiale* Jones, 1985 (Pogonophora, Vestimentifera) and the problem of the position of vestimentifera in the system of animal kingdom. I. General anatomy, obturacula and tentacles. *Russian Journal of Marine Biology,* **22(2)**, 63 - 74.

MALAKHOV, V.V., POPELYAEV, I.S. & GALKIN, S.V. 1996. Microscopic anatomy of *Ridgeia phaleophiale* Jones, 1985 (Pogonophora, Vestimentifera) and the problem of the position of vestimentifera in the system of animal kingdom. III. Rudimentary digestive system, troposome, and blood vascular system. *Russian Journal of Marine Biology,* **22(4)**, 189 - 198.

MALAKHOV, V.V., POPELYAEV, I.S. & GALKIN, S.V. 1996. Microscopic anatomy of *Ridgeia phaleophiale* Jones, 1985 (pogonophora, vestimentifera) and the problem of the position of vestimentifera in the system of animal kingdom. IV. Excretory and reproductive systems and coelom. *Russian Journal of Marine Biology,* **22(5)**, 249 - 260.

MALAKHOV, V.V., POPELYAEV, I.S. & GALKIN, S.V. 1996. Microscopic anatomy of *Ridgeia phaleophiale* Jones, 1985 (Pogonophora, Vestimentifera) and the problem of the position of vestimentifera in the system of animal kingdom. *Russian Journal of Marine Biology,* **22(3)**, 125 - 136.

MANDELBROT, B.B. & EVERTSZ, C.J.G. 1990. The potential distribution around growing fractal clusters. *Nature,* **348**, 143 – 145.

MANDERNACK, K.W. & TEBO, B.M. 1999. *In situ* rate measurements of microbial sulfide removal and CO_2 fixation at deep-sea hydrothermal vents and at the chemocline of Framvaren Fjord, Norway. *Marine Chemistry.* **66**:201-213.

MANDERNACK, K.W. & TEBO, B.M. 1993. Manganesse scavenging and oxidation at hydrothermal vents and in vent plumes. *Geochim. Cosmochim. Acta.,* **57**, 3907 – 3923.

MANN, S. 1983. Mineralisation in biological systems. *Structural Bonding*, **54**, 125 – 174.

MANN, S., J. WEBB, AND R.J.P. WILLIAMS 1989. *Biomineralization: Chemical and Biochemical Perspectives*. VCH Publishers, New York, pp 385.

MARCHIG, V. 2000. Hydrothermal activity on the Southern, ultrafast-spreading segment of the East Pacific Rise. *In:* Cronan, D (Ed.) *Handbook of Marine Mineral Deposits,* CRC Marine Science Series. pp 406

MARCHIG, V., ROSCH, H., LALOU, C., BRICHET, E. & OUDIN, E. 1988. Mineralogical zonation and radiochronological relations in a large chimney from the East Pacific Rise at 18°25'S. *Canadian Mineralogist*, 26, 541 – 554.

MARCHIG, V., PUCHELT, H., ROSCH, H. & BLUM, N. 1990. Massive sulphides from the ultra-fast spreading ridge, East Pacific Rise at 18-21°S: a geochemical stock report. *Marine Mining*, **9**, 459 – 493.

MARCHIG, V., BLUM, N. & ROONWAL, G. 1997. Massive sulphide chimneys from the East Pacific Rise at 7°24'D and 16°43'S. *Marine Geosources and Geotechnology,* **15**, 49 – 66.

MARTILL, D.M.; DAVIS, P.G. 1998. Did dinosaurs come up to scratch? *Nature,* **396**, 528 – 529.

MASSOTH, G.J., BUTTERFIELD, D.A., LUPTON, J.E., MCDUFF, R.E., LILLEY, M.D. AND JONASSON, I.R., 1989, Submarine venting of phase separated hydrothermal fluids at Axial Volcano, Juan de Fuca Ridge. *Nature,* **340**, 702-705.

McDUFF, R. E. AND J. M. EDMOND. 1982. On the fate of sulphate during hydrothermal circulation at Mid-ocean Ridges. *Earth Planet. Sci. Lett.***57**, 117 - 132.

McKAY, D.S., GIBSON, E.K., THOMAS-KEPTRA, K.L., VALI, H., ROMANEK, C.S., CLEMENT, S.J., CHILLIER, X.D.F., MAECHLING, C.R. & ZARE, R.N. 1996. Search for past life on Mars: possible relic biogenic activity in Martian meteorite ALH84001. *Science*, **273**, 924 – 930.

MCKIBBEN, M. A., & ELDRIDGE, C. S., 1990, Radical sulphur isotope zonation of pyrite accompanying boiling and epithermal gold deposition; a SHRIMP study of the Valles Caldera, New Mexico. *Economic Geology*, **85,** 1917 - 1925.

MCKIBBEN, M. A., & RICIPUTI, L. R., 1998, Sulphur isotopes by ion microprobe, *in:* McKibben, M. A., Shanks, W. C. I., and Ridlye, W. I., (Eds.) *Applications of micrananalytical techniques to understanding mineralizing processes: Reviews in Economic Geology.* Chlesea, Bookcrafters, Inc., 141-154.

MILLERO, FJ. 1986. The thermodynamics and kinetics of the hydrogen sulfide system in natural waters. *Mar. Chem* **18,** 121-147.

MILLS, R.A., THOMSON, J., ELDERFIELD, H., HINTON, R.W. & HYSLOP, E. 1994. Uranium enrichment in metaliferous sediments from the Mid-Atlantic Ridge. *Earth and Planetary Science Letters,* **124**, 35 - 47.

MIROSHNICHENKO, M.L., KOSTRIKINA, N.A., L'HARIDON, S., JEANTHON, C., HIPPE, H., STACKEBRANDT, E., & BONCH-OSMOLOVSKAYA, E.A. 2002. *Nautilia lithotrophica* gen. nov., sp nov., a thermophilic sulphur-reducing epsilon-proteobacterium isolated from a deep- sea hydrothermal vent. *International Journal of Systematic and Evolutionary Microbiology,* **52**, 1299-1304.

MIZUTANI, S. 1977. Progressive ordering of crystobolite in the early stages of diagenesis. *Contrib. Mineral. Petrol.* **61.** 129 – 140.

MOLLER, M.M., NIELSEN, L.P. & JORGENSEN, B.B. 1985. Oxygen responses and mat formation by *Beggiatoa* spp. *Applied and Environmental Microbiology,* **50(2)**, 373 – 382.

MONNIN C, JEANDEL C, CATTALDO T, DEHAIRS F. 1999. The marine barite saturation state of the world's oceans. *Marine Chemistry,* **65 (3-4),** 253-261

MOREIRA, D & LOPEZ-GARCIA, P. 2002. The molecular ecology of microbial eukaryotes unveils a hidden world. *Trends in Microbiology*, **10 (1)**, 31 – 36

MORTON, J.L., SLEEP, N.H., NORMARK, W.R & THOMKINS, D.H. 1987. Structure of the Southern Juan de Fuca Ridge from Seismic Reflection Records. *Journal of Geophysical Research,* **92,** 11315 - 11325.

MOXON, T.J. 1996. The co-precipitation of Fe^{3+} and SiO_2 and its role in agate genesis. *N. Jb. Miner. Mh.* **H.1.** 21- 36.

MURROWCHICK, J.B., BARNES, H.L., 1986. Marcasite precipitation from hydrothermal solutions. *Geochim. Cosmochim. Acta.* **50**, 2615-2630.

MUROWCHICK, J.B. 1990. Iron monosulphide precursors in low temperature pyrite and marcasite ancestry. *GSA Abstr. Prog.*, **22**, A207 (abstract).

NELSON, D.C. & FISHER, C.R. 1995. Chemoautotrophic and methanotrophic endosymbiotic bacteria at deep-sea vents and seeps. *In:* Karl, D.M. (ed.) *The Microbiology of Deep-Sea Hydrothermal Vents.* CRC Press, Boca Raton. 125 – 168.

NIELSEN, H., 1979, Sulfur isotopes, *in:* Jager, E., and Hunziker, J. C., (Eds.) Lectures in: *Isotope Geology.* Berlin, Springer, 283 - 312.

OHMOTO, H & RYE, R.O. 1979. Isotopes of sulphur and carbon. *In:* Barnes, H.L (Ed.). *Geochemistry of Hydrothermal Ore deposits.* J. Wiley & Sons. 509 – 567.

OHMOTO, H. 1986. Stable isotope geochemistry of ore deposits. *In:* (Valley, J.W., Taylor, H.P. & O'Neil, J.R.) *Stable Isotopes in High Temperature Geological Processes.* Reviews in Mineralogy, Mineral Society of America. **16**, 491 – 559.

OHMOTO, H., KAKEGAWA, T. & LOWE, D.R. 1993. 3.4 Billion-year-old biogenic pyrites from Barberton, South Africa: Sulphur isotope evidence. *Science*, **262**, 555 - 557 .

OHMOTO, H. AND GOLDHABER, M. 1997. Sulfur and carbon isotopes In: Barnes, H.L. ed. *Geochemistry of Hydrothermal Ore Deposits, V.III.* John Wiley & Sons, New York, 517-611.

ORTOLEVA, P., MERINO, E., MOORE, C. & CHADAM, J. 1987. Geochemical self-organisation I: Reaction-transport feedbacks and modeling approach. *American Journal of Science,* **287**, 979 – 1007.

OUDIN, E. 1983. Hydrothermal sulphide deposits of the East Pacific Rise (21°N): 1. Descriptive mineralogy. *Marine Mining,* **4,** 39 – 72.

OUDIN, E., CONSTANTINOU, G., 1984. Black smoker chimney fragments in Cyprus sulphide deposits. *Nature.* **308,** 349-353.

OUDIN, E.,MARCHIG, V. ROSCH, H., LALOU, C. & BRICHET, E. 1990. Observations of a natural occurance of CuS_2 in an hydrothermal chimney from the South-Pacific. *C. R. Acad. Sci. Ser. II.,* **310**, 221 - 226.

PARADIS, S., JONASSON, I.R., LE CHEMINANT, G.M., WATKINSON, D.H., 1988. Two zinc-rich chimneys from the plume site, Southern Juan de Fuca. *Canadian Mineralogist.* **26**, 637-654.

PENTECOST, A. 1991. Calcification processes in algae and cyannobacteria. *In*: Riding, R. (Ed.) *Calcareous Algae and Stromatolites.* Springer Verlag, Berlin. 3 - 20.

PENTECOST, A. 1996. High temperature ecosystems and their chemical interactions with their environment *In:* Bock, G.R. & Goode, J.A. (eds.) *Evolution of*

Hydrothermal Ecosystems on Earth (and Mars?) - Ciba Foundation Symposium; 202. John Wiley & Sons, London. 91 - 107.

PISCOTTO, K.A. 1981. Diagenetic trends in the siliceous facies of the Monteray shale in the Santa Maria region, California. *Sedimentology,* **28**, 247 – 571.

PLYUSNIN, A.M. & GUNIN, V.I. 1998. Self-organisation of the oxidation zone at sulphide deposits: A computer aided model. *Doklady Earth Sciences* **361A (6)**, 862 - 865.

PRACEJUS, B. & HALBACH, P. 1996. Do marine moulds influence Hg and Si precipitation in the hydrothermal JADE field (Okinawa Trough)? *Chemical Geology,* **130**, 87 – 99.

PRIEUR, D., CHAMROUX, S., DURAND, P., ERASUO, G., FERA, P.H., JEANTHON, C., LE BORGNE, L., MEVEL, G., VINCENT, P., 1990. Metabolic diversity in epibiotic microflora associated with the Pompeii worms *Alvinella pompejana* and *A. caudata* (Polychaetae: Annelida) from deep-sea hydrothermal vents. *Marine Biology*, **106**, 361 – 367

PURNELL, M.A. & VON BITTER, P.H. 1992. Blade-shaped conodont elements functioned as cutting teeth. *Nature*, **359**, 629 – 631.

RAISWELL, R & CANFIELD, D.E., 1998. Sources of iron for pyrite formation in marine sediments. *Amer. J. Sci.* **298**, 219-245.

RAISEWELL, R., BUCKLEY, F., BERNER, R.A. & ANDERSON, T.F. 1988. Degree of pyritisation of iron as a paleoenvironmental indicator of bottom water oxygenation. *Journal of Sedimentary Petrology,* **58**, 812 – 819.

RAISWELL, R., 1997. A geochemical framework for the application of stable sulphur isotopes to fossil pyritization. *J. Geol. Soc. Lond.* **154**, 343-356.

RAISWELL, R., WHALER, K., DEAN, S., COLEMAN, M. L., BRIGGS, D. E. G., 1993, A simple three-dimensional model diffusion-with-precipitation applied to localized pyrite formation in framboids, fossils and detrital iron minerals: Mar. Geol., 113, 89-100.

RAVIZZA, G., MARTIN, C.E., GERMAN, C.R. & THOMPSON, G. 1996. Os isotopes as tracers in seafloor hydrothermal systems: metalliferous deposits from the TAG hydrothermal area, 26°N Mid-Atlantic Ridge. *Earth and Planetary Science Letters,* **138**, 105 – 119.

REES, C.E., JENKINS, W.J. & MONSTER, J. 1978.The sulphur isotope geochemistry of ocean water sulphate. *Geochim. Cosmochim. Acta.,* **42**, 377 – 382.

REYES, A.O., MOORE, W.S. & STAKES, D.S. 1995. $^{228}Th/^{228}Ra$ ages of a barite-rich chimney from the Endeavour segment of the Juan de Fuca Ridge. *Earth and Planetary Science Letters,* **131**, 99 - 113.

RICHARDS, A.G. 1951. *The integument of arthropods.* University of Minnesota Press, Minneapolis, Minnesota.

RICKARD, D.T. 1975. Kinetics and mechanisms for pyrite formation at low temperatures. *American Journal of Science,* **275**, 636 – 652.

RILEY, J.P. & CHESTER, R. 1971. Introduction to Marine Chemistry. *Academic Press, New York.* pp 465.

RIMSTIDT, JD AND BARNES, HL 1980. The kinetics of silica-water reactions. *Geochimica et Cosmochimica Acta*, **44**, 1683-1699.

ROESIJADI, G AND EA CRECELIUS. 1984. Elemental composition of the hydrothermal vent clam *Calyptogena magnifica* from the East Pacific Rise. *Marine Biology.* **83,** 155-161.

RONA, P.A. 1988. Hydrothermal mineralisation at oceanic ridges. *Canadian Mineralogy*, **26**. 431.

RONA, P.A., KLINKHAMMER, G., NELSEN, T.A., TREFRY, J.H. & ELDERFIELD, H. 1986 Black smokers, massive sulphides and vent biota at the Mid-Atlantic Ridge. *Nature,* **321**, 33-37.

ROSENBAUER, R.J. & BISCHOFF, J.L. 1983. A note on the chemistry of seawater in the range 350°C – 500°C. *Geochem. Cosmochem. Acta.*, **47**, 139 – 144.

RUDALL, K.M. 1965. *In:* Goodwinn, T.W. & Rudall, K.M. *(Eds.). Aspects of insect biochemistry.* Academic Press, London & New York. pp83.

RUDNICKI, M.D. & ELDERFIELD, H. 1992. Helium, radon and manganese at the TAG and Snake-Pit Hydrothermal Vent Fields, 26° and 23°N, Mid-Atalntic Ridge. *Earth Planet. Sci. Lett.,* **113**, 307 – 321.

SAKAI, H., 1968. Isotope properties of sulphur compounds in hydrothermal processes. *Geochemical Journal*, **2**, 29-49.

SAKAI, H., MIYOSHI, T. & CHIBA, H. 1984. Experimental-study of sulphur isotope fractionation factors between sulphate and sulphide in high-temperature melts. *Geochem. J.,* **18,** 75 - 84.

SANDERS, N. K. AND J. J. CHILDRESS. 1990. Adaptations to the deep-sea oxygen minimum layer: Oxygen binding by the hemocyanin of the bathypelagic mysid, *Gnathophausia ingens Dohrn. Biol. Bull.* **178**: 286-294.

SANGSTER, D.F. & SCOTT, S.D. 1976. Precambrian strata bound, Cu-Zn-Pb sulphide ores of North America. *In:* Wolf, K.H. (ed.) *Hand Book of Strata-Bound and Stratiform Ore Deposits, Volume 6. Cu, Zn and Ag Deposits.* Elsevier, New York. 129 - 222.

SAVENKO, A.V. 1998. The coprecipitation of phosphorous, arsenic, and vanadium along with iron hydroxide in hydrothermal plumes. *Doklady Earth Sciences* **361A (6),** 866 – 868.

SCHOONEN, M.A.A., BARNES, H.L., 1991a. Reactions forming pyrite and marcasite from solution: I. Nucleation of FeS_2 below 100°C. *Geochim Cosmochim. Acta.* **55,** 1495-1504.

SCHOONEN, M.A.A., BARNES, H.L., 1991b. Reactions forming pyrite and marcasite from solution: II. Via FeS precursors below 100°C. *Geochim. Cosmochim Acta.* **55,** 1505-1514.

SCHULTZ, A., DELANEY, J.R. & MCDUFF, R.E. 1992. On the partitioning of heat flux between diffuse and point source seafloor venting. *Journal of Geophysical Research* , **97**, 12299 - 12314.

SCOTT, K. M., C. R. FISHER, J. S. VODENICHAR, E. NIX AND E. MINNICH., 1994. Effects of inorganic carbon concentrations, pH, and temperature on autotrophic carbon fixation by the chemoautotrophic symbionts of *Riftia pachyptila. Phys. Zool.* **67**: 617-638.

SCOTT, S.D. 1987. Seafloor polymetallic sulphides: Scientific curiosities or mines of the future. *In:* Teleki, Dobson, Moore & von Stackelberg (eds.), *Marine Minerals: Resource Assessment Strategies.* D. Reidel, Dordrecht. 277 - 300.

SEEWALD, J.S. & SEYFRIED, W.E., Jr. 1990. The effect of temperature on metal mobility in sub-seafloor hydrothermal systems: Constraints from basalt alteration experiments. *Earth Planetary Science Letters,* **101**, 308.

SEGONZAC, M. 1992. Les peuplemants associes a l'hydrothermalisme oceanique du Snake Pit (dorsal medio-atlantique: 23°N, 3480m): compostion et microdistribution de la megafaune. *C. R. Acad. Sci. Paris, Series III.,* **314**, 593 – 600.

SEYFRIED, W.E., Jr. & BISCHOFF, J.L. 1979. Low temperature basalt interaction with seawater: an experimental study at 70°C and 150°C. *Geochim. Cosmochim. Acta.,* **43**, 1937 – 1947.

SEYFRIED, W.E., Jr., & MOTTL, M.J. 1995. Geological setting and chemistry of deep-sea hydrothermal vents. *In:* Karl, D.M. (ed.) *The Microbiology of Deep-Sea Hydrothermal Vents.* , CRC Press, Boca Raton. 1 - 34.

SHANKS, W.C., BOHKLE, J.K. & SEAL, R.R. 1995. Stable Isotopes in Mid-Ocean Ridge hydrothermal systems: interactions between fluids, minerals, and organisms. *In:* Humphris, S.E. (ed.) *Seafloor Hydrothermal Systems: Physical, Chemical, Biological and Geological Interactions.* American Geophysical Union, Washington DC. 194 – 221.

SHOCK, E.L. 1996. Hydrothermal systems as environments for the emergence of life. *In:* Bock, G.R. & Goode, J.A. (eds.) *Evolution of Hydrothermal Ecosystems on Earth (and Mars?)* - Ciba Foundation Symposium; 202. John Wiley & Sons, London. 40 – 51.

SIEBURTH, J. McN. 1975 Contrary habits for redox-specific processes: methanogenesis in oxic waters and oxidation in anoxic waters. *In:* Sleigh, M.A. (ed) "Microbes in the Sea". *Ellis Horwood Ltd., Chichester.* 11 – 31.

SILLTOE, R.H., HANNINGTON, M.D. & THOMPSON, J.F.H. 1996. High sulphidation deposits in the volcanogenic massive sulphide environment. *Economic Geology*, **91**, 204 - 212.

SOMERO, G.N., CHILDRESS, J.J. & ANDERSON, A.E. 1989. Transport, metabolism, and detoxification of hydrogen sulphide in animals from sulphide-rich marine environments. *Reviews in Aquatic Sciences* , **1(4)** , 591-614.

SOUTHWARD, E.C. 1988. Development of the gut and segmentation of newly settled stages of *Ridgeia* (vestimentifera): Implications for relationship between vestimentifera and pogonophora. *Marine Biological Association, UK,* **68**, 465 - 487.

STAKES, D. & MOORE, W.S. 1991. Evolution of hydrothermal activity on the Juan de Fuca Ridge: Observations, mineral ages, and Ra isotope ratios. *Journal of Geophysical Research*, **96**, 21739 – 21752.

STAKES, D. & O'NEIL. 1982. Mineralogy and stable isotope geochemistry of hydrothermally altered oceanic rocks. *Earth Planet. Sci. Lett.*, **57**, 285 – 304.

STAUDIGEL, H., CHASTAIN, R.A. YAYANOS A., PLANK, T., VERDURMEN, E., DAVIES, G. SCHIFFMAN, P. 1998 Chemical exchange between volcanic glass and seawater: Effects of biomediation and temperature, *Geol. Soc. Am.*, **Annual Mtg**.

STEIN, H.J. & CATHLES, L.M. 1997. A special issue on the timing and duration of hydrothermal events. *Econmic Geology,* **92**, 763 – 765.

STEIN, C.A. & STEIN, S. 1994. Constraints on hydrothermal heat flux through the oceanic lithosphere from global heat flow. *J. Geophys. Res.* **99**, 3081 – 3096.

STEPHENS, G.C. 1975. Uptake of naturally occurring primary amines by marine annelids. *Biological Bulletin.* **149**. 397 – 407

STERN, K.H. 1954 The Liesgang Phenomenon. *Chem. Revs.* **54**, 79 - 99.

STETTER, K.O. 1982. Ultrathin mycelia-forming organisms from submarine volcanic areas having an optimum growth temperature of 105°C. *Nature*, **300**, 258 – 262.

STETTER, K.O. 1996. Hyperthermophiles in the history of life. *In:* Bock, G.R. & Goode, J.A. (eds.) *Evolution of Hydrothermal Ecosystems on Earth (and Mars?)* - Ciba Foundation Symposium; 202. John Wiley & Sons, London. 1 -10.

STRAUSS, H., 1997, The isotopic composition of sedimentary sulfur through time. *Palaeogeography, Palaeoclimatology, Palaeoecology,* **32**, 97 - 118.

STRAUSS, H., BENGTSON, S., MYROW, P. M., & VIDAL, G., 1992, Stable isotope geochemistry and palynology of the late Precambrian to Early Cambrian sequence in Newfoundland. *Canadian Journal of Earth Sciences*, **29**, 1662 - 1673.

SWEENEY, R.E. & CAPLAN, I.R. 1973. Pyrite framboid formation: Laboratory synthesis and marine sediments. *Economic Geology*, **68**, 618 - 634.

TAYLOR, C. D AND C. O. WIRSEN.1997. Microbiology and ecology of filamentous sulfur formation. *Science,* **277,** 1483-1485

THOMAS E, TUREKIAN KK, WEI KY. 2000. Productivity control of fine particle transport to equatorial Pacific sediment. *Global Biogeochemical Cycles,* **14 (3)**, 945-955

THOMPSON, G., BRYAN, W.B., BALLARD, R., HAMURO, K. & MELSON, W.G. 1985. Axial processes along a segment of the East Pacific Rise, 10-12°N. *Nature,* **318,** 429 - 433.

THOMPSOM, J.B. & FERRIS, F.G. 1990. Cyanobacterial precipitation of gypsum, calcite, and magnesite from natural alkaline lake water. *Geology*, **18**, 995 – 998.

THORSETH, I. H., T. TORSVIK, H. FURNES, AND K. MUEHLENBACHS. 1995b. Microbes play an important role in the alteration of oceanic crust. *Chem. Geol.* **126**, 137-146.

THODE, H. G., & MONSTER, J., 1965, Sulfur-isotope geochemistry of petroleum, evaporites, and ancient seas. *American Association of Petroleum Geologists, Memoir,* **4,** 367 - 377.

TIVEY, M.K. 1995. Modelling chimney growth and associated fluid flow at seafloor hydrothermal vent sites. *In:* Humphris, S.E. (ed.) *Seafloor Hydrothermal Systems: Physical, Chemical, Biological and Geological Interactions.* American Geophysical Union, Washington DC. 158 - 177.

TIVEY, M.K., HUMPHRIS, S.E., THOMPSON, G., HANNINGTON, M.D. & RONA, P.A. 1995. Deducing patterns of fluid flow and mixing within the active TAG hydrothermal mound, using mineralogical and geochemical data. *Journal of Geophysical Research,* **100**, p 12527 – 12555.

TOONEN, R.J. & PAWLIK, J.R. 1994. Foundations of gregariousness. *Nature,* **370**, 511 - 512.

TREWIN, N.H. 1996. The Rhynie cherts: An Early Devonian ecosystem preserved by hydrothermal activity. *In:* Bock, G.R. & Goode, J.A. (eds.) *Evolution of Hydrothermal Ecosystems on Earth (and Mars?)* - Ciba Foundation Symposium; 202. John Wiley & Sons, London. 131 - 144.

TRUDINGER P.A., MEYER T.E., BARTSCH R.G. & KAMEN M.D. 1985. The major soluble cytochromes of the obligately aerobic sulphur bacterium, *Thiobacillus Neopolitanus. Archives of Microbiology*, **141 (4),** 273 – 278.

TUFAR, W., 1990. Modern hydrothermal activity, formation of complex massive sulfide deposits and associated vent communities in the Manus back-arc basin (Bismarck Sea, Papua New Guinea). *Mitteilungen zur Osterreichen Geologischen Desaushaft.* **82**, 183-210.

TUNNICILFFE, V., 1992. Hydrothermal vent communities of the deep-sea. *American Scientist,* **80**, 336 - 349.

TUNNICLIFFE, V, & FOWLER, M.R. 1996. Influence of seafloor spreading on the global hydrothermal vent fauna. *Nature,* **379**, 531-533.

TUNNICLIFFE, V. 1991. The biology of hydrothermal vents: ecology and evolution. *Oceanography and Marine Biology Annual Reviews,* **29**, 319-407.

TUNNICLIFFE, V. AND JENSEN, R.G. (1987) Distribution and behaviour of the spider crab *Macroregonia macrochira Sakai* (Brachyura) around the hydrothermal vents of the northeast Pacific. *Canadian Journal of Zoology*, **65**, 2443-2449.

TUNNICLIFFE, V., FONTAINE, A.R., 1987. Faunal composition and organic surface encrustations at hydrothermal vents on the southern Juan de Fuca Ridge. *J. Geophys. Res.* **92**, 11303-11314.

TUNNICLIFFE, V., GARRETT, J.F. & JOHNSON, P.H. 1990. physical and biological factors affecting the behaviour and motility of hydrothermal vent tubeworms (vestimentiferans). *Deep-Sea Research*, **37**, 103 – 125.

TUTTLE, J.H., WIRSEN, C.O. & JANNASCH, H.W. 1983. Microbial activities in emitted hydrothermal waters of the Galapagos Rift vents. *Mar. Biol.,* **73**, 293 – 299.

URCUYO, I.A., MASOTH, G.J., MACDONALD, I.R. & FISHER, C.R..1998. *In situ* growth of the vestimentiferan *Ridgea Piscesae* living in highly diffuse low environments in the main Endeavour Segment of the Juan de Fuca Ridge. *Cahiers de Biologie Marine*, **39(3/4)**, 267 - 270.

URRUITA, M.M. & BEVERIDGE, T.J. 1993a. Mechanism of silicate binding on the bacterial cell wall in *Bacillus subtilis. J. Bacteriology*, **175**, 1936 – 1945.

URRUITA, M.M. & BEVERIDGE, T.J. 1994. Formation of fine-grained metal and silicate precipitates on a bacterial surface (*Bacillus subtilis*). *Chem. Geol.,* **116**, 261 – 280.

VAN DOVER, C.L. & FRY, B. 1994. Micro-organisms as food resources at deep-sea hydrothermal vents. *Limonology and Oceanography*, **39**, 51-57.

VAN DOVER, C.L. & HESSLER, R.R. 1990. Spatial variation in faunal composition of hydrothermal vent communities on the East Pacific Rise and Galapagos Spreading Center. *In:* McMurray, G.R. (ed.) *Gorda Ridge: A Seafloor Spreading Center in the United States Exclusive Economic Zone.* Springer Verlag, New York, 253-264.

VAN DOVER, C.L. 1994. *In situ* spawning of hydrothermal vent tubeworms (*Riftia pachyptila*). *Biological Bulletin*, **186**, 134-135.

VAN DOVER, C.L. 1995. Ecology of Mid-Atlantic Ridge hydrothermal vents. *In:* Parson, L.M., Walker, C.L. & Dixon, D.R. (eds.) *Hydrothermal Vents and Processes.* Geological Society Special Publication, **87**, 257-294.

VAN DOVER, C.L. 2000. The Ecology of Dee-Sea Hydrothermal Vents. *Princeton University Press, Princeton USA.* 352pp.

VAN DOVER, C.L., D. DESBRUYERES, M. SEGONZAC, T. COMTET, L. SALDANHA, A. FIALA-MEDIONI AND C. LANGMUIR. 1996. Biology of the Lucky Strike hydrothermal field. *Deep-Sea Research* **43,** 1509-1529.

VERATI, C, DE DONATO, P., PRIEUR, D., LANCELOT, J., 1999. Evidence of bacterial activity from micrometer-scale layer analyses of black-smoker sulfide structures (Pito Seamount Site, Easter microplate). *Chem. Geol.* **158,** 257-269.

VICSEK, T., CSERZO, M. & HORVATH, V.K. 1990. Self-affiine growth of bacterial colonies. *Physica A,* **167**, p315 – 321.

VICZEK, T. 1989. 'Fractal growth phenomena'. *World Scientific Publishing Co, Singapore.*

VON DAMM, K.L. & BISHOFF, J.L. 1987. Chemistry of hydrothermal solutions from the Southern Juan de Fuca Ridge. *Journal of Geochemical Research,* **92**, 11334 - 11346.

VON BITTER, P.H., SCOTT, S.D. & SCHENK, P.E. 1990. Early Carboniferous low-temperature hydrothermal vent communities from Newfoundland. *Nature*, **344**, 145 – 148.

WAGNER, T., BOYCE, A.J. AND FALLICK, A.E. (In Press) Laser combustion analysis of $\delta^{34}S$ of sulfosalt minerals: determination of the fractionation systematics and some crystal-chemical considerations. *Geochimica Cosmochimica Acta.*

WALTER, M. 1996. Old fossils could be fractal frauds. *Nature*, **383**, 385 - 386.

WALTER, M.R. 1996. Ancient hydrothermal ecosystems on Earth: A new palaeobiological frontier. *In:* Bock, G.R. & Goode, J.A. (eds.) *Evolution of Hydrothermal Ecosystems on Earth (and Mars?)* - Ciba Foundation Symposium; 202. John Wiley & Sons, London. 112 - 126.

WEISS, R.P., LONSDALE, P., UPTON, J.E., BAINBRIDGE, A.E. & CRAIG, H. 1977. Hydrothermal plumes in the Galapagos Rift. *Nature*, **267**, 600.

WESTALL, F. 1994. How bacteria fossilise: experimental observations and some theoretical considerations. *In:* Awramik, S.M. (ed.) *Death Valley International Stromatolite Symposium (Abstracts).* Laughlin, Nevada. 88 - 89.

WESTALL, F., BONI, L. & GUERZONI, E. 1995. The experimental silicification of microorganisms. *Palaeontology,* **38(3)**, 495 – 528.

WILBY, P. R.; WHYTE, M. A. 1995. Phosphatized soft tissues in bivalves from the Portland Roach of Dorset (Upper Jurassic). *Geological magazine,* **132(1),** 117 – 122.

WILBY, P.R., BRIGGS, D.E.G., RIOU, B. 1996.mineralisationof soft-bodied invertebrates in a Jurassic metaliferous deposit. Geology 24. 847-850.

WILBY, PHILIP R., BRIGGS, DEREK E., G., RIOU, BERNARD. 1996.mineralisationof soft-bodied invertebrates in a jurassic metalliferous deposit. *Geology,* **24(9)**, 847 – 851.

WILKIN, R.T., BARNES, H.L., 1996. Pyrite formation by reactions of iron monosulphides with dissolved inorganic and organic sulfur species. *Geochim. Cosmochim. Acta.* **60,** 4167-4179.

WILLIAMS, D.L. & VON HERZEN, R.P. 1974. Heat loss from the earth: New estimate. *Geology*, **2**, 327.

WILLIAMS, R.J.P. 1981. Physico-chemical aspects of inorganic element transfer through membranes. *Philos. Trans. R. Soc. London,* **B294**, 57 – 74.

WINN, C.D., COWEN, J.P. & KARL, D.M. 1995. Microbes in deep-sea hydrothermal plumes. *In:* Karl, D.M. (ed.) *The Microbiology of Deep-Sea Hydrothermal Vents.* CRC Press, Boca Raton. 255 - 273.

WOODRUFF, L.G., & SHANKS, W.C. 1988. Sulphur Isotope Study of Chimney Minerals and Vent Fluids from 21°N, East Pacific Rise - Hydrothermal Sulphur Sources and Disequilibrium Sulphate Reduction. *Journal of Geophysical Research-Solid Earth and Planets*, **93**, 4562-4572.

WRIGHT, D.W., HAYMON, R.M., WHITE, S.M.,& MACDONALD, K.C. 2002. Crustal Fissuring on the Crest of the Southern East Pacific Rise, 17°15'-40'S. *J. Geophys.l Res.-Solid Earth,* **107,** 1029 – 1042.

YOUNG, C.M., VAZQUEZ, E., METAXAS, A. & TYLER, P.A. 1996. Embryology of vestimentiferan tube worms from deep-sea methane/sulphide seeps. *Nature*, **381**, 514 - 516.

ZAL, F., 1998. Sulphide binding processes of *Riftia pachyptila* haemoglobins. *Biology*, **39,** 327 – 328.

ZBINDEN, M.; MARTINEZ, I.; GUYOT, F.; CAMBON-BONAVITA, M. A.; GAILL, F. 2001. Zinc-iron sulphide mineralisation in tubes of hydrothermal vent worms. *European Journal of Mineralogy,* **13**, 653 - 658.

ZBINDEN, M., LE BRIS, N., COMPERE, P., MARTINEZ, I., GUYOT, F. & GAILL, F. 2003. Mineralogical gradients associated with alvinellids at deep-sea hydrothermal vents. *Deep Sea Research Part I,* **50**, 269 – 280.

ZIERENBERG, R.A. & 27 OTHERS. 1998. The deep structure of a sea-floor hydrothermal deposit. *Nature*, **392**, 485 – 488.

"If I have seen further it is by standing on the shoulders of Giants"

Sir Isaac Newton

"Why are things as they are and not otherwise?"

Johannes Kepler

".....at the heart of science is an essential balance between two seemingly contradictory attitudes - an openness to new ideas, no matter how bizarre or counterintuitive, and the most ruthlessly skeptical scrutiny of all ideas, old and new"

Carl Sagan

"If we knew what it was we were doing, it would not be called research, would it?"

Albert Einstein

"The difference between the almost-right word and the right word is really a large matter - it's the difference between the lightning bug and the lightning"

Mark Twain

My sincerest, and heart felt thanks go to all of those who put their faith in me.....

.....I hope I haven't let you down.